Ultrahigh energy density physics and ion acceleration in nano- and microstructures

Inaugural-Dissertation

zur Erlangung des Doktorgrades der
Mathematisch-Naturwissenschaftlichen Fakultät der
Heinrich-Heine-Universität Düsseldorf

vorgelegt von

Vural Kaymak

geb. in Oberhausen

Düsseldorf
Oktober 2019

Aus dem Institut für Theoretische Physik I
der Heinrich-Heine-Universität Düsseldorf

Gedruckt mit der Genehmigung der
Mathematisch-Naturwissenschaftlichen Fakultät der
Heinrich-Heine-Universität Düsseldorf

Berichterstatter:
1. Prof. Dr. Alexander Pukhov
2. Prof. Dr. Dr. Carsten Müller
3. Prof. Dr. Malte Kaluza

Tag der mündlichen Prüfung:
12.12.2019

Abstract

The recent progress in the engineering of nanostructured materials and their promising features that come to light in numerous studies motivates their extensive investigation. Particularly nanowires have been shown to significantly enhance the absorption of laser light and consequently are potent candidates for the utilization as x-ray emitters and in fields such as high energy density physics, nuclear fusion and particle acceleration. In this thesis, the different applications of nanowire targets in laser-plasma interactions are illuminated by using PIC simulations. The major part of this work was conducted in a collaboration with experimental groups.

First, the ionization dynamics in carbon nanowires is analyzed. Optical field ionization takes place at the surfaces of the targets. Subsequently, impact ionization leads to ionization of the nanowire cores. The targets are fully ionized in a few laser cycles. Next, the occurrence of the Z-pinch in nanowires is investigated. It is seen that the laser light produces strong return currents, thereby generating an azimuthal magnetic field that in turn compresses the nanowires. In this process, tremendously high particle densities, temperatures and values in the ultrahigh energy density regime are produced.

One related parameter for quantifying the deposited laser energy into the target is the penetration depth of the heat. We conduct PIC simulations, which agree with the experimental results obtained by our collaborators at the Colorado State University, yielding a heating depth of at least four micrometers. We then use our numerical simulations to extrapolate to higher laser intensities. The results predict enormous pressures, exceeding even those produced in experiments that use spherical compression.

The deep penetration depth in the nanowire material also means that a large volume of near-solid matter is subject to heating. This, on the other hand, is a key requirement for the efficient emission of x-ray pulses from heated plasmas. We investigate this advantageous feature numerically by performing PIC simulations, which are used by our colleagues to conduct hydrodynamic simulations. It is found that nanowires are significantly more efficient x-ray emitters compared to flat targets. The simulations are also used to model the results of our partners' experimental findings, which obtain a record conversion efficiency of laser energy into picosecond x-ray pulses.

The efficient plasma heating is also studied with regard to a possible occurrence of fusion reactions. Our partners have conducted experiments and detected a record value of neutrons per pulse, implying an efficient drive of nuclear fusion. Motivated by these findings, we carry out numerical PIC simulations, which reveal the creation of energetic deuterons that enable the fusion reactions. Simulations at higher irradiation intensities predict a further increase of D-D fusion reactions.

Next, the impact of changing the laser wavelength from UV to midinfrared is examined. A longer wavelength relaxes the laser intensity requirement to access the relativistic regime and reduces disruptive preplasma formation. We perform PIC computations, which are used by our collaborators in Jena to produce synthetic emission spectra in order to confirm the results obtained by their experiments. Our simulations obtain a high laser light absorption of about 80 %, producing long-lasting keV-level plasma temperatures and highly charged ions.

The nanowire target parameters are evaluated also with respect to an enhanced proton acceleration. We carry out three-dimensional PIC simulations, which are used by our partners at the University of Michigan and the Colorado State University to validate their two-dimensional PIC calculations. These results are utilized to model experiments performed by our colleagues. The number of nanowires per focal spot is identified to be the crucial factor for an efficient laser-plasma interaction and thus for an improved proton acceleration.

The ion acceleration is also studied in an ultrathin foil with stamped hemispherical shells, in which besides the target normal sheath acceleration mechanism the radiation pressure acceleration becomes significant. Along with experimental results of our collaborators at the Heinrich-Heine-University in Düsseldorf, our PIC simulations prove that these targets are able to produce proton energies comparable to those achieved in large laser systems by only using joule-level laser pulses.

Zusammenfassung

Die jüngsten Fortschritte in der Konstruktion von nanostrukturierten Materialien und ihre vielversprechenden Eigenschaften, die in zahlreichen Studien zutage treten, motivieren ihre umfassende Untersuchung. Insbesondere in Nanodrähten wurde eine signifikant erhöhte Absorption von Laserlicht festgestellt, die sie zu leistungsstarken Kandidaten für die Verwendung als Röntgenquellen und in Bereichen wie der Physik von hohen Energiedichten, nuklearer Fusion und der Teilchenbeschleunigung machen. In dieser Dissertation werden die verschiedenen Anwendungsbereiche von Nanodrähten in Laser-Plasma-Wechselwirkungen in Form von PIC Simulationen beleuchtet. Der Großteil dieser Arbeit wurde in Zusammenarbeit mit experimentellen Gruppen ausgeführt.

Zuerst wird die Ionisationsdynamik in Kohlenstoffnanodrähten analysiert. An den Oberflächen der Targets findet optische Feldionisation statt. Anschließend führt Stoßionisation zu der Ionisation des Inneren der Nanodrähte. Die Targets sind in einigen Laserzyklen vollständig ionisiert. Als Nächstes wird das Auftreten des Z-Pinch-Effektes in den Nanodrähten untersucht. Es stellt sich heraus, dass die Laserwelle starke Ströme und dadurch ein azimutales Magnetfeld induziert, das wiederum die Nanodrähte komprimiert. In diesem Prozess werden enorm hohe Teilchendichten, Temperaturen und Werte im Regime ultrahoher Energiedichten erzeugt.

Ein verwandter Parameter, um die im Material deponierte Laserenergie zu charakterisieren, ist die Aufheiztiefe. Wir führen PIC Simulationen durch, die mit den experimentellen Ergebnissen unserer Kollegen an der Colorado State University übereinstimmen, welche eine Aufheiztiefe von mindestens vier Mikrometern ergeben. Folglich extrapolieren wir mit unseren Simulationen zu höheren Laserintensitäten, welche enorme Drücke prognostizieren, die sogar die Werte in Experimenten mit sphärischer Kompression übersteigen.

Das tiefe Eindringen in das mit Nanodrähten beschichtete Material bedeutet gleichzeitig, dass ein großes Materialvolumen bei annähernd Festkörperdichte aufgeheizt werden kann. Dies wiederum ist eine wichtige Bedingung für effiziente Röntgenstrahlung aus heißen Plasmen. Wir untersuchen diese Eigenschaft, indem wir numerische PIC Simulationen durchführen, welche anschließend von unseren Partnern verwendet werden, um hydrodynamische Simulationen auszuführen. Es stellt sich heraus, dass Nanodrähte im Vergleich zu flachen Targets signifikant bessere Röntgenquellen sind. Die Simulationen werden auch für die Modellierung der Ergebnisse aus den experimentellen Untersuchungen unserer Kollaborateure verwendet, welche einen Rekordwert für die Umwandlungseffizienz von Laserenergie zu pikosekunden langen Röntgenpulsen erreichen.

Das effiziente Aufheizen von Plasmen wird auch in Bezug auf das mögliche Vorkommen von Fusionsreaktionen studiert. Unsere Kollegen haben in Experimenten einen Rekordwert für Neutronenpulse gemessen, der sich auf das effiziente Antreiben von nuklearer Fusion zurückführen lässt. Dieses Ergebnis hat uns veranlasst, numerische Simulationen durchzuführen, welche auf energetische Deuteronen als Ursache hinweisen. Das Anwenden von höheren Bestrahlungsintensitäten prognostiziert eine Zunahme der D-D Fusionsreaktionen.

Weiterhin wird der Einfluss untersucht, der entsteht, wenn die Laserwellenlänge vom UV zum mittleren Infrarot verändert wird, da eine größere Wellenlänge die benötigte Intensität für das relativistische Regime reduziert und störendes Vorheizen des Plasmas verringert. Wir haben PIC Simulationen ausgeführt, welche von unseren Partnern aus Jena für die Berechnung von numerischen Emissionsspektren verwendet werden, um die in ihren Experimenten ermittelten Ergebnisse zu bestätigen. Unsere Simulationen ergeben eine hohe Laserlichtabsorption von etwa 80 %, die zu langlebigen keV-Plasmatemperaturen und Ionen in hohen Ladungszuständen führt.

Ferner wird die Fähigkeit der Nanodraht-Targets zu verstärkter Protonenbeschleunigung erforscht. Von uns durchgeführte dreidimensionale PIC Simulationen dienen unseren Partnern von der University of Michigan und der Colorado State University dazu, ihre zweidimensionalen PIC Berechnungen zu bestätigen. Diese Ergebnisse werden von ihnen eingesetzt, um ihre experimentellen Ergebnisse zu modellieren. Die Anzahl an Nanodrähten pro Laserfokus wird als der entscheidende Faktor für eine effiziente Laser-Plasma-Wechselwirkung und somit für verbesserte Protonenbeschleunigung identifiziert.

Die Ionenbeschleunigung wird auch in einer ultradünnen Folie mit eingestanzten Halbkugeln untersucht, in der neben des Target Normal Sheath Acceleration Mechanismus die Radiation Pressure Acceleration einen wesentlichen Einfluss hat. Unsere PIC Simulationen zeigen zusammen mit den experimentellen Ergebnissen unserer Kollegen von der Heinrich-Heine-Universität in Düsseldorf, dass das eingesetzte Target in der Lage ist, unter Verwendung von Laserpulsen von nur einigen Joule, Protonenenergien vergleichbar zu denen in großen Lasersystemen zu erzielen.

Eidesstattliche Erklärung

Ich versichere an Eides Statt, dass die Dissertation von mir selbständig und ohne unzulässige fremde Hilfe unter Beachtung der “Grundsätze zur Sicherung guter wissenschaftlicher Praxis an der Heinrich-Heine-Universität Düsseldorf” erstellt worden ist.

Ort, Datum	Unterschrift

Contents

Chapter 1

Introduction

The recent progress in technology allows to highly modernize industrial processes and everyday life, impacting the social environment as we know it in a perceptible way already today. The progressive efficiency of automation increasingly enables to break free from laboring and to pursue higher goals. The exploration of artificial intelligence will foreseeably speed up this development in a direction hardly imaginable today. If not abused, these trends offer the possibility to evolve as a civilization in many respects. In essence, these advances are owed to fundamental scientific research and particularly physics. Keeping this path will not just allow to further proceed the technological progress, but more importantly to gain a better understanding of nature. To pave the way for this journey in the long run, however, challenges such as increasing population, environmental issues and most notably the energy problem need to be overcome. One candidate for an energy source with promising features is the nuclear fusion, which is intensively studied and one of the driving motivations of plasma physics research.

The progress of plasma physics in the second half of the last century was motivated by space exploration and fusion. After controlled thermonuclear fusion research was started in the early 1950s and was declassified in 1958 at the second Geneva Conference on the Peaceful Use of Atomic Energy, it became official in 1972 when Nuckolls *et al.* published a paper about it in Nature [1]. Since then a lot of effort has been put into fusion research, especially in the large laser facilities such as the National Ignition Facility (NIF), in which *inertial confinement fusion* (ICF) is applied. In this scheme, deuterium and tritium containing fuel pellets are spherically irradiated by strong laser beams with the aim of achieving sufficiently high densities and temperatures to meet the requirements for thermonuclear fusion. While these laser pulses have a duration typically on the nanosecond scale ($10^{-9}\,$s), ultrashort pulses of femtosecond duration ($10^{-15}\,$s) allow for investigation of ultrafast phenomena on the femto- and picosecond scale. The technique called *chirped pulse amplification* (CPA) made it possible to massively increase the intensity of femtosecond laser pulses. It was first applied to lasers by Gerard Mourou and his co-worker in 1985 [2] and was recently awarded with the Nobel Prize (2018). Since the direct amplification of a short laser pulse would damage the optical elements due to overheating, the CPA first stretches the pulse to the picosecond scale, to give the components enough time to cool during the process. This is usually done with a set of diffraction gratings, which give the pulse a chirp, i.e. a continuous temporal frequency variation. The chirped pulse can then be amplified in a conventional way and recompressed by a compressor, performing the optical inverse process of the stretcher. Besides the transverse focusing that was already possible at that time, the CPA allowed for the first time the temporal compression of a laser pulse, which greatly increased the achievable irradiation intensities. At present, upcoming petawatt facilities pursue intensities as high as $10^{23} - 10^{24}\,\mathrm{W\,cm^{-2}}$ [3], enabling research in a variety of fields.

In the course of fusion research investigations a new inherent branch was created, that is motivated by the characteristic features occurring during fusion: the high energy density physics (HED). According to a report of the National Academy of Sciences in the U.S. [4], the threshold to the HED regime is positioned at energy densities above $1 \times 10^5\,\mathrm{J\,cm^{-3}}$, or, equivalently expressed in terms of pressures, 1 Mbar. The historical background of high energy density physics goes back to the 1930's, when the focussing of particles into small areas started with the development of particle accelerators, followed by nuclear weapons that created (uncontrollable) HED conditions in the 1940's. Then the attempt to achieve controlled thermonuclear fusion using the Z-pinch failed in the 1950's. The laser was invented and developed in the late 1950's and during the 1960's, which raised the question whether lasers are able to generate controlled fusion. After Nuckolls *et al.* stated in their key paper [1] that this might be possible, plans for ICF were implemented in the U.S., the Soviet Union, Europe and Japan. During the 1980's HED investigations with lasers became practical, after elaborate experiments for HED physics could be designed in facilities for inertial fusion and were sophisticated enough around 1979. The fast evolution of high-intensity laser pulses with sub-picosecond duration known as "ultrafast lasers" following the invention of CPA a few years later [2] further boosted HED research. Recent advances in laser technology, particle beam production, Z-pinch generators as well as the many distinguished existing or planned facilities with sophisticated laboratory instruments allow for exploration of matter under extreme conditions that were not accessible before. They approach those in astrophysical systems and help to understand exciting phenomena such as supernovae, astrophysical jets, accreting black holes and stellar and planetary interiors within a laboratory setup. The field of HED holds an extensive amount of new phenomena and relates to a large number of areas of physics such as plasma physics, laser and particle beam physics, intense radiation-matter interaction, condensed matter physics, nuclear physics and astrophysics. Moreover, the progress made in scientific highperformance computing has enabled to model many of the HED systems, which were out of reach before due to their complexity. Gaining knowledge about how to control HED matter in the laboratory will help to broaden our understanding of the universe by addressing fundamental questions such as: How do dramatic conditions as extreme temperature, pressure, density and electromagnetic fields affect matter? What was the character of matter in the beginning of the universe? How were mid-Z and high-Z elements created? On the other hand, also the fusion research as the initial key driver will benefit from advances made in HED physics.

The creation of matter in these extreme conditions is however a challenging task in conventional laser-target setups. The use of targets covered with nanowires have been found to be an efficient way to address this obstacle [5]. Nanomaterials are usually defined by a width of 1 nm to 100 nm, however there is no internationally acknowledged specification and different institutions use different definitions [6]. The first reported preparation of nanoparticles in the modern scientific age goes back to Michael Faraday in 1857, who synthesized a colloidal solution of gold nanoparticles [6]. Today, they gain in popularity owed to their material enhancing properties. They are used in solar cells [7], as antibacterial components in household appliances [6], in ferrofluids (liquid magnets) for tumor therapy [8] and magnetically deformable mirrors [9], and as constituent in the automobile industry to improve tyre adhesion as well as surface resistance and shine [6]. In the laser-plasma community, the capability of nano- and microstructures to enhance the absorption of laser pulses is also found to be beneficial in the acceleration of ions [10].

Finally, the exploration of matter in extreme conditions is of high interest and is expected to simultaneously lead to new insights in fundamental physics and open the path to applications for a foreseeable use in practice. The particular functionality of nanowire targets in this field is therefore a versatile and promising research topic and lie at the heart of this thesis. The goal of this work is to examine different aspects of these targets for suitability in the enhanced generation of high energy densities, x-ray emission, the production of fusion neutrons and proton acceleration. The method used for these investigations are numerical PIC simulations, either in purely theoretical studies or along with experimental measurements of collaborators.

1.1 Structure of the thesis

The theoretical framework needed to understand the terms and concepts used in the following chapters are introduced in chapter 2. After defining what a plasma is and which ionization mechanisms lead to its production, the interaction of laser fields with electrons in vacuum and with plasmas is discussed. The relevant laser energy absorption mechanisms in laser-plasma theory are then explained. Next, the role of the nanowire arrays in the context of high energy density physics is shown, along with some examples of applications. These sections cover the theory of the majority of studies presented. Subsequently, the topic of ion acceleration with its two important schemes (target normal sheath acceleration and radiation pressure acceleration) and some applications is introduced.

All results produced by the author are obtained by performing PIC simulations, which form the basis of the presented investigations. Chapter 3 explains the motivation for using PIC simulations, how its numerical algorithm works and describes the typical simulation scenario and its parameters.

The first results of this thesis are illustrated in chapter 4. It first deals with the ionization of the simple case of carbon nanowires. We show the temporal and spatial dynamics of ionization, which lead to the transformation of the initially solid material into the plasma state. Then we investigate the specific phenomenon of the Z-pinch, which occurs when certain laser-target parameter conditions are met. We illustrate how the laser pulse produces a return current, which leads to a self-generated magnetic field, causing the nanowire to compress itself. Next, we study the influence of the irradiation intensity with regard to the strength of the compression and the plasma temperatures.

Chapter 5 presents results on the depth of the heat penetration in laser-irradiated nanowire arrays. We carry out PIC simulations that are used to study the energy density and the charged states that accompany the heating. This data is evaluated by our collaborators at the Colorado State University to produce synthetic emission spectra that are compared to experimental measurements conducted by them. The numerical and experimental examination is done by using nanowires composed of two different materials, which have their own characteristic radiation. From that x-ray emission, the heating depth is inferred. Our PIC simulations are used to extrapolate to higher laser intensities to predict the plasma regime that can be accessed in this way.

In chapter 6 the capability of nanowire targets to produce x-ray emission in comparison to ordinary flat targets is investigated. The method consists of tailoring the laser-plasma parameters to meet conditions necessary for an improved x-ray emission. We construct a numerical model by performing PIC simulations that are used for hydrodynamic simulations and atomic kinetic simulations by our partners at the Colorado State University. The model helps to estimate the achieved plasma temperatures and the difference in radiation from nanowires and flat targets. The atomic kinetic simulations compute the relevant timescales for an enhanced emission of x-rays and explain the different radiation characteristics in both types of targets. The numerical simulations were conducted at the conditions of experiments performed by our collaborators, which both show an enhanced radiation from the nanowire targets.

The possibility to produce ultrahigh energy densities in nanowire targets raises the question, if fusion can be achieved using them. To address this question, our partners at the Colorado State University conducted experiments using neutron detectors, which confirm the presence of neutrons generated in fusion reactions. The results are illustrated in chapter 7. We perform PIC simulations that are used to obtain the particle spectra with regard to the necessary energies for fusion. Further simulations are conducted by us at irradiation intensities higher than those in the experiments, allowing our colleagues to estimate the neutron production yield. Our simulations are also used by them to evaluate where in the targets the fusion reactions can take place.

Chapter 8 demonstrates an alternative way to produce a relativistic laser-plasma interaction in nanowire targets. The works presented in the preceding chapters employed laser pulses of sufficiently high intensities to achieve this. In this study, a midinfrared laser pulse with a longer wavelength of 3.9 µm is used, in contrast to the 400 nm laser wavelength in the previous chapters. This choice allows using lower intensities, which practically reduces the harmful effect of a preplasma formation. In this manner, it is investigated what plasma parameters can be achieved by using laser pulses of only 20 mJ energy, compared to the joule-level beams used in related works before. To understand the physics in the present laser-plasmas, we conduct PIC simulations, which are subsequently evaluated and used by our colleagues at the Friedrich-Schiller-University and the Helmholtz Institute in Jena to run FLYCHK simulations. The numerical results are compared to experiments our collaborators have performed.

As is known and will be described, nanowire arrays facilitate enhanced laser energy absorption. This was shown to lead to improved hot electron production, which enhances the acceleration of protons [10]. Chapter 9 deals with the influence of the nanowire targets on the proton acceleration. An experimental parametric study is conducted by our collaborators at the University of Michigan, using nanowires with different lengths, diameters and distances. We have performed three-dimensional PIC simulations, which allowed our partners in Michigan and at the Colorado State University to validate their two-dimensional PIC simulations. The latter are used by them along with their experimental results to find out what role the different parameters play.

Another kind of target is investigated in chapter 10. This time an ultrathin foil with imprinted hemispheres are irradiated by femtosecond laser pulses. The goal is to determine the gain in energetic accelerated protons that can be achieved in those targets compared to ordinary foils. We use our PIC simulations to analyze the different dynamics in those targets and compare the data with experimental spectra obtained by our collaborators at the Heinrich-Heine-University in Düsseldorf.

The thesis is concluded in chapter 11. The work is summarized and its relevance is considered within the research field. The chapter closes with concluding thoughts about possible extending works and the future development of the research subject.

The sources used for the introduction above were [11–13] for the background of fusion and the chirped pulse amplification, references [4, 14–16] for the part about high energy density physics and [6] for the short paragraph about nanostructures.

The cgs unit system will be used throughout the whole thesis. In the summaries at the end of chapters 4- 10 a description of the author's contribution will be given.

1.2 Publications

During the time of the doctorate the following publications by the author or with contributions of the author were published:

- V. Kaymak, A. Pukhov, V. N. Shlyaptsev, and J. J. Rocca. *Strong ionisation in carbon nanowires.* Quantum Electronics 46(4), 327–331 (2016)
- V. Kaymak, A. Pukhov, V. N. Shlyaptsev, and J. J. Rocca. *Nanoscale Ultradense Z-Pinch Formation from Laser-Irradiated Nanowire Arrays.* Phys. Rev. Lett. 117, 035004 (2016)
- C. Bargsten, R. Hollinger, M. G. Capeluto, V. Kaymak, A. Pukhov, S. Wang, A. Rockwood, Y. Wang, D. Keiss, R. Tommasini, R. London, J. Park, M. Busquet, M. Klapisch, V. N. Shlyaptsev, and J. J. Rocca. *Energy penetration into arrays of aligned nanowires irradiated with relativistic intensities: Scaling to terabar pressures.* Science Advances 3(1) (2017)
- R. Hollinger, C. Bargsten, V. N. Shlyaptsev, V. Kaymak, A. Pukhov, M. G. Capeluto, S. Wang, A. Rockwood, Y. Wang, A. Townsend, A. Prieto, P. Stockton, A. Curtis, and J. J. Rocca. *Efficient picosecond x-ray pulse generation from plasmas in the radiation dominated regime.* Optica 4(11), 1344–1349 (2017)
- A. Curtis, C. Calvi, J. Tinsley, R. Hollinger, V. Kaymak, A. Pukhov, S. Wang, A. Rockwood, Y. Wang, V. N. Shlyaptsev, and J. J. Rocca. *Micro-scale fusion in dense relativistic nanowire array plasmas.* Nature Communications 9(1), 1077 (2018)
- Z. Samsonova, S. Höfer, V. Kaymak, S. Ališauskas, V. Shumakova, A. Pugžlys, A. Baltuška, T. Siefke, S. Kroker, A. Pukhov, O. Rosmej, I. Uschmann, C. Spielmann, and D. Kartashov. *Relativistic Interaction of Long-Wavelength Ultrashort Laser Pulses with Nanowires.* Phys. Rev. X 9, 021029 (2019)
- M. Dozières, G. M. Petrov, P. Forestier-Colleoni, P. Campbell, K. Krushelnick, A. Maksimchuk, C. McGuffey, V. Kaymak, A. Pukhov, M. G. Capeluto, R. Hollinger, V. N. Shlyaptsev, J. J. Rocca, and F. N. Beg. *Optimization of laser-nanowire target interaction to increase the proton acceleration efficiency.* Plasma Physics and Controlled Fusion 61(6), 065016 (2019)
- V. Kaymak, E. Aktan, M. Cerchez, B. Elkin, M. Papenheim, R. Prasad, A. Pukhov, H.-C. Scheer, A.-M. Schroer, O. Willi, and B. Aurand. *Boosted acceleration of protons by tailored ultra-thin foil targets.* Scientific Reports 9(1), 18672 (2019)

Chapter 2

Theoretical basics

2.1 Laser-Plasma interaction

This thesis deals with the interaction of strong laser pulses with (near-)solid matter, where the material is strongly ionized and transferred into the plasma state. The following sections are therefore meant to introduce the basic concepts in laser-plasma interactions such as the definition of a plasma (section 2.1.1), the ionization processes (section 2.1.2), the values characterising the laser pulse and the relativistic motion of free electrons (section 2.1.3), the relevant parameters describing the propagation of laser light in plasmas (section 2.1.4) as well as laser absorption mechanisms (section 2.1.5). The information of these sections can be found in textbooks [11, 12, 14, 25–28] and reviews and publications [4, 13, 15, 16, 29, 30], which were used as sources (besides the referenced publications at the respective positions).

2.1.1 Plasma basics

A plasma is generally speaking a substance that is disassembled into its negatively charged electrons and positively charged ions. Besides the solid, liquid and gaseous states, the plasma state is considered as the fourth state of matter. Nearly all the matter in the universe is assumed to be in the plasma state. In particular, the sun and generally stellar interiors as well as interstellar hydrogen are plasmas. In contrast to this, the matter on earth is mainly in the other three states and only a few examples like lightning bolts and auroras represent naturally occurring plasmas. Plasmas exist in fluorescent tubes and neon signs, and are also created artificially in the laboratory.

The basic difference between the states of matter is the binding energy between the constituent particles, which is high in the solid, moderate in the liquid and basically absent in the gaseous state. The presence of one of those states in a given material depends on the kinetic energy of its atoms or molecules, i.e., on its temperature. Therefore, one way a plasma can be produced is by increasing the temperature of a given material, which will eventually lead to ionization of the atoms. Another way to create a plasma is a gas discharge, in which an electric field is applied across an ionized gas. The free electrons are accelerated in the field and gain kinetic energies high enough to free further electrons by collisions with atoms. Historically, gas discharges initiated plasma research when in the 1920's Langmuir, Tonks and their collaborators observed an electric oscillation in a rarefied gas discharge and referred to it as "plasma oscillation". Of particular importance for this work is the field ionization directly carried out by an external field, which in the present context stems from a laser pulse and turns the material into a plasma. The relevant ionization mechanisms will be described in the next section.

An important property of plasmas is the "*quasineutrality*", which means that without external forces there are no large electric fields or net charges on macroscopic distances L, as they cancel out on a microscopic level. When an external test charge is introduced, freely moving charges of the plasma will surround it and effectively screen its potential ϕ_0. This screening can be calculated in a simple model by solving Poisson's equation to yield

$$\phi = \phi_0 e^{-r/\lambda_D}, \tag{2.1}$$

where λ_D is the so-called *Debye length*

$$\lambda_D = \left(\frac{k_B T_e}{4\pi n_e e^2} \right), \tag{2.2}$$

with k_B the Boltmann constant, n_e the electron number density, e the electron charge and T_e the electron temperature. The contribution of the much heavier ions is neglected due to their lower mobility, particularly on short timescales of femtoseconds. The Debye length is a measure of the shielding distance, i.e. the distance over which the electric field of the test particle can be felt by the plasma particles, as the potential (Eq. 2.1) diminishes much more rapidly than the bare Coulomb potential for $r \gtrsim \lambda_D$. As one would expect, the Debye length decreases with the electron density n_e, as more electrons can shield more efficiently. A higher temperature increases the Debye length, as it is the kinetic motion of the particles that overcomes the electric potential and prevents the charge sheath from collapsing into the screened test particle. The shielding is a consequence of the *collective behaviour* in the plasma, resulting from the long-ranged electromagnetic forces that all participating particles exert on each other. To consider an ionized gas in a meaningful way as a plasma, the dimensions L of the system need to be much larger than the *Debye length*,

$$\lambda_D \ll L. \tag{2.3}$$

This ensures that local charge perturbations are screened on a distance shorter than the extension of the system, such that the plasma is mostly free of large fields. On the other hand, an adequate shielding requires a large number of particles in the sheath, which can be expressed as the number of particles in the *Debye-Sphere*

$$N_D = \frac{4}{3}\pi \lambda_D^3 n_e. \tag{2.4}$$

The second condition for a plasma then reads

$$N_D \gg 1 \tag{2.5}$$

and is required for the collective character of plasmas.

2.1.2 Ionization

The process in which atoms and molecules release electrons is called ionization. A neutral gas needs to undergo this procedure to become a plasma. Ionization can be caused by external fields or by collisions. Both mechanisms are relevant for the present work, as laser pulses can act as an external field interacting with the surface of the target, ionizing the material up to a certain degree.

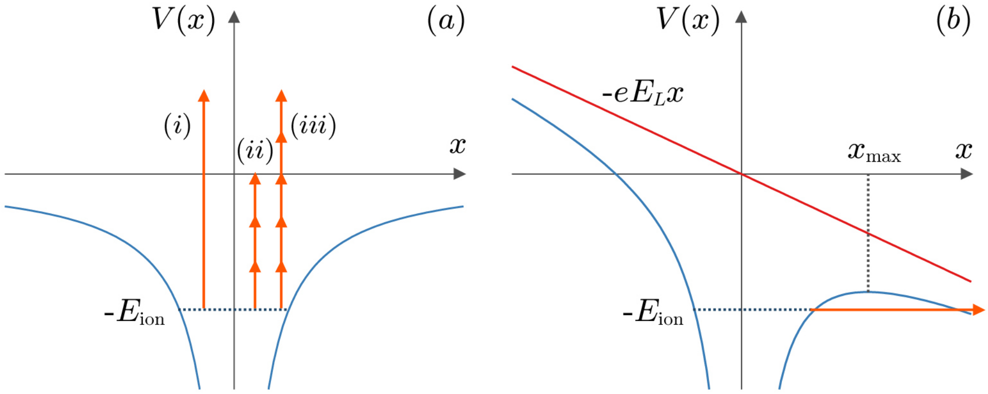

Figure 2.1: Schematic illustration of the electron bound by the ionization potential E_{ion} in the Coulomb potential of an atom. (a) The three ionization mechanisms for an unperturbed Coulomb potential are the (i) photoelectric effect, (ii) multiphoton ionization and (iii) above-threshold ionization. (b) An external field E_L strong enough to suppress the Coulomb barrier allows the electron to escape by tunnelling.

The strength of the electric field or laser intensity determines if an ionization event takes place. The electron to be ionized is assumed to be situated in the Coulomb potential of the atom, as illustrated in Fig. 2.1(a). The electron can either absorb a high-frequency photon (*photoelectric effect*) or several lower frequency photons (*multiphoton ionization*, MPI) to gain enough energy to overcome the ionization potential E_{ion} and be released from the atom. After the MPI was first measured in the 1960's, it was found in the late 1970's that electrons can absorb energies beyond the ionization potential by absorbing more photons than necessary for the ionization (*above-threshold ionization*, ATI). A higher light intensity provides a higher photon density and thus a higher probability for ionization. These considerations, however, assume that the Coulomb potential is not perturbed by the external field. This is not the case when the applied field approaches the electric field strength E_a that operates in an atom

$$E_a = \frac{e}{a_B^2} \approx 5.1 \times 10^9\,\mathrm{V\,cm^{-1}} \tag{2.6}$$

at the Bohr radius

$$a_B = \frac{\hbar^2}{m_e e^2} = 5.3 \times 10^{-9}\,\mathrm{cm}, \tag{2.7}$$

where $\hbar$ is the Planck constant divided by 2π, m_e the electron mass and c the speed of light. It is practical for comparison to compute the corresponding intensity

$$I_a = \frac{cE_a^2}{8\pi} \approx 3.4 \times 10^{16}\,\mathrm{W\,cm^{-2}}. \tag{2.8}$$

Laser intensities I_L greater than I_a will assuredly lead to ionization of any material, although lower values might also suffice when MPI occurs. The Keldysh parameter γ classifies which ionization mechanism will take place and is defined as the ratio [31]

$$\gamma = \sqrt{\frac{E_{\text{ion}}}{2E_{\text{os}}}} \tag{2.9}$$

of the ionization potential E_{ion} and the quiver energy of an oscillating electron [31]

$$E_{\text{os}} = \frac{e^2 E_L^2 (1+\alpha^2)}{4 m_e \omega^2} \tag{2.10}$$

in a laser pulse with frequency ω and electric field E_L, and $\alpha = 1$ for circular polarization and $\alpha = 0$ for a linear one. The MPI will be the dominant mechanism for large values of the Keldysh parameter, $\gamma \gg 1$. However, in the opposing case, $\gamma \ll 1$, the electron will either tunnel through the barrier or be released spontaneously. A simple model to describe this *optical field ionization* (OFI) is the mechanism called *barrier suppression ionization* (BSI). In this scenario, the electron is positioned in the initially unperturbed Coulomb potential [Fig. 2.1(a)], which becomes bent due to the presence of the external field [Fig. 2.1(b)] that is assumed to be static since the laser frequency is usually lower than that of atomic transitions. The resulting barrier (on the right hand side of Fig. 2.1(b)) lies below the ionization potential $-E_{\text{ion}}$ for $x \gg x_{\text{max}}$, where x_{max} is the position of the local maximum, such that the electron can quantum mechanically tunnel through the barrier. In their comprehensive study, Ammosov, Delone and Krainov have investigated the tunneling probability, known as the ADK model [32]. When the resulting local maximum $V(x_{\text{max}})$ of the perturbed potential is suppressed to or even below the ionization potential, the electron can escape directly. The threshold laser intensity can be found by equating the perturbed potential and the ionization potential, which yields [12]

$$I_{\text{BSI}} \approx 4 \times 10^9 (E_{\text{ion}}/\text{eV})^4 Z^{-2}\,\text{W}\,\text{cm}^{-2}, \tag{2.11}$$

where Z is the ion charge. For high-density (near-solid) targets of interest in this thesis, collisional ionization will take over from optical field ionization after a sufficient number of electrons have been ionized. That is particularly important for the deeper area of a (locally) solid target, in which the laser light cannot penetrate, as we will see in the section 2.2.1. A widely used simple empirical estimation for the electron impact cross section σ was provided by Lotz [33]

$$\sigma = \sum_{i=1}^{N} a_i q_i \frac{\ln(E/E_{\text{ion}})}{E E_{\text{ion}}} \left\{1 - b_i \exp[-c_i(E/E_{\text{ion}} - 1)]\right\}, \tag{2.12}$$

where a_i, b_i and c_i are empirical parameters and E the energy of the colliding electron. The summation goes over the N subshells of the atom, starting at the outermost shell with $i = 1$, where q_i is the number of equivalent electrons of a subshell.

2.1.3 Free electron in a laser field

According to Eq. 2.11, laser pulses with intensities up to $10^{16}\,\text{W}\,\text{cm}^{-2}$ are capable of ionizing the electrons on the outer atomic shells [13]. Pulses with intensities above this value, which we deal with in the context of this work, will therefore ionize the target already with its leading front. Thus, the peak of the pulse will interact with a plasma and, depending on the interaction configuration, will face single electrons or bunches of electrons (see chapters 4 and 10). The plane wave of a laser field with the wavelength λ propagating in the z direction can be described by its vector potential

$$\vec{A}(\vec{r},t) = \mathrm{Re}\left\{\vec{A_0}e^{i\psi}\right\}, \tag{2.13}$$

where $\psi = kz - \omega t$ is the phase, $\omega = kc$ the dispersion relation in vacuum with $k = 2\pi/\lambda$ and

$$\vec{A_0} = A_0 \left\{ \begin{array}{ll} \hat{e_y} & \text{for linear polarization (LP)} \\ \hat{e_y} \pm i\hat{e_x} & \text{for circular polarization (CP)} \end{array} \right. , \tag{2.14}$$

the polarization. The electric and magnetic fields $\vec{E}$ and $\vec{B}$ of the wave can then be expressed as

$$\vec{E} = -\frac{1}{c}\frac{\partial}{\partial t}\vec{A} = \mathrm{Re}\left\{\frac{i\omega}{c}\vec{A_0}e^{i\psi}\right\} \tag{2.15}$$

and

$$\vec{B} = \nabla \times \vec{A} = \mathrm{Re}\left\{i\vec{k} \times \vec{A_0}e^{i\psi}\right\}. \tag{2.16}$$

The equation of motion for an electron can be derived from the Euler-Langrange equation of the corresponding Lagrange function and yields the Lorentz force

$$\vec{F_L} = -e\left(\vec{E} + \frac{\vec{v}}{c} \times \vec{B}\right), \tag{2.17}$$

where the magnetic field component is neglectable for non-relativistic electrons with velocity $|\vec{v}| \ll c$. In that case the motion is dictated by the electric field and the equation of motion can be integrated to yield

$$\frac{\vec{v}}{c} = \frac{eA_0}{m_e c^2}\mathrm{Re}\left\{\frac{\vec{A_0}}{A_0}e^{i\psi}\right\}, \tag{2.18}$$

where maximum velocity of the electron is given by the dimensionless parameter introduced as the relativistically normalized laser vector potential

$$a_0 = \frac{eA_0}{m_e c^2}. \tag{2.19}$$

The relativistic threshold is therefore given by $a_0 = 1$, when the electron quiver velocity approaches the speed of light. The laser amplitude a_0 and the peak laser intensity I_0 are often used synonymously, their relation can be derived by averaging the poynting vector $\vec{S}$ over a laser period

$$\begin{aligned} I_0 = \left\langle|\vec{S}|\right\rangle = \left\langle\frac{c}{4\pi}|\vec{E} \times \vec{B}|\right\rangle = \frac{\pi}{2}\frac{m_e^2 c^5}{e^2}\frac{\zeta a_0^2}{\lambda^2} \\ = \frac{1.37 \times 10^{18}}{(\lambda/\mathrm{\mu m})^2}\zeta a_0^2\,\mathrm{W\,cm^{-2}}, \end{aligned} \tag{2.20}$$

where $\zeta = 1$ for linear polarization and $\zeta = 2$ for circular polarization. These basic variables can now be used to consider the electron motion. By making use of the variable $\tau = t - z(t)/c$, the equations of motion for an electron can be expressed as [29]

$$\frac{\mathrm{d}}{\mathrm{d}\tau}x = ca_x, \qquad \frac{\mathrm{d}}{\mathrm{d}\tau}y = ca_y, \qquad \frac{\mathrm{d}}{\mathrm{d}\tau}z = c\frac{a^2}{2}, \tag{2.21}$$

for a given normalized laser amplitude $\vec{a}(\tau)$ with $\vec{a} = e\vec{A}/(m_e c^2) = (a_x, a_y, a_z)^T$ and $|\vec{a}| = a$. Choosing the simple case of a linearly polarized plane wave $\vec{a} = a_0 \cos(\omega\tau)\hat{e}_y$ and an electron initially at rest with $\vec{r}(\tau = 0) = \vec{0}$, its trajectory takes the form [29]

$$\begin{aligned} y(\tau) &= \frac{c a_0}{\omega} \sin(\omega\tau), \\ z(\tau) &= \frac{c a_0^2}{4} \left[\tau + \frac{1}{2\omega} \sin(2\omega\tau) \right]. \end{aligned} \tag{2.22}$$

Besides the oscillatory (figure-8) motion in the $y - z$ plane, the longitudinal component contains a drift, which is given by [29]

$$z_d(t) = \frac{a_0^2}{a_0^2 + 4} ct \tag{2.23}$$

in the laboratory frame. While the transverse component is linear in a_0, the longitudinal motion is proportional to a_0^2. Consequently, the electron is pushed forward strongly by the $\vec{v}/c \times \vec{B}$ part of the Lorentz force for large laser amplitudes $a_0 \gg 1$, whereas it mostly oscillates transversal for lower intensities $a_0 \ll 1$. Besides the cycle-averaged force that pushes electrons towards lower intensities in transversally focused pulses, the $\vec{v}/c \times \vec{B}$ term is also called *ponderomotive force*. As we will see, this behaviour at relativistic intensities is of crucial importance for the results obtained in chapters 4 and 10.

2.1.4 Laser propagation in plasmas

In the next step, we consider the interaction of the laser light with the plasma as a whole. When the target is already in a plasma state caused by the ionizing leading front of the laser pulse, the free electrons will be accelerated by the electric field. Due to the restoring force of their corresponding atoms, they will however be forced to oscillate around the ions with the *(electron) plasma frequency*

$$\omega_p = \sqrt{\frac{4\pi n_e e^2}{m_e}}, \tag{2.24}$$

where the plasma is assumed to be cold, i.e. the thermal electron motion is neglected and the ions are immobile. To understand the propagation of the electromagnetic wave in the plasma, we need to consider the corresponding dispersion relation

$$\omega^2 = \omega_p^2 + c^2 k^2, \tag{2.25}$$

which differs from the vacuum dispersion relation by the additional plasma frequency term. For a light wave of given frequency ω, the wave number will be modified in the plasma to $k = \sqrt{\omega^2 - \omega_p^2}/c$. An increased electron density and thus an increased plasma frequency (Eq. 2.24) will lead to a smaller wavenumber, up to a point where it becomes zero and then imaginary. This cut-off happens for $\omega = \omega_p$, which occurs at the *critical density*

$$n_{\mathrm{cr}}(\lambda) = \frac{m_e \omega^2}{4\pi e^2} \approx 1.1 \times 10^{21} (\lambda/\mu\mathrm{m})^{-2}\,\mathrm{cm}^{-3}. \tag{2.26}$$

A light wave cannot propagate in a plasma that has an electron density $n_e \geq n_{\mathrm{cr}}$, because the wave number becomes imaginary and the electrons screen the light out by their oscillations. Note that for relativistic electrons the mass is modified to $m_e' = \gamma m_e$, where $\gamma = [1 - (v/c)^2]^{-1/2}$ is the relativistic factor, which alters the plasma frequency to $\omega_p' = \omega_p/\gamma$ and increases the critical density

$$n_{\mathrm{cr}}' = \frac{m_e \gamma \omega^2}{4\pi e^2} = \gamma n_{\mathrm{cr}}. \tag{2.27}$$

At relativistic intensities, the mass gain of the electrons causes their oscillations to slow down, which raises the threshold density of the material for entry of light into the plasma at fixed wavelength. This effect is called *relativistically induced transparency.* In the case that the plasma has a higher particle density than the (relativistic) critical density (also called *overcritical*, *supercritical* or *overdense*), the wave will only penetrate into the target up to the *skin depth* δ. A plasma of a density below the critical density is correspondingly called *underdense.* The skin depth is given by the attenuation of the wave to the e^{-1} value

$$e^{ikz} = e^{-\sqrt{\omega_p^2 - \omega^2} z/c} = e^{-z/\delta}, \qquad \delta = \frac{c}{\sqrt{\omega_p^2 - \omega^2}} \approx \frac{c}{\omega_p}. \tag{2.28}$$

The approximation on the right hand side is for highly overdense targets with $n/n_{\mathrm{cr}} \gg 1$ and yields a practical estimation of the skin depth. The irradiation will lead to heating of the matter, and with enough time (like in the long-pulse cases in ICF), the built-up pressure causes the material to blow off with approximately the *ion sound speed* [12]

$$c_s = \sqrt{\frac{Z k_B T_e}{m_i}} \approx 3.1 \times 10^7 \sqrt{(k_B T_e)/\mathrm{keV}} \sqrt{Z/A}\, \mathrm{cm\, s^{-1}}, \tag{2.29}$$

where m_i is the ion mass and A the atomic number. Under the assumption of an isothermal expansion, the particle density will have an exponential decaying profile on a length scale [12]

$$L = c_s t_{\mathrm{L}} \approx 0.26 \sqrt{(k_B T_e)/\mathrm{keV}} \sqrt{Z/A}\, t_{\mathrm{fs}}\, \mathrm{nm}, \tag{2.30}$$

after the pulse has interacted, where $t_{\mathrm{L}} = 10^{-15}\, (t_{\mathrm{fs}}/\mathrm{fs})/\sqrt{2\ln(2)}\, \mathrm{s}$ is the e^{-1} laser duration and t_{fs} the full width at half maximum (FWHM) pulse duration in femtoseconds. A representative example for the studies in this work is a 400 nm laser pulse of 60 fs duration and a fully ionized carbon target with 1 keV-1 MeV electron temperatures, which yields lengths of $L/\lambda = 0.04 - 1.2$. This scale can be considered as a steep density profile compared to the expansion on the scale of hundreds of micrometers in ICF setups with $L/\lambda \approx 100$. This consideration assumes that the *contrast* of the laser is sufficiently high. It is given by the intensity ratio of the main pulse and the pedestal or *prepulse* that is created by *amplification of spontaneous emission* (ASE). A too low contrast leads to heating of the target by the prepulse, giving rise to a premature target ablation called *preplasma* before the arrival of the main pulse. Either way, the extent of the ablated underdense plasma plays an important role for the absorption mechanism of the laser energy. Unlike in a perfect step-like overcritical density profile, the laser pulse can enter an undercritical plasma up to the point where the critical density is reached. This is shown schematically in Fig. 2.2 for a step-like profile, which is assumed to stay unchanged while an exponentially decreasing preplasma is formed, which is $n_e(z) = 1\, n_{\mathrm{cr}}$ for $z = -L \ln(n_0) \approx 5$.

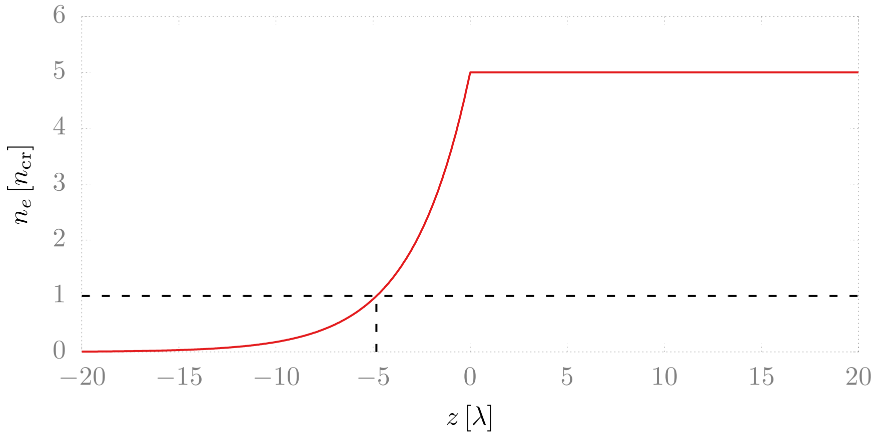

Figure 2.2: Step-like electron density profile $n_e(z) = n_0\,\theta(z)$ with an exponential preplasma $n_e(z) = n_0\,e^{z/L}$ for $n_0 = 5\,n_{\mathrm{cr}}$ and $L = 3\,\lambda$, where $\theta(z)$ is the Heaviside step function.

2.1.5 Laser absorption

To understand the absorption of laser energy into the target, it is appropriate to take interparticle collisions into account. This can be done by supplementing the equation of motion of the electrons (Eq. 2.17)

$$\vec{F}_L = -e\left(\vec{E} + \frac{\vec{v}}{c} \times \vec{B}\right) - m_e \nu_{ei} \vec{v} \tag{2.31}$$

with a collisional term in the underdense part of a plasma, where ν_{ei} is the electron-ion collision frequency. It is an important parameter for the classification of the absorption mechanism and is given by [27]:

$$\nu_{ei} \propto Z n_e T_e^{-3/2}. \tag{2.32}$$

The electrons oscillate in the laser field and convert energy drawn from the laser pulse into thermal energy by performing collisions with the ions, which is referred to as *collisional absorption* or *inverse Bremsstrahlung*. This mechanism is dominant for plasmas with high densities, high charges and low temperatures. When the laser intensities were comparably low ($10^{12} - 10^{14}\,\mathrm{W\,cm^{-2}}$) in the late 1980's, the absorption was justifiably assumed mainly collisional. After the accessible intensities increased, the present theoretical models started to deviate from the experimental measurements. This is owed to the increased plasma temperature that scales with the irradiation intensity. On the other hand, the effective collision frequency ν'_{ei} also depends on the electron quiver velocity v_{os} [34, 35]

$$\nu'_{ei} \approx \frac{v_{\mathrm{th}}^3}{(v_{\mathrm{os}}^2 + v_{\mathrm{th}}^2)^{3/2}} \nu_{ei}, \tag{2.33}$$

which reduces the collision frequency if it is on the order of the thermal electron velocity v_{th}. Beyond intensities of $\approx 10^{15}\,\mathrm{W\,cm^{-2}}$, the collision frequency is sufficiently reduced to render the collisions ineffective [12]. Therefore, collisionless absorption mechanisms were needed to be able to understand the absorption at higher temperatures. Some well-known collisionless absorption schemes are *resonance absorption*, and two for this thesis relevant ones, *vacuum heating* and *$\vec{j} \times \vec{B}$ heating*.

In resonance absorption, an oblique p-polarized pulse, i.e. one that has an electric field component along the particle density gradient, reaches the critical density surface (where $n_e = n_{\mathrm{cr}}$) and tunnels through it. There it resonantly (frequency of light and plasma coincide) generates a plasma wave, which first grows during some laser periods and finally realizes the absorption via damping of the wave. At low intensities, this takes place by collisions, and at high intensities by particle trapping and wave breaking [27].

A sharp vacuum-plasma interface with a short length scale L (Eq. 2.30), which is exceeded by the electron quiver amplitude, however, cannot support the generation of electron plasma waves. An obliquely incident pulse, with a component perpendicular to the target surface and negligible magnetic field, will pull electrons out of the target in the first half-period. After the electric field changes its direction, it will push the electrons back into the target. Besides a penetration into the skin depth, the electric field is shielded out. Therefore the electrons can, without being influenced by the electric field, gain energy due to their excursion and carry it into the target, where their energy is transferred to other particles by collisions and is thus effectively absorbed. This vacuum heating mechanism was first investigated by Brunel [36] and is also called *Brunel mechanism*.

The picture in another collisionless absorption mechanism, that was first explained by Kruer and Estabrook [37], is similar to the vacuum heating as it deals with a step-like target profile where electrons are accelerated directly by the laser field. This time the magnetic component $\vec{v}/c \times \vec{B}$ of the Lorentz force is taken into account, which has double the frequency of the laser light. Taking a linearly polarized light wave $\vec{E}(z,t) = E_0(z)\sin(\omega t)\hat{e}_y$ results in a longitudinal force component [12]

$$f_z = -\frac{m}{4}\frac{\partial}{\partial z} v_{\mathrm{os}}^2(z)(1 - \cos 2\omega t), \tag{2.34}$$

where $v_{\mathrm{os}}(z)$ is the electron quiver velocity in propagation direction imposed by the field component. The first term is responsible for the longitudinal electron motion that leads to a forward push of the electron density profile, which is of importance for the hole boring that will be described in section 2.3.3. The second term is the high-frequency "$\vec{j} \times \vec{B}$" component that leads to heating, similar to a parallel electric field component along a density gradient. As it originates from the magnetic part of the Lorentz force, it becomes relevant for relativistic intensities (see section 2.1.3) and works best at normal incidence. It is present at any but circular polarization, since the oscillatory component is absent there. The circular polarization is of particular interest, when heating of the target is undesirable (see section 2.3.3).

2.2 Nanophotonics in ultrahigh energy density physics

As we have seen in the previous section, the laser-plasma parameters of interest here lead to a situation in which a laser pulse effectively interacts with a solid-density plasma, since it does not have enough time to expand during the ultrashort pulse duration. In the case where no absorption takes place, the plasma acts, besides a penetration depth given by the skin depth into the overdense region (Eq. 2.28), as a reflecting mirror due to the shielding by its overcritical density. If absorption is facilitated, however, the laser energy can be deposited in matter of much higher densities than in typical nanosecond scenarios. This can lead to unmatched energy densities, which is the characteristic feature of the HED research field. Reviews and reports about this relatively new and rapidly developing field can be found in [5, 12, 19, 21, 38, 39], which were used as sources (besides the referenced publications at the respective positions) for the coming sections 2.2.1 and 2.2.2. In the section 2.2.1 a motivation for the use of nanowires is given, followed by some applications in section 2.2.2.

2.2.1 The role of nanowires

Depositing high energies into small volumes of matter is synonymous with the creation of hot and dense plasmas. The term “hot dense plasma” can be defined as plasmas with keV-scale temperatures and solid particle densities [40], which corresponds to energy densities of $\approx 1 \times 10^7\,\mathrm{J\,cm^{-3}}$. At an order of magnitude higher, the *ultrahigh energy density* (UHED) conditions ($1 \times 10^8\,\mathrm{J\,cm^{-3}}$ [5]) come closer to the astrophysical values and their investigations as outlined in the introduction 1. The access to this plasma regime was however limited to the very expensive ICF experiments with the world’s strongest lasers [41, 42]. Therefore, it is of high interest to find ways to produce those extreme states of matter in compact laboratory setups. The applications additionally require a larger plasma volume under these conditions, which makes this undertaking a very challenging task.

In the last decade, several experiments have been conducted, whose results approach this plasma regime. Some experiments used metallic films surrounded by plastic at high densities, irradiated with picosecond or subpicosecond laser pulses of 3 - 40 J energy, yielding sub-keV temperatures [43–46]. A higher temperature of 5 keV was obtained by using 0.8 ps, 400 J laser pulses, which dropped down to 0.6 keV at a depth of 1.3 µm [47]. Another experiment using laser pulses of high energy (100 J and 0.5 ps duration), irradiating aluminium foils buried in plastic gave rise to a temperature of 0.6 keV at $1.5\,\mathrm{g\,cm^{-3}}$. A more recent study used 45 fs laser pulses of only 200 mJ energy and achieved a temperature of 1.8 keV at an electron density of $2 \times 10^{23}\,\mathrm{cm^{-3}}$ in metallic films, however only within a depth of 150 nm [48].

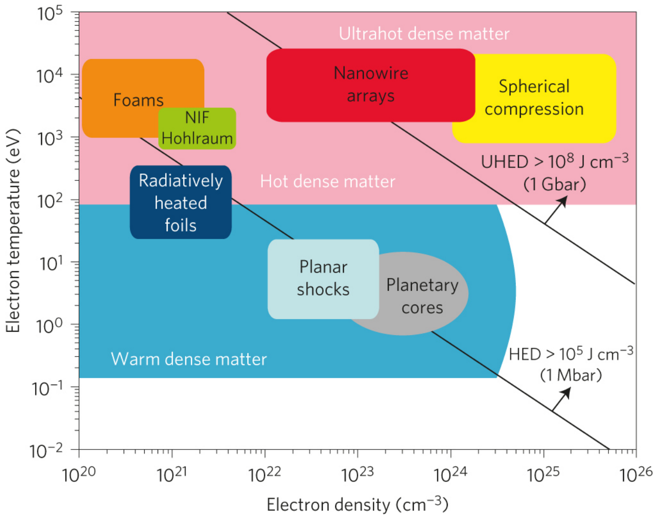

Figure 2.3: Plasma parameter (temperature T over electron density n_e) diagram illustrating the new plasma regime accessible with laser-irradiated nanowire arrays compared to other HED plasmas. The two diagonal lines represent the limits of HED ($1 \times 10^5\,\mathrm{J\,cm^{-2}}$) and UHED ($1 \times 10^8\,\mathrm{J\,cm^{-2}}$). Reprinted by permission from Macmillan Publishers Ltd: Nature Photonics [5], copyright 2013.

On the other hand, some reports about enhanced x-ray emission from "smoked" targets [49], nanospheres [50], gratings [51, 52], and "velvet" nanowire targets [53–56] indicated increased laser absorption and possible formation of hot and dense plasmas. These promising results motivated a study on laser-irradiated vertically aligned nanowire arrays by our experimental collaborators at the Colorado State University [5], which at the time of its publication was the first report of volumetric heating of plasmas with keV temperatures and near-solid-densities by using femtosecond laser pulses of only 0.5 J energy. The laser pulse was found to be absorbed almost completely and the created energy density was calculated to be $2 \times 10^9\,\mathrm{J\,cm^{-3}}$, which deeply lies in the ultrahigh energy density regime. The created conditions were comparable to those generated in the NIF experiments in the hot spot of the compressed fusion capsule [57] and are exceeded only in the case of a highly compressed capsule [58]. In fact the remarkable plasma parameters that can be achieved by irradiation of nanowire arrays create a new plasma regime (Fig. 2.3), accessible with only joule-class tabletop lasers.

In general, nanostructures are capable of focussing the light down to subwavelength dimensions, bypassing the diffraction limit. This allows to control the flow of light, possibly in form of optical circuits in the future, which would be superior to today's technology of electronic integrated circuits. Their prominent high absorptivity is also due to the coupling of light into plasmons on the surface of the metal-vacuum interface, which are subsequently guided by the structure and lose energy to the material due to ohmic losses [59]. The field dealing with this topic is called *nanophotonics* [59].

The uniqueness of these targets in terms of UHED matter is characterized by the space between the wires that, in contrast to solid targets, allows the laser light to enter into the structure and propagate down to the substrate. Once the light is in the gaps, it can be absorbed by interacting with the material surface. Optical field ionization will first ionize the outer layer of the wires to a certain charge, given by the laser intensity and the ionization potentials of the material (see section 2.1.2). Since the laser pulses of interest here are femtosecond pulses, the laser light deals with locally solid dense objects where the vacuum heating takes place (see section 2.1.5). The electrons are ripped off from the surfaces by the laser electric field and are pushed back into the wires, effectively absorbing laser energy by carrying the gained energy into the inner core and transferring it by collisions. In this process, these electrons also perform impact ionization to produce charge states above those that can be generated by field ionization (see section 2.1.2). At some point, the heating caused by collisions with the energetic electrons will lead to explosion of the wire structures and filling of the initially empty interwire gaps. In this way, an overcritical surface layer is formed at the tips, which prohibits further laser light penetration. These considerations point out two critical factors, which need to be taken into account if one desires to draw on the full potential of these targets. First, the laser pulse duration is required to be sufficiently short to ensure the absorption to be as high as possible before the structure explodes. This requirement dynamically depends on the timescale of expansion, which is given by the temperature (Eq. 2.29) and thus by the irradiation intensity. Another dependence is given by the target parameters such as the wire thickness, as thinner wires are decomposed easier than thicker ones. The second important factor is the laser contrast. The prepulse of a low-contrast laser can cause the delicate nanowires to dissolve even before the arrival of the main pulse, which negates the advantage of light penetration into the wire gaps.

The realization of this absorption scenario is shown in Fig. 2.4 as published in the opening work of our collaborators [5]. On the basis of the electric field the free propagation of the laser beam in the structure is demonstrated [Fig. 2.4(a)] up to $t = 55$ fs, where the plasma starts to dissolve at the tip [Fig. 2.4(c)] and effectively closes the gaps at $t = 85$ fs -120 fs.

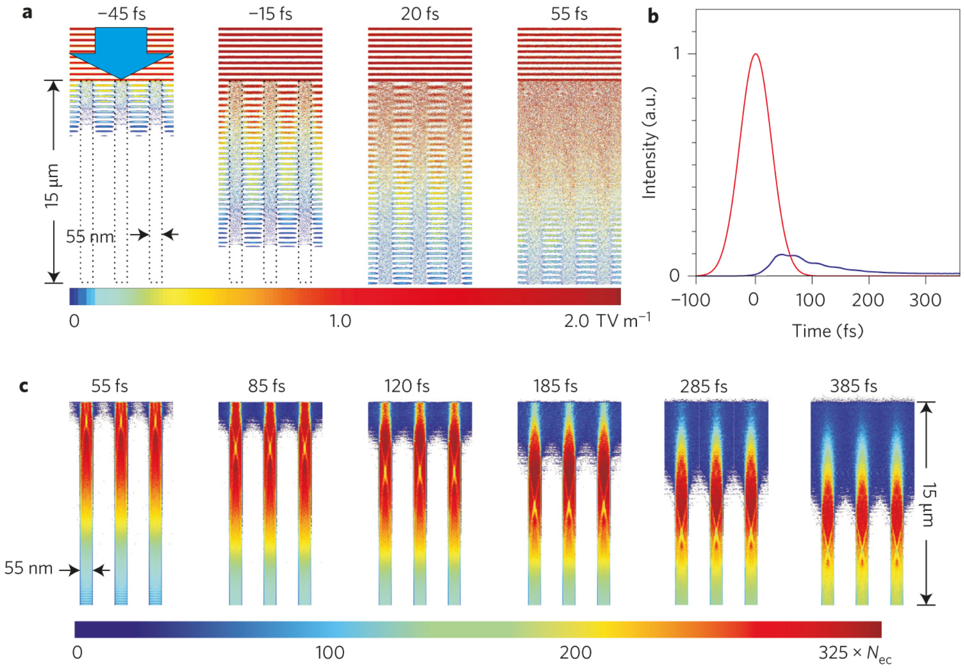

Figure 2.4: PIC simulation results from nickel nanowires 55 nm in diameter and 15 µm in length and a center-to-center distance corresponding to a filling factor of 12 % of solid density (see Eq. 3.24 in section 3.5 below). The irradiating 400 nm laser pulse has an intensity of $5 \times 10^{18}\,\mathrm{W\,cm^{-2}}$. (a) Time evolution of the electric field strength [$\mathrm{TV\,m^{-1}}$]; (b) laser intensity that impinges onto the target (red) and is reflected from it (blue); (c) time evolution of the electron particle density [n_{cr}] with $n_{\mathrm{cr}} = 7 \times 10^{21}\,\mathrm{cm^{-3}}$. The time is normalized to the peak of the laser pulse reaching the tip of the wire at $t = 0$ fs. Adapted (cut-out from the original) by permission from Macmillan Publishers Ltd: Nature Photonics [5], copyright 2013.

The pulse is shown to be almost fully absorbed [Fig. 2.4(b)] after $t \approx 100$ fs, indicating that a favourable set of laser-target parameters was chosen that eventually leads to a volumetric heating of near-solid-density material and the generation of extreme plasma parameters. This publication has aroused interest and, as we will see in the following chapters, it has initiated further studies on laser-irradiated nanowire arrays for fundamental studies and HED applications.

2.2.2 Applications

The generation of plasmas in extreme conditions as those of UHED in the laboratory is helpful to address some fundamental key questions about the universe, as outlined above, for instance by modeling astrophysical phenomena [60–62].

Furthermore, it is presumed to support achieving the aim of inertial confinement fusion [63, 64] by gaining a better understanding of the basic physics. In ICF high energy beams of laser light or particles are fired at the fuel pellet which causes an implosion and shock waves that symmetrically travel towards the center of the target where a sufficiently high particle density drives fusion reactions before the target plasma cools due to expansion. If the required fusion conditions are met, fusion reactions will take place, which produce new particles that further heat the surrounding fuel. As a result, a burn wave propagates in outward direction and fuses the remaining fuel. Generally, different nuclear reactions are possible, two of which are [38]

$$\begin{aligned} \mathrm{D} + \mathrm{D} &\longrightarrow \mathrm{He}^3\ (0.82\mathrm{MeV}) + \mathrm{n}\ (2.45\mathrm{MeV}), \\ \mathrm{T} + \mathrm{D} &\longrightarrow \mathrm{He}^4\ (3.52\mathrm{MeV}) + \mathrm{n}\ (14.06\mathrm{MeV}), \end{aligned} \tag{2.35}$$

where D and T denote a deuterium and a tritium atom, which are hydrogen isotopes with one and two additional neutrons, respectively. As products of the reaction, a neutron n and He^3 are produced. He^3 is, besides the ordinary Helium atom He^4, a stable isotope, but with two protons and only one neutron. The neutron that is produced in the reactions carries the characteristic kinetic energy of either 2.45 MeV or 14.06 MeV, which can be measured by detectors to infer the occurrence of fusion reactions. The sum of kinetic energies of the resulting products, Δmc^2, arises from the so-called *mass defect* Δm, which stands for the amount of mass that is missing in the conservation of mass after the fusion has taken place. It is the conversion of this mass to energy that represents a potential energy source.

As a prominent example, the fusion generated in ICF experiments powered by multi-kilojoule lasers produce a large number of neutrons. Typical yields are $10^4 - 5 \times 10^5$ neutrons per joule [65–67]. A record of 4×10^9 neutrons per joule was recently achieved at the NIF by using 1.9 megajoule laser pulses [64]. Furthermore, fusion neutrons from D-D reactions were generated by using laser pulses with sub-nanosecond duration and a few hundred joules of energy [68, 69], and by using petawatt lasers systems [70–72]. The realization of fusion is, however, not limited to the ICF research and other large facilities. Around twenty years ago, the production of fusion neutrons was reported for the first time by using a compact femtosecond laser and deuterated (i.e., deuterium containing) plastic targets. A modest 140 neutrons per shot were measured at an intensity of $10^{18}\,\mathrm{W\,cm^{-2}}$ [73]. Since then, a number of different laser-target parameters were studied for fusion using compact lasers. The neutrons that are produced in these experiments have some useful applications of their own, such as neutron radiography and tomography [74] that have the advantage of deeper penetration compared to x-rays. Other examples are neutron scattering [75] and diffraction [76], representing a fundamental tool to recover three-dimensional structures from samples.

Another great impulse in this field was given by the intense x-rays that heated plasmas are able to radiate. The hot electrons that are present in those plasmas can undergo three different emission processes to emit x-rays, which are free-free, free-bound and bound-bound mechanisms [39]. In the first process, free electrons interact with the Coulomb potentials of the ions and convert their lost kinetic energy caused by deceleration into radiation with a continuous spectrum, which is called *bremsstrahlung*. The second mechanism is referred to as *recombination*, where a free electron is caught by an ion, lowering its positive charge. The electron radiates a continuous spectrum, since it initially has a continuous kinetic energy. In the third process, an electron undergoes a transition from excited to lower states and thereby emits characteristic line radiation. One such example is the K_α radiation (Fig. 2.5), which is of particular importance to draw conclusions about the heating process and the electron energies in plasmas. It requires energetic electrons from the hot laser focal region, which can move to the colder part of the target thanks to their long mean free path, and remove bound, inner-shell electrons by collisions [12].

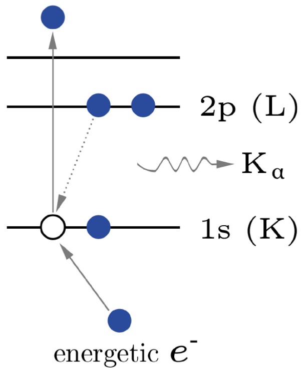

Figure 2.5: Scheme of K_α spectral line formation: A hot electron kicks out a bound inner-shell electron, which gives rise to a $2p \longrightarrow 1s$ transition from an L-shell electron down to the K shell and emits K_α radiation.

The vacant state in the innermoust K shell is then filled by an electron that transitions down from the second L shell ($2p \longrightarrow 1s$). The energy difference of the two states is emitted as K_α emission of characteristic energy. The analogous emission in the case of the hydrogen atom is the Lyman-alpha line, denoted as Ly_α. Another important diagnostic tool are the helium-like (He-like) or hydrogen-like (H-like) line emissions, which are radiated from atoms that have been stripped down to two electrons (He-like) or one electron (H-like) in their shell (and thus the resemblance to the helium or hydrogen atom) by ionization. In contrast to the K_α spectral line, these line radiations require a hot plasma that is capable of creating these highly charged states by performing collisional ionization. Therefore, the occurrence of those spectral lines can be used to deduce the presence of a hot thermal plasma. The He-like or H-like ions can have different transitions, leading to different emissions denoted as He_α, He_β, He_γ or Ly_α, Ly_β, Ly_γ etc. [39]. One typical example where the measurements of these lines are used as a diagnostic tool is the intensity ratio of emission lines from different charged states, which can be used to estimate the electron temperature [39]. Furthermore, intense x-ray pulses play a substantial role in the *indirect drive* scheme in inertial confinement fusion experiments [77], in which the high power lasers are focused on the inner side of a small cavity, where the fuel capsule is positioned. The walls of the cavity absorb the laser light and radiate mainly x-rays, which then irradiate the fuel capsule surface and drive the implosion [78, 79]. In the *direct drive* scheme, the capsule is irradiated directly by the lasers. The advantage of the indirect drive method is the much higher degree of symmetry of the capsule compression, but comes at the expense of a higher required driving energy due to the limited conversion efficiency to x-rays [80]. Moreover, the creation of intense x-ray emission is an essential requirement for opacity measurements in laboratory plasmas at the conditions of the solar interior to infer element compositions [81] as well as for imaging ultrafast atomic dynamics with simultaneous temporal and spatial resolution on the atomic scale [82, 83].

2.3 Laser-driven ion acceleration

Section 2.1.3 dealt with the acceleration of electrons in the laser field. As the lightest charged particles, they are the first to react to the laser field and are key for absorbing the pulse energy (section 2.1.5). Another topic in this thesis is the acceleration of ions, or more specifically, protons, and is the subject of discussion in the chapters 9 and 10. The following section 2.3.1 is adopted literally (with minor changes for a matched integration) from the introduction of the publication [84] that chapter 10 is based on.

The simplest idea for ion acceleration would be realized in the laser field, following the consideration for electrons in section 2.1.3. Calculated analogously to Eq. 2.19, the quiver velocity v_i of ions in the laser field is

$$\frac{v_i}{c} = \frac{ZeA_0}{m_i c^2} = \frac{Zm_e}{m_i} a_0, \tag{2.36}$$

where m_i is the ion mass and a_0 is given by the definition for electrons 2.19. Assuming the ions to be protons, the acceleration to relativistic velocities $v_i \approx c$ requires a normalized laser amplitude of $a_0 \approx 2000$ or intensities of $I_0\lambda > 10^{24}\,\mathrm{W\,cm^{-2}\,\mu m^2}$, which is way beyond the capability of today's laser technology. Yet, energetic ions are observed in laser-matter experiments. These are, however, not ions accelerated by the laser field directly, but rather in the strong charge separation fields that arise in plasmas due to heated electrons.

First, an introduction to the development of ion acceleration is given in section 2.3.1. Then, the most prominent acceleration mechanisms are explained in sections 2.3.2 and 2.3.3. The chapter closes with some applications in section 2.3.4.

2.3.1 Past and present

Almost two decades ago, the acceleration of protons and ions by the interaction of high-intensity laser pulses with µm-thick foil targets were performed [85,86]. This “all-optical” (meaning laser-driven) approach is capable of reaching tens of mega-electron volts (MeV) of kinetic energy over a sub-mm length with low emittance, high laminarity [87] and ultrashort duration [88] and holds promise for numerous applications, as will be listed in section 2.3.4 below.

Nowadays different mechanisms, depending on the laser energy/intensity as well as on the target parameters (mainly the target thickness) are known. The most studied process, the so-called target normal sheath acceleration (TNSA, see section 2.3.2 below) [89, 90] creates a broad energy spectrum particle beam, following a thermal distribution up to a certain cut-off energy ($E_{\text{cut-off}}$) which scales with $E_{\text{cut-off; TNSA}} \propto I_0^{0.5}$ [91], where I_0 is the laser intensity. For many applications, however, monoenergetic ion beams similar to those from conventional particle accelerators are desirable and different attempts have been made to achieve this by using micro-structured targets [92], droplet targets [93, 94], microlenses [95], layered foils [96], a two-stage setup [97] or laser beam shaping [98]. Other shortcomings are the typical low conversion efficiency of laser energy into proton energy of just a few percent [99] and the still low particle energy by laser-driven processes with regard to applications. In the example of cancer therapy that will shortly be described, protons with an energy of 200-300 MeV are required for most therapies in order to penetrate the necessary depth into tissue [100]. Based on the well known scaling laws [91], higher laser intensities lead to higher particle energies, with the drawback that every Joule of additional laser energy comes with a nonlinear increase of investment cost. This can only be realized in a very few international projects, like the upcoming European-Light-Infrastructure (ELI) facilities [3]. Therefore, it is of vital importance, especially for multi-Joule laser systems, to have alternative routes to access higher ion energies. One extensively studied way is the modification of the target design in order to obtain a reinforcement of the hot electron sheath population responsible for the accelerating TNSA field. On these grounds investigations have addressed, among others, the influence of the target thickness [101], laser pulse duration [99], plasma gradients [102] and the use of so-called mass limited targets [103, 104]. Another category of studies aims for enhanced absorption of the laser energy into the target by applying targets covered with structures on the scale of the laser wavelength or below, taking advantage of the larger interaction surface compared to ordinary foils. Some recent examples for the use of such targets are microstructures [105], microwires [10], nanogratings [106], nanospheres [107], nanowires [23, 106, 108], nanocones and nanoholes [109]. An alternative route is to increase the laser intensity, so that other acceleration schemes like radiation pressure acceleration (RPA, see section 2.3.3 below) using ultrathin targets become favourable [110–112]. The RPA process benefits from the use of circular polarized light [111]. It was demonstrated that the use of a linear polarized light leads to a hybrid acceleration regime in which TNSA and RPA coexist [113–117], which has been shown numerically to be able to surpass the RPA [118] despite its expectedly lower energy scaling. The highest ion energy achieved so far by a laser driven source of about 94 MeV [119] has been produced by a linearly polarized laser in the hybrid regime.

2.3.2 Target normal sheath acceleration

The TNSA mechanism is an extensively studied topic and reviews can be found in [120, 121], which serve as the information basis of this section. After the early measurements of protons from laser-solid interactions by using petawatt lasers [85, 86, 122], the underlying acceleration mechanism was an open question. A group at Lawrence Livermore then proposed a successful explanation [86, 123], which was based on the TNSA mechanism. It is assumed to be the dominant acceleration mechanism in the majority of measurements so far [124]. The TNSA model requires irradiation intensities of $I_0\lambda^2 > 10^{18}\,\mathrm{W\,cm^{-2}\,\mu m^2}$ ($a_0 > 1$) in order to produce relativistic electrons (section 2.1.3), and a thin solid foil (submicrometer scale up to a few tens of micrometers). The interaction of the intense laser pulse and the solid target produces hot electrons, which form a strong electrical current penetrating through the target and reaching the rear side. After arriving there, a certain number of electrons can escape into the vacuum according to the target's capacitance, and form a sheath over a Debye length (see Eq. 2.2). This space charge induces electric fields of the order of several $\mathrm{TV\,m^{-1}}$, surpassing those in conventional accelerators by several orders of magnitude. They are capable of ionizing the ions at the initially unperturbed surface and accelerate them to MeV energies along trajectories normal to the local surface. A special case of ions are protons, which are naturally provided by the hydrogen atoms in plastic targets, and are contained in the hydro-carbon contamination layers at the surfaces of metallic targets. The proton's higher charge to mass ratio with respect to heavier ions lets them dominate the acceleration and gain the most energy. If the hydrogen-containing contaminants are however removed, which can for instance be accomplished by carefully heating the target with a current as shown in [96], the dominant acceleration of higher-Z elements can be facilitated.

2.3.3 Radiation pressure acceleration

An alternative ion acceleration scheme is given by the radiation pressure acceleration, which is described in detail in [110–112, 121, 125–128], which are used as sources for this subchapter. The RPA attracted attention in the past decade due to its promising properties such as a proton cut-off energy scaling of $E_{\text{cut-off; RPA}} \propto I_0$ [91] and its expected high conversion efficiency of almost 100 % at ultra-relativistic intensities [112]. It not just offers the possibility of very high ion energies ($> 100\,\mathrm{MeV}$), but also quasi-monoenergetic beams. In theoretical works [101, 110, 129] it was found that in ultrathin foils with a sub-micrometer thickness and at intensities above $10^{23}\,\mathrm{W\,cm^{-2}}$ the dominant acceleration mechanism might be RPA instead of TNSA. This may be the case also at lower intensities by using circularly polarized light [111], which supresses the oscillating component of the $\vec{j} \times \vec{B}$ force (see Eq. 2.34). That oscillation would otherwise lead to strong absorption and heat the electrons [130], which in turn would favour TNSA.

The theoretical picture of RPA consists of an electromagnetic wave of intensity I_0 that irradiates a flat target and exerts a pressure p_{rad} (at normal incidence) of [124]

$$p_{\mathrm{rad}} = (1 + R - T)\frac{I_0}{c}, \tag{2.37}$$

where R and T are the reflection and transmission coefficients, respectively. For a perfect mirror, one has $R = 1$ and $T = 0$ and therefore a maximum pressure of $p_{\mathrm{rad}} = 2I_0/c$. Microscopically, the pressure is mediated by the temporal average of the $\vec{j} \times \vec{B}$ force, acting directly on the electrons and pushing them into the target, which in turn builds up a charge separation field that pulls the ions.

At sufficiently high irradiation intensities and overdense targets, the laser pressure may overcome the thermal plasma pressure and cause the particle density profile to be pushed inwards like a piston. This is the first mode of RPA, in which the laser bores a hole into the target. It is known as *"hole boring"* (HB), where the surface recedes with the HB velocity [125]

$$\begin{aligned} \Sigma &:= \frac{I_0}{\rho c^3} \\ v_{\mathrm{HB}} &= c\frac{\sqrt{\Sigma}}{1+\sqrt{\Sigma}} \approx \sqrt{\frac{I_0}{\rho c}}, \end{aligned} \tag{2.38}$$

with the target mass density ρ. This is the relativistically correct expression, which is approximated to yield the non-relativistic ($v_{\mathrm{HB}} \ll c$) result on the right hand side of the second line. Assuming a cold plasma and perfect reflection, the ion kinetic energy per nucleon can calculated to be [125]

$$\begin{aligned} E_{\mathrm{HB}} &= m_p c^2 \frac{2\Sigma}{1+2\sqrt{\Sigma}} \\ &\approx 2m_p c^2 \Sigma = m_e c^2 \frac{Z n_{\mathrm{cr}}}{A n_e} \zeta a_0^2 \end{aligned} \tag{2.39}$$

where m_p is the proton mass, A the ion mass number and the second line is again the non-relativistic approximation. The laser intensity was replaced by $I_0 = 1/2 n_{\mathrm{cr}} m_e c^3 \zeta a_0^2$, which results from the definition of the critical density in Eq. 2.26 plugged into the laser intensity in Eq. 2.20. The mass density is approximated by $\rho \approx A m_p n_i = A/Z m_p n_e$, where n_i is the ion density and is related to the electron density by the quasineutrality condition $n_e = Z n_i$ (see section 2.1.1). According to Eq. 2.39, typical values of $n_e > 100 n_{\mathrm{cr}}$ for solid targets do not lead to the desired high energies. One way to increase the ion energy is thus to have a target density n_e/n_{cr} as low as possible, i.e. slightly above the critical density. Underdense targets on the other hand are unsuitable as they allow the laser pulse to penetrate into the target, which would no longer function as a mirror. Such a low density coupled with the second option in Eq. 2.39, namely ultrahigh laser intensities, may open up the way to ion energies in excess of 100 MeV, as was explored in theoretical works [128, 131, 132].

In very thin targets, the above mentioned hole boring will push the target inwards, until it reaches the rear side of the thin foil. This occurs for a thickness $l < v_{\mathrm{HB}}\tau_{\mathrm{L}}$, where τ_{L} is the laser pulse duration. The laser pulse is then irradiating the already crushed target and starts to accelerate the foil as a whole (more precisely: the focal region of the target). The functioning is however limited by the breakthrough of the light through the foil, facilitated by relativistic transparency (see section 2.1.4). Assuming $l \ll \lambda$, it occurs for [124]

$$a_0 > \pi \frac{n_e}{n_{\mathrm{cr}}} \frac{l}{\lambda}, \tag{2.40}$$

which reflects the fact that thicker and denser targets support higher intensities. This regime can be modeled in one dimension as a thin mirror that is pushed by the radiation pressure exerted by a plane wave, and thus suggestively called *"light sail"* (LS). This principle was thought through as a means to overcome the limitations of rocket propulsion for spaces travel by instead propelling a space vehicle by terrestrial laser beams [133,134]. The target is assumed to consist of one ion specie with charge Z, mass number A and mass density ρ. The model then predicts an energy per nucleon of [127]

$$\begin{aligned} \mathcal{F} &= \frac{2I_0\tau_{\mathrm{L}}}{\rho l c^2} = 2\frac{Z n_{\mathrm{cr}}}{A n_e}\frac{m_e}{m_p}\frac{\tau_{\mathrm{L}} c}{l} a_0^2 \\ E_{\mathrm{LS}} &= m_p c^2 \frac{\mathcal{F}^2}{2(1+\mathcal{F})}, \end{aligned} \tag{2.41}$$

with the proton mass m_{p}. It is evident, that a lighter and thinner target enables higher energies, since $A/Z m_p n_e$ and l are in the denominator of $\mathcal{F}$. Including the optimal case of the condition in Eq. 2.40, in which the target density and length are chosen as small as possible for a given laser amplitude, and considering non-relativistic ions ($\mathcal{F} \ll 1$), one gets the optimum energy per nucleon [121]

$$E_{\mathrm{LS,opt}} = m_p c^2 \frac{\mathcal{F}^2}{2} = 2\pi^2 m_e c^2 \frac{m_e}{m_p}\left(\frac{Z}{A}\frac{c\tau_{\mathrm{L}}}{\lambda} a_0\right)^2. \tag{2.42}$$

This scaling reflects the descriptive fact that stronger laser pulses as well as a longer irradiation times (i.e. pulse durations) will benefit the gained kinetic energy due to the squared dependence. The optimal condition in Eq. 2.40 requires $l \approx 10^{-2}\,\lambda$ for solid densities and the higher intensities available nowadays, which can be fulfilled by the available technology to fabricate nm-thin targets. Along with the availability of laser pulses of high contrast to preserve the target for the interaction with the short pulse, the LS regime and its promising properties are accessible in experiments today.

2.3.4 Applications

One important example is proton therapy [135], in which malignant tumors are irradiated with sufficiently strong doses to destroy them. These proton beams can be focussed quite well onto the target tissue, since the protons are hardly scattered by the atomic electrons, and the deceleration length is fixed at a given energy. These properties ensure that the healthy tissue surrounding the tumor is not harmed. In contrast to other beams such as x-rays, gamma radiation or electrons, the irradiation dose at different continuous depths can be manipulated by adjusting the proton spectra [136]. This is based on a sharp maximum for energy losses (called *Bragg peak*) at a certain depth for a monochromatic proton beam. By widening the proton energy spectrum, it is possible to have a lower dose at the entrance, a homogeneous dose along the target and zero dose behind it. In comparison to conventional accelerators such as linacs, cyclotrons and synchrotrons, laser-driven proton sources have the advantage of being compact and therefore present a promising alternative.

Proton beams are also a potentially advantageous candidate for the *fast ignition* concept [137,138] in ICF, first proposed by Tabak *et al.* [139] in 1994. The potential advantage of it is a higher energy gain at a lower driver energy. In addition, the requirements for the compression symmetry would be reduced. In this scheme, the compression and ignition are separated in that the fuel capsule is first imploded by the conventional ICF methods. After the compression has taken place, a laser pulse of 100 ps duration and intensity between $10^{17} - 10^{19}\,\mathrm{W\,cm^{-2}}$ is used to bore a channel through the blow-off plasma in front of the capsule with the ponderomotive force. That channel is necessary to guide a second, petawatt pulse of $1-10$ ps duration to the critical density surface, where electrons of MeV energies are produced and travel to the dense core of the capsule to ignite the thermonuclear fusion. It is, however, not yet clear whether the highly relativistic electrons will propagate as a collimated beam through the precompressed plasma to deposit their energy in the desired volume. On the contrary, focused ion beams may keep an almost straight trajectory when moving through the coronal and compressed plasma. The abovementioned tunability of the ion absorption depth up to the Bragg peak additionally allows for efficient energy deposition in the targeted volume.

Accelerated ions can also be used for the creation of warm dense matter or high energy density matter [99, 140] or for time-resolved probing of transient electric and magnetic fields [141,142]. The latter represents a potentially useful diagnostic tool for ICF research to investigate instabilities occurring in dense plasmas or the unexplored complex fields that arise in the indirect drive setup.

Chapter 3

Particle-in-cell method

In order to explain experimental observations or conduct fundamental theoretical studies, models for the particles and fields involved in plasmas are needed. A comprehensive analytic description is extremely difficult due to the nonlinear nature of the electron motions and the laser-plasma interaction. The remaining alternative is the use of numerical methods. The most plasma models in the short pulse, high-intensity field can be categorized into *static, fluid / hydrodynamic* and *kinetic* codes. The first case is mainly for plasmas of low density, in which the interaction timescales are shorter than the plasma period $2\pi/\omega_p$ (see Eq. 2.24). The fluid approach assumes local thermodynamic equilibrium in the plasma, which means that the corresponding particle distributions have well-defined temperatures for electrons and ions, and are Maxwellian. This allows to describe the plasma by macroscopic quantities such as fluid velocity, pressure and density. The ion motion determines the timescales, which span from a picosecond to several nanoseconds. Kinetic codes, on the other hand, basically follow the trajectories of single particles (electrons and ions) without the assumption of Maxwellian distributions. One example where this becomes particularly important is the interaction between particles and waves as occurring in plasma waves. The kinetic approach is obviously more accurate, but also more computationally complex. As a more economical approach, there are also hybrid models, which describe some components as a fluid and others in the kinetic scheme [143].

Kinetic codes would ideally follow the trajectory of every single particle and calculate their interactions. However, despite today's progress in computer technology, the computation of such high numbers of particles is still a highly demanding task. As was described in chapter 2.1, a solid target is easily ionized to a plasma for intensities of interest of $I_0 \geq 10^{18}\,\mathrm{W\,cm^{-2}}$, leading to a very high number of free electrons. We take ionized nanowire targets as an example, as they cover the major part of this thesis. A single nanowire of 500 nm diameter, 5 µm length and a solid density of $10^{23}\,\mathrm{cm^{-3}}$ contains $\approx 10^{11}$ electrons. In other setups, the number of electrons can be even as high as 10^{18} electrons or more.

One possible solution to this problem is the *particle-in-cell* (PIC) method. It belongs to the kinetic category of codes and uses the fundamental electromagnetic equations and the equation of motion of particles without much approximation. This allows a comprehensive depiction of the plasma by retaining the full nonlinear, collective and space charge effects. This is achieved by coupling the charged particles and currents self-consistently to the fields via the source terms in the fundamental equations. The issue with the high number of particles is addressed very illustratively by introducing numerical *macroparticles*, where one of them represents a large number of real particles. This way the number of particles that need to be tracked can be drastically reduced, bringing the numerical procedure within reach of available computer systems. The first steps were already made in the late 1950's and early 1960's by Buneman [144] and Dawson [145] and after further advances in the 1960's the PIC scheme was formalized in the 1970's. The classic references were then published a decade later by Birdsall and Langdon [146] and Hockney and Eastwood [147] and are still prominent today. The PIC method has proven to be successful in the past decades [147–149], as many important discoveries and verifications were made using it.

The simulations presented in the following chapters were conducted using the PIC method. Therefore, this chapter provides an introduction to how it works. In section 3.1 the Vlasov method as a first approach to numerical computation is described, which proves to be too costly. The more economic finite element method is subsequently explained in section 3.2. After showing how physical variables can be discretized using the finite difference method in section 3.3, it will then be deployed in the next part 3.4, where the PIC algorithm is presented. The typical numerical setup for the simulations of nanowires is illustrated in subchapter 3.5. The information presented in this short introduction and all following sections of this chapter is taken from [12, 13, 28, 149–151] and is described there in greater detail.

3.1 Vlasov approach

The simplest approach in the kinetic picture is to consider the single-particle distribution function $f(\vec{x}, \vec{p}, t)$ for each particle species, that gives the number of particles in a 6-dimensional differential volume element in phase space $f(\vec{x}, \vec{p}, t)\mathrm{d}^3x\mathrm{d}^3p$. The volume elements for position and momentum are given by $\mathrm{d}^3x = \mathrm{d}x_1\mathrm{d}x_2\mathrm{d}x_3$ and $\mathrm{d}^3p = \mathrm{d}p_1\mathrm{d}p_2\mathrm{d}p_3$. Furthermore, the function f is normalized to N total particles

$$N = \int \mathrm{d}^3x \int \mathrm{d}^3p\, f(\vec{x}, \vec{p}, t). \tag{3.1}$$

The local particle density $n(\vec{x})$ and hydrodynamic velocity $\vec{V}(\vec{x})$ can be recovered from the moments

$$n(\vec{x}) = \int \mathrm{d}^3p\, f(\vec{x}, \vec{p}), \qquad \vec{V}(\vec{x}) = \int \mathrm{d}^3p\, f(\vec{x}, \vec{p}) \frac{\vec{p}}{m\gamma}. \tag{3.2}$$

The evolution of the distribution function is given by the Boltzmann-Vlasov equation [28]

$$\frac{\partial f}{\partial t} + \frac{\vec{p}}{m\gamma}\nabla f + \frac{\vec{F}}{m}\nabla_{\vec{p}} f = \left(\frac{\partial f}{\partial t}\right)_{\mathrm{coll}}, \tag{3.3}$$

where m is the particle mass of the corresponding species, $\gamma = \sqrt{1 + \vec{p}^2/(mc)^2}$ the relativistic factor, $\vec{F}$ the electromagnetic force given by the Lorentz force (Eq. 2.17), $(\partial f/\partial t)_{\mathrm{coll}}$ the change rate of f caused by collisions, ∇ the usual gradient operator and $\nabla_{\vec{p}} = \hat{e}_x\partial/\partial p_x + \hat{e}_y\partial/\partial p_y + \hat{e}_z\partial/\partial p_z$ the gradient operator in momentum space.

The distribution function f operates on a six-dimensional space (6D) and thus the general analytical calculation of equation 3.3 is unsolvable for most cases of interest, which is why one has to rely on numerical methods.

One possibility is to discretize equation 3.3 on a grid (*finite difference method*, see subchapter 3.3) and solve it. The codes using this method are referred to as *Vlasov codes*. This is a simple approach and thanks to the detailed incorporation of the phase space it is capable of producing "smooth" output. On the other hand, it means a massive computational effort. Even if one treats a one-dimensional problem, one typically has to have two or three additional dimensions for the velocity components to take into account the adequate electron motion, and yet, one has to deal with a three- or four-dimensional problem, requiring the use of supercomputers.

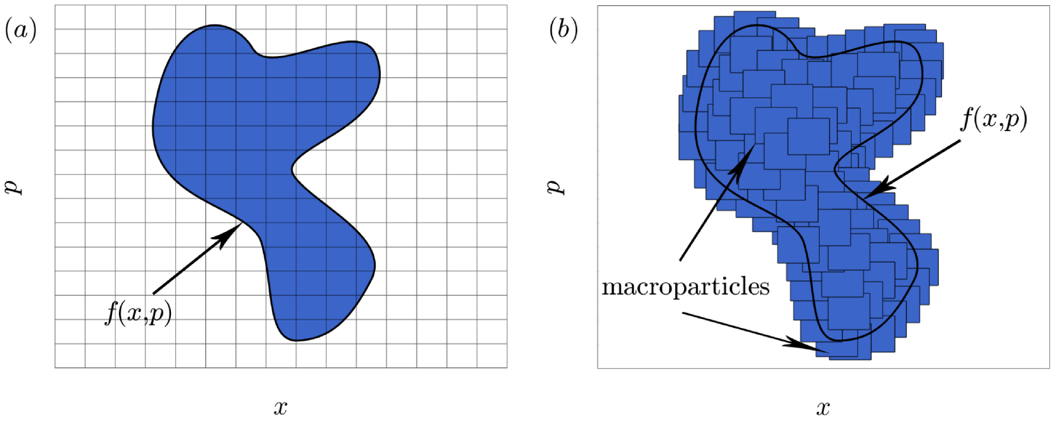

Figure 3.1: Phase space in one dimension (p over x) on an Eulerian grid of a kinetic computation. (a) In the Vlasov approach, the blue indicated area represents a nonzero distribution function f, the remaining white area is the part of the phase space that is not occupied by the plasma. (b) The PIC method substitutes the grid containing the distribution function f by a list of a large number of macroparticles that sample the area occupied by f.

A crucial reason for the costliness of the Vlasov codes can be seen in Fig. 3.1(a). It illustrates an example of a 1d1v Vlasov code, which is a notation that stands for one spatial component and one velocity component. The mesh on which the computation operates is an *Eulerian* grid, whose cells stand for fixed spatial positions through which the plasma moves as time passes. The distribution function f occupies only a certain area of the phase space in this two-dimensional example, the unmarked white area does not contain any plasma. In the technical realization of the code, however, the equation 3.3 must be solved in each cell of the complete grid, since the behaviour of the plasma is not known beforehand and could theoretically reach every cell. This inevitably amounts to a vast number of unnecessary operations in the empty cells, wasting great resources. The efficiency drops exponentially for an increasing number of dimensions, and is very low for the actual important 3d3v case, where the major part of the 6D grid is basically empty. As the performance of available computers grows, the popularity of this approach however increases.

3.2 Finite element (PIC) approach

A more economical strategy is the *finite element method*, which breaks the plasma, represented as the distribution function in phase space, down into N separate *finite phase-fluid elements* (FPFE) that have their centers at $\vec{x}_n, \vec{p}_n$, a "phase shape" defined by the function $S^{\mathrm{ph}}(\vec{x}, \vec{p})$ and a "weight" given by W_n^{ph}. Consequently, the distribution function can be sampled as the sum of those elements

$$f(\vec{x},\vec{p}) \approx \sum_{n}^{N} W_n^{\mathrm{ph}} S^{\mathrm{ph}}(\vec{x}-\vec{x}_n,\vec{p}-\vec{p}_n). \tag{3.4}$$

This is visualized in Fig. 3.1(b) by blue squares that are meant to cover the area occupied by the distribution function. It is a common choice to model the shape of the elements as a hypercube, with a spatial extent Δx_i in the directions $i = x, y, z$

$$S^{\mathrm{ph}}(\vec{x}-\vec{x}_n,\vec{p}-\vec{p}_n) := \begin{cases} 1, & \text{for } |(\vec{x})_i - (\vec{x}_n)_i| < \frac{\Delta x_i}{2} \ \forall i \ \text{ and } \ \vec{p} = \vec{p}_n \\ 0 & \text{else,} \end{cases} \tag{3.5}$$

where $(\vec{x})_i$ denotes the i'th component of the vector $\vec{x}$. There is no extent in the momentum space, since a FPFE has only one momentum, implying that the condition $\vec{p} = \vec{p}_n$ needs to be met to have $S^{\mathrm{ph}} \neq 0$. The motions of the FPFE, which represent the evolution of the distribution function, obey the relativistic equations of motion

$$\frac{\mathrm{d}}{\mathrm{d}t}\vec{p}_n = \vec{F} + \vec{F}_{\mathrm{coll}}, \tag{3.6}$$

$$\frac{\mathrm{d}}{\mathrm{d}t}\vec{x}_n = \frac{\vec{p}_n}{m\gamma}, \tag{3.7}$$

where $\vec{F}_{\mathrm{coll}}$ is the effective force acting on the FPFE due to collisions, resulting from the collisional term in Eq. 3.3.

The PIC method essentially deploys the aforementioned macroparticles as the fluid elements to achieve a kinetic description of the plasma. Compared to the Vlasov approach, this procedure has the advantage that instead of the full phase space, only a list of numerical particles needs to be preserved. Thus, one gets rid of the empty phase space volume and has to compute only the actual plasma. Even though the solving of the field equations, as we will see in the next subchapters, requires the use of a grid, it is only three-dimensional and thus still less cumbersome than the six dimensions in Vlasov codes. Furthermore, the concept of macroparticles that can be thought of as a "clump" of real particles with the same charge to mass ratio and therefore same velocity, is quite intuitive and allows for a straightforward handling. The consideration of particles also allows for inclusion of relativistic effects. A lot of information is stored in the form of particle properties such as position, momentum, weight (representing the number of real particles that are contained), charge state and depending on the implemented modules, some more. Thus, the results can be evaluated on a very high level of detail. Moreover, one has the ability to freely run any imaginable setup in contrast to experiments. These points make PIC simulations so powerful. In spite of these advantages, there are however also weaknesses. For instance may complex simulations still need great computational resources in the form of memory and processors, especially for simulations where a large space and/or a high resolution (spatial and temporal) are/is needed. PIC codes are well suited for short pulse durations, and we have used those throughout the projects presented in this thesis. On the contrary, longer pulse durations are another weakness of the PIC method and require other methods or further approximations.

In the meantime, the PIC method is well established in the plasma physics community. Several PIC codes have been developed and are in use in different groups worldwide. All the simulations in the following chapters were performed using the *Virtual Laser Plasma Laboratory* (VLPL) code, developed by Pukhov [152, 153]. It is a fully electromagnetic three-dimensional relativistic PIC code. It utilizes OpenMPI [154] as an implementation of the message passing interface, that allows to massively parallelize the code to run it on supercomputers with large numbers of processors. For instance for some of the results presented in this thesis, the code operated on more than 1500 processors on the RMACC Summit supercomputer in Colorado [155]. The data volume that is produced can be huge (on the TB scale) and is saved in the Hdf5 format [156], that is especially well suited for large and complex datasets. Modules for optical field ionization in the simple BSI model (ADK model [32]) and for collisional ionization (Lotz formula [33]) are incorporated (see subchapter 2.1.2) that allow to start simulations with neutral targets and observe ionization dynamics. This is particularly important in the regime of short pulses and high target densities that we are interested in, as the higher charged states are important for the emission of x-rays (see subchapter 2.2.2) and therefore an important interface to experimental results.

3.3 Finite difference method

In the following subchapters, we will use the finite difference method to discretize the relevant equations for particles and fields, which contain derivatives in space and time. With the time step Δt in time, the discretized times can be expressed as multiples of it $t_i = i\Delta t$. Let us consider the taylor expansion of a function f at the time $t_i + \Delta t$

$$f(t_i + \Delta t) = f(t_i) + \Delta t \frac{\partial}{\partial t} f \bigg|_i + \frac{1}{2}\Delta t^2 \frac{\partial^2}{\partial t^2} f \bigg|_i + \mathcal{O}(\Delta t^3). \tag{3.8}$$

Solving for the first derivative and using the notation $f(t_i + \Delta t) \mathrel{\widehat{=}} f_{i+1}$, we get

$$\frac{\partial}{\partial t} f \bigg|_i = \frac{f_{i+1} - f_i}{\Delta t} - \frac{1}{2}\Delta t \frac{\partial^2}{\partial t^2} f \bigg|_i - \mathcal{O}(\Delta t^2). \tag{3.9}$$

The largest error for finite time step is caused by the Δt^1 term (second on the right-hand side) which makes this expression *first-order accurate.* Without much effort, it can be improved by first solving for the first derivative of the taylor expansion for $f(t_i - \Delta t)$, resulting in

$$\frac{\partial}{\partial t} f \bigg|_i = \frac{f_i - f_{i-1}}{\Delta t} + \frac{1}{2}\Delta t \frac{\partial^2}{\partial t^2} f \bigg|_i - \mathcal{O}(\Delta t^2), \tag{3.10}$$

and then taking the average of Eq. 3.9 and Eq. 3.10. The resulting derivative

$$\frac{\partial}{\partial t} f \bigg|_i = \frac{f_{i+1} - f_{i-1}}{2\Delta t} + \mathcal{O}(\Delta t^2), \tag{3.11}$$

is now a centered difference quotient, has eliminated the Δt term and is now improved to *second-order accuracy.* The first-order accuracy in the time will lead to numerical problems because even by decreasing the time step, the accumulated error is still too large. This emphasizes the importance of the second-order accuracy for the finite difference method. The derivative in Eq. 3.11 does however not depend on f_i. This can be circumvented, if one is willing to define the position of the derivative at the mid-points

$$\frac{\partial}{\partial t} f \bigg|_{i+\frac{1}{2}} = \frac{f_{i+1} - f_i}{\Delta t} + \mathcal{O}(\Delta t^2). \tag{3.12}$$

Shifting i by half a step yields another possible representation

$$\left.\frac{\partial}{\partial t} f\right|_i = \frac{f_{i+\frac{1}{2}} - f_{i-\frac{1}{2}}}{\Delta t} + \mathcal{O}(\Delta t^2). \tag{3.13}$$

In contrast to Eq. 3.11, both Eq. 3.12 and Eq. 3.13 involve two directly adjacent steps of f for the calculation. The second derivative can be obtained by differencing Eq. 3.9, and higher derivatives can be calculated in the same fashion by using the next lowest gradient.

3.4 Particle-in-cell algorithm

As we have seen in subchapter 3.2, the PIC method uses macroparticles, which are advanced in time by solving their equations of motion 3.6 and 3.7. Now we want to discretize these equations as shown in the previous chapter. To express the momentum, we define the velocity as $\vec{u} := \gamma\vec{v}$, which is computed according to Eq. 3.6, where the Lorentz force 2.17 is to be used for $\vec{F}$. The finite difference discretization of the equations of motion has the form [150]

$$\frac{\vec{u}_{i+\frac{1}{2}} - \vec{u}_{i-\frac{1}{2}}}{\Delta t} = \frac{q}{m}\left(\vec{E}_i + \frac{\vec{u}_i}{c\gamma_i} \times \vec{B}_i\right), \tag{3.14}$$

$$\frac{\vec{x}_{i+1} - \vec{x}_i}{\Delta t} = \frac{\vec{u}_{i+\frac{1}{2}}}{\gamma_{i+\frac{1}{2}}}. \tag{3.15}$$

First, the equation 3.14 is taken at time t_i, such that the time derivative of $\vec{u}$ needs to be expressed in terms of the difference 3.13. The velocities are therefore defined at the mid-points. The velocity components at integer steps on the right hand side of Eq. 3.14 are given by the temporal averages [150]

$$\vec{u}_i = \frac{1}{2}(\vec{u}_{i-\frac{1}{2}} + \vec{u}_{i+\frac{1}{2}}), \tag{3.16}$$

$$\gamma_i = \frac{1}{2}(\gamma_{i-\frac{1}{2}} + \gamma_{i+\frac{1}{2}}). \tag{3.17}$$

Once the new velocity is known, the new position can be calculated from Eq. 3.7. The fact that the velocity is defined at the mid-point makes it necessary to take the time derivative of the position at the mid-point, as specified by Eq. 3.12. The resulting equation 3.15 shows that the position values are then defined at integer steps. This interleaved scheme as shown in Fig. 3.2 between velocity and position values is referred to as *leapfrog method.* Besides the second-order accuracy, it has the advantage that it needs just few operations and requires little storage, since the new values can be calculated in place. This procedure of handling the particles described so far is suggestively called *particle pusher*. One efficient way to integrate this scheme is the Boris algorithm, proposed by Boris in 1970 [157]. It is still the standard particle pusher today due to its long term accuracy [158].

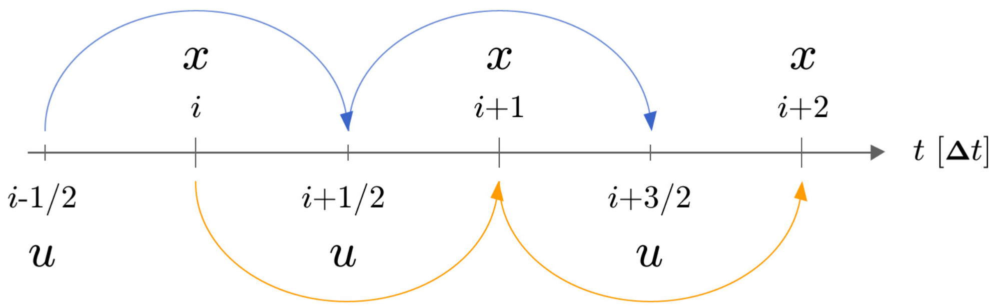

Figure 3.2: Scheme of the leapfrog method: The starting point are initial values for position x and velocity u. From there, the velocities are calculated at half-integer times $t = (i-1/2)\Delta t, (i+1/2)\Delta t, \ldots$, and the positions at integer times $t = i\Delta t, (i+1)\Delta t, \ldots$ by using the finite difference method. In the PIC algorithm, the currents j and magnetic field components B are calculated at the same time as the velocities, and the charge densities ρ and electric field components E are calculated at the same time as the positions.

Besides the particles, the fields also need to be worked out. The fundamental electromagnetic equations are given by Maxwell's equations, which are given by

$$\frac{\partial}{\partial t}\vec{E} = c\nabla \times \vec{B} - 4\pi\vec{j}, \tag{3.18}$$

$$\frac{\partial}{\partial t}\vec{B} = -c\nabla \times \vec{E}, \tag{3.19}$$

$$\nabla \cdot \vec{E} = 4\pi\rho, \tag{3.20}$$

$$\nabla \cdot \vec{B} = 0. \tag{3.21}$$

The time evolution of the fields are given by the time-dependent Ampère's law 3.18 and Faraday's law 3.19. The currents $\vec{j}$ produced by our numerical particles are self-consistently related to the fields via Eq. 3.18. As is well known, we can apply the scalar multiplication with $\nabla\cdot$ to Eq. 3.18 and use the Gauss law 3.20 to get the continuity equation of the charge

$$\frac{\partial}{\partial t}\rho + \nabla \cdot \vec{j} = 0. \tag{3.22}$$

Given that one ensures that the continuity equation 3.22 for the charge density is fulfilled numerically, the Gauss law 3.20 is automatically satisfied, if it was valid in the beginning. The same holds for the magnetic field and since magnetic charge are not found to exist, Eq. 3.21 stays satisfied. This consideration reduces the computation of the fields to only two time-dependent equations 3.18 and 3.19, whereas the static equation 3.20 and 3.21 serve as initial conditions.

An efficient way to discretize Maxwell's equations is the *finite-difference time-domain method* (FDTD), proposed by Yee in 1966 [159]. It is a simple and fast algorithm and has been improved by several contributors over the decades [159]. It is a three-dimensional formulation, which defines the field components on a grid with discretizations $x = k\Delta x$, $y = l\Delta y$ and $z = m\Delta z$. It uses central difference approximations as discussed in subchapter 3.3 for both, temporal and spatial derivatives. The novelty of it is that it applies the leapfrog method not just in time, but also in space to achieve second order accuracy. In the Yee grid, the electric field components are placed at the surfaces of the cell, while the magnetic field components are at the edges. The reason for this arrangement is that a simple order in which all these components are at the same position leads to numerical errors. This interleaving in space is depicted in Fig. 3.3.

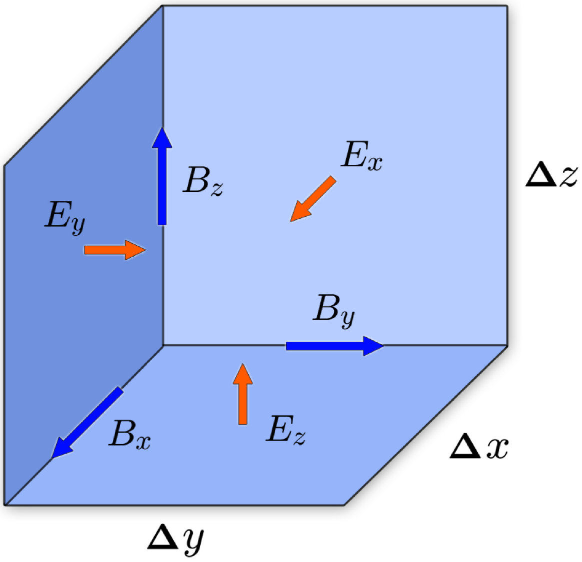

Figure 3.3: The arrangement of the field components in the unit cell of a Yee grid: The electric field components (orange arrows) are positioned at the cell faces and the magnetic field components (blue arrows) point along the cell edges.

However, to have numerical stability, one needs to take care for an appropriate choice of the time and grid steps. An important relation between time and grid steps for stability is given by the Courant-Friedrichs-Lewy condition [149, 151, 160]

$$(c\Delta t)^2 < \frac{1}{\frac{1}{\Delta x^2} + \frac{1}{\Delta y^2} + \frac{1}{\Delta z^2}}, \tag{3.23}$$

which, if violated, will lead to phase errors or unphysical growth in the $\vec{E}$ and $\vec{B}$ field.

After having explained how the particles and fields are advanced, we can now look at how these procedures are embedded in the whole iteration that the PIC algorithm runs within one time step Δt:

- Since the electromagnetic fields are saved at different positions, they need to be interpolated to the continuous position of the particle, in order to get the accurate force acting on the particle.
- The particle can now be pushed, by applying the interpolated fields and solving the equations of motion as seen above. At this time, additional modules regarding the particles can be loaded, such as ionization, collisions or quantum mechanically generated particles. Corresponding to the choice of boundary conditions, the particle needs now to be checked for an event like absorption in case of absorbing boundaries.

- The currents generated by the particles' displacement are interpolated to the discretized grid points.
- The electromagnetic fields can now be advanced using the Yee algorithm.

This is the sequence that is repeatedly executed in each time step and each cell of the grid, up to the desired endpoint of the simulation. A typical grid used in this thesis has the extent of 60×60×2000 cells, yielding millions of cells, along with millions of particles that need to be computed. Due to this complexity, the parallelization of the simulation is an indispensable part. The simulation box is basically divided into subcubes, which are processed by separate cores independently. At the end of a time step, the processors communicate to exchange the necessary information like crossing particles or adjacent field components. Despite the speed-up gained by a massive parallelization on 480 (on our local cluster) or 1536 (on the RMACC Summit supercomputer in Colorado [155]) cores, simulations may still take several days, illustrating the costliness of PIC simulations.

3.5 Nanowire simulation setup

The nanowire targets used in experimental setups usually are samples made of a substrate that supports a large number of nanowires, forming a grass-like structure. There are different methods to grow nanowire arrays [161–163]. Those samples can either be purchased readily, or be produced manually, which allows tailoring the parameters to meet conditions for specific applications. Our collaborators in Colorado, for example, use the electrodeposition method [161–163], which for instance allows to have compositional changes along the nanowire axis (see chapter 5).

As described in the previous section, PIC computations can be expensive and one needs to find ways to reduce the computational effort while still being able to produce meaningful and informative results. We wish to simulate the targets in three dimensions to receive the physics as complete as possible, since some effects might get lost in the structured targets when using only two dimensions. This however, limits us to the simulation of just one wire, as the target needs to be resolved properly while ensuring numerical stability (see Eq. 3.23). An important feature that allows us to compute just one wire, while effectively simulating a full array of infinite nanowires, is the use of *periodic boundary conditions* in the direction transverse to the nanowire axis. Here, a particle leaving the box on one side will be reinjected on the opposite boundary, mimicking a particle entering the box from the adjacent wire due to the same behaviour, illustrating the periodicity in the transverse plane. This is presented in Fig. 3.4, where the blue box indicates the simulation box containing the nanowire, surrounded by an infinite number of virtual equivalent nanowires. Next, the typical focal spot of a laser pulse is much larger than the diameter of a single nanorod. Thus, it can be assumed that one nanowire faces a large focal spot of constant intensity, which in turn allows us to use a plane wave, instead of a focused laser pulse. The use of a plane wave is consistent with the periodic boundary conditions, which ultimately allows us to save computational resources. When comparing the numerical results to experimental measurements, it might however be necessary to run further simulations with varying intensities. This way one can take into account the areas of different intensities surrounding the focal center and interpolate the results to get a better agreement with experimental results. In case of the simulation of a flat target, there is typically no way around a focused laser beam, which on the other hand requires a sufficiently large box to include the full pulse.

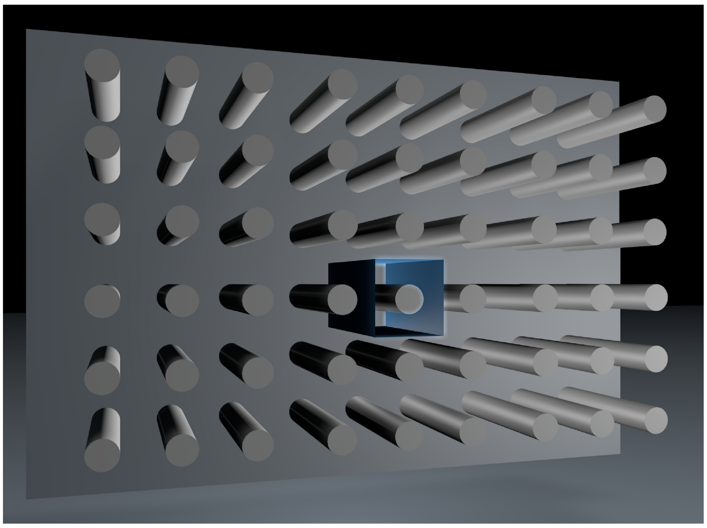

Figure 3.4: Illustration of simulating a nanowire array in a PIC simulation. In fact, only one nanowire is simulated, as indicated by the blue box. A plane wave approximation and periodic boundary conditions create the effect of an infinite number of surrounding nanowires that are irradiated at a constant laser intensity.

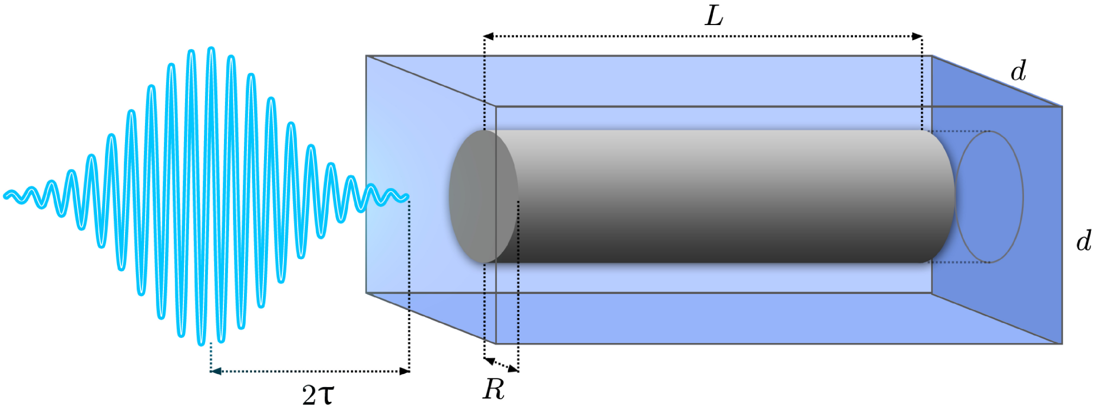

Figure 3.5: Schematic representation of the typical setup for the simulation of a nanowire array.

A typical simulation setup is shown in Fig. 3.5. The nanowire of length L and diameter $2R$ is placed in the center of the simulation box of edge length d. Usually, a space of 1-2 wavelengths in front of the tip and behind the bottom of the nanorod is left empty to allow for expansion. A further important parameter for the targets is the filling factor f, which determines how much volume the wire occupies in the unit cell compared to a solid target. It is given by the ratio of the circle area and the full square $f = \pi R^2/d^2$, and equivalently yields the period (transverse extent) of the simulation box for given target parameters f and R

$$d = \sqrt{\frac{\pi}{f}}R, \tag{3.24}$$

which is a common parameter that needs to be calculated when simulating given experimental conditions. The laser pulse normally has a Gaussian temporal profile

$$a(t) = a_0 \, e^{-t^2/\tau^2}, \tag{3.25}$$

where τ is the time at which the amplitude $a(t)$ drops to e^{-1} times its maximum value a_0. It is related to the FWHM duration t_{FWHM} of the intensity, which is usually the known parameter in the experiments, by

$$\tau = \frac{t_{\mathrm{FWHM}}}{\sqrt{2 \ln 2}}. \tag{3.26}$$

For an easier handling, the pulse is cut at distances of $\pm 2\tau$ around its maximum, which has proven to not cause any significant numerical problems. The pulse is initially placed outside of the box, where its leading front is just at the boundary. As soon as the simulation starts, it enters the box and interacts with the wire afterwards.

Chapter 4

Nanoscale Z-pinch

4.1 Introduction

In this chapter, we will look at an effect that occurs in the interaction between relativistic laser pulses and nanowires, namely the Z-pinch on the nanoscale. Once its creation is understood, one realizes that it enables a variety of fundamental studies and applications. Its contracting and confining nature increases the time for a longer absorption duration of the laser pulse before the plasma explodes due to heating and creates a light-reflecting critical surface caused by the closure of the interwire gaps. Consequently, it can improve the volumetric heating [5] which opens up the way to access the extreme UHED regime [19], which in turn supports the generation of efficient x-rays [20] and bursts of neutrons [21]. The advantage is that the use of merely joule-level lasers can achieve record values in these fields, as shown in the chapters 5, 6 and 7.

We will first introduce the Z-pinch and its background in section 4.2. In all following parts we will present results that we produced by performing PIC simulations and subsequent evaluation of the numerical data. The ionization of the nanowires is investigated in subchapter 4.3, followed by the analysis of the formation of a return current in section 4.4 and the consequent generation of a magnetic field and the nanowire compression in sections 4.5 and 4.6. The role that the laser intensity plays is examined in subchapter 4.7. The chapter concludes with a summary in section 4.8.

4.2 The Z-pinch

Z-pinches, also called Bennett pinches [164], are defined by an axial current in a plasma that gives rise to a self-generated azimuthal magnetic field, causing a compression by the radially inward $\vec{j} \times \vec{B}$ force. While Z-pinches occur in nature in the form of interstellar filaments, solar flares and lightning bolts [165, 166], they are routinely produced in the laboratory and have been studied thoroughly [167, 168]. Since the early fifties, they have aroused interest due to their ability to focus high energies into small volumes. Initially, efforts were made to use them as potential fusion devices, hoping to achieve a thermonuclear burn by generating a sufficiently strong current. In fact, the occurring magneto-hydrodynamic instabilites [167,169,170] have rendered these attempts unsuccessful. However, Z-pinches are still of interest at present for the creation of x-rays [171] and neutrons [172, 173] and to investigate astrophysical aspects like radiation absorption by stellar matter [81, 174]. These dense plasmas can be controlled to a certain degree by recently developed methods of using exploding nanowire arrays [175] and the fast-discharge excitation of capillary channels filled with preionized gas [176], opening the way to the creation of tabletop soft x-ray laser beams [177, 178] and the generation of unparalleled energy [179].

The principle of the Z-pinch is not bound to a certain size. It scales from typically millimeters to micrometers in diameter in laboratory pinches up to astronomical units in pinches occuring in nature. In this chapter we present a new type of Z-pinch with a radial extent on the nanometer scale that has an ultrahigh plasma density n_e greater than 9×10^{24} cm^{-3}. It can be produced by irradiating vertically aligned nanowires by relativistically intense high-contrast femtosecond laser pulses along the nanowire axis. Extracted electrons lead to a large forward current in the vicinity of the wires, giving rise to a strong return current within the nanowires to maintain quasineutrality. By using a laser pulse of 4.95×10^{21}W/cm^2 intensity (which corresponds to a normalized vector potential of $a_0 = 17$) in our simulations, we measure a return current as large as 96 MA/µm^2. This current in turn creates a strong quasistatic azimuthal magnetic field surrounding the nanowires, leading to a compression by the inward-directed $\vec{j} \times \vec{B}$ force. As a result an extremely hot and dense plasma is formed in which the electron particle density reaches 1000 critical densities. This value surpasses those Z-pinches generated in pulse power machines [180] and the recently described micro-capillary discharges [181] by two to three orders of magnitude. Jiang *et al.* [182] have shown the presence of a self-generated magnetic field induced by return currents within laser-irradiated micrometer Si wires. The sideward irradiation of 20 µm thick wires with intense laser pulses of picosecond duration and 60-80 J energy has been reported to lead to an electron density of 20 critical densities. Similar to discharge driven Z-pinches, MHD m = 0 instabilities on the nanoscale were observed, leading to field emission from secondary wires placed close by [183, 184]. In the late seventies and early eighties the heating by laser-driven return currents by using $\lambda = 10.6$ µm lasers of nanosecond duration were studied in 10 µm thick glass fibers [185] and uses for implosion in 130 µm diameter hollow rods [186].

Since this thesis mainly deals with nanowires as targets of interest, the present study reports a new kind of Z-pinch in these structures with a dimension two to three orders of magnitude thinner, yielding densities of more than 1000 critical densities. Initially, optical field ionization and vacuum heating [36] (see section 2.1.5) at the wire boundaries will produce free electrons. Further electrons will be set free by means of collisional ionization by both the returning Brunel electrons, that carry their energy gained by the excursion back into the plasma, and the cold electrons of the reverse current. The contribution of the latter is, however, bigger due to the larger collision cross section. We show that the electron density additionally increases by up to nearly two orders of magnitude as a result of the nanoscale Z-pinch caused by the return current. The pinch presented here is not observed to be subject to considerable instabilities that would otherwise prevent a uniform compression.

4.3 Nanowire ionization

One of the main consequences of the laser-wire interaction is the ionization of the solid material, which transfers it into the plasma state. The presence of a plasma, and thus the presence of a critical number of free charges, is of fundamental importance for the nanoscale Z-pinch and in general within the scope of the results presented in this thesis. Before we move on to analyze the formation of the new kind of Z-pinch, we will first consider the ionization process within the nanowire targets. For this purpose, we study simulation results of an array of 400 nm thick and 5 µm long carbon nanowires with an average density of 13 % solid density (which corresponds to a periodicity of 1 µm). The array is irradiated by a $\lambda = 400$ nm laser pulse of 60 fs full width at half maximum (FWHM) duration and a normalized laser amplitude of $a_0 = 18$, propagating into the z direction.

Figure 4.1 shows the temporal evolution of the electron particle density n_e for the case of a linearly polarized (in y-direction) laser pulse. The carbon ions initially have an ionization state of $Z = 1$, corresponding to a particle density of about $n_e \approx 16 n_{\mathrm{cr}}$, seen as the dark blue area. The laser pulse enters the simulation box from the left boundary at $x = 0$. As the tip of the wire gets into contact with the laser pulse, it starts to get ionized [Fig. 4.1(a)], and the particle density increases to about $n_e \approx 60 n_{\mathrm{cr}}$. It can be seen that the outer layer of the wire is ionized first, see the right end of the green areas in Figs. 4.1(a) - 4.1(c). Only after that, since there is also collisional ionization, the ionization reaches the inner core of the wire. Even before the whole wire has gained a minimum particle density of about $n_e \approx 60 n_{\mathrm{cr}}$, the left half of the wire already gets ionized to values of about $n_e \approx 90 n_{\mathrm{cr}}$ [Fig. 4.1(c) and 4.1(d)]. For Figs. 4.1(a) - 4.1(d) a linearly polarized laser was used. In principle, these cross sections do not change for circular polarization.

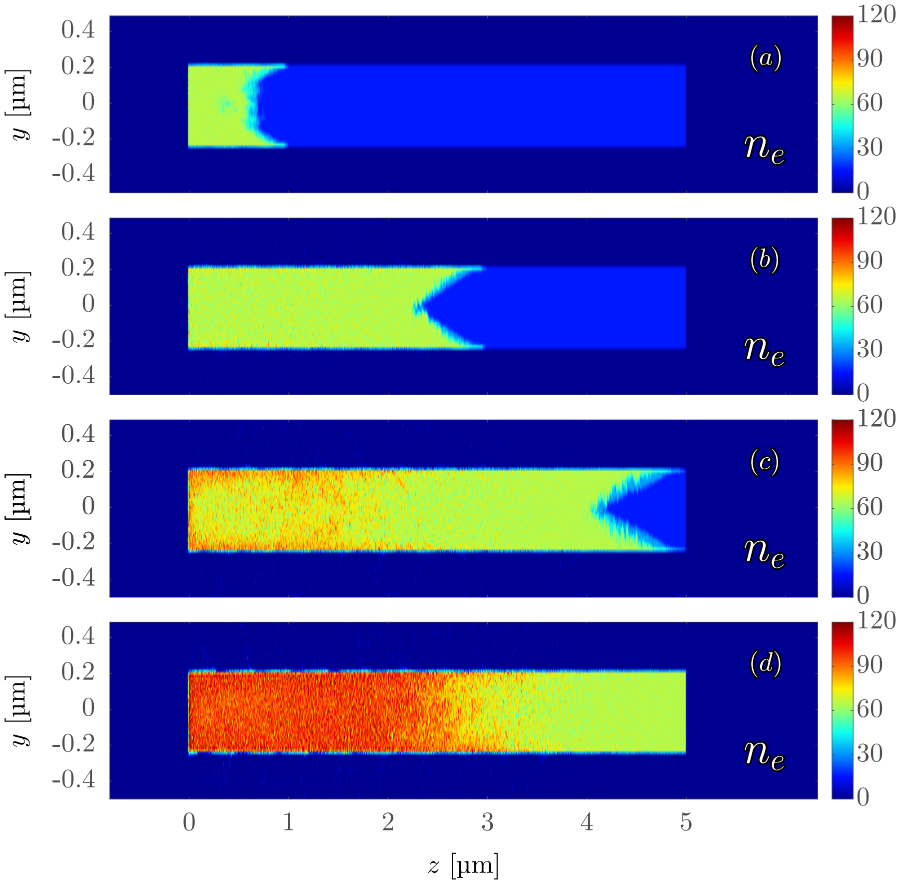

Figure 4.1: Longitudinal (cut along $z = 0$) cross sections of the electron particle density n_e [n_{cr}] (n_{cr}: critical plasma density, with $n_{\mathrm{cr}} = 7 \times 10^{21}\,\mathrm{cm}^{-3}$ for a 400 nm laser) at (a) $t = -51\,T_0$, (b) $t = -46\,T_0$, (c) $t = -41\,T_0$ and (d) $t = -36\,T_0$ before the peak of the (linearly polarized) laser pulse (in y-direction) hits the surface. *(Source: [17], see summary 4.8 below for details.)*

A more direct way to observe the strength of the ionization is to consider the (averaged) ionization state Z of the carbon ions along the nanowire axis z, see Fig. 4.2. They provide a direct comparison between the ionization by a linearly [Fig. 4.2(a)] and a circularly polarized laser beam [Fig. 4.2(b)] at four different times. At the first time step $t = -48.5\,T_0$ the curves for linear and circular polarization mostly coincide. The carbon wire is fourfold ionized up to 1.4 µm into the tip and falls to the initial state of $Z = 1$ within a length of 0.8 µm. 7.5 laser cycles later, the state $Z = 4$ reaches up to 4 µm into the wire for linear polarization and 4.3 µm for circular polarization. Whereas the interval $1\,\mu\mathrm{m} < z < 3.6\,\mu\mathrm{m}$ has averaged charged states up to $Z = 4.6$ for linear polarization, the circular polarization reaches higher states of up to $Z = 5.5$. At $t = -33.5\,T_0$ the first 2 µm of the wire (linear polarization) and 3 µm (circular polarization) are fully ionized. At the last step $t = -26\,T_0$ the wire is basically fully ionized by the circular polarized beam. In the case of linear polarization, the last 1 µm has charge states between 6 and 5.5.

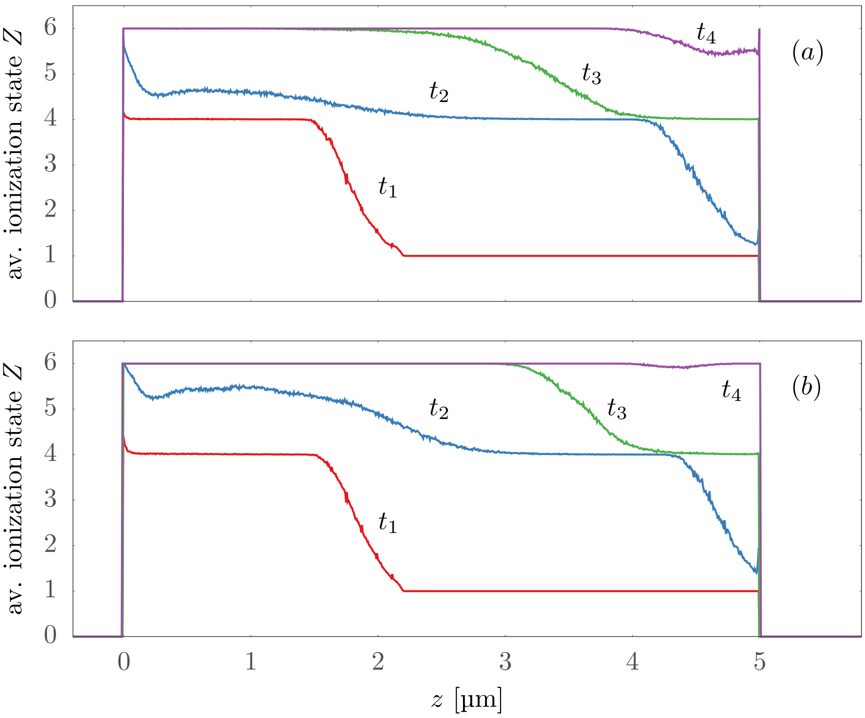

Figure 4.2: Averaged ionization state Z of the carbon ions along the wire axis x for a (a) linearly polarized and (b) circularly polarized laser pulse at $t_1 = -48.5\,T_0$, $t_2 = -41\,T_0$, $t_3 = -33.5\,T_0$ and $t_4 = -26\,T_0$ before the peak of the pulse hits the wire. *(Source: [17], see summary 4.8 below for details.)*

We have seen that the nanowire is firstly ionized at the surface. The electrons that are set free this way are subject to the laser electric field vector that acts on the surface of the wire and pulls the electrons out of the wire into the voids. Thus, the structure of how those electrons are arranged is a trace of the electric field vector, as can be seen in the cross sections of the current density distributions j_y and j_x shown in Figs. 4.3(a) - 4.3(d). They illustrate the motion of electrons in the plane perpendicular to the wire axis z. It can be observed that the currents have a periodicity of one wavelength, confirming that they are caused by the laser electric field. While they are only ordered in the polarization plane $y-z$ for linear polarization [Fig. 4.3(a)] and not in the perpendicular $x-z$ plane [Fig. 4.3(b)], they move along a spiral around the wire along the z-axis for a circular polarized pulse [Figs. 4.3(c) - 4.3(d), and Fig. 4.4(a)].

The strength and time of the ionization dynamics considered here strongly depend on the intensity of the laser pulse. The ionization potentials of the underlying atoms determine the intensity threshold to achieve certain charge states on the surface of the wires, where the field interacts with them. The field ionization releases electrons which are then subject to the Brunel effect (see section 2.1.5). These Brunel electrons penetrate into the plasma and then lead to ionization of the wire core by collisional ionization. In the example presented above the leading front of the laser pulse with an intensity $I \approx 5.5 \times 10^{19}\,\mathrm{W/cm^2}$ (at $t_4 = -26\,T_0$ the intensity at the bottom of the wire is $\approx 0.01\,I_0$ with the peak intensity $I_0 = 5.5 \times 10^{21}\,\mathrm{W/cm^2}$ for circular polarization) was strong enough to fully ionize the carbon atoms.

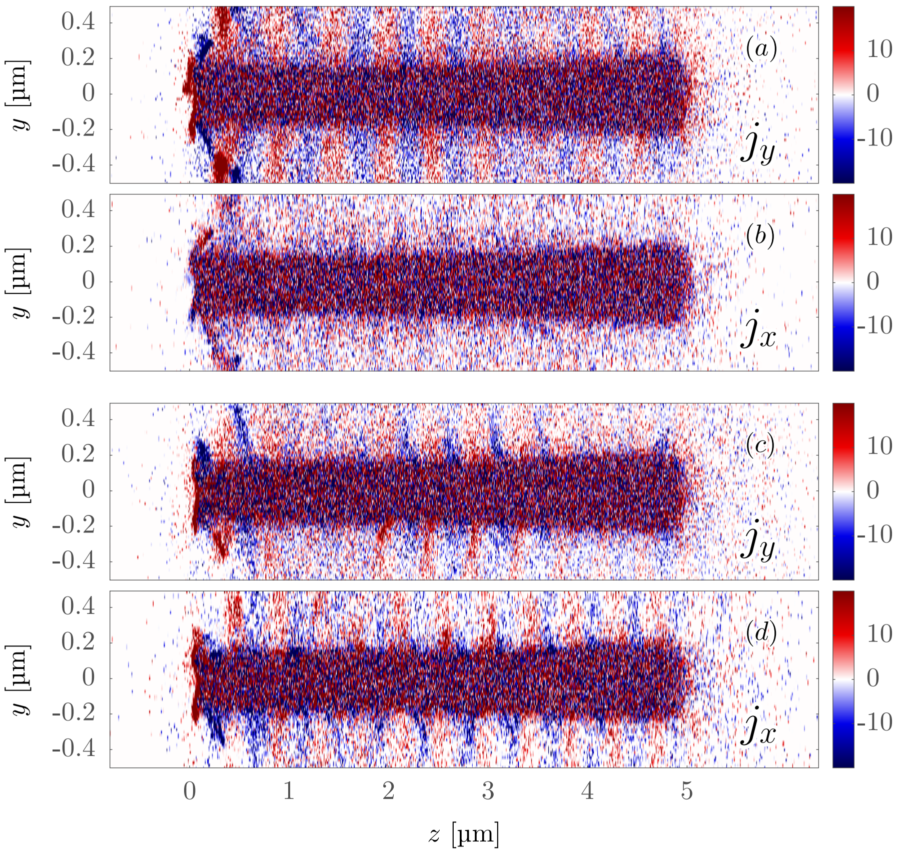

Figure 4.3: Longitudinal cross sections (in the y-z plane) of the transverse current density components j_y and j_x $[en_{\mathrm{cr}}c]$ (e: electron charge, n_{cr}: critical density, with $n_{\mathrm{cr}} = 7 \times 10^{21}\,\mathrm{cm^{-3}}$ for a 400 nm laser, c: speed of light) at $t = 4\,T_0$ after the peak of the pulse hits the surface for a linearly polarized laser. *(Source: [17], see summary 4.8 below for details.)*

The ionization process described this way takes place at the early stage of the interaction and is separated in time by the extraction of the electrons into the gaps between the wires. This is owed to the very high laser intensity that ionizes the material very soon, leaving time for the absorption of the more intense part of the pulse and the subsequent occurrence of further effects as described in the next sections.

4.4 Return current

The current density components considered in the previous chapter apply to the $y-x$ plane perpendicular to the nanowire axis z and are the starting point in the formation of the new nanoscale ultra-dense Z-pinch. We discuss this effect in the following by presenting results of full three-dimensional (3D) relativistic particle-in-cell simulations for an array of aligned carbon nanowires of 300 nm diameter and 5 µm length.

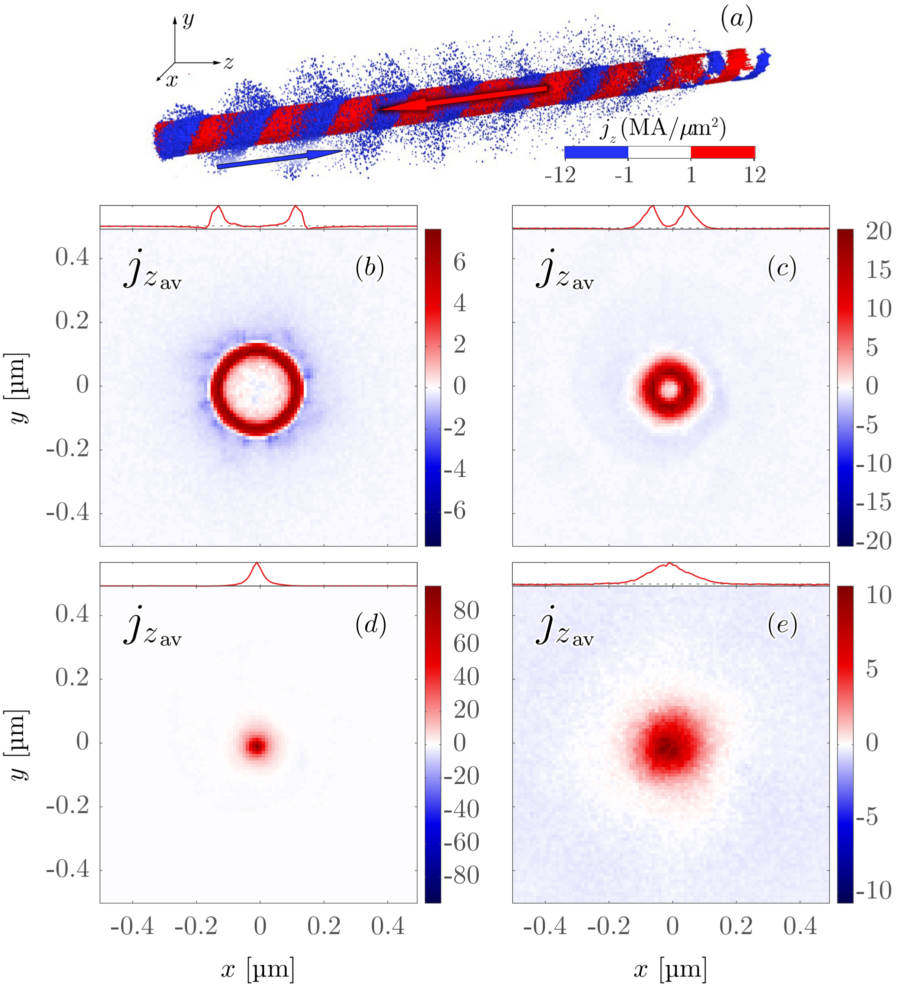

Figure 4.4: Frame (a): Current density j_z at $t = -44.5\,T_0$ before arrival of the peak of the pulse to the target surface. Electrons pulled out of the wire move in the laser propagation direction (blue color, from left to right). A return current is created (red color, from right to left). Frames (b)-(e): Cross sections of the averaged current density distribution, $j_{z\mathrm{av}}$ [MA/µm^2]. The times are (b) $t = -26\,T_0$, (c) $t = -13\,T_0$, (d) $t = -7\,T_0$ and (e) $t = 8\,T_0$. The times of the snapshots are given with respect to the peak of the pulse reaching the target surface in units of the laser period ($T_0 = 1.33$ fs). The wires are 300 nm in diameter and are irradiated by a $\lambda = 400$ nm laser pulse of 60 fs duration with $a_0 = 17$. *(Source: [18], see summary 4.8 below for details.)*

The periodicity of the array is 1 µm, which corresponds to an average density of 7 % solid density. The array is irradiated by 400-nm-wavelength laser pulses of 60 fs FWHM duration and a vector potential of $a_0 = 17$, corresponding to an intensity of 4.95×10^{21} W cm^{-2}.

The laser beam is modeled as a circularly polarized plane wave with a Gaussian temporal profile impinging at normal incidence onto the nanowire array. The irradiation of the nanowires with pulses of relativistic intensity leads to rapid ionization of the material. The low Z carbon atoms are completely ionized and the plasma becomes transparent for x-rays. Thus, the radiation cooling time is estimated to exceed that of the hydrodynamic expansion by 2-3 orders of magnitude in the entire range of densities (up to $1 \times 10^{25}\,\mathrm{cm}^{-3}$) and temperatures (keV to MeV) of interest here. This includes the case of extreme electron densities of nearly 1300 times the critical density and MeV temperature encountered at large a_0. Therefore, radiative effects were not included in the simulations. The intense laser pulse pulls out electrons along the electric field $\vec{E}$ and can be seen as transverse currents discussed previously (Fig. 4.3). Once they are located in the interwire gaps, they are accelerated forward via the $\vec{v} \times \vec{B}$ force by the laser pulse. This forward-moving electrons in the surrounding of the wires will lead to electrostatic fields due to the resulting charge separation, which is compensated by a large return current inside the nanorod such that quasineutrality is maintained. At this point the relativistic character becomes apparent, as the forward momenta of the electrons moving in the laser field scale like a_0^2, in contrast to the transverse momentum which is $\sim a_0$ (see subchapter 2.1.3). Therefore, the forward current that drives and sets the speed of the return current is substantially determined by the laser intensity. The circular laser polarization arranges these currents along a spiral path. This is illustrated in Fig. 4.4a, where the forward-moving electrons in the voids of the wires, defined here as a negative current, are indicated in blue, while the positive current densities corresponding to the return current of the backward flowing electrons is indicated in red. The domains of the forward and return current are spatially separated (Fig. 4.4). The return current is initially located in the skin layer of the nanowire [Fig. 4.4(b)]. However, an emerging quasistatic azimuthal magnetic field caused by this current exerts a radially symmetric inward directed $\vec{j} \times \vec{B}$ force on the electrons. Consequently, the return current is radially compressed [Fig. 4.4(c)]. This process compresses the backward flowing electrons to a thin filament of high current, concentrated at the nanowire axis [Fig. 4.4(d)]. The backward-flowing electrons are thereby accelerated to an average velocity of up to $v \approx 0.23c$ and the return current density reaches a value of $j_z = 96\,\mathrm{MA}/\mu\mathrm{m}^2$ [Fig. 4.4(d)], where T_0 is the laser period (1.33 fs). The corresponding total current through the cross section is $\approx 21 I_0$, with $I_0 \approx 17\,\mathrm{kA}$ the Alfvén current.

4.5 Azimuthal magnetic field

The longitudinal cross sections of the magnetic field components illustrated in Fig. 4.5 reveal the emerging quasistatic field. The laser propagation direction is from left to right. Initially this field is located at the surface of the nanowire, separated from the alternating component of the laser [Figs. 4.5(a) and 4.5(b)]. As the laser pulse propagates deeper into the nanowire array, the quasistatic field fills the space initially occupied by the nanorod [Figs. 4.5(c) and 4.5(d)], surrounding the compressed wire. To separate the quasistatic magnetic field from the laser field, one can average the components B_x and B_y of the magnetic field along the wire axis as shown in Fig. 4.6. This way the alternating field components from the laser field will cancel out and the quasistatic field remains. Considering the filtered B_x and B_y components together, it becomes clear that an azimuthal quasistatic magnetic field surrounding the wire is present. The clockwise polarity of that field indicates that it originates from the backward-flowing electrons.

As can be seen in the averaged current density profiles (Fig. 4.4) and the magnetic field cross sections (Fig. 4.5), the averaged transverse magnetic field component encircles a wire of a drastically reduced radius at a time close to the peak of the pulse. A more clear way to illustrate the spatial relation between the current and the magnetic field is depicted in Fig. 4.7. The magnetic field is shown in a plane near the tip as arrows whose color and length indicate the magnitude, whereas the density of the return current is described by isosurfaces for different values with different colors. The arrows in the center of the plane are circularly arranged around the backward current, whereas at the edges of the plane they point in downward direction, corresponding to the magnetic field direction of the laser field at this time. Followed in a time evolution, it can be seen that a stronger return current is surrounded by a stronger quasistatic magnetic field component. This observation of the temporal dependence is verified by plotting the averaged return current density and the averaged transverse magnetic field component $B_\perp^2 = B_x^2 + B_y^2$ over time (Fig. 4.8) for $a_0 = 6$ and $a_0 = 17$. To obtain the values, the variables are first averaged along the nanowire axis in the range occupied by the wire, and then averaged in the resulting transverse plane. For $a_0 = 6$ [Fig. 4.8(a)] the return current at first rises and grows up until around the peak of the pulse at $t = 0\,T_0$, where it then drops off. The magnetic field has similar development and reaches its maximum around the same time despite a slight time delay in the rising part. This can be attributed to the fact that besides the backward current there is also the forward current of electrons. It will have an influence on the formation of the magnetic field that becomes insignificant as the return current reaches its peak. The sloping part of the quasistatic magnetic field has a slower and roughly linear evolution. It persists up to the time $\approx 70\,T_0$ where it falls below the noise level of the current, as the tail of the laser pulse keeps the process running until it passes the wire at $66.5\,T_0$.

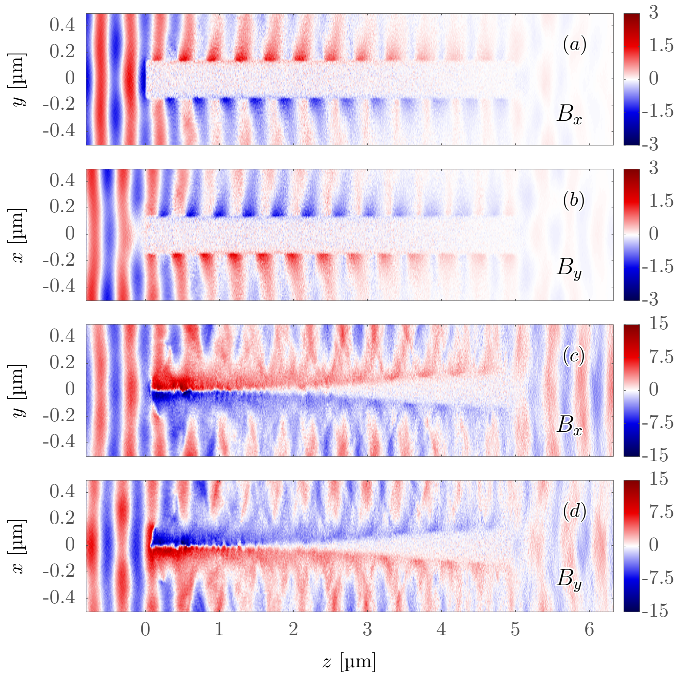

Figure 4.5: Longitudinal cross sections of magnetic field components B_x and B_y (in Gigagauss) at $t = -35\,T_0$ (frames a,b) and $t = -7\,T_0$ (frames c,d). Laser propagation is from left to right. *(Source: [18], see summary 4.8 below for details.)*

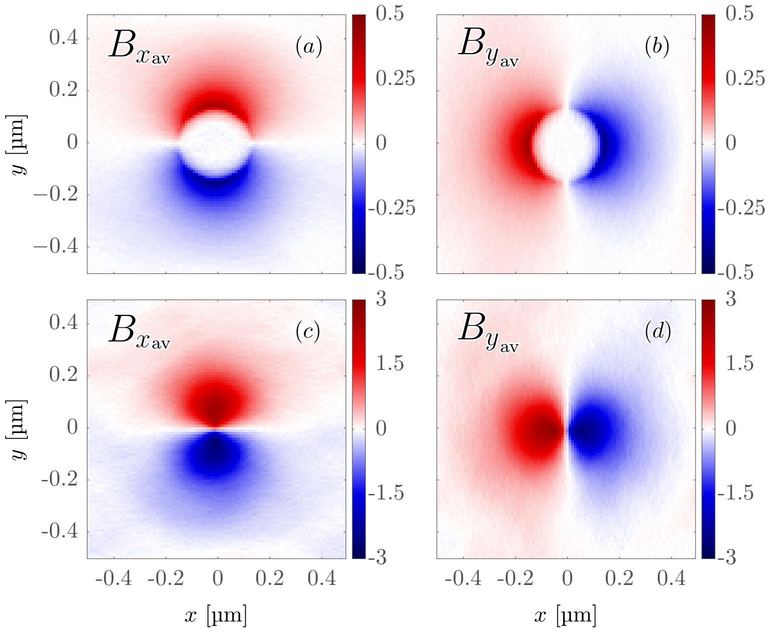

Figure 4.6: Quasi-static magnetic field components in Gigagauss at (a-b) $t = -35\,T_0$ and (c-d) $t = -7\,T_0$. The quasi-static field is extracted from the total field provided by the simulation code by averaging over the nanowire axis, which cancels out the alternating component stemming from the laser light. *(Source: [18], see summary 4.8 below for details.)*

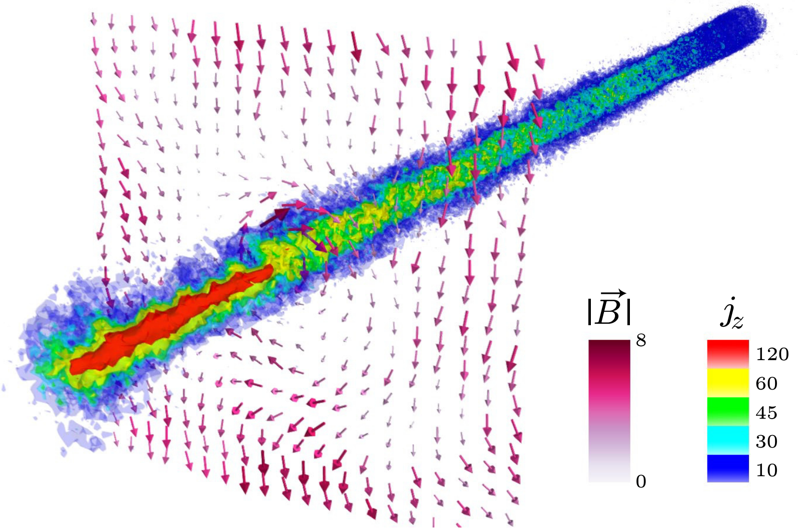

Figure 4.7: Magnetic field $\vec{B}$ [GGauss] represented as a vector plot in a plane near the tip, where the arrow color and length indicate the magnitude. The density profile of the return current j_z [MA/µm^2] is depicted as isosurfaces of different colors, corresponding to different values. The laser pulse enters the simulation box at the bottom left and the time of the snapshot is $t = -10\,T_0$.

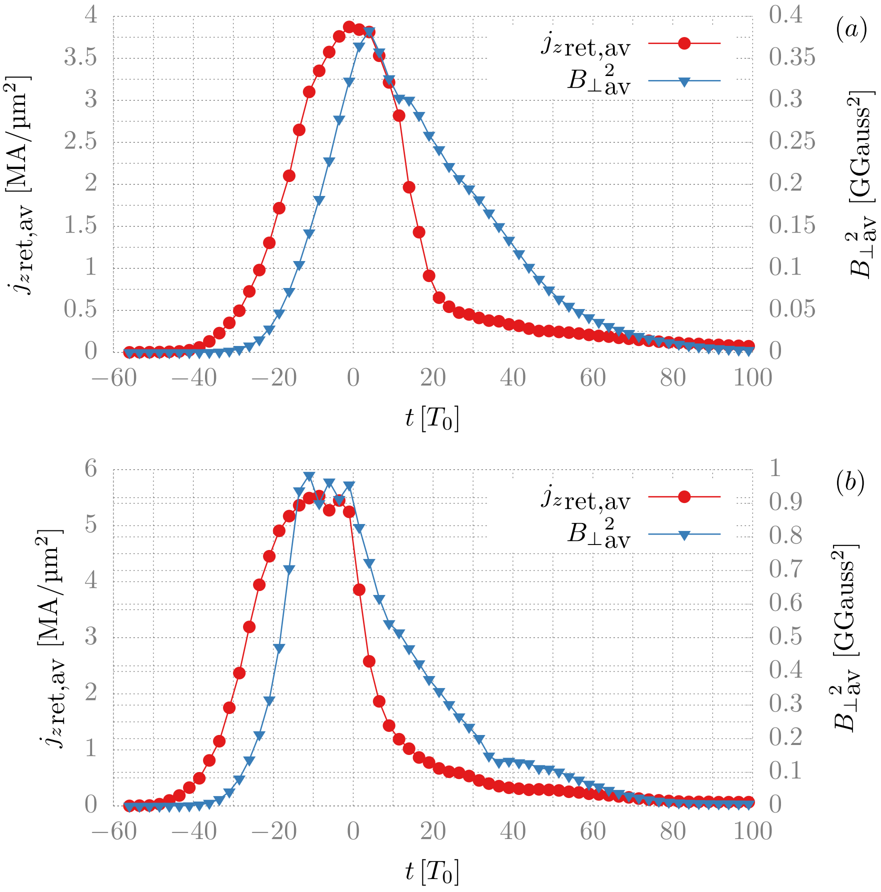

Figure 4.8: Averaged return current $j_{z\mathrm{ret,av}}$ [MA/µm^2] (red curve) and averaged transverse magnetic field $B^2_{\perp\mathrm{av}}$ [GGauss^2] (blue curve) plotted against the time $t\,[T_0]$ with respect to the peak of the pulse hitting the target tip for $a_0 = 6$ (a) and $a_0 = 17$ (b).

At the higher intensity $a_0 = 17$ [Fig. 4.8(b)] the curves essentially coincide with Fig. 4.8(a), except for the magnetic field being slightly less steady from the peak on and that the peak is reached at an earlier time. This is due to the stronger pinch leading to a faster heating, causing more irregularities after the onset of the explosion that takes place earlier.

4.6 Compression

The quasistatic magnetic field compresses the nanowire, leading to a reduction of the radius and an increase in the particle densities. These observables enable us to measure the strength of the pinch. We need to consider that the increase in the electron density, n_e, is due to two different processes: the strong optical field ionization of the carbon ions by the laser pulse, subsequent electron impact ionization, and the spatial compression by the pinch effect. Since all the atoms are fully ionized long before the peak of the laser pulse (at $t = -26\,T_0$), any further electron density increase is attributed to the pinch effect.

The scheme of the nanopinch formation is shown in Fig. 4.9 as a sequence of single steps. As the laser pulse extracts electrons out of the nanowire [Fig. 4.9(a)] and drives them forward in vacuum [Fig. 4.9(b)], a large backward flow of electrons is generated [Fig. 4.9(b)]. The return current creates a quasistatic azimuthal magnetic field [Fig. 4.9(c)], which exerts a radially symmetrical inward directed Lorentz force [Fig. 4.9(d)].

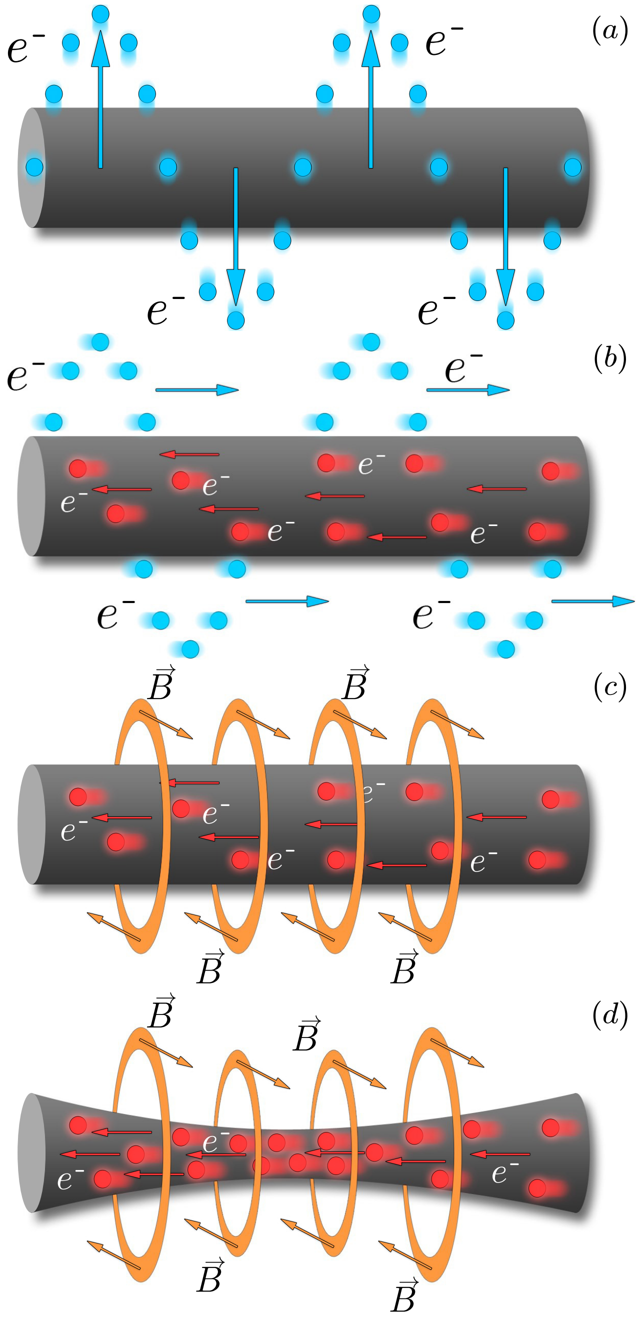

Figure 4.9: Scheme of the nanoscale Z-pinch.

After having explored the generation of the return current and the according magnetic field, we now observe the process of compression in an end-on view of the averaged electron number density [Figs. 4.10(a) - 4.10(d)]. They are obtained by averaging the electron density over the uniform segment of higher density at each of the stages. The compression starts at the surface layer, seen as a high-density ring, and the whole wire is squeezed until the average density is highly concentrated at the wire center. Since the return current, and hence the quasistatic magnetic field, have a limited lifetime, at some point the plasma pressure becomes stronger than the confining magnetic pressure giving rise to an expansion of the wire, and consequently to a decrease of the density [Fig. 4.10(d)].

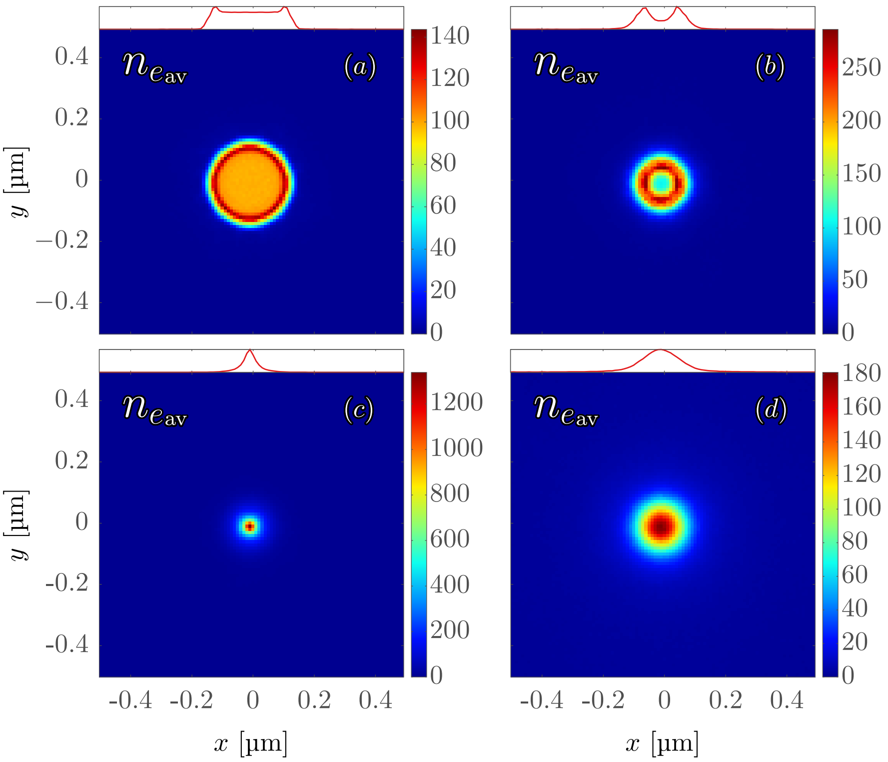

Figure 4.10: Cross sections of the electron number density distribution, n_e (in units of the critical electron density $n_{\mathrm{cr}} = 7 \times 10^{21}$ cm^{-3}). The frame times are (a) $t = -26\,T_0$, (b) $t = -13\,T_0$, (c) $t = -7\,T_0$ and (d) $t = 8\,T_0$. *(Source: [18], see summary 4.8 below for details.)*

Figures 4.11a-4.11d present $y-z$ cross sections of the electron density of the irradiated nanowire, giving insight to the pinch effect along the longitudinal axis. Electron bunches form a periodic structure ($\approx \lambda$ in size, where λ is the laser wavelength) on the surface of the wire [Fig. 4.11(a)]. These electron bunches are pulled out from the nanowire and pushed back into it by the laser field. The high-density layer forming around the wire tip is a sign of the pinch effect kicking in around -13 T_0. As the propagating laser pulse pulls out more electrons along the wire, the return current and therefore the quasistatic magnetic field become stronger. The compression by the pinch effect then leads to an ultrahigh average peak density of $n_e = 1300 n_{\mathrm{cr}} = 9.4 \times 10^{24}\,\mathrm{cm}^{-3}$ [Fig. 4.10(c)] over a length of ≈ 2.4 µm [Fig. 4.11(c)]. As the wire expands the density decreases and the periodic structure of the electrons becomes visible [Fig. 4.11(d)]. A further representation of the particle density compression is by means of three-dimensional isosurfaces as shown in Fig. 4.12. Going to higher densities, the corresponding areas lie deeper in the nanowire core such that the outer surfaces are made transparent in a staggered way to provide visibility. In this sense, one should note that the pinch does not compress the whole plasma uniformly, and that there are low-density layers which are less compressed. For the $n_e = 50\,n_{\mathrm{cr}}$ surface indicated in dark blue one can see a stripe of electrons pulled out and arranged spirally on the outside of the wire due to the circularly polarized laser pulse. In the inner core slight MHD m = 1 kink instabilities develop that are seen as deviations from the perfectly straight thin rod in the form of transverse displacements. However, as can be seen, they do not affect the unfolding of this nanoscale Z-pinch in a major way.

Besides the increase in particle density, the reduction of the wire radius is an essential feature of the pinch effect. The radius as a function of the nanowire axis is depicted for both involved particle species in Fig. 4.13. It is computed by first generating a histogram of the particle density over the radius as the distance from the wire center and then the FWHM value of that distribution is taken. This yields a radius value for a specific position along the wire axis. In order to get a smoothed result, the moving average method is deployed, which computes this radius for a subset of several surrounding transverse planes at each longitudinal position instead of just for one slice. Since the simulation box is on a Cartesian grid, the resolution of the radius computation is limited by the granularity imposed by the grid steps. Besides the radius the particle densities of both species along the center of the wire are also shown in Fig. 4.13. As expected, a reduction of the radius comes along with an increase of the number density. One finds high densities of $\approx 1000\, n_{\mathrm{cr}}$ at the first half of the structure and extraordinarily high values above $2500\, n_{\mathrm{cr}}$ at the tip. At the same time the radius in this segment in $z \in [0, 2.5]$ µm is reduced to $\approx 15\,\%$ of its initial value, which coincides with the resolution limit of $\Delta r / r_{\mathrm{ini}} = 16\,\%$ (where $\Delta r = \sqrt{\Delta x^2 + \Delta y^2}$ with Δx and Δy the grid steps in these directions).

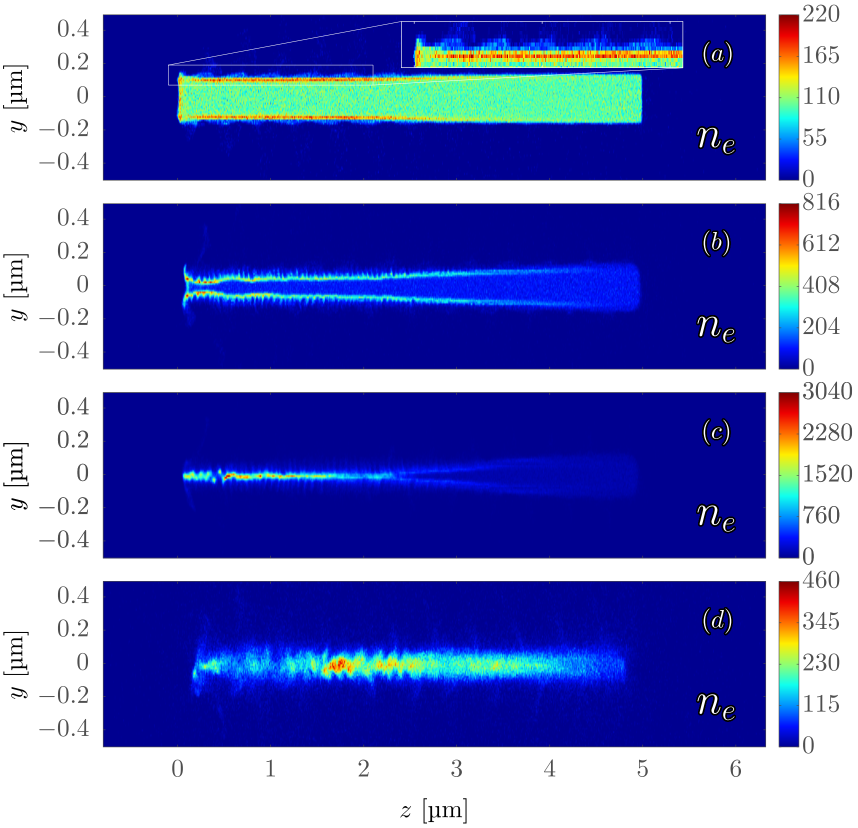

Figure 4.11: Longitudinal cross sections of electron particle density, n_e (in units of the critical electron density $n_{\mathrm{cr}} = 7 \times 10^{21}$ cm^{-3}), at times (a) $t = -26\, T_0$, (b) $t = -13\, T_0$, (c) $t = -7\, T_0$ and (d) $t = 8\, T_0$. The inset in frame (a) shows a zoom of the moving periodic structure on the surface of the nanowire plasma. *(Source: [18], see summary 4.8 below for details.)*

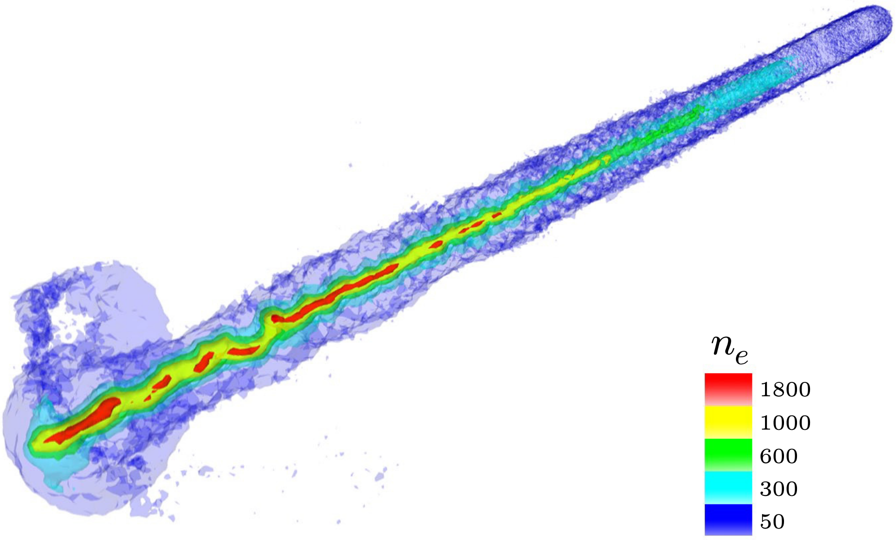

Figure 4.12: Electron particle density distribution $n_e\,[n_{\mathrm{cr}}]$ at $t = -7\,T_0$, represented as isosurfaces of different colors, corresponding to different values. The laser pulse enters the simulation box at the bottom left.

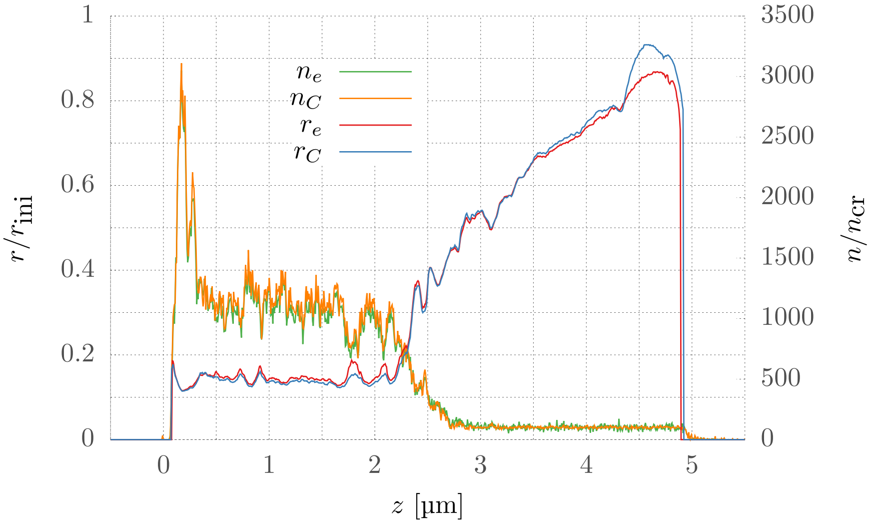

Figure 4.13: Particle densities of the carbon ions n_C and electrons n_e at the center of the wire and the radii of both particle distributions (electrons and carbon ions) normalized to the initial radius r_{ini} at $t = -8\,T_0$.

The lowest part of the wire shows diverging radii for the carbon and electron distributions, which is attributed to ablating and accelerating layers of carbon ions in transverse and longitudinal direction. This can be explained by a Coulomb explosion due to the return current exhausting electrons from the bottom of the wire and leaving behind bare positively charged carbon ions, which repel each other. In general, the nanowires will explode either due to a hydrodynamic expansion or due to a Coulomb explosion and since the pinch heats up the plasma rapidly, this dissolution takes place right after the compression and therefore earlier than in typical cases without a pinch.

4.7 Intensity dependence

All results presented so far, except for Fig. 4.8(a), were simulated with a laser amplitude of $a_0 = 17$. Since we have seen that the onset of the pinch is a relativistic effect, the dependence on the laser intensity is a key factor. For this reason, several simulations with different intensities were conducted. Figure 4.14 shows the current density and quasistatic magnetic field as a function of time for the different simulated laser amplitudes.

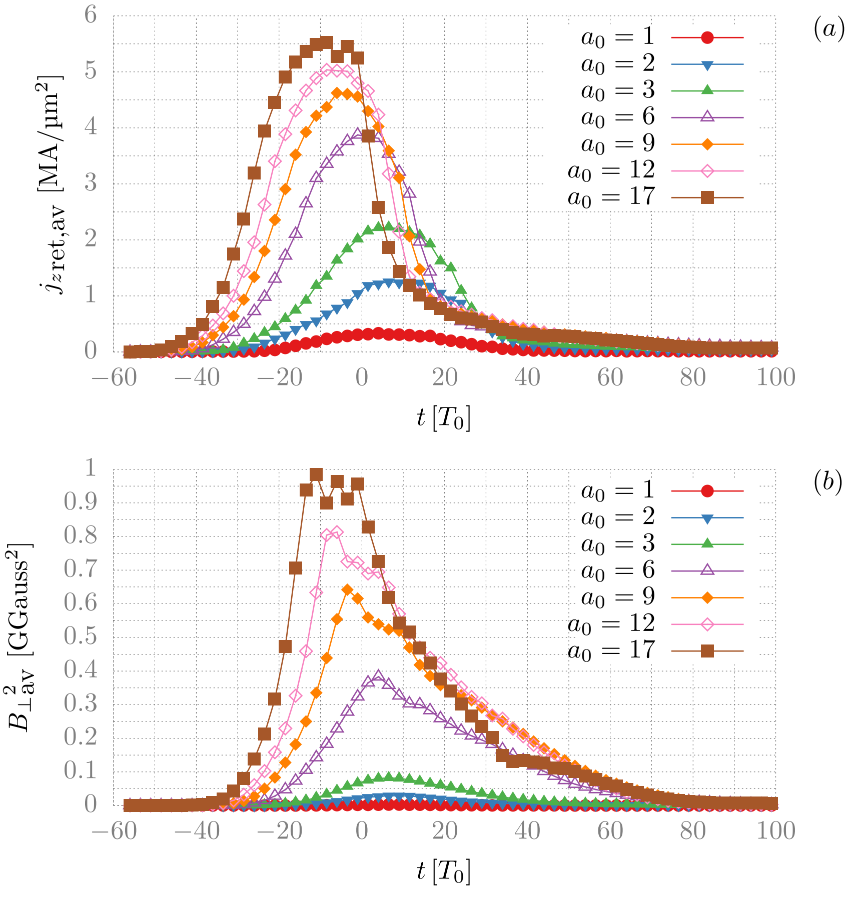

Figure 4.14: Averaged return current $j_{z\mathrm{ret,av}}$ [MA/µm^2] (a) and averaged transverse magnetic field $B^2_{\perp\mathrm{av}}$ [GGauss^2] (b) plotted against the time $t\,[T_0]$ with respect to the peak of the pulse hitting the target tip for $a_0 = 1, 2, 3, 6, 9, 12$ and 17.

It can be seen that a higher laser intensity will produce a stronger return current, which in turn generates a stronger quasistatic magnetic field. Moreover, the peak values are reached at earlier times, which is owed to a faster buildup of plasma pressure that overcomes the confining magnetic pressure, which leads to a faster explosion of the material. This provokes a sooner drop of the current and magnetic field strength and becomes apparent as a shift of the peaks to earlier times. As a consequence of the stronger return current and self-generated field, the radial compression goes up by means of the inward $\vec{j} \times \vec{B}$ force. The averaged wire radius as a function of time are presented in Fig. 4.15 for different laser intensities. The radius is first computed as explained in Fig. 4.13 and averaged along the wire axis at each step to yield the shown figure. The common trend at $a_0 > 1$ for both the electrons and carbon ions, which essentially coincide, is to be compressed and then to widen. This expansion is seen for $a_0 \geq 9$ as a rise above the initial radius r_{ini}, whereas for $a_0 < 9$ seems to have an unpredicted behaviour. That is explained by the disassembling of the wire, which yields unreasonable values in the calculation of the wire radius as explained in Fig. 4.13.

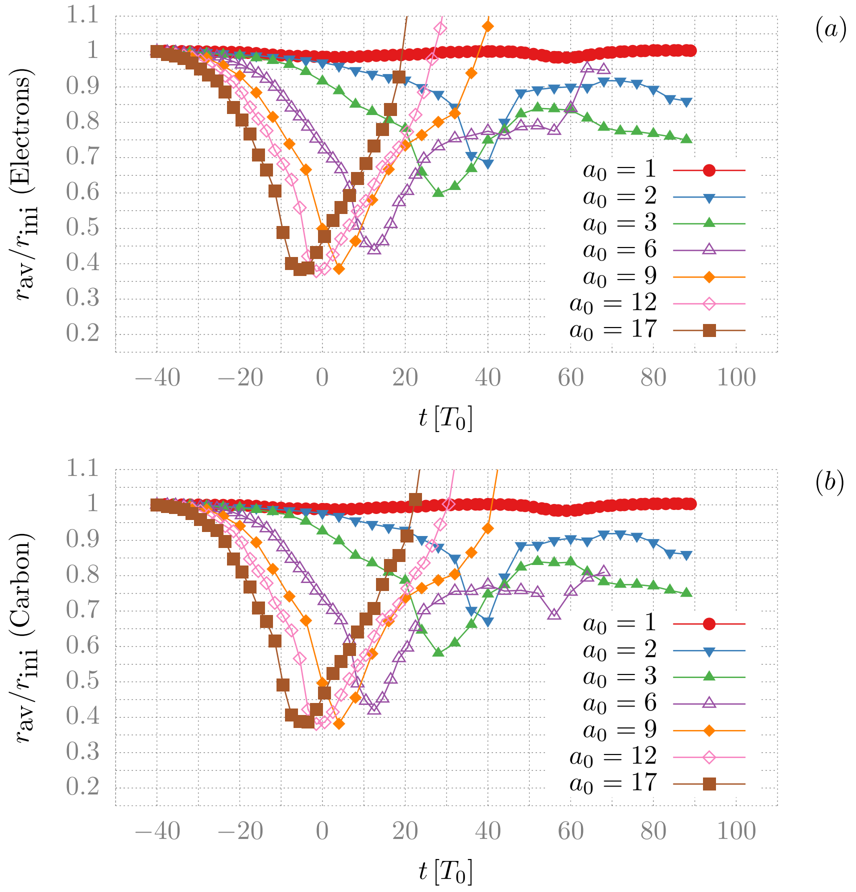

Figure 4.15: Averaged nanowire radius normalized to the initial value $r_{\text{av}}/r_{\text{ini}}$ for particle densities of electrons (a) and carbon ions (b) plotted against the time $t\,[T_0]$ with respect to the peak of the pulse hitting the target tip for $a_0 = 1, 2, 3, 6, 9, 12$ and 17.

Another striking feature is the delayed time of radial minimum with respect to the peak of the magnetic field [Fig. 4.14] at the lower intensities. The onset of the inward directed Lorentz force will cause electrons and ions to radially move towards the center and for lower laser amplitudes fewer particles are affected with lower velocities. This lesser compression weakens the magnetic field as it follows the high density layer of ions and electrons into the plasma, such that for weaker laser amplitudes there is a bigger temporal shift between maximum radial compression and magnetic field. Closely related to this is the temporal correlation of a dip around the peak of the magnetic field strength at the time of the minimum average radius. On the contrary, there is essentially no compression for $a_0 = 1$, which is also observed in Fig. 4.16. It shows the minimum radii, r_{min}, as a function of the laser amplitude a_0.

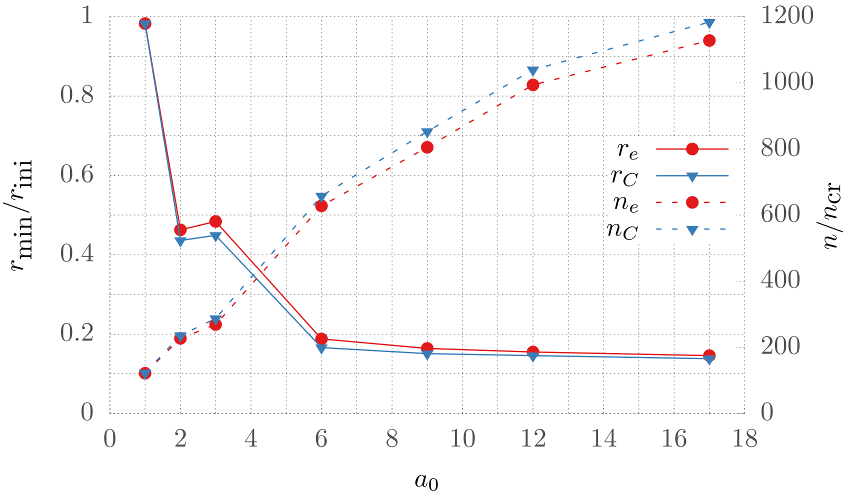

Figure 4.16: Minimum radii normalized to the initial nanowire diameter (solid lines) and corresponding averaged particle densities of electrons and carbon ions (dashed lines) in units of the critical electron density, $n_{\mathrm{cr}} = 7 \times 10^{21}\,\mathrm{cm}^{-3}$, for seven different laser amplitudes. The values were computed by averaging over the nanowire segment with the narrowest radius and highest density. While the minimum radius for $a_0 = 2$ is $\approx 2\,\%$ smaller than for $a_0 = 3$ (see also dashed line), the average radius of the whole wire is $\approx 7\,\%$ larger (Fig. 4.15). *(Source: [18], see summary 4.8 below for details.)*

The values were calculated by first evaluating the radii and densities in the same way as in Fig. 4.13 and then averaging the values over the segment of the nanowire with the smallest radius, highest density and longest uniform compression length. For an ultraintense laser pulse of $a_0 = 17$ the minimum observed radii normalized by the initial wire radius are $r_{\mathrm{min}}/r_{\mathrm{ini}} = 15\,\%$ for the electrons and $r_{\mathrm{min}}/r_{\mathrm{ini}} = 14\,\%$ for the carbon ions. This slight difference results from the fact that when 60 cells are used in the transverse direction the minimum radii values are slightly below the resolution limit of $\Delta r/r_{\mathrm{ini}} = 16\,\%$ with respect to the initial radius r_{ini}. For a higher number of 100 cells in the transverse direction the resolution improves to $\Delta r/r_{\mathrm{ini}} = 9\,\%$, and the minimum radius at $a_0 = 17$ are computed to be $r_{\mathrm{min}}/r_{\mathrm{ini}} = 13\,\%$ and $12\,\%$ for electrons and carbon ions respectively. The minimum radii for $a_0 \geq 9$ in Fig. 4.16 are limited by the simulation resolution. The dashed curves in Fig. 4.16 show the particle densities for both, electrons and carbon ions. Due to the Gaussian density profile of the nanowire plasma (Fig. 4.10) and as already seen in the isosurfaces in Fig. 4.12, the particle density does not scale with the square of the radius as one would expect for a uniformly cylindrical compression. Judging by the radial contraction seen in Fig. 4.16 and Fig. 4.15, the pinch onset takes place between $a_0 = 1$ and $a_0 = 2$. This is not surprising as the forward drive of the electrons in the wire surroundings by the ponderomotive force which is crucial for the occurrence of the pinch becomes significant for relativistic intensities. The electron temperature at this transition point increases from 35 keV to 100 keV at the end of the laser pulse, and from 1 keV to 5 keV at the time the nanowires dissolve into a nearly homogeneous plasma about 600 fs after the peak of the laser pulse. The carbon ion kinetic energy increases from 1-3 MeV when no pinch occurs to 10-15 MeV when it does. For the highest simulated laser amplitude of $a_0 = 17$ the electron temperature reaches 4 MeV and the carbon ions gain energies > 100 MeV.

a_0	Particle sort	Time $t\,[T_0]$	Temperature T
1	Electrons	41.5	35 keV
2	Electrons	41.5	100 keV
1	Electrons	439.0	1 keV
2	Electrons	439.0	5 keV
1	Carbon	41.5	1-3 MeV
2	Carbon	41.5	10-15 MeV
1	Carbon	439.0	0.1-0.2 MeV
2	Carbon	439.0	1-2.5 MeV
17	Electrons	56.5	4 MeV
17	Carbon	56.5	130-150 MeV
17	Electrons	439.0	77 keV
17	Carbon	439.0	50-70 MeV

Table 4.1: Temperatures of electrons and carbon ions for $a_0 = 1$ and $a_0 = 2$, where the pinch onset takes place, and for the highest simulated intensity $a_0 = 17$ at a time during the laser-plasma interaction and at a later stage where the plasma has homogenized. *(Source: partly from [18], see summary 4.8 below for details.)*

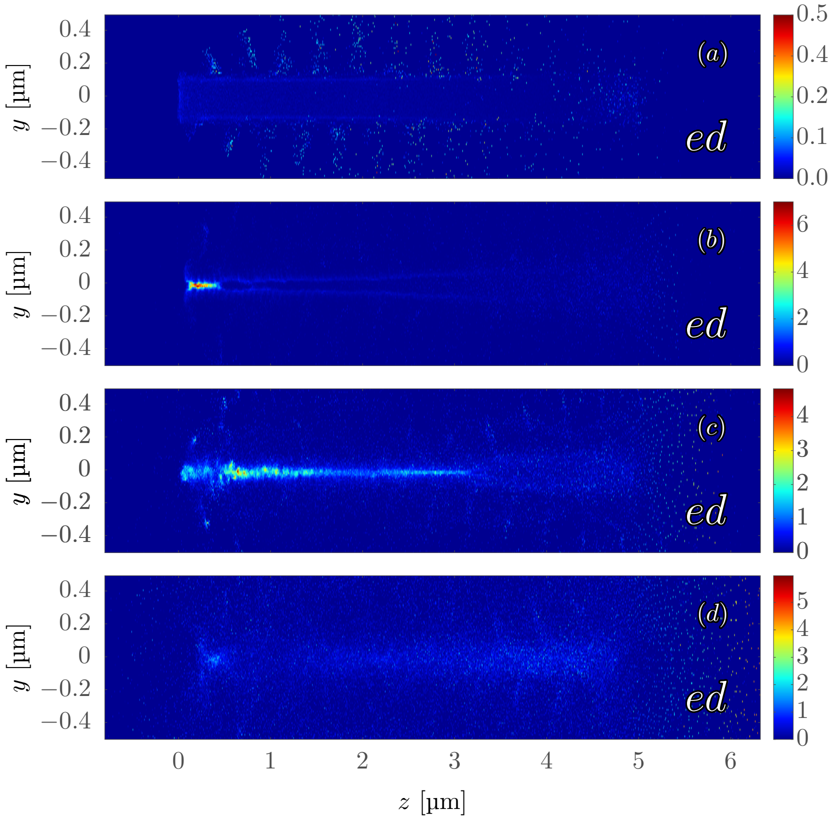

Figure 4.17: Longitudinal cross sections of the total energy density (electrons and ions) (in TJ cm^{-3}), at times (a) $t = -26\,T_0$, (b) $t = -11\,T_0$, (c) $t = -3.5\,T_0$ and (d) $t = 11.5\,T_0$ for a normalized laser amplitude of $a_0 = 17$. *(Source: [19], see summary 5.6 below for details.)*

The temperatures are enlisted with some additional values for later simulation times in Tab. 4.1, which might be useful as a potential signature of the pinch effect for experimental studies. To see the energy density that is realized in the course of the simulation for $a_0 = 17$, one can summarize the energy density value of each PIC particle (as a product of its kinetic energy and particle density) in a grid according to its position. The result of this computation is shown in Fig. 4.17 as a time evolution. The unit of the snapshots is $\mathrm{TJ\,cm^{-3}}$, which is four orders of magnitude above the characterization of ultrahigh-energy density matter ($1 \times 10^8\ \mathrm{J\,cm^{-3}}$). At first the extracted electrons exhibit energy densities of above $0.1\,\mathrm{TJ\,cm^{-3}}$ [Fig. 4.17(a)], which is significantly surpassed by values of up to $6\,\mathrm{TJ\,cm^{-3}}$ in the pinch regime [Fig. 4.17(b)]. At the later stages after the wire dissolves, ions at the bottom of the wire undergo Coulomb explosion and reach values of $5\,\mathrm{TJ\,cm^{-3}}$ [Fig. 4.17(d)]. By using a deuterated nanowire material with a sufficiently thick substrate, these energetic particles are able to drive fusion reactions that lead to production of neutrons [21], as will be shown in chapter 7. The limitations of the pinch effect can be roughly narrowed down as follows. The lower limit is, as already seen, given by relativistic intensities $a_0 > 1$. The upper limit is given by the extraction of too many electrons, which on the one hand can weaken or prevent the laser absorption, and on the other hand leads to rapid Coulomb explosion. Thinner nanowires ($< 100\,\mathrm{nm}$ diameter) at $a_0 \geq 1$ are typically more prone to undergo a Coulomb explosion quickly as the electrons extracted at the surface cannot be balanced by the lower number of electrons in the core. This leaves the positively charged ions behind which experience the Coulomb repulsion, leading to a rapid explosion of the whole structure. In thicker nanowires, the dissolution mechanism tends to be the hydrodynamic expansion, that naturally occurs after the more stable wire is able to absorb more laser energy and heats up as a whole on a longer timescale. This implies the expansion of the ions that are pulled by the electrons through electrostatic charge separation fields, which causes a gradual energy transfer from electrons to ions over time.

4.8 Summary

The basic interaction between a femtosecond laser pulse of $a_0 = 17$ and 18 intensity and carbon nanowire arrays was investigated. It is seen that the wire gets ionized on the surface first where it interacts with the laser field via field ionization. After electrons are set free this way, they lead to further ionization via impact ionization up into the core, such that the interior of the wire is ionized shortly afterwards. A circularly polarized laser pulse is shown to ionize the wire slightly faster. The whole carbon nanowire is fully ionized after the first 28 laser cycles of irradiation. Furthermore, one observes transverse currents in the voids between the wires with a direction corresponding to the laser polarization. These electrons located in vacuum are pushed in forward direction by the driving laser pulse, leading to the creation of a large return current as a means to maintain quasineutrality. It is shown that this results in the generation of a new kind of nanoscale Z-pinch, which was subsequently studied. As a consequence of the backward current a quasistatic azimuthal magnetic field arises, which due to the inward Lorentz force uniformly compresses the nanowire. We have investigated the compression, which is seen as a reduction of the radius to a fraction of its initial value as well as an increase in the particle density. An analysis of the intensity dependence of the effect reveals its relativistic nature and hints at its limitations characterized by the target dimension. Moreover, the effect proves to easily reach the UHED regime by producing energy densities four orders of magnitude above the threshold. The principle of this extremely dense pinch opens up the way to new fundamental studies and applications. The strong compression extends the time that the laser pulse has to be absorbed in the vacant space between the nanowires, before the gaps are closed by the expansion of the nanorods. This advances the volumetric heating of these near-solid-density structures and thus enhances the generation of x-rays as well as fusion neutrons, which can be produced when the nanowires are made of a deuterium-containing material.

The publication of the nanoscale Z-pinch lead to a recent follow-up study on the generation of strong magnetic fields [187].

The results presented in the section 4.3 are reproduced from [17]. The text was largely adopted literally, with some adaptations for a matched integration. The figures were redesigned to fit into the thesis, but contain the same data. The results and contents from sections 4.2 (rephrased), 4.4, 4.5, and parts of section 4.6, 4.7 and 4.8 are reproduced from [18] Physical Review Letters © copyright (2016) American Physical Society. The major part was adopted literally (with some adaptations), the figures (Figs. 4.4, 4.5, 4.6, 4.10, 4.11, 4.16) were taken unchanged and Tab. 4.1 stems only partially from the publication. All other figures and data are unpublished material, the corresponding descriptive text is newly written. The author has conducted the PIC simulations, analyzed and interpreted the data and has written the manuscripts to which co-authors have contributed. All figures and tables were created by the author.

Chapter 5

Energy penetration

5.1 Introduction

In the last chapter, we have seen in numerical simulations that laser-irradiated nanowires are able to produce extremely high energy densities far into the ultrahigh energy density regime. In this chapter, we will focus on a study that has the aim to determine the depth of the heating in the nanograss, which is a key parameter when it comes to the heated volume and therefore the deposited energy density in the target. For this purpose the nanowires are composed of two different materials, nickel at the top and cobalt at the bottom. Both have their own characteristic x-ray radiation lines, which are emitted when the material is heated. This feature represents a diagnostic tool (see also section 2.2.2) that allows to experimentally register how deep the heating goes when different lengths of the nickel tip are utilized by monitoring the signal strength of the buried cobalt tracer material. Our collaborators at the Colorado State University have conducted experiments using such composite nanowires. They found that the energy penetrates several micrometers into the nanowires. To establish a theoretical model, we have performed PIC simulations at the experimental conditions. Our colleagues used a transient atomic kinetics and radiation transport model based on our PIC results, which allowed our computations to be directly compared to the experimental results, showing a good agreement. After this verification of our calculations, we have conducted further simulations, which predict energy densities in excess of $8 \times 10^{10}\,\mathrm{J\,cm^{-3}}$ that can be achieved by scaling to higher irradiation intensities. These values for the energy density coincide with the results obtained in the previous chapter.

Section 5.2 briefly deals with the UHED regime in laboratory setups and introduces the measurement technique, which produced the experimental results of our colleagues described in section 5.3. They are modeled by the simulation results in section 5.4. Subchapter 5.5 presents the scaling to higher intensities after which the chapter is concluded with a summary in section 5.6.

5.2 Measurement technique

In section 2.2.1 we have seen the advantages of using laser-irradiated nanowire targets as a means of producing UHED conditions in the laboratory using table-top, joule-class, femtosecond lasers. Considering that the aligned nanowire arrays are highly optically absorbent, the heat penetration depth into the arrays is the key unknown parameter for determining the plasma volume heated and, thus, the deposited energy density. In this chapter, the first definitive determination of the volume of heated material in arrays of high aspect ratio aligned nanowires irradiated by femtosecond pulses of relativistic intensity is presented. The results of our partners' experiments at an intensity of $4 \times 10^{19}\,\mathrm{W\,cm^{-2}}$ that show heating of near-solid-density matter to multi-kilo-electron volt temperatures over depths of several micrometers are presented. The results serve to validate a model of the relativistic interaction that is used to study the physics of these unique plasmas and to predict the UHED conditions that will be achieved when the intensity is increased to the limit of currently available laser systems and beyond. As shown below, this approach promises to achieve unprecedented energy densities in excess of $8 \times 10^{10}\,\mathrm{J\,cm^{-3}}$, equivalent to 0.35-Tbar pressures using existing ultrafast laser facilities.

The measurement technique consists of monitoring the He_α line emission from buried nanowire segments of a selected tracer material. As described in section 2.2.2, this specific line radiation needs the presence of highly charged states up to only two remaining electrons in the atomic shell. The use of this technique required our partners to grow arrays of ordered nanowires that have a compositional change along the length of each nanowire [Fig. 5.1(a) and 5.1(b)]. They found it to be advantageous to choose neighboring elements on the periodic table that have similar ionization dynamics for the top and buried (tracer) segments to form an array that does not differ significantly from one of uniform composition. This selection also allows the characteristic spectral lines of both materials, such as the He_α lines, to be recorded simultaneously within the spectral window of a single crystal spectrometer. In this experiment, the composition of the top segment of the nanowires was nickel ($Z = 28$), and the buried tracer element was cobalt ($Z = 27$). The experiments were simulated using the combination of our PIC code with a transient atomic kinetics and radiation transport model of our collaborators.

5.3 Experimental setup and results

The experiments were conducted by our colleagues irradiating the segmented nanowire arrays with $\lambda = 400\,\mathrm{nm}$, ultrahigh-intensity contrast ($> 10^{12}$) pulses of 0.6 J of energy, and 55-fs FWHM duration from a frequency-doubled titanium-sapphire laser at the Colorado State University. The laser pulses were focused onto the nanowire arrays using an f/2.7 parabolic mirror. The emitted x-ray radiation was analyzed using a von Hamos crystal spectrometer [188] in which a mica crystal spectrally disperses the signal onto a 2D back-thinned charge-coupled device (CCD) sensor array.

Figure 5.1(c) shows a single-shot spectrum from an irradiated dual composition Ni-Co nanowire array in which the He-like (see section 2.2.2) lines of the Ni and Co segments were simultaneously recorded. Both materials have a high Young's modulus (or modulus of elasticity, which is measure of the stiffness of the material [189]), which facilitates the growth of arrays of well-aligned, high aspect ratio nanowires. The nanowire arrays were grown by our partners by sequential electrodeposition of the selected metals into porous anodic aluminum oxide membranes. Subsequent dissolution of the membranes results in freestanding aligned nanowire arrays. The compositional change was thus created by first growing 3- to 4-µm-long Co nanowires at the base of each array followed by the growth of segments of Ni of several selected lengths on top. The change in composition along the nanowires is visible in the scanning electron microscope energy-dispersive spectroscopy (EDS) measurement performed by our colleagues as shown in Fig. 5.1(b). The arrays used in their experiment consisted of 55-nm-diameter nanowires spaced such that the array had an average atomic density corresponding to 13 % of solid density.

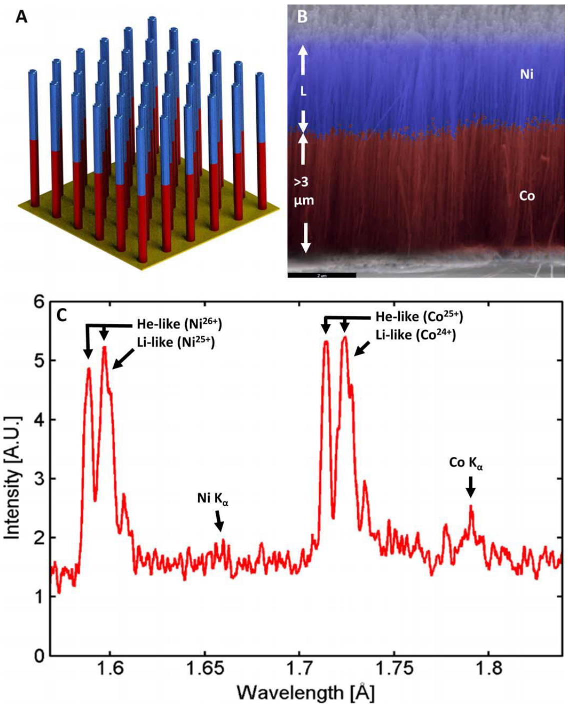

Figure 5.1: Schematic diagram, composition map, and x-ray spectrum of a two-composition Ni-Co nanowire array. (a) Schematic diagram of segmented two-composition Ni-Co nanowire array. The top Ni segment ranges in length from 1 to 6 µm. The nanowires are 55 nm in diameter and form an array that is 13 % of solid density. (b) Scanning electron microscopy image with energy-dispersive spectroscopic elemental composition measurement indicating the concentration of Ni (blue) and Co (red). (c) Example spectra showing the He-like line dominance over the K$_\alpha$ lines for the two elements as recorded using a von Hamos crystal spectrometer. A.U., arbitrary units. *(Source: [19], see summary 5.6 below for details.)*

Figure 5.2 shows a series of spectra measured by our colleagues resulting from irradiating Ni-Co nanowire targets in which the top wire segment of Ni increases in length from 1.5 to 5 µm. The spectra show an increase in the He-like Ni line emission signal and a corresponding decrease in the He-like Co signal as the length of the top Ni nanowire segment increases. In the case of the array with a 1.5-µm-long top Ni layer, the Co lines dominate. This is a first clear indication that the heat penetrates more than 3 µm along the length of the nanowires. A decrease in intensity of the Co lines is subsequently seen as the length of the top nickel layer is increased. The emission from He-like Co ions is observed for targets with up to 4 µm of Ni on top. As the top nickel layer reaches 5 µm in thickness, the Co lines decrease in intensity to a level near that of the continuum background signal that results from bremsstrahlung and radiative recombination. In agreement with the simulations discussed below, this demonstrates that sufficient heat to ionize Co ions to the He-like stage penetrates at least 4-µm-deep into the near-solid-density material. Figure 5.3 plots the peak intensity of the Co and Ni He$_\alpha$ lines measured by our collaborators as a function of Ni nanowire segment length. The Ni lines become stronger as the length of the top segment of this material is increased up to 3 to 4 µm, the length beyond which their strength saturates. Simultaneously, the strength of the Co lines decreases until they disappear into the continuum when the Ni segments reach 5 µm in length.

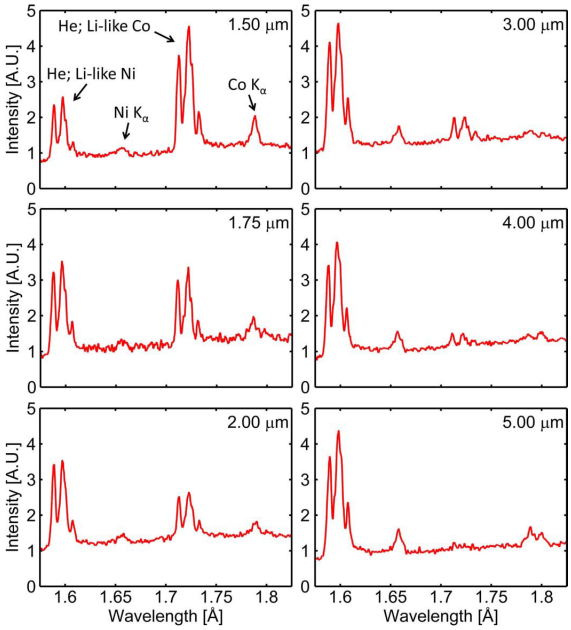

Figure 5.2: Measured spectra of Ni-Co-segmented nanowire arrays with different lengths of Ni wires (listed in the top right corner of each plot) on top of cobalt wires, irradiated by 55-fs pulses at an intensity of ≈ $4 \times 10^{19}\,\mathrm{W\,cm^{-2}}$. The vertically aligned wires are 55 nm in diameter and form an array that has an average atomic density that is 13 % of solid density. Lines of He-like and Li-like Ni and Co are visible along with their respective K$_\alpha$ lines. *(Source: [19], see summary 5.6 below for details.)*

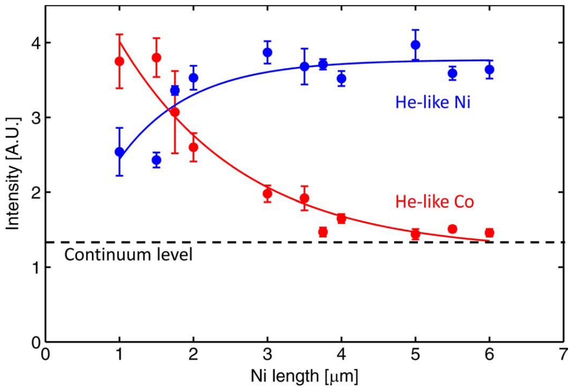

Figure 5.3: Measured intensities of the He-like Co and Ni lines as a function of the length of the top Ni nanowire segment. The target and laser parameters are the same as those in Fig. 5.2. *(Source: [19], see summary 5.6 below for details.)*

5.4 Simulation results

To get a theoretical description of the experimental results, we conducted PIC simulations of nanowire arrays with top Ni segments of different length using the parameters given by the experiment. Subsequently, our collaborators used two post-processor atomic models based on the code Radex [190] using atomic data from the HULLAC code [191]. Our partners used the first of these atomic models to compute the intensity ratio of Co/Ni He-like lines. It used the exact particle energy distribution we computed with the PIC code. The second model, used by our colleagues to simulate the spectra (Fig. 5.4, top), is a very detailed atomic code that considered a large number of excited levels from all the ionization stages present. This greatly more computational intensive model used a two-temperature approximation to the electron energy distribution we computed with the PIC code. Our collaborators computed lines taking into account the natural, Doppler, collisional, and Stark broadening. The Biberman-Holstein approximation [192, 193] was used by them for radiation transport of the He_α lines. For comparison with their experiments, our partners added instrumental broadening to their synthesized spectra (Fig. 5.4). They simulated the continuum by simple approximations for bremsstrahlung and radiative recombination radiation. In our PIC simulations we used a linearly polarized plane wave with 400-nm wavelength and Gaussian time envelope to simulate the laser pulse where the normalized vector potential $a_0 = 2.16$ corresponds to a laser intensity of $I_0 = 4 \times 10^{19}\,\mathrm{W\,cm^{-2}}$ and a 55-fs FWHM pulse duration. We assumed the laser pulse to impinge on the nanowire array at normal incidence. The synthetic spectra (Fig. 5.4, top) closely replicate the observed features of the experimental data. The bottom panel of Fig. 5.4 illustrates the agreement between the measured and simulated Co/Ni line ratios as a function of Ni wire segment length. Figure 5.5 shows the spatial distribution of He-like Ni and Co ions simulated by us for an array with a top segment of 3-µm Ni nanowires after the peak of the laser pulse. It illustrates the generation of He-like Co ions several micrometers under the top Ni nanowire layer. The agreement between measurement and simulations validates the model, which is used below to predict the plasma conditions that could be obtained by increasing the irradiation intensity.

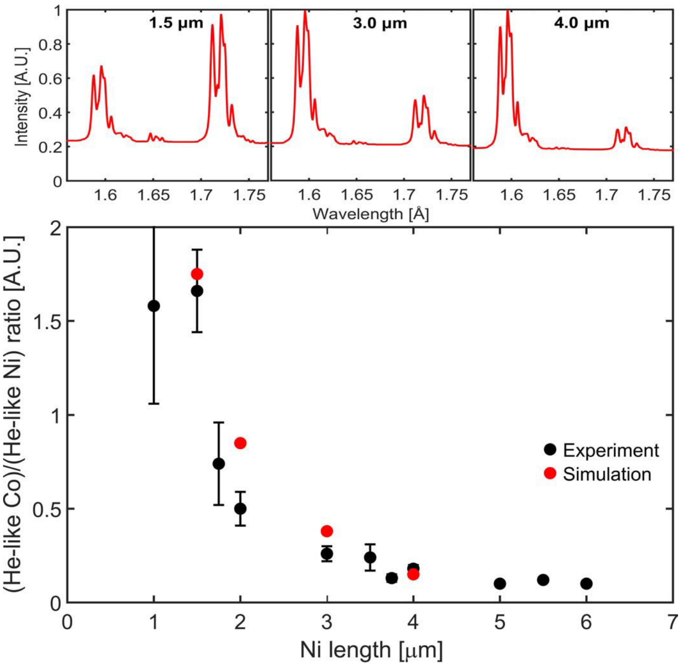

Figure 5.4: Simulated spectra corresponding to arrays with different wire lengths used in the experiment are shown in the top three plots. The target and laser parameters are the same as those in Fig. 5.2. Measured and simulated (Co He_α)/(Ni He_α) line ratios as a function of Ni nanowire segment length are shown on the bottom. *(Source: [19], see summary 5.6 below for details.)*

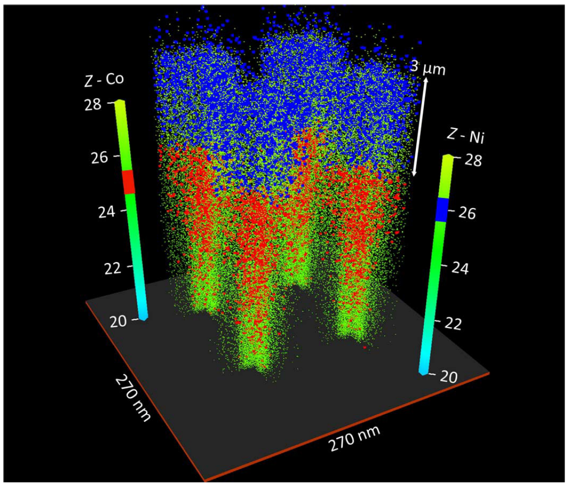

Figure 5.5: PIC simulation of the density of He-like ions in an array composed of segments of vertically aligned Ni and Co nanowires (blue, He-like Ni; red, He-like Co). The target and laser parameters are the same as those in Fig. 5.2. The top Ni wires are 3.0 µm in length. The laser pulse impinges from the top at normal incidence to the array. The one simulated wire was replicated for the sake of vividness. *(Source: [19], see summary 5.6 below for details.)*

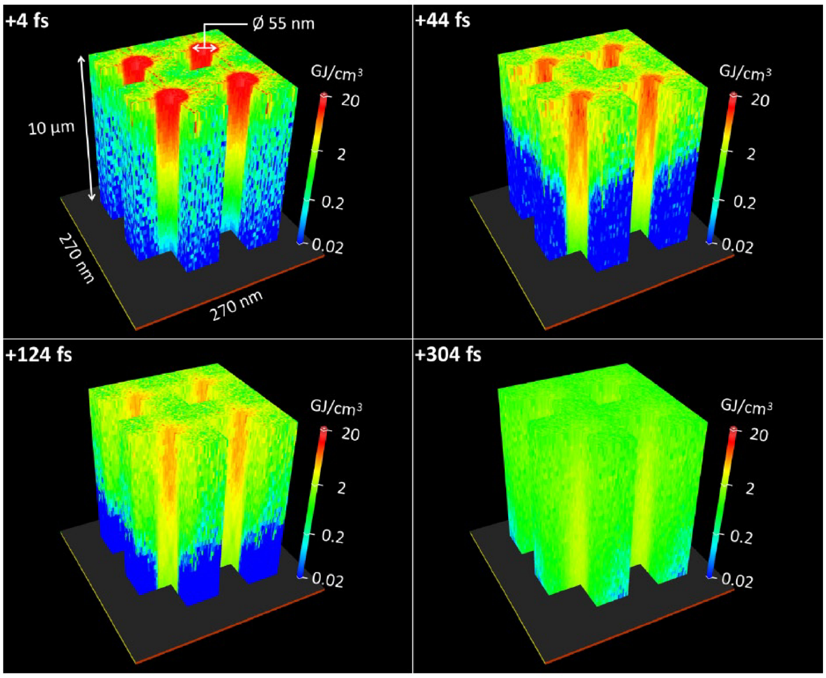

Figure 5.6: Energy density distribution computed by PIC simulation. The target and laser parameters are the same as those in Fig. 5.5. Each frame corresponds to a different time with respect to the peak of the laser pulse as indicated by the time stamp in the top left corner of each frame. The laser pulse impinges into the array from the top at normal incidence. The one simulated wire was replicated for the sake of vividness. *(Source: [19], see summary 5.6 below for details.)*

The energy density and pressure for hot electron gases are given by integrals of the energy and momentum-velocity product, weighted by the distribution function. Our partners have calculated the energy density directly from the particle data from our PIC simulation and estimated the pressure from that, using a formula for an equilibrium relativistic gas, accurate to 1 % [194]. Computed maps of the kinetic energy density at four different times during the plasma evolution are shown in Fig. 5.6. Optical field ionization is observed to begin the heating process at the nanowire surface, with the strong electric field of the laser pulse stripping electrons and creating ionization states up to $Z = 18$. The electrons are rapidly accelerated into the gaps. Collisional electron impact ionization produces higher ionization states as the hot electron population deposits its energy deep into the nanowire cores. The electrons stripped from the wires are accelerated toward the substrate. As described in the previous chapter, charge balance demands the generation of a large laserinduced return current through the nanowires, producing a strong quasi-static self-generated azimuthal magnetic field that pinches the nanowires into a hot, extremely dense plasma [18]. A plasma density surpassing $10^{24}\,\mathrm{cm}^{-3}$ with an energy density of $22\,\mathrm{GJ\,cm}^{-3}$ and pressure of 125 Gbar is quickly reached within the wires near their tips (+4-fs frame; Fig. 5.6).

The laser pulse continues to propagate down the length of the wires and deep into the array as long as the interwire gaps remain free of dense plasma. As the wires expand, the interwire gaps are filled with a supercritical-density plasma. Collisions homogenize the plasma, creating a uniform plasma layer several micrometers thick in which the atoms are ionized up to the He-like stage observed in the measurements. In the two earliest frames in Fig. 5.6 (+4 and +44 fs), the wire tips appear to be loosely connected by regions of higher energy density. This is a result of the array geometry in which the gaps are narrower in the directions directly between wires. These narrower gap regions thus fill with particles more quickly and reach higher energy densities faster than the diagonal regions. Expansion of the wires continues to progressively close the interwire gaps along the length of the wires (+124-fs frame; Fig. 5.6) until the whole target cross section is filled with material at an energy density of $1\,\mathrm{GJ\,cm}^{-3}$ and pressure of 7 Gbar (+304-fs frame; Fig. 5.6). A thermalized electron temperature of ≈ 14 keV is reached over the plasma volume with an average electron density greater than $3 \times 10^{23}\,\mathrm{cm}^{-3}$. Even higher plasma densities can be obtained by irradiating arrays with higher wire filling factors, arrays made of a higher Z material, or a combination of both.

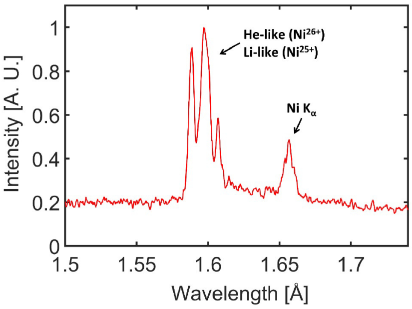

Figure 5.7: Spectrum of an array of 55-nm-diameter Ni nanowires with an average atomic density corresponding to 30 % of solid density irradiated at $4 \times 10^{19}\,\mathrm{W\,cm}^{-2}$ with an ultrahigh contrast $\lambda = 400\,\mathrm{nm}$ laser pulse of 55-fs duration. Strong He-like, Li-like Ni lines are observed. *(Source: Supplementary material in [19], see summary 5.6 below for details.)*

An example spectrum of a Ni nanowire target with an average atomic density corresponding to 30 % of solid density irradiated at an intensity of $4 \times 10^{19}\,\mathrm{W\,cm^{-2}}$ is shown in Fig. 5.7. It was produced as described above for Fig. 5.4. The spectrum is again dominated by He-like (Ni^{+26}) and Li-like (Ni^{+25}) lines, which indicate the high degree of ionization is maintained. In this case, the average electron density of the homogenized plasma increases up to $\approx 7 \times 10^{23}\,\mathrm{cm^{-3}}$, nearly 100 times the critical density.

5.5 Scaling to higher intensities

We conducted additional PIC simulations to predict the plasma conditions that could be achieved by further increasing the laser irradiation intensity to $1 \times 10^{22}\,\mathrm{W\,cm^{-2}}$ ($a_0 = 34$). The results suggest the generation of unprecedented energy densities and pressures. This is illustrated in Fig. 5.8 for an array of 400-nm-diameter Au nanowires with an average atomic density corresponding to 12 % of solid density, irradiated with a 30-fs duration pulse.

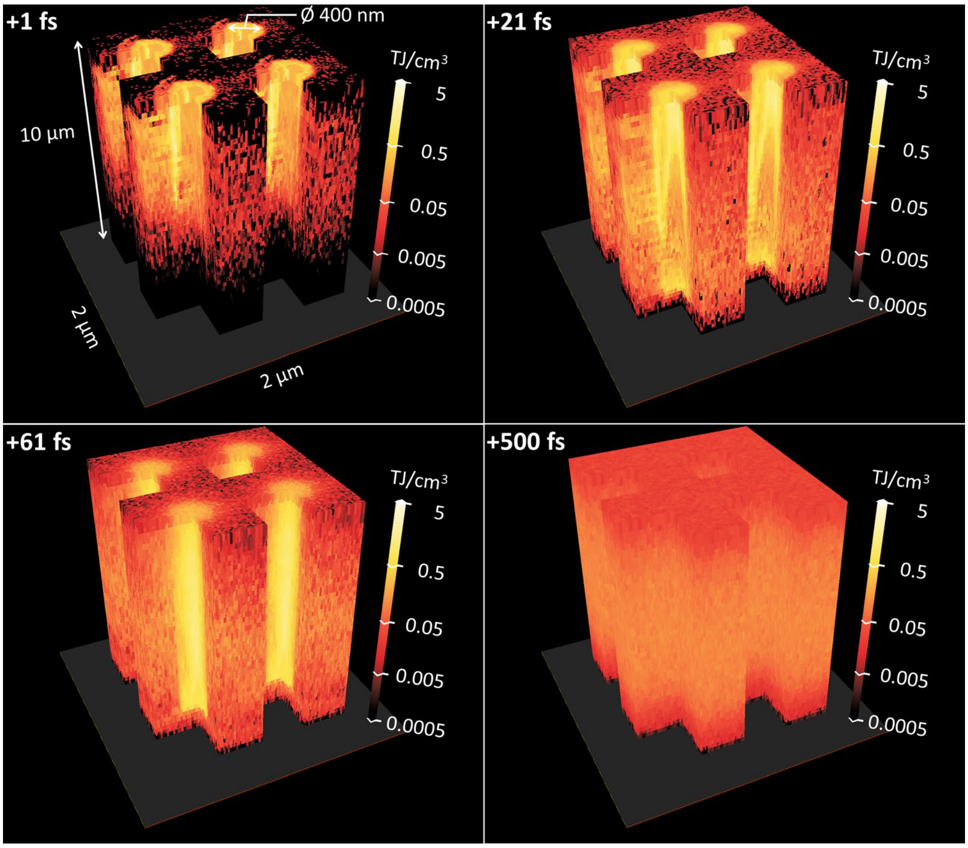

Figure 5.8: PIC-simulated energy density distribution in an array of vertically aligned 400-nm-diameter Au nanowires irradiated with an intensity of $1 \times 10^{22}\,\mathrm{W\,cm^{-2}}$ ($a_0 = 34$) using a 400-nm wavelength pulse of 30-fs duration. The average atomic density is 12 % of solid density. Each frame corresponds to a different time with respect to the peak of the laser pulse. The laser pulse impinges into the array from the top at normal incidence. The one simulated wire was replicated for the sake of vividness. *(Source: [19], see summary 5.6 below for details.)*

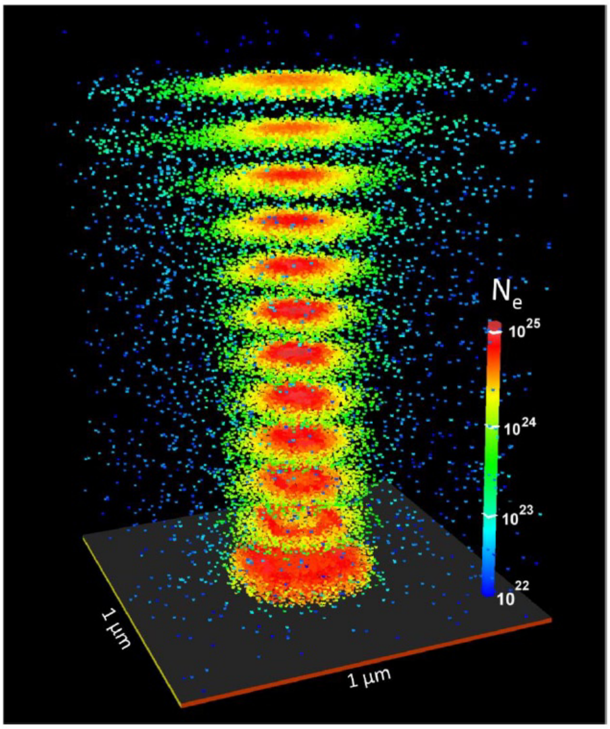

Figure 5.9: Computed electron density distribution in 400-nm-diameter gold nanowire irradiated at an intensity of 1×10^{22} W cm^{-2} with a 30-fs laser pulse, corresponding to the conditions in Fig. 5.8. The plasma column has been sliced to facilitate viewing. The time corresponds to 40 fs after the peak of the laser pulse. During the nanopinch compression phase the electron density reaches 2×10^{25} cm^{-3}. The electron density values are identified in the logarithmic color scale. *(Source: Supplementary material in [19], see summary 5.6 below for details.)*

The plasma density in the gold nanowires during the nanoscale pinch compression phase reaches 2×10^{25} cm^{-3}, which corresponds to nearly 3200 times the critical density (Fig. 5.9). Other laser-target configurations could reach even higher densities during the nanopinch (for example, 6×10^{25} cm^{-3}). These extreme peak densities would approach those obtained from fusion hot spots using megajoule laser energies at the National Ignition Facility ($\approx 1 \times 10^{26}$ cm^{-3}) [195] while potentially reaching higher temperatures. The energy density within the nanowires is predicted to reach a peak value of 2 TJ cm^{-3}, equivalent to a pressure of 7 Tbar near the end of the laser pulse (+21-fs frame; Fig. 5.8). The expansion of the heated nanowires is computed to create a plasma layer in which the energy density is 80 GJ cm^{-3}, equivalent to a 0.35-Tbar pressure (+500-fs frame; Fig. 5.8), larger than the solar interior pressure. The electron energy can be described by a two-temperature distribution, which rapidly thermalizes into a single-temperature distribution defined by an electron temperature of $\approx$ 500 keV, 500 fs after the peak of the laser pulse. Figure 5.10 shows that the gold atoms are predicted to reach extreme degrees of ionization. At 20 fs after the peak of the laser pulse, Ni-like Au ions are dominant, whereas ions up to Ne-like (Au^{+69}) are also predicted to be present within the nanowires for depths up to several micrometers. A few hundred femtoseconds after the end of the laser pulse (for example, +500 fs in Fig. 5.8), the plasma is still hot, and ionization still continues, creating charge states up to Au^{+70}.

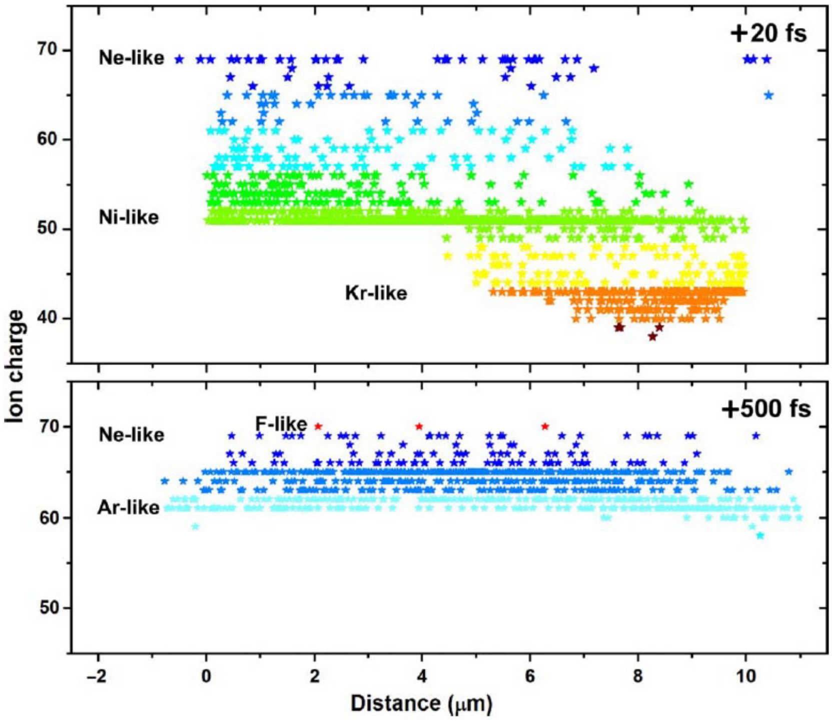

Figure 5.10: Ion charge distribution as a function of depth for an array of 400-nm-diameter Au nanowires with 12 % of solid density, irradiated at an intensity of $1 \times 10^{22}\,\mathrm{W\,cm^{-2}}$ as in Fig. 5.8. This plot was obtained by randomly choosing a fraction of the ions and placing a star at each charge and position. Groups of ionization stages are assigned different colors (for example, $Z = 66$ to 70 is blue) to accentuate the ion distribution and identify rare ions, such as the F-like ions in the bottom. *(Source: [19], see summary 5.6 below for details.)*

Moreover, irradiation of an array of 150-nm-diameter Au nanowires with an initial average density of 30 % solid is predicted to result in denser plasma in which Au atoms near the tip of the array could potentially be ionized to the Be-like stage (Au^{+75}). Irradiation of higher Z elements is expected to result in even higher charge states. These extreme energy densities offer important advantages for the efficient generation of ultrashort pulses of x-rays and neutrons. In the case of x-ray generation, the large plasma density decreases the radiative lifetime. This results in an increase in the hydrodynamic-to-radiative lifetime ratio that leads to a large increase in conversion efficiency. Accordingly, in experiments our collaborators at the Colorado State University have conducted with aligned gold nanowires, they have measured a record conversion efficiency into ultrashort pulses of > 1-keV photons of 10 % in $2\,\pi\,\mathrm{str}$ [20], as we will see in chapter 6. In the case of the generation of neutrons by deuterium-deuterium or deuterium-tritium fusion reactions, the high density of energetic ions is an important advantage because the reaction rate is proportional to the square of the density. These aligned nanostructure plasmas share some similarities to the efficient volumetric heating of clusters in a supersonic gas jet [196], but with the additional advantage of having several orders of magnitude higher-average density, leading to record fusion neutron yields with compact lasers [21], as will be shown in chapter 7.

It is also of interest to gain insight into how the energy density scales with irradiation intensity.

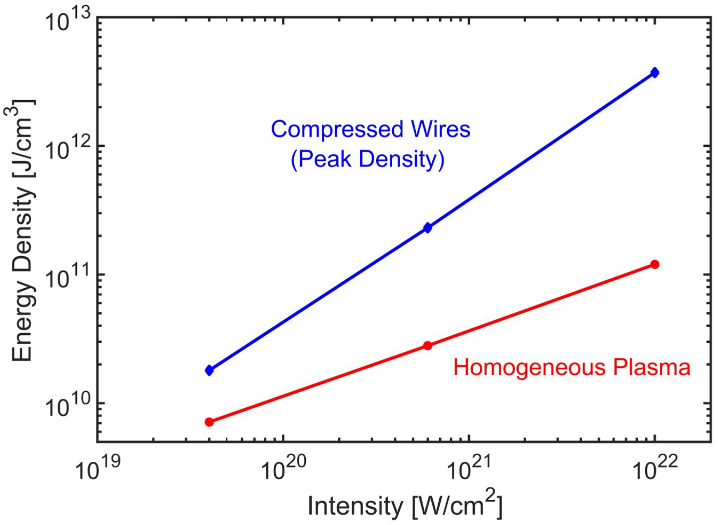

Figure 5.11: Computed scaling of the energy density deposited into Au nanowire arrays as a function of the irradiation intensity for two different times during the plasma evolution. (a) Near the end of the laser pulse (blue trace, energy density scaling as energy density $\propto I$), and (b) when the nanostructure is completely dissolved and the plasma becomes nearly homogeneous, but before the plasma expands as a whole (red trace, energy density scaling as energy density $\propto I^{0.5}$). The average atomic density of the array is 12 % of solid density. The nanowire diameter for each intensity was scaled to maintain the penetration depth approximately constant (55 nm, 150 nm, and 400 nm respectively for the three intensities in increasing order). The laser pulse duration is 30 fs. *(Source: Supplementary material in [19], see summary 5.6 below for details.)*

However, this scaling would have a very limited range of applicability without the simultaneous change of the nanostructure target parameters, for example, the nanowire diameter. The ideal configuration for many applications, such as neutron generation, efficient conversion into x-rays, and creation of highest-Z ions, requires obtaining a plasma lifetime as large as possible compared to the characteristic times of the fusion reactions, radiation cooling, and ionization time, respectively. That means that the laser energy deposition depth has to be typically of the order of the laser focal spot size, which, in our case, is 4 to 6 µm. As the irradiation intensity is increased, scaling of the interwire distance is required to maintain this constant energy penetration depth. Otherwise, not only would the laser energy penetration depth be either too short or too long, but the efficiency of the laser energy deposition would also decrease. This is because there exists a time for the closure of the interwire space for the laser by the expanding plasma, after which a continuous critical density layer is formed, which increases the fraction of laser energy reflected [5]. Therefore, to determine the energy density scaling, our collaborators suggested the strategy of keeping the energy penetration depth approximately constant and comparable to focal spot size while scaling the interwire spacing and nanowire diameter (the latter is required to keep the average atomic density constant). For this case of approximately constant energy deposition depth, the peak value of the energy density occurring near the end of the laser pulse is computed by our PIC simulations and the subsequent evaluation of our partners to scale approximately linear with intensity I, energy density $\propto I$ (see Fig. 5.11). In comparison, at later times when the nanowires are completely dissolved into a homogeneous plasma, the energy density behaves as a sublinear function of the laser intensity, energy density $\propto I^{0.5}$, because of the faster thermal spread of the hotter plasma at larger intensities.

5.6 Summary

The heat penetration depth of the laser energy into nanowire arrays was investigated by using dual composition nanorods consisting of cobalt as a tracer material at the bottom and nickel at the top. The x-ray line radiation of the two ion species in the highly charged He-like states, which require a hot thermal plasma and thus sufficient heating, were monitored. By using different lengths for the Ni tip, one observes a decrease in the tracer signal due to the lower amount of heat that reaches through the tip down to the cobalt segment. Experimentally, our collaborators observed that the heat penetrates at least 4 µm deep into the nanowires, which is in good agreement with the numerical model consisting of our PIC simulations and a transient atomic kinetics and radiation transport model of our partners. We conducted further PIC simulations, which predict that experiments at an increased intensity of $1 \times 10^{22}\,\mathrm{W\,cm^{-2}}$ will result in the generation of unprecedented Tbar-level pressures in laboratory plasmas, surpassing even those in spherical compression laser fusion experiments. As we will see in chapters 6 and 7, these plasmas lead to record conversion efficiency of optical laser light into ultrafast x-ray flashes and to the efficient production of ultrafast neutron pulses by fusion in near-solid-density plasmas.

The results presented in this chapter are reproduced from [19] © The Authors, some rights reserved; exclusive licensee American Association for the Advancement of Science. Distributed under a Creative Commons Attribution NonCommercial License 4.0 (CC BY-NC). The figures were taken unchanged and the text was adopted literally with adaptations for fitting into the thesis. The author has conducted the PIC simulations, provided our collaborators with the data necessary for post-processing and has contributed to the writing of the published manuscript (proofreading and suggestions).

Chapter 6

X-ray generation

6.1 Introduction

As demonstrated in the previous chapter, nanowire arrays are able to absorb laser light and heat up several micrometers deep into the target structure, allowing for deposition of high energy densities. The strongly charged states that are achieved in this process mean that at the same time the electron number density must be very high due to the ionization. In this chapter, we will see that in contrast to flat solid targets, both these features, the deep volumetric heating and high electron densities, are crucial in the generation of picosecond x-ray pulses in these dense nanowire plasmas. As we will see below, these properties enable a record value in the conversion efficiency (CE) compared to related work done before. The critical condition is to accomplish that the plasma cools via radiation instead of expansion. This can be expressed in terms of cooling times. A radiative cooling time τ_{rad} shorter than the hydrodynamic cooling time τ_{hydro} means that electrons can convert their kinetic energy to x-ray emission before their energy is lost to the plasma expansion. Our collaborators at the Colorado State University have measured the x-ray emission from nanowires and flat targets. To have a theoretical description of the involved physics, we have performed three-dimensional PIC simulations at the experimental conditions. The resulting data was in turn used by our colleagues to run hydrodynamic and atomic kinetic calculations. From this numerical model, plasma parameters, the volume of the radiation and the involved radiation and hydrodynamic times in nanowires and flat targets could be computed, providing an explanation for the superiority of the nanograss that is observed in the experimental measurements of our partners.

Section 6.2 describes the special role of nanowires in emitting x-ray pulses. The experimental setup and results are described in section 6.3 and the theoretical modeling by simulations is presented in section 6.4. The chapter closes with a summary in subchapter 6.5.

6.2 Nanowire plasmas as x-ray emitters

In the introduction, it was shown that solid density targets that are irradiated by intense ultrashort laser pulses are able to radiate intense x-ray pulses (see sections 2.2.1 and 2.2.2). However, different factors contribute to limit the CE into ultrafast x-ray pulses. First, only a fraction of the laser energy is absorbed by the plasma. Second, the radiation typically originates from a shallow plasma volume whose rapid expansion results in hydrodynamic cooling rates that exceed the radiation cooling rate. The result is poor conversion efficiency.

Efforts to increase the ultrafast x-ray yield have largely focused on addressing the first of these two limitations by improving the coupling of the laser energy into the material using structured targets. Targets investigated include micro-lithographic gratings [51, 52, 197], nanometer-size dielectric spheres or ellipsoids [50, 54], "smoked" clustered surfaces [49, 52, 53], and nanowire arrays [5, 53, 55, 198, 199]. Increased CE with respect to flat solid targets has been reported [5,49,51,53,55,199,200]. In the case of nanowires, the increased x-ray yield was often adjudicated to increased absorption [53, 199], including enhanced absorption due to a "lightning rod effect" that increases the number of hot electrons as a result of an enhancement of the electric field at the tip of nanostructures [55, 200]. In addition to increased absorption, Kulcsar *et al.* suggested other causes that include a larger number of heated atoms [53]. However, the CE into $h\nu > 0.9\,\mathrm{keV}$ x-rays was limited to $\approx 0.1\,\%$, a value similar to that obtained using smoke targets. In all the experiments with different types of nanostructured targets, the x-ray CE into $h\nu > 1\,\mathrm{keV}$ photons has remained less than $1\,\%$, in spite of the increase in energy coupling. This CE into picosecond x-ray pulses is significantly lower than that achieved in converting laser light into nanosecond x-ray pulses in underdense gas or cavity and pre-exploded foil plasmas [201–205].

We will see in this chapter that an increase of more than one order of magnitude in optical to picosecond x-ray CE can be achieved by tailoring the plasma characteristics to reach a smaller radiative cooling time, τ_{rad}, than the hydrodynamic cooling time, τ_{hydro}, resulting in a larger radiative to hydrodynamic cooling rate ratio that effectively overcomes hydrodynamic cooling. The radiative cooling time is defined here as the time needed to radiatively dissipate the thermal energy of the plasma. In the simple case of an ideal plasma with ions of average charge Z, this characteristic time can be expressed as the ratio of the kinetic energy of free electrons to their rate of radiated energy loss by collisions: $\frac{3Zk_BT_e}{2E}\frac{1}{\langle\sigma\nu\rangle n_e}$, where σ is the effective electron collision cross section for all three major radiative processes (line radiation, photorecombination, and bremsstrahlung), T_e and n_e are the electron temperature and density, respectively, E is the average energy radiated per collision event and k_B the Boltzmann constant. The hydrodynamic cooling time is defined here as $\Delta L/C_{\mathrm{s}}$, where ΔL is plasma size and C_{s} is the acoustic velocity. Considering that, within the range of high electron densities and high temperatures of interest for x-ray generation, τ_{rad} is inversely proportional to the electron-density-dependent total collision rate $\langle\sigma\nu\rangle\, n_e$ and τ_{hydro} is proportional to the plasma size ΔL, this condition requires a large electron density and/or large plasma size such that [20]

$$\tau_{\mathrm{rad}} \propto \frac{1}{\langle\sigma\nu\rangle\, n_e} < \frac{\Delta L}{C_{\mathrm{s}}} \propto \tau_{\mathrm{hydro}}. \tag{6.1}$$

The experimental measurement of our colleagues shows, as we will see, that this approach results in an $\approx 20\,\%$ CE of optical laser light into $h\nu > 1\,\mathrm{keV}$ x-rays in $4\pi\,\mathrm{sr}$, more than one order of magnitude increase in CE with respect to previous work. The inequality in Eq. 6.1 was fulfilled by volumetrically heating supercritical density plasmas by irradiating arrays of high aspect ratio Au or Ni nanowires at an intensity of $I \approx 4 \times 10^{19}\,\mathrm{W\,cm^{-2}}$ with ultrahigh contrast femtosecond laser pulses. The interaction was tailored to simultaneously achieve deep volumetric heating (large ΔL) to multi-keV temperatures, and plasma densities of the order of 100 times the critical density in which the collisional rates are greatly increased with respect to plasmas generated from solid targets.

6.3 Experimental setup and results

The experiments were conducted by our partners by irradiating arrays of freestanding, vertically aligned Au and Ni nanowires with diameters of 55, 80, or 100 nm and 4-6 µm in length. The laser beam impinged parallel to the nanowire axis, normal to the nanowire array target surface. Our collaborators synthesized the nanowire arrays by electrodeposition into anodic aluminum oxide templates [206]. The nanowires were grown with an average density of 12 % solid density for the targets composed of 55 or 80 nm diameter nanowires, and 15 % of solid density for the 100 nm diameter nanowire targets. After dissolving the template, an array of ordered, high aspect ratio ($\approx 50-100:1$) nanowires is exposed. This corresponds to an interwire spacing of 85 and 130 nm for the 55 and 100 nm diameter wire arrays, respectively. Each nanowire target was imaged by our partners using a scanning electron microscope. They irradiated the nanostructured targets by ultrahigh ($> 10^{12}$) contrast $\lambda = 400\,\mathrm{nm}$ pulses of $\approx 55\,\mathrm{fs}$ duration with energy up to 1 J from a frequency-doubled Ti:sapphire CPA laser. The laser consists of a conventional front end followed by three Ti:sapphire power amplifiers pumped by Nd:glass slab lasers designed to operate at up to 5 Hz repetition rate [207]. The beam was expanded to 9 cm, and the pulses were compressed using a gold grating vacuum compressor. Frequency doubling in a 0.8 mm thick Type I KDP crystal with an efficiency of 40-50 % greatly improves the contrast, as the second-harmonic generation process is proportional to the square of the intensity. The duration of the frequency-doubled pulse was measured in a single-shot self-diffraction autocorrelator. The wavefront was corrected with a deformable mirror (Imagine Optic). The high contrast pulses were focused onto the target by a 90 deg off-axis parabolic mirror with a 15.4 cm focal length, resulting in a spot size of $\approx 4.5\,\mu\mathrm{m}$ to obtain an intensity of $\approx 4 \times 10^{19}\,\mathrm{W\,cm^{-2}}$.

The angular distribution of the x-ray emission was measured by our partners using an array of four filtered Si photodiodes mounted at equally spaced polar angles on a 28 cm radius circular rail centered on the laser beam focus where the target was placed. Polished Ni or Au flat solid targets were shot by them immediately preceding each nanowire target shot for comparison. The diodes were placed on a plane that forms an angle of 20 deg with respect to the plane of incidence. Magnet pairs were placed in the front of each of the photodiodes to deflect electrons up to 6 MeV energy away from the diodes. Our colleagues verified that increasing the magnetic field strength by 2× and the length of the magnets by the same factor did not change the photodiode signals, ensuring that the photodiode/filter assembly is in practice only detecting x-rays. The spectrally resolved x-ray emission was simultaneously recorded using a von Hamos mica crystal spectrometer and a front illuminated CCD. Time integrated spectral emission of the plasmas showed He-like Ni ion lines that dominate over the characteristic K_α emission by over one order of magnitude.

For photon energies $h\nu > 1\,\mathrm{keV}$, both Au and Ni nanowires display a convex angular emission profile with maximum intensity in the direction normal to the target (Fig. 6.1), resulting from increased opacity in the periphery of the plasma. Integration of these emission profiles over a hemisphere gives the total x-ray yields shown in Fig. 6.2. Comparison of the x-ray CE for Au and Ni nanowire array targets of different wire diameters shows that the x-ray emission is higher for Au. CE is defined here as the ratio of the measured x-ray energy for photons $h\nu > 1\,\mathrm{keV}$ (or $> 6\,\mathrm{keV}$) emitted into $4\pi\,\mathrm{sr}$ divided by the laser drive energy impinging onto the target. The highest yield corresponds to targets with 80 nm diameter Au nanowires, with an average CE of 18 % and individual shots reaching values up to 22 % in $4\pi\,\mathrm{sr}$ [Fig. 6.2(a)]. This CE for $h\nu > 1\,\mathrm{keV}$ exceeds the highest reported values using any type of target by more than one order of magnitude [51] and those reported for nanowire targets by two orders of magnitude [53]. Figure 6.2(b) compares the $h\nu > 6\,\mathrm{keV}$ plasma emission from Au nanowire targets of different nanowire diameters to that from a Au foil target irradiated with the same pulses. At these energies, the active region of the Si detector starts to become transparent to the radiation. Our collaborators corrected the measured photodiode signal for the 50 µm thickness of the Si detector active region, and also for the energy dependency of the filter transmissivity. For the latter, since model simulations show there is no line radiation above 6 keV for these transient Au plasmas, our collaborators assumed the spectral distribution is that resulting from bremsstrahlung plus photorecombination.

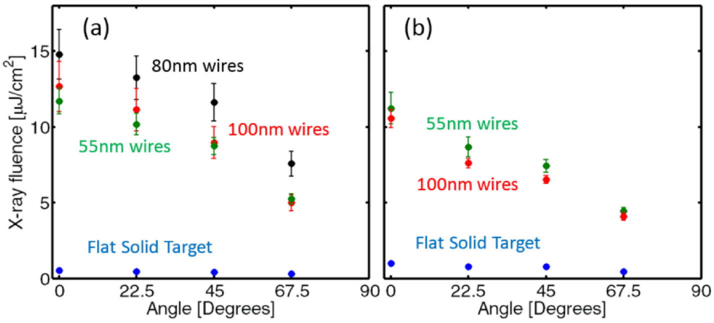

Figure 6.1: Measured angular distribution of the x-ray fluence on each diode from nanowire arrays at photon energies $> 1\,\mathrm{keV}$ for (a) Au and (b) Ni nanowire targets of different nanowire diameters. Measurements for flat solid targets of the same materials are included for comparison. The irradiation intensity was $4 \times 10^{19}\,\mathrm{W\,cm^{-2}}$. Error bars correspond to one standard deviation. Fluctuations in x-ray CE result mostly from irregularities and imperfections in the ordered wire array. The angle is measured with respect to the normal to the target surface. *(Source: [20], see summary 6.5 below for details.)*

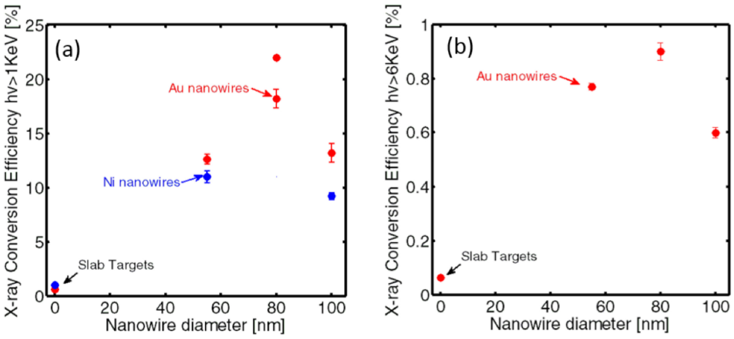

Figure 6.2: (a) X-ray CE ($h\nu > 1\,\mathrm{keV}$) for Au and Ni nanowires arrays of different wire diameters compared to flat solid targets of the same material. $I = 4 \times 10^{19}\,\mathrm{W\,cm^{-2}}$. The values are averages of 10 shots. Error bars correspond to one standard deviation. The maximum measured single-shot CE for 80 nm diameter wires exceeded 22 % in 4π sr, which is represented by the point without an error bar. This yield corresponds to an increase of 35× with respect to a polished flat target; (b) CE into $h\nu > 6\,\mathrm{keV}$ x-rays. An enhancement of 14× in x-ray emission is observed compared to flat targets. *(Source: [20], see summary 6.5 below for details.)*

This continuum radiation was calculated by our partners using the electron energy distribution computed by us in form of PIC simulations (see below). With these corrections, the 80 nm Au nanowire targets are estimated to radiate at $h\nu > 6\,\mathrm{keV}$ with a CE that exceed 0.8 % in 4π sr, an increase of 14 times over Au foils irradiated by the same laser pulses.

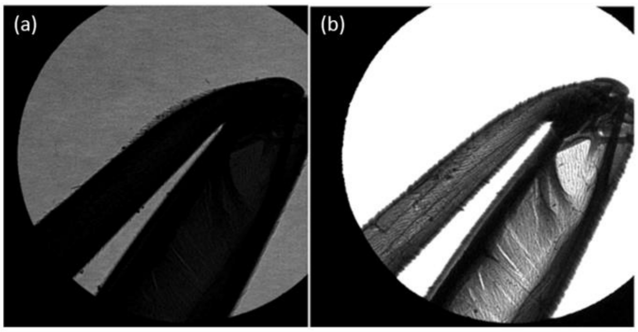

Figure 6.3: Single-shot radiograph of a wasp's knee using the x-ray flash emitted from: (a) a flat Ni target, and (b) an array of 100 nm Ni nanowires. A 13 µm Be filter was used to block photons of $h\nu < 1\,\mathrm{keV}$. The sample was placed at 4 cm from the plasma and a CCD array was placed at a distance of 35 cm from the sample leading to an effective magnification of 8.75× with a field of view of 425 µm. Both images are plotted on the same intensity scale. The laser energy on target was 25 mJ. *(Source: [20], see summary 6.5 below for details.)*

The increase in x-ray flux, the small source size of ≈ 5 µm deduced by our colleagues from the penumbra in a knife edge test, and the picosecond pulse duration makes these plasmas an excellent x-ray point source for time-resolved flash radiography. To illustrate this, our collaborators conducted a single-shot radiography experiment of a wasp's knee. Figure 6.3(b) compares a single-shot radiograph taken by irradiating an array of 100 nm diameter Ni nanowires with 15 % solid density to that obtained by irradiating a flat Ni solid target with a similar laser pulse [Fig. 6.3(a)]. The radiograph taken with the nanowire target shows that a single laser shot with a laser pulse energy of only 25 mJ on target is sufficient to produce a detailed image. In comparison, the image obtained with the flat Ni target shows insufficient flux and would require over one order of magnitude more shots to obtain a similar image.

6.4 Simulation results

To model these experimental findings, we have performed three-dimensional PIC simulations using the parameters given by the experiments. Figure 6.4 illustrates the electron temperature and electron density evolution in an array of Au nanowires at three different times after the laser pulse computed by our PIC simulation. The array is composed of wires 55 nm in diameter with an average density corresponding to 12 % of solid density, and the laser pulse has a 55 fs FWHM duration. In contrast to flat solid targets, where a thin plasma layer is heated, in nanowire arrays the ultrafast laser pulses propagate several micrometers within the interwire gaps. The heated nanowires explode, creating a thick plasma layer of nearly solid density, reaching $n_e \approx 4 \times 10^{23}\,\mathrm{cm}^{-3}$ 311 fs after the peak of the laser pulse, while the electron temperature is ≈ 15 keV [Figs. 6.4(c) and 6.4(f)]. Later the plasma cools, but 1 ps after the peak of the laser pulse the temperature still remains at a few keV. To illustrate the major radiative differences between a flat solid target and a volumetrically heated nanowire array, Fig. 6.5 shows the x-ray radiation power density spatial distribution as a function of time up to 10 ps after the laser pulse, computed by our colleagues.

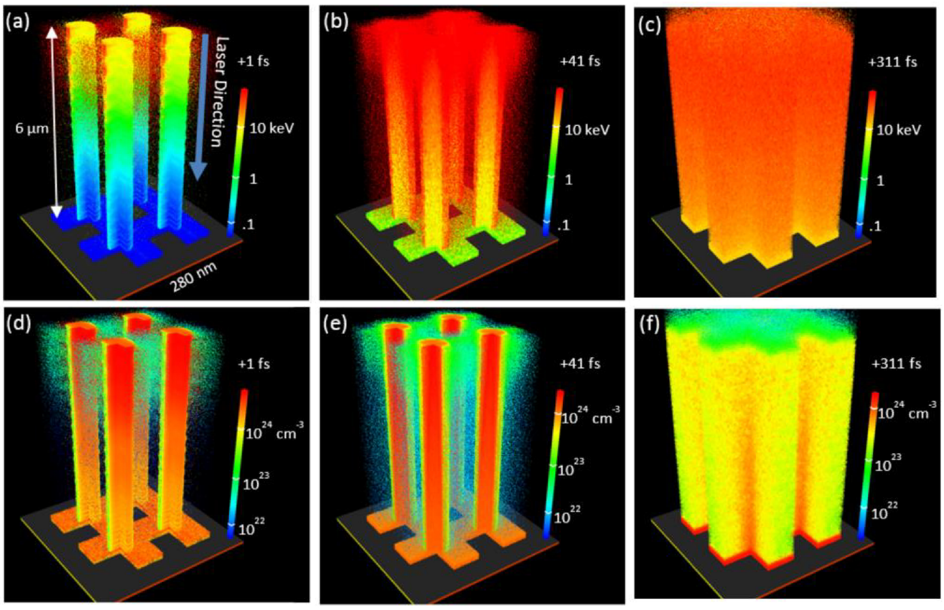

Figure 6.4: (a-c) PIC simulation of the electron temperature distribution in a 55 nm diameter Au nanowire array irradiated by a $\lambda = 400$ nm laser pulse of 55 fs duration at an intensity of 4×10^{19} W cm^{-2} at three different times after the laser pulse. (d-f) shows the corresponding electron density maps. The one simulated wire was replicated for the sake of vividness. *(Source: [20], see summary 6.5 below for details.)*

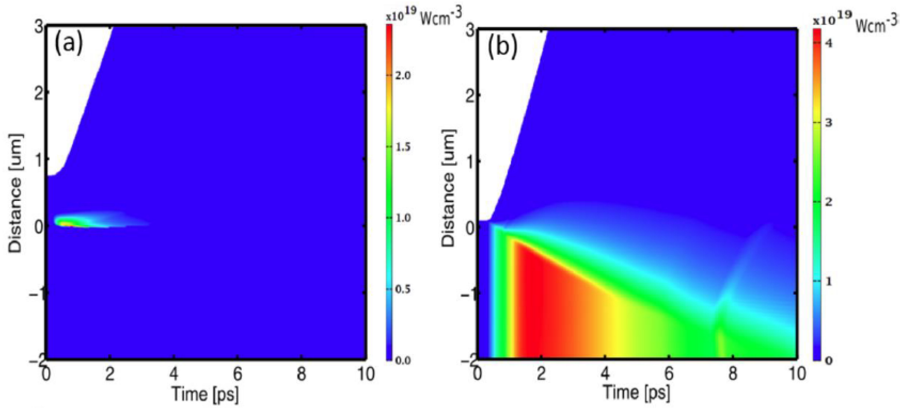

Figure 6.5: Computed evolution of the x-ray radiation power for a Au flat target (a), and a Au nanowire target (b), both irradiated at an intensity of 4×10^{19} W cm^{-2} with a 55 fs FWHM pulse. The array of nanowires is assumed to be composed of 55 nm diameter wires with an average density of 12 % solid. Time is measured with respect to the peak of the laser pulse, and the distance is in the direction normal to the target surface. *(Source: [20], see summary 6.5 below for details.)*

The simulations are the result of hydrodynamic model computations with transient atomic kinetics performed by our colleagues in which they used the PIC simulation results we conducted to simulate the first stages of nanowire plasma formation until the nanowires are fully dissolved. Both targets are assumed to be irradiated with an intensity of $4 \times 10^{19}\,\mathrm{W\,cm^{-2}}$. It is shown that irradiation of the Au nanowire array results in both a large increase in the radiating volume and a larger emitted power density. In the case of the flat solid target, most of the x-ray emission takes place in a very thin supercritical layer heated by conduction, where acceleration and expansion cooling take place, with the plasma density rapidly dropping orders of magnitude in 1 mm. The much larger heated plasma depth in the nanowire plasma greatly increases the plasma hydrodynamic cooling time. Simultaneously, the larger plasma density results in an increased electron collisional excitation rate, leading to a shorter radiative cooling time.

The magnitude of these effects is quantitatively illustrated in Fig. 6.6 by atomic kinetic calculations of our partners that compare the characteristic radiative and hydrodynamic cooling times of a Au flat target plasma and a Au nanowire array plasma. The computations were conducted by our collaborators with the hydrodynamic/atomic physics code Radex [208]. Figure 6.6(a) shows the cooling times for Au plasma with a density of $n_e = 6\times10^{22}\,\mathrm{cm^{-3}}$ and a thickness of 0.2 µm. These are the typical parameters of the x-ray emitting layer computed by both PIC and hydrodynamic models for plasmas created by irradiating a solid Au target. Both models give similar source thickness values in spite of the fact that Radex is approaching the validity limit of the hydrodynamic approximation. In this case, the great majority of the laser energy is lost in the hydrodynamic expansion before collisions have time to convert the electron kinetic energy into radiation. For the electron temperatures of interest, the hydrodynamic cooling time is much shorter than the radiative cooling time, resulting in a small CE.

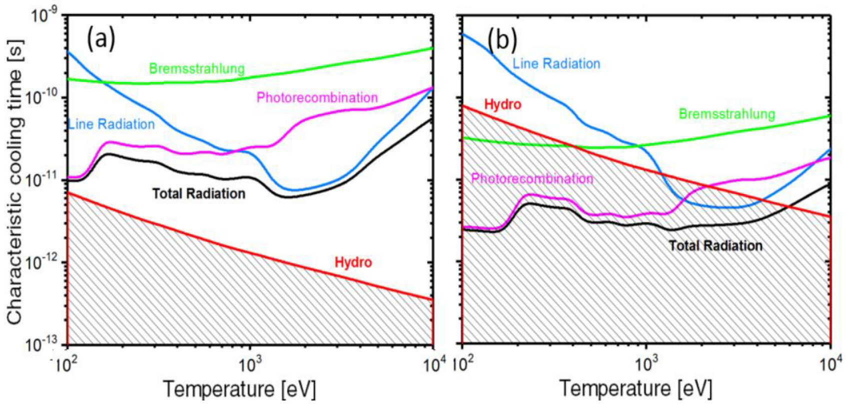

Figure 6.6: Comparison of radiative and hydrodynamic cooling times as a function of electron temperature for two different Au plasmas with the characteristics corresponding to the x-ray emitting region of: (a) a flat solid target, $n_e = 6 \times 10^{22}\,\mathrm{cm^{-3}}$, plasma size $L = 0.2$ µm, and (b) a nanowire array plasma $n_e = 4\times10^{23}\,\mathrm{cm^{-3}}$ and plasma size $L = 4$ µm. The total radiation time is the effective radiative cooling time computed from the photorecombination, bremsstrahlung and line radiation rates. *(Source: [20], see summary 6.5 below for details.)*

This result is in contrast to Fig. 6.6(b) for a supercritical Au plasma with a density of $n_e = 4 \times 10^{23}\,\mathrm{cm^{-3}}$, a value approaching 100 times the critical density, typical of the conditions resulting from irradiating the nanowire arrays with the intensity our collaborators used in the experiments. In this case, the radiative cooling time is smaller than the hydrodynamic cooling time, leading to greatly increased radiation efficiency.

For larger average density nanowire arrays irradiated at increased intensities, even higher electron densities will result [19], further driving the plasma into a radiation loss dominated regime.

The large increase in CE shown here is made possible by a combination of irradiation and target parameters that need to be considered to exploit the nanograss targets to their fullest potential, as already described in subchapter 2.2.1. Taking this into account, these parameters achieve the condition in Eq. 6.1. First, ultrahigh contrast $> 10^{12}$ laser pulses are used that avoid destroying the nanowires and establishing a critical density layer before the main pulse arrives. Second, short laser pulses (55 fs) are used that allow for nearly all of the laser energy to be deposited deep into the array before the nanowires explode and close the interwire gap, forming a continuous critical density surface. Third, the use of long nanowires allows for volumetric heating to occur to depths of 4-5 µm [19] (see previous chapter 5), increasing the hydrodynamic expansion time. Fourth, dense arrays are used, in which the plasma density reaches nearly 100 times the critical density, which results in high collisional rates and, consequently, in very short radiative cooling times. Fifth, relativistic irradiation intensities are used that heat the plasmas to multi-keV temperatures deep into the array, which leads to a high degree of ionization [5], an increased electron density, and a decreased radiation lifetime. This simultaneous set of conditions differs from those in previous experiments that measured x-ray yield from nanowire targets. Prior work used either picosecond pulses [53], short wires [53, 199], relatively low contrast pulses [53, 198, 199], or non-relativistic intensities [49, 53, 198, 199]. This limited the radiation fraction obtained for $h\nu > 1\,\mathrm{keV}$ to values nearly two orders of magnitude smaller than that is reported here.

6.5 Summary

In conclusion, we have seen that the CE of optical laser pulses into picosecond x-ray pulses can be greatly improved by increasing the radiative to hydrodynamic energy loss rate ratio in volumetrically heated supercritical density plasmas. A numerical model, based on our PIC simulations with subsequent post-processing by our partners, has shown that a significantly larger radiating volume and a greater emitted power density is found in the nanowire targets in comparison to flat targets. By tailoring these nanostructured targets irradiated at relativistic intensities to fulfill this condition, ultrafast pulses of $h\nu > 1\,\mathrm{keV}$ photons with a record efficiency of $\approx 20\,\%$ into $4\pi\,\mathrm{sr}$ could be generated experimentally by our colleagues. This increase of more than one order of magnitude in the efficient generation of picosecond line and continuum x-ray radiation will open new opportunities in flash radiography, including the backlighting of imploding capsules in laser fusion experiments, in opacity measurements of matter at the conditions of stellar interiors, and in table-top applications requiring intense picosecond flashes of x-rays. Furthermore, the results will also motivate more efficient x-ray generation experiments at larger laser facilities.

The results presented in this chapter are reproduced from [20], with the permission of AIP Publishing. The figures were taken unchanged and the text was adopted literally with adaptations for fitting into the thesis. The author has conducted the PIC simulations, provided our collaborators with the data necessary for post-processing and has contributed to the writing of the published manuscript (proofreading and suggestions).

Chapter 7

Fusion neutron generation

7.1 Introduction

In section 2.2.2 it was described that large laser facilities are capable of producing high yields of neutrons in the process of fusion reactions. However, all these experiments are limited to repetition rates of a few shots per hour or less. In this chapter, we will see that by using deuterated nanowire array targets, the requirements concerning the laser can be significantly reduced to joule-level compact lasers. This can be seen by the capability of the deuterated nanowires to produce remarkably high neutron yields as shown in the experimental results of our colleagues at the Colorado State University. Our PIC simulations, conducted at the conditions of our partners' experiments, show that a high number of deuterons gain energies near the cross section peak of the D-D fusion reaction, enabled by the already mentioned efficient laser light absorption and heating of the plasma in these structures (see section 2.2.1).

After discussing the use of compact lasers to generate fusion neutrons in part 7.2, the experimental and simulation results are explained in sections 7.3 and 7.4, respectively. The chapter is concluded at the end with a summary in subchapter 7.5.

7.2 Compact-laser-generated fusion neutrons

The ability to drive fusion reactions with compact lasers that can be fired at much higher repetition rates than in facilities like the NIF is of significant interest for fusion science, high energy density studies, and neutron pulse generation. Neutrons, in turn, have their own applications, some of which are listed in section 2.2.2. After Pretzler *et al.* demonstrated the first definite observation of fusion reactions by measuring 140 fusion neutrons [73], several other studies with different laser-target parameters explored fusion by using compact lasers. A significant advance in driving fusion reactions with compact lasers was the irradiation of deuterated clusters formed in gas jets with low energy femtosecond laser pulses, that allows for efficient volumetric heating of plasmas with an average ion density of $\approx 1 \times 10^{19}\,\mathrm{cm}^{-3}$ [196] in which cluster explosions accelerates ions to multi-keV average energy [72]. Neutron generation efficiencies of $\approx 1 \times 10^{5}$ neutrons per joule were obtained in the form of short sub-ns bursts, a value similar to those obtained with multi-kilojoule lasers. The ultrafast irradiation of ordered nanowire arrays share with nanoclusters the advantage of efficient volumetric heating, but have the additional advantage of creating a medium with several orders of magnitude higher average plasma density [5]. As we have seen in chapter 5 and was recently shown in [5], irradiation of aligned arrays of metallic nanowires with femtosecond laser pulses of relativistic intensity can volumetrically heat dense plasmas to multi-keV temperatures, reaching pressures only achieved in the laboratory in spherical compression with the world's largest lasers [63]. This feature qualifies nanowire targets as potent candidates to produce a high number of fusion neutrons.

Arrays of aligned high aspect ratio nanowires made of deuterated polyethylene (CD_2) exhibit the same behavior (in accordance to the general interaction description in section 2.2.1) as the carbon nanowires shown in chapter 4 (where the work on the nanopinch was actually motivated by investigations on the CD_2 nanowires presented here), especially in Fig. 4.11, as the laser and target parameters mostly coincide. This can be seen in the PIC simulations that we conducted using CD_2 nanowires: The vacant spaces surrounding the wires [Fig. 7.1(a)] that allow for the deep penetration of ultrafast optical laser pulse energy into near-solid-density material, where light is trapped and practically totally absorbed [5]. Electrons are ripped off the nanowire surface by the large laser field and are accelerated to high energy in the voids. These energetic electrons interact with the nanowires, rapidly heating the material to extreme temperatures, causing the nanowires to explode [Fig. 7.1(b)-(d)]. Ions are rapidly accelerated between the nanowires, and the voids are filled with plasma, creating a continuous critical electron density layer that forbids further coupling of laser energy into the material [Fig. 7.1(d)]. Assuming total laser energy absorption and volumetric heating of the target, the average energy per particle can be estimated to be [21]

$$E_{\mathrm{av}} \approx \frac{a_0^2}{2} m_e c^2 \frac{n_{\mathrm{cr}}}{n_{\mathrm{av}}} \frac{Z}{Z+1} \frac{c\tau}{L} \tag{7.1}$$

where n_{av} is the average particle density, τ is the laser pulse duration, Z is the mean ion charge and L is the absorption depth in a target. For the conditions of the experiments discussed below ($a_0 \approx 3$, $\lambda = 400\,\mathrm{nm}$, $n_{\mathrm{av}} = 6.4 \times 10^{22}\,\mathrm{cm}^{-3}$, $Z = 2.67$, $\tau = 60\,\mathrm{fs}$, and $L \approx 5\,\mu\mathrm{m}$), E_{av} can be calculated to be $\approx 0.6\,\mathrm{MeV}$. These energetic particles close the gaps between 400 nm diameter wires in an array with an average density corresponding to 15 percent solid density in $< 100\,\mathrm{fs}$. After homogenization of the material, the plasma as a whole, with ions of mass m_i, begins to expand in the normal direction toward the laser pulse with a characteristic time scale $\tau_s \approx L/c\sqrt{m_i c^2/E_{\mathrm{av}}} \approx 1.5\,\mathrm{ps}$ (see Eq. 2.29), but also toward the substrate, where the energetic deuterons moving into the target cause additional fusion reactions.

We will see below that the irradiation of deuterated nanowire arrays with pulses of relativistic intensity can accelerate a large number of deuterons to energies near the peak of the D-D fusion cross section, opening the possibility to efficiently drive D-D fusion reactions and generate bright quasi-monoenergetic ultrashort neutron pulses from a point source with compact high repetition rate lasers. Our PIC simulation results illustrated in Fig. 7.1 show the computed spatio-temporal energy distribution of energetic deuterons in an array of 400 nm diameter deuterated polyethylene nanowires irradiated at an intensity of $8 \times 10^{19}\,\mathrm{W\,cm^{-2}}$ by laser pulses of 60 fs duration. The average density of the target was assumed to correspond to 16% of solid density. The plasma is rapidly fully ionized and the electron density is computed to reach $6.4 \times 10^{22}\mathrm{cm}^{-3}$. The deuteron spectra calculated 60 fs after the peak of the laser pulse show that energetic ions with kinetic energy up to 3 MeV are generated. This energy greatly exceeds what was measured by our colleagues for D ions generated from solid targets irradiated under the same conditions. Moreover, the deep penetration of the heat in the nanowires results in a much larger volume of heated material (see chapter 5), leading to the acceleration of a greater number of deuterons.

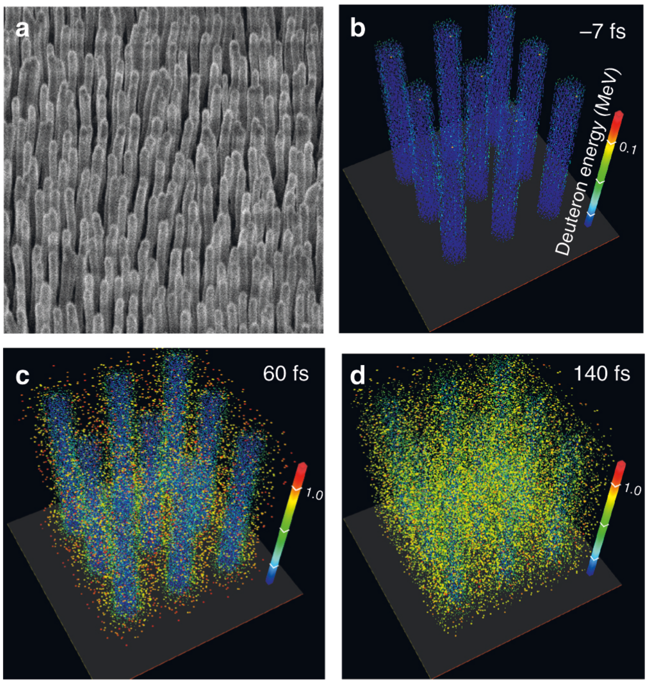

Figure 7.1: SEM image and 3D PIC simulation of energy distribution of deuterons. (a) SEM image of an array of 200 nm diameter CD_2 nanowires. (b)-(d) Three-dimensional particle-in-cell simulation of the evolution of the energy distribution of deuterons in an array of 400 nm diameter CD_2 nanowires irradiated at an intensity of $8 \times 10^{19}\,\mathrm{W\,cm^{-2}}$ by an ultrahigh contrast $\lambda = 400\,\mathrm{nm}$ laser pulse of 60 fs FWHM duration. The laser pulses penetrate deep into the array where they rapidly heat the nanowires to extreme temperatures, causing the nanowires to explode [Figs. 7.1(c) and 7.1(d)]. Deuterons are rapidly accelerated into the voids up to MeV energies, producing D-D fusion reactions and characteristic 2.45 MeV neutrons. Times are measured with respect to the peak of the laser pulse. The average density of the nanowire array corresponds to 16 % solid density. The one simulated wire was replicated for the sake of vividness. *(Source: [21], see summary 7.5 below for details.)*

In experiments conducted at these conditions by our collaborators, a ≈ 500 times increase in the number of 2.45 MeV D-D neutrons produced as compared to flat CD_2 targets irradiated with the same laser pulses was observed. The highest yield shots produced 2.2×10^6 neutrons per joule of laser energy. This corresponds to more than an order of magnitude increase with respect to the favorable yield reported for deuterated clusters [72, 196]. Applying a post-processing of our simulation results, our partners have also observed a strong superlinear increase of the neutron yield as a function of the laser irradiation intensity. The PIC simulations we have performed by further increasing the irradiation intensity to $5 \times 10^{20}\,\mathrm{W\,cm^{-2}}$ predict a shift of the ion energy distribution to higher energies, practically depleting the population of the low energy deuterons and leading to a significant further increase in the neutron yield.

7.3 Experimental setup and results

Our colleagues conducted the experiments by irradiating arrays of aligned deuterated polyethylene (CD_2) nanowires with $\lambda = 400\,\mathrm{nm}$, ultrahigh contrast ($> 10^{12}$) pulses of

60 s FHWM duration with energy up to 1.65 J. They generated the laser pulses by a frequency-doubled titanium:sapphire laser and focused them at normal incidence onto the nanowire arrays using an f/1.7 parabolic mirror. The energy spectra of the plasma ions were recorded by our partners using a Thomson parabola spectrometer (TPS) placed at 75 cm from the target along the target normal. Ions reached the TPS through a 100 µm hole on the axis of the focusing parabola. The primary diagnostics for neutron detection consisted of four EJ-228 plastic scintillator/photomultiplier detectors for time of flight measurements. In addition, two neutron bubble dosimeters were stationed outside the target chamber.

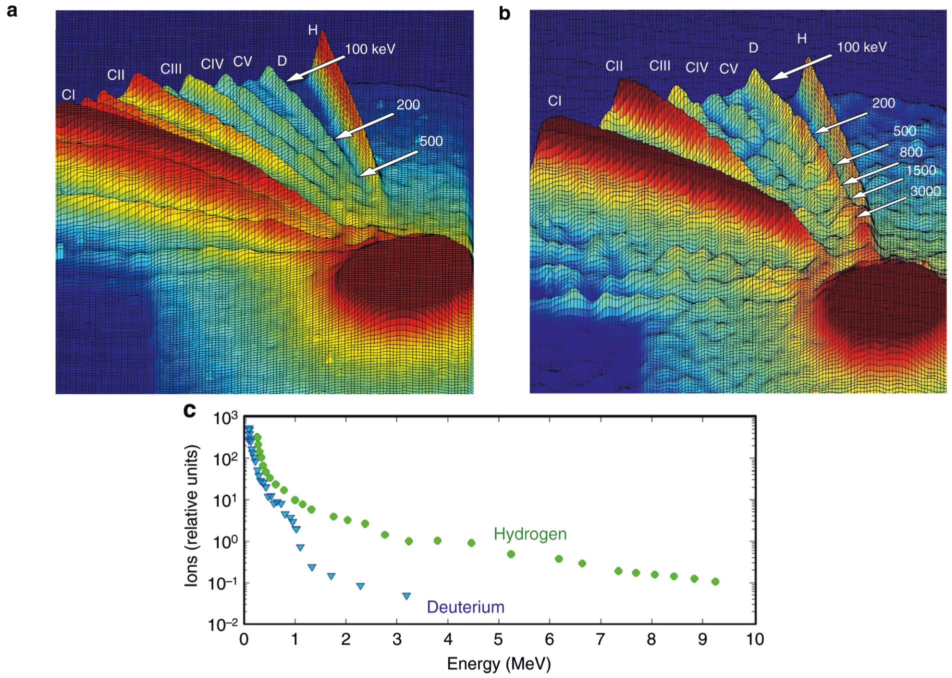

Figure 7.2: Measured single-shot Thomson parabola ion energy spectra: (a) flat solid CD_2 target irradiated at an intensity of $\approx 8 \times 10^{19}$ W cm^{-2}. Traces corresponding to H, D, and C ions are recorded. The tail of the deuteron energy spectrum reaches 0.5 MeV, (b) array of 400 nm diameter, 5 µm long, CD_2 nanowires. (c) Deuteron and proton energy distribution for the CD_2 nanowire array. The tail of the energy spectrum of the D and H spectra approaches 3 MeV and 10 MeV, respectively. *(Source: [21], see summary 7.5 below for details.)*

The measurements were conducted by our colleagues with arrays of aligned CD_2 nanowires either 200 or 400 nm diameter and $\approx$ 5 µm in length. The average density of the arrays corresponded to 16 and 19 % solid density, respectively. Our collaborators developed a method to fabricate the arrays of aligned CD_2 nanowires by heated extrusion of CD_2 into porous membranes. Flat solid targets of the same CD_2 material and arrays of CH_2 were also fabricated and shot for comparison with every CD_2 nanowire array target. Fig. 7.2(a) shows a measured single-shot TPS spectrum from a flat CD_2 target irradiated at an intensity of 8×10^{19} W cm^{-2}. Traces corresponding to D, H, and C ions are recorded. The energy of the deuterons in the flat solid target spectrum approaches 0.5 MeV. In comparison, arrays of CD_2 nanowires irradiated at the same conditions are observed to produce deuterons of up to 3 MeV energy and protons with energy as high as

10 MeV. A comparison of the ion energy spectra of CD_2 and CH_2 (Fig. 7.3) shows that the trace identified as corresponding to deuterons does not have a significant contribution of C VI ions, which have the same charge to mass ratio. The angular distribution of the fast deuterons was measured by our partners placing CR-39 plates at different angles from the target normal.

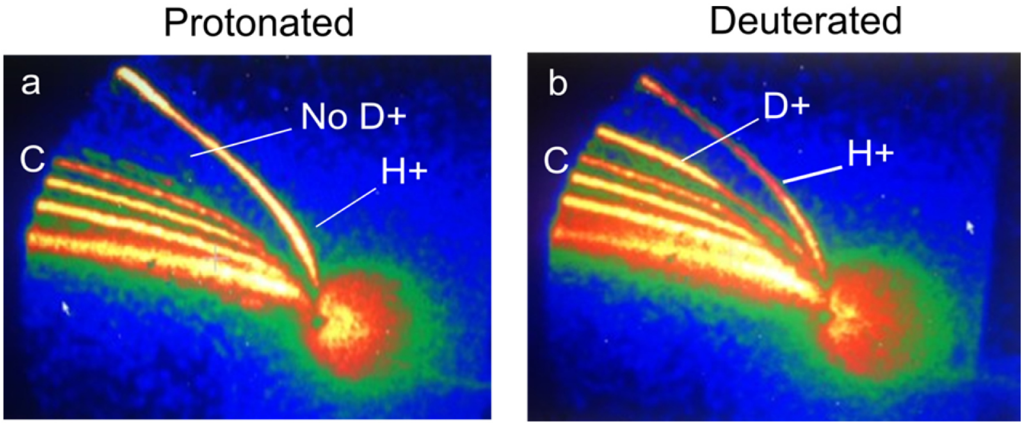

Figure 7.3: Measured single-shot Thomson parabola energy spectra for protonated and deuterated nanowire arrays. (a) CH_2 target irradiated at an intensity of $8 \times 10^{19}\,\mathrm{W\,cm^{-2}}$. The traces corresponding to H, and C ions are recorded; (b) array of 400 nm diameter, 5 µm long, CD_2 nanowires. A trace corresponding to D (charge to mass ratio 0.5) is observed. *(Source: Supplementary material in [21], see summary 7.5 below for details.)*

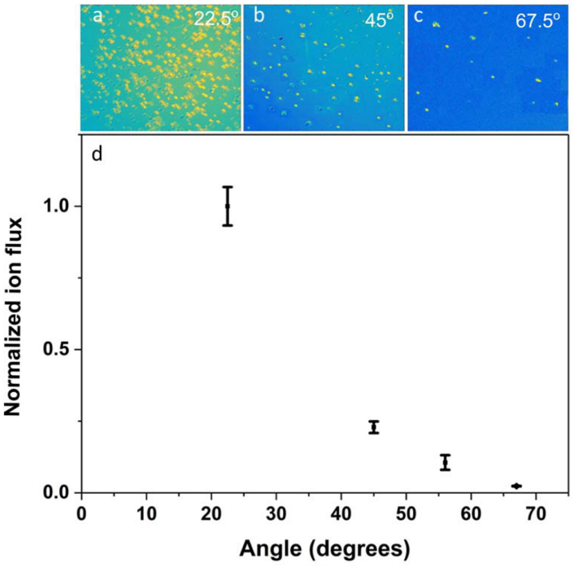

Figure 7.4: Measured fast deuteron angular distribution. (a)-(c) Images of exposed CR-39 plates placed at different angles with respect to the target normal. The size of each image was adjusted to show the same solid angle. (d) D flux as a function of angle. The nanowires were 200 nm in diameter and the laser pulse energy on target was 1.38 J. Error bars represent standard deviation. *(Source: Supplementary material in [21], see summary 7.5 below for details.)*

To differentiate the deuteron flux from that of fast carbon ions, our partners covered part of each of the CR-39 plates with 2.5 or 4 µm thick Al foils that stop practically all carbon ions and let through deuterons with energies $\gtrsim$ 270 keV and $\gtrsim$ 400 keV, respectively. They observed the deuteron flux to peak in the direction of the target normal and to decrease as a function of angle, to become practically extinct for angles $>$ 67 degree (Fig. 7.4). Figure 7.2(c) shows the deuteron and proton energy spectra extracted from Fig. 7.2(b). The deuteron spectrum is in good agreement with that resulting from our PIC simulations discussed below, and has a good overlap with the cross section for D-D fusion reactions [209].

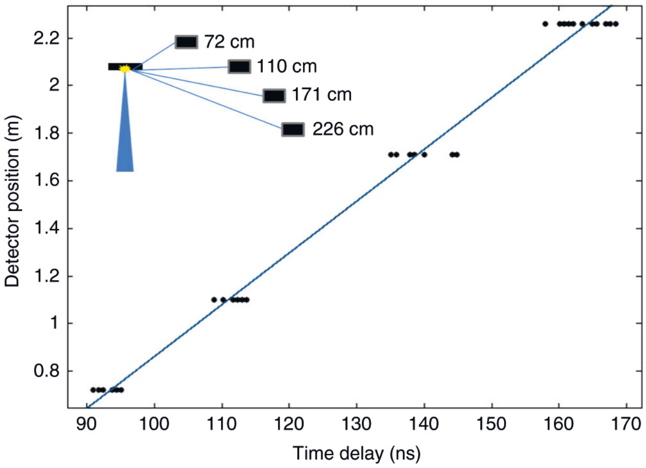

Figure 7.5: Time of flight neutron measurements. Time of flight PMT/scintillator neutron data from four detectors located at different distances from the target. The trigger was the plasma x-ray signal preceding the neutrons. The slope of the line fitting the data corresponds to the velocity associated with (2.48 ± 0.14) MeV neutrons. *(Source: [21], see summary 7.5 below for details.)*

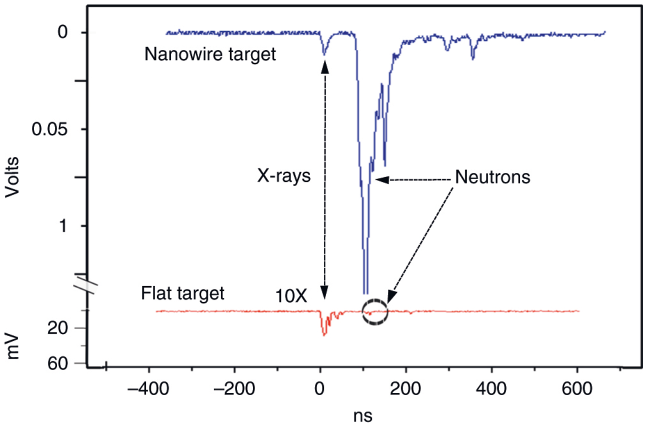

Figure 7.6: Comparison of time of flight neutron signals. Comparison of TOF neutron signals from a nanowire array target and a flat target. The flat target neutron signal (in red) was multiplied by 10 for clarity. The ratio of the average neutron yield of eleven nanowire shots to the average yield of six flat target shots at the same irradiation conditions yielded a value of 492. *(Source: [21], see summary 7.5 below for details.)*

Consistently, time of flight traces our collaborators recorded for several different target-detector distances show large neutron peaks at the expected arrival time for 2.45 MeV D-D neutrons (Fig. 7.5 and Fig. 7.6). Data corresponding to solid CD_2 flat targets is also shown in Fig. 7.6. When compared, the integrated neutron signals of the nanowire targets around 2.45 MeV are $\approx$ 500 times larger. The maximum number of neutrons per shot our partners measured was 3.6×10^6 for a laser pulse energy of 1.64 J, corresponding to 2.2×10^6 neutrons per joule, the largest fusion neutron yield obtained to date for joule-level laser pulse energies. If the same experiment with deuterated nanowires were to be conducted on a tritium containing substrate layer, the increase in the fusion cross section combined with its shift towards lower ion energy, a significantly larger number of fusion neutrons could result.

7.4 Simulation results

To understand the physics behind these measured results, we conducted PIC simulations using the parameters given by the experiment. We used a linearly polarized plane wave with 400 nm wavelength and Gaussian time envelope to simulate the laser pulse where the normalized vector potential is $a_0 = 3$ or 3.3 with a 60 fs FWHM pulse duration. We assumed the laser pulse to impinge on the deuterated polyethylene nanowire array at normal incidence. The PIC simulation space consisted of a box encompassing the wires and interwire gaps, as well as space above the array to allow for expansion of the wire material as it explodes and thermalizes. The grid size used ranged from $50 \times 50 \times 1120$ to $100 \times 100 \times 2208$ on a mesh volume of $0.81 \times 0.81 \times 6.2\,\mu m^3$. The time step was 0.00266 fs. Simulations of neutron production dependence on laser irradiation energy were conducted by our partners with a post-processor code based on the code Radex [190] using the ion energy distributions we computed with our PIC code.

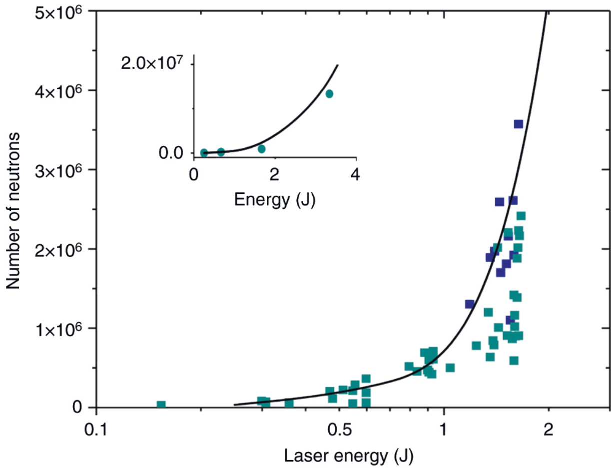

Figure 7.7: Neutron yield as a function of laser pulse energy on target. The dark blue squares are shots corresponding to a target with 200 nm diameter wires. All the other shots (light blue squares) are for targets consisting of 400 nm diameter wire arrays. Each point resulted from the average of four scintillator/PMT time of flight detector signals. The line shows the simulated energy dependence of the neutron yield calculated using deuteron energy distributions computed by the PIC model and nuclear kinetics. The inset extends the simulation to 3.5 J, where the green circles are computed values of the neutron yield. *(Source: [21], see summary 7.5 below for details.)*

Our colleagues measured the number of neutrons to increase superlinearly with laser pulse energy (Fig. 7.7). The rapid increase is in good agreement with the simulations that were conducted using the deuteron ion energy distributions resulting from our PIC simulations and the nuclear kinetics simulations of our collaborators. For these measurements and simulations, the laser spot size was kept constant (in the simulations it was assumed to be 5 µm) while the pulse energy was varied. The neutron yield is a function of the D-D fusion cross section and the stopping power of a deuteron in the target material; both of these are energy-dependent. Our partners used the stopping power to calculate the distance travelled by a particle in the material as it decreases in energy from E_i to E_{i+1} due to multiple scattering. Using the cross section corresponding to this energy range, they calculated the probability of fusion in that interval. Integration of these values from the initial energy gives the total fusion probability for that deuteron. Our colleagues took the cross sections from the Evaluated Nuclear Data File database [210]. The stopping power was calculated by them using SRIM [211]. Accurate neutron generation modeling at intensities significantly beyond 2 J will require a new model that takes into account effects, which can be neglected at energies of the experiments reported here but that will play a role at significantly higher intensities, such as heating of the substrate material. Our simulations show that the measured increase in neutron yield is caused by a shift of the deuteron energy distribution to higher energies.

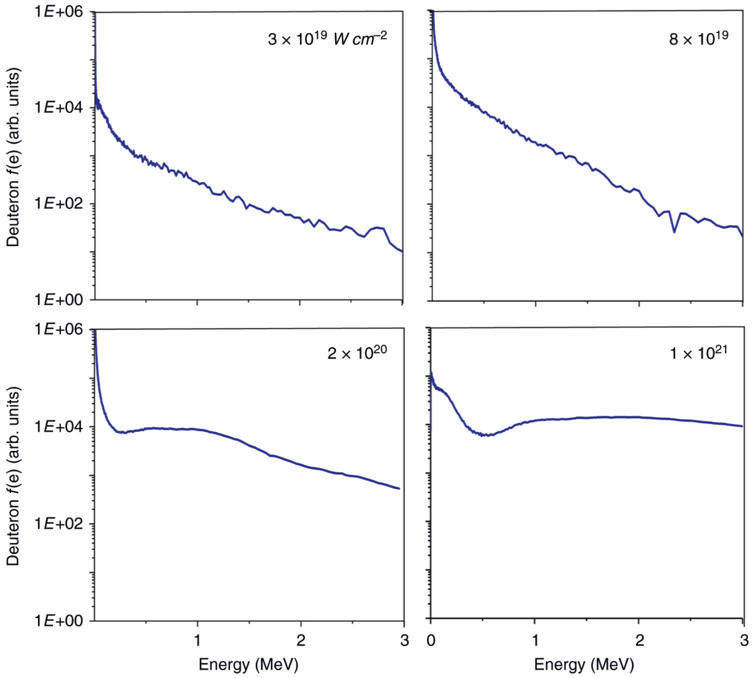

Figure 7.8: Deuteron energy spectra ($f(e)$, arb. units). Computed deuteron energy spectra for 400 nm diameter CD_2 nanowires at different irradiation intensities. The target average density corresponds to 16 % of solid density. *(Source: [21], see summary 7.5 below for details.)*

This deuteron energy increase computed by us is illustrated in Fig. 7.8 for arrays of CD_2 nanowires irradiated at intensities between $3 \times 10^{19}\,\mathrm{W\,cm^{-2}}$ and $1 \times 10^{21}\,\mathrm{W\,cm^{-2}}$. An increase of the intensity to $1 \times 10^{21}\,\mathrm{W\,cm^{-2}}$ is seen to nearly deplete the low energy deuterons shifting a significant fraction of the distribution to multiple MeV energy. Our simulations also show that at the lowest irradiation intensities used in this experiment, $\approx 1 \times 10^{19}\,\mathrm{W\,cm^{-2}}$, the majority of the neutrons are produced within the plasma volume. In contrast, at the highest irradiation intensities explored, a significant fraction of the neutrons is produced in collision of accelerated deuterons with deuterium atoms in the material that surrounds the plasma. This includes neutrons generated by deuterons streaming into the CD_2 substrate layer ($\approx 200\,\mu\mathrm{m}$ thick in the experiment). This fraction increases with the irradiation intensity. At intensities $> 1 \times 10^{21}\,\mathrm{W\,cm^{-2}}$, the majority of the fusion reactions will occur in the substrate layer, outside the plasma volume. Therefore maximizing neutron production at higher irradiation intensities will require the use of a thicker CD_2 substrate layer. Also, as the laser pulse energy is further increased beyond the values explored here, the optimum D-D neutron production might require a tradeoff between a further increase in the intensity and an increase in the irradiated volume. The higher intensities are also expected to generate a directed flux of high-energy deuterons that could be made to impinge in low Z convertors to drive “pitcher-catcher” neutron sources that have been demonstrated to create a large number of high-energy neutrons [69, 212, 213]. Finally, our simulations also show the occurrence of the pinch effect in a similar way as shown in chapter 4, since the laser-target parameters are nearly the same. This means that the laser pulse drives a large forward electron current in the area around the wires which at higher irradiation intensities (eg. $5 \times 10^{21}\,\mathrm{W\,cm^{-2}}$) is computed to induce return current densities of tens of Mega-amperes per $\mu\mathrm{m}^2$ through the nanowires (as published in [18]). The resulting strong quasi-static self-generated azimuthal magnetic field will pinch the deuterated nanowires into hot plasmas with a peak electron density exceeding 1000 times the critical density.

7.5 Summary

In summary, a near-solid-density plasma regime in which deuterons from aligned nanostructures are accelerated up to MeV energies was realized. In experiments conducted by our colleagues, the volumetric heating of aligned deuterated polyethylene nanowire arrays irradiated at relativistic intensity is shown to produce ultrashort neutron pulses with a ≈ 500 times larger number of D-D neutrons than a deuterated flat solid target. A total of 2×10^6 neutrons per joule was generated in their measurement, the largest D-D fusion neutron yield reported to date for plasmas generated by laser pulse energies in the 1 J range. We have simulated a further increase of the irradiation intensity, predicting a shift of the deuteron energy distribution to significantly higher energies, which can be expected to lead into a further increase in D-D fusion reactions. This volumetrically heated dense fusion environment that can be created at high repetition rates with compact lasers is of interest for high energy density science and nuclear science. The approach can also lead to the efficient generation of ultrafast pulses of quasi-monoenergetic neutrons from a point source for time-resolved material studies, ultrafast neutron radiography, and spectroscopy, and for high-energy science applications such as neutrino detector development.

The results presented in this chapter are reproduced from [21] © The Authors, which is licensed under CC BY 4.0. Fig. 7.2 was rearranged to save space, all other figures were taken unchanged; the text was adopted literally with additions and adaptations for fitting into the thesis. The author has conducted the PIC simulations, provided our collaborators with the data necessary for post-processing and has contributed to the writing of the published manuscript (description of the simulation parameters, proofreading and suggestions).

Chapter 8

Long-wavelength interaction regime

8.1 Introduction

In the previous chapters we have seen that (near-)solid density, (multi-)keV-temperature plasmas open new perspectives for realizing table-top, intense x-ray sources (chapter 6), laser-induced nuclear physics (chapter 7), and experiments on laboratory astrophysics (chapter 5) by accessing the UHED regime (chapters 4 and 5). Given a laser wavelength of 400 nm, generated by a frequency-doubled titanium-sapphire laser of our experimental collaborators in Colorado, the laser intensity needed to be chosen high enough (according to Eq. 2.20) to achieve relativistic pulses with a laser amplitude $a_0 \geq 1$ to generate plasmas with those characteristics.

In this chapter, we will see results, which show that the relativistic regime can alternatively be entered by choosing a sufficiently long wavelength at comparably lower intensities (section 8.2). Next, we describe the experimental setup our collaborators at the Friedrich-Schiller-University and the Helmholtz Institute in Jena used and the results that they measured (section 8.3). We will carry on with a discussion of the simulation results, consisting of our PIC simulations and the post-processing of our partners used to model the experimental results (section 8.4) and a summary (section 8.5).

8.2 Relativistic laser-plasma interaction in long-wavelength interaction regime

As we have seen in section 2.1.3, the velocity of the laser-field-driven free electrons approaches the speed of light in the relativistic regime of laser-matter interaction. A common way to enter the relativistic regime is to increase the laser intensity. For a given laser pulse energy, higher intensities can be reached easier with short-wavelength laser sources by entering the so-called λ^3 regime, defined by focusing the shortest possible pulses (given by the length of a single cycle) to the diffraction limited spot given by the wavelength [214]. However, such single-cycle, short-wavelength ultraintense pulses will only interact with an extremely small volume of plasma. It is also worth mentioning that pulse compression down to a single cycle becomes extremely challenging with a shortening of the laser wavelength.

In the preceding chapters, we have increased the normalized laser amplitude a_0 by applying higher intensities at a fixed wavelength of 400 nm. Alternatively, a_0 can be increased by using long-wavelength laser sources. In this case, highly relativistic interaction can be realized with moderate laser-pulse energies paving the way to high-repetition-rate experiments in a relatively large volume. This new regime of relativistic, ultrashort-pulse laser-solid interaction was inaccessible so far, because CO_2 lasers, the only high-energy, midinfrared (mid-IR) laser sources available, emit pulses with a duration $> 1\,\mathrm{ps}$ [215, 216]. At this timescale, the hydrodynamic expansion during the pulse prevents efficient laser light absorption. Because of the recent progress in the development of high-energy optical parametric chirped pulse amplification (OPCPA) femtosecond laser systems, nowadays femtosecond laser pulses of terawatt peak power level in mid-IR spectral range are available [217, 218].

As mentioned in section 2.1.4, the requirement of high temporal contrast of a relativistically intense, ultrashort laser pulse is one of the necessary conditions to achieve high density and sharp (on the laser wavelength scale) spatial gradients in plasmas. A sharp gradient of the density enables an efficient vacuum heating mechanism of the laser energy absorption [36, 219–222], thus ensuring a high temperature of generated dense plasmas. For high power laser systems in the near-IR spectral range, commonly used for relativistic laser-solid interactions, the requirement of the high temporal contrast inevitably invokes frequency doubling of the output radiation, reducing the ionization threshold to a few- or even single-photon absorption. Significant reduction of the ionization rate at mid-IR frequencies in comparison to near-IR-visible-UV laser sources [223], together with long wavelength in mid-IR laser pulses, substantially relax the problem of preplasma formation and achieving sharp spatial gradients of the plasma density. In particular, an advantage of mid-IR femtosecond driver pulses, compared to near-IR pulses, for the efficiency of vacuum heating of solid target under nonrelativistic interaction, resulting in a much higher yield of the K_α emission from a Cu tape, was recently demonstrated [224, 225].

In this chapter, we will present the experimental results of our colleagues on a new regime of relativistic laser-solid interaction drawing on the combination of midinfrared wavelength, high peak power, high temporal contrast femtosecond laser source, and advanced nanostructured silicon samples as the target. Motivated by these findings, we have conducted numerical PIC simulations for modeling. Our colleagues have used our simulation results in a collisional radiative population kinetics [226] code for post-processing, which together with their experimentally measured characteristic line and bremsstrahlung x-ray spectra reveal that the nanowire morphology allows for overcoming a problem of the unfavorable scaling of the critical electron density with the wavelength $n_{\mathrm{cr}}[\mathrm{cm}^{-3}] \approx 10^{21}\lambda^{-2}\,[\mu\mathrm{m}]$ (see Eq. 2.26 in section 2.1.4). The generated plasmas have solid density, corresponding to an unprecedented $> 10^3\, n_{\mathrm{cr}}$ at the driving laser wavelength.

8.3 Experimental setup and results

The experiments were carried out by our partners at the high-energy OPCPA laser system delivering 90-fs laser pulses at 3.9 µm idler wavelength with an energy on the target up to 25 mJ at 20-Hz repetition rate [217, 218]. They focused the beam by an off-axis parabolic mirror to a 12-µm (FWHM) focal spot under 45° angle with respect to the target's normal [see Fig. 8.1(a)]. The maximum peak intensity at the target was estimated to be $10^{17}\,\mathrm{W\,cm^{-2}}$, resulting in the maximum value of the relativistic parameter $a_0 \approx 1.1$. All the measurements were conducted in a single-shot regime.

In conventional CPA laser systems based on the laser principle of amplification, the temporal contrast at the nanosecond-picosecond timescale is determined by the level of the amplified spontaneous emission and amplification of any parasitic prepulses [227]. For OPCPA, the temporal structure of the output pulse is mainly defined by the emission of superfluorescence having the duration of the pump laser pulse (80 ps for the system of our collaborators). To get an estimate of the temporal contrast in the experiments, our partners blocked the seed signal beam to measure the energy of the superfluorescence radiation. The background signal is below the milliwatt level, which is the sensitivity threshold of the used detector for the 20-Hz repetition rate. This number has to be compared with the amplified idler signal at the 25-mJ output energy resulting in 500-mW measured average power. Thus, the energy in the $\approx$ 80-ps superfluorescence pulse is below 50 µJ and the corresponding peak intensity of $\approx 10^{11}\,\mathrm{W\,cm^{-2}}$ at 3.9 µm is too low to generate any significant amount of plasma before the arrival of the main pulse.

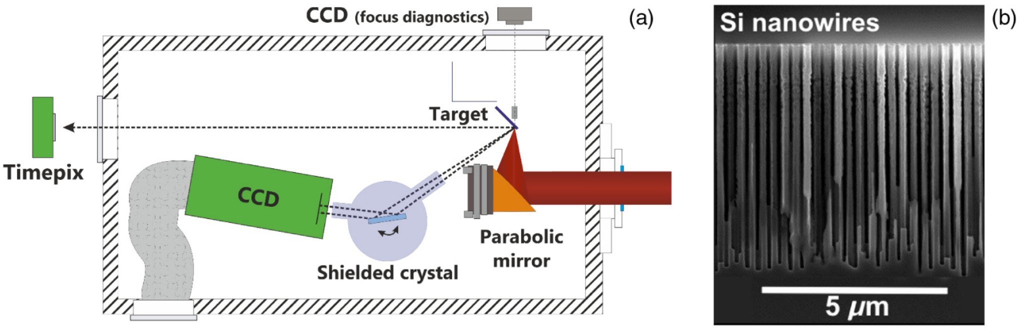

Figure 8.1: (a) Experimental setup. (b) Scanning electron microscope (SEM) image of the Si nanowire target. *(Source: [22], see summary 8.5 below for details.)*

The targets represent single crystalline Si nanowire arrays [Fig. 8.1(b)] on a silicon substrate, transparent in the broad spectral range of 1.2-7 µm. The details of how the target was fabricated by our colleagues are given in Ref. [228]. The density of the Si nanowires is about 35 % solid material density, which means that a focal spot of 12 µm contains roughly 1600 nanowires. Each nanowire is 6 µm long and has a diameter of 200 nm. The spacing between the nanowires is about 100 nm. The reference target is a 500-µm-thick polished Si wafer. All samples have an area $\approx 1\,\mathrm{cm}^2$ allowing several tens of shots per sample with pretty good reproducibility of the measured x-ray spectra and hard x-ray spectra due to low (below 5 %) shot-to-shot fluctuations of the laser energy.

The experimental diagnostics our partners used include a high-resolution x-ray crystal spectrometer for the range of 1.7-2.1 keV covering K-shell characteristic emission lines from Si (from K_α to K_β) for all charge states up to H-like, and a detector for characterizing the hard x-ray-gamma-ray bremsstrahlung emission spectrum. The hard x-ray and gamma-ray spectra in a broad energy range are measured with a Timepix detector, based on a CMOS pixel readout chip working in a single photon counting mode. A 1-mm-thick CdTe sensor chip enables the registration of photons with energies up to 800 keV [228]. Our colleagues placed the focusing parabola, the targets, and the spectrometer in a vacuum chamber pumped below 10^{-4}-mbar pressure. The Timepix detector is located in ambient air $\approx$ 5 m away from the target and oriented at 45° to the target normal observing it through a 230-µm-thick Kapton window.

The spectra of the characteristic line emission from the polished and nanowire targets recorded by our partners are shown in Fig. 8.2(a). Under conditions of their experiment, the efficiency of the K_α emission from weakly ionized Si ("cold" emission) is essentially the same from both morphologies. This result is strikingly different from the results known in the nonrelativistic regime of interaction [54–56] and suggests that in the relativistic limit nanostructure arrays have no advantages in comparison to the flat surface in terms of the efficiency of the characteristic line emission from weakly charged states.

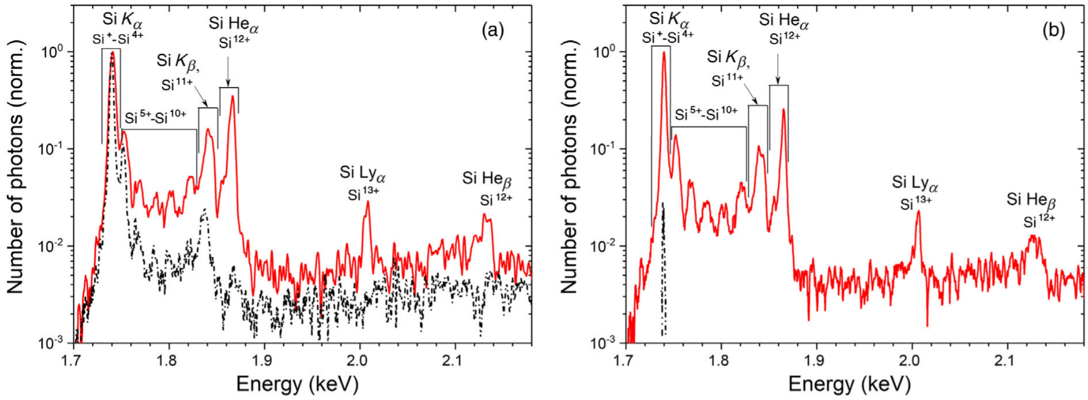

Figure 8.2: (a) Spectrum of K-shell line emission from the polished (black dash-dotted line) and the nanowire array (red solid line) Si targets in the logarithmic scale measured at (a) 45° and (b) 0° incidence angles (with respect to the target's normal). *(Source: [22], see summary 8.5 below for details.)*

In contrast to the characteristic emission from Si^{+}-Si^{4+} contributing to the K_α line, Fig. 8.2(a) demonstrates a dramatic increase in the efficiency of the line emission from highly charged ion species for the nanowire arrays in comparison to the flat surface. Emission from Li-like (Si^{11+}), He-like (Si^{12+}) and H-like (Si^{13+}) ions, such as He_α, He_β, and Ly_α is detected from the nanowire arrays only. Note that emission of KL transitions from Si^{11+} overlaps with K_β emission line of Si^{+} ions. Though their maxima are slightly shifted with respect to each other, this shift is not resolved by the spectrometer. It is known that the ratio of the intensities of K_α and K_β emission lines in Si is about 50:1 [229, 230], which matches well to the measured ratio of 42:1 in the emission spectrum from the polished target [Fig. 8.2(a)]. In contrast, this ratio for the nanowires is 6:1 suggesting a dominant contribution of the KL-transition emission from the Li-like Si charge state in the spectral range 1.83-1.85 keV (the spectral range covering Si^{11+} emission marked in Fig. 8.2(a)). Because of the relatively high stability of the laser pulse energy, shot-to-shot variations in the intensity of He-like and H-like emission lines are within 20 % rms, whereas variations in the intensity of "cold" K_α emission are within 14 % rms.

The same measurements are also performed by our colleagues for 0° incidence angle (normal to the target surface) [Fig. 8.2(b)]. In this case, the intensity of the K_α emission line of Si^{+} ions from the polished target drops by more than an order of magnitude, whereas emission at characteristic lines of high-charge-state ions is not detected at all. Such behavior can be explained assuming the Brunel mechanism of absorption, for which the absorption efficiency approaches zero when the laser polarization becomes parallel to the target surface [36] (see section 2.1.5). Also, the results for "cold" K_α emission are in a good agreement with the results published in Ref. [224] for a Cu target and explained by the Brunel mechanism of electron heating. At the same time, the spectrum obtained by our partners with the nanowire target remains essentially unchanged. This insensitivity of nanowire morphology to the orientation of the laser polarization is observed in the experiments on interactions in the nonrelativistic regime [231] and can be explained by the fact that there is always a significant component of the laser field perpendicular to the local surface for this target morphology. In the following discussions, we focus on the results our collaborators obtained in the interaction under the 45° incidence angle.

Similar to the measurements of "cold" K_α emission, the high-energy bremsstrahlung spectra recorded by our partners show almost no difference in the flux up to 140 keV for the flat and nanostructured targets (Fig. 8.3). By applying an exponential fit to the hard x-ray photon distribution [232], for both target morphologies, our partners estimate approximately the same hot electron temperature $T_e \approx 26\,\text{keV}$ for the electron fraction responsible for the emission of the photons in the energy range 40-140 keV.

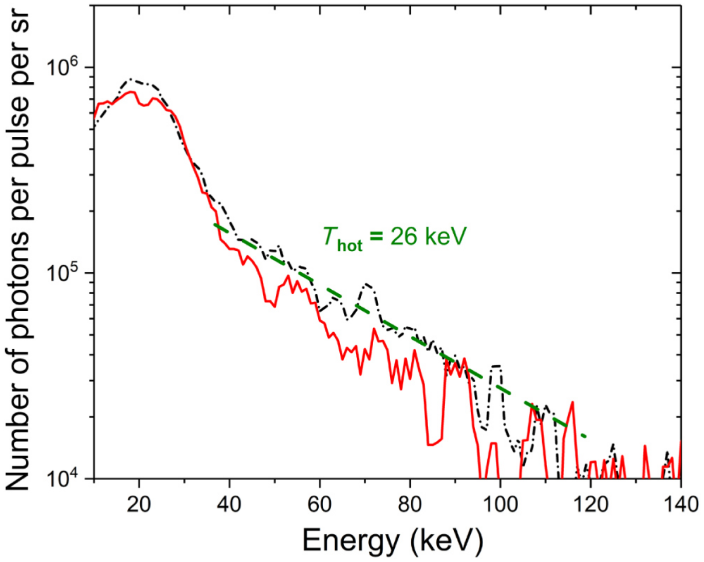

Figure 8.3: Hard x-ray emission spectrum measured from the polished Si target (black dash-dotted line) and the nanowire array (red solid line). The green dashed line is the exponential fit providing an estimate of the hot electron temperature $T_{\text{hot}} = 26\,\text{keV}$. *(Source: [22], see summary 8.5 below for details.)*

The "hot" electron temperature estimated by our colleagues from the hard x-ray spectrum in Fig. 8.3 is a temperature of the electron fraction heated during the laser pulse via the Brunel mechanism [36, 219–222]. The general structure of the electron energy distribution function (EEDF) for a relativistic laser-plasma interaction is up to now an open question because numerical simulations in the entire energy range, from the relatively cold major part of EEDF to the ultrafast relativistic tail controlling ion acceleration, are extremely challenging. Also, it is sensitive to several parameters like the spatial gradient of the plasma density and a_0 [36, 219–222]. However, from the general physical point of view, it is reasonable to expect that the EEDF should consist of at least three fractions of electrons. The first one, commonly termed as "hot" electrons in the particle acceleration community, constitutes only a tiny fraction of the total amount of electrons. They are accelerated and pushed out by the ponderomotive force in the laser pulse and leave the target forming the charge separation sheet at the surface [124, 233]. The second fraction, which are called "hot" in this study, is forming an energetic tail of the EEDF due to the Brunel heating mechanism in the laser pulse. According to our PIC simulations (see below), under the conditions of the experiments this fraction contains less than 1 % of the total amount of electrons. Finally, the third fraction, containing the absolute majority of electrons, has the bulk electron temperature, which can be estimated from simulations of the measured line-emission spectra (see below). Examples of such a three-temperature EEDF are described, e.g., in Refs. [48, 234].

8.4 Simulation results

To get insight into the physics of processes occurring at different timescales under the conditions of the experiments, two sets of numerical simulations were performed. First, PIC simulations performed by us are used to retrieve the parameters of plasma and their dynamics under relativistic interaction of ultrahigh-temporal contrast ultrashort laser pulses with Si nanowire arrays. The obtained temperature for hot and bulk electrons and their temporal evolution is used by our partners for calculating the line-emission spectra using the FLYCHK atomic kinetic code [226]. For FLYCHK a constant ion density of 5×10^{22} cm^{-3} is assumed, implying that the nanowires stay intact over the simulation time of 1.5 ps, while the electron density evolution is considered by the code.

To model the experimental conditions, we used the laser-target parameters given by the experiments in our PIC simulations. We carried out the nanowire PIC simulation in a box with the size 17.55 µm×0.3 µm×0.3 µm. The grid steps are 6.65 nm×5.77 nm×5.77 nm and the time step is 5.2 as. The flat target simulation is done in a 82.73 µm×137.39 µm box with grid steps 73.86 nm×73.86 nm and a time step of 1.3 as. The laser pulse has a Gaussian temporal profile of 90-fs duration and a normalized vector potential of $a_0 = 1.05$. We modeled it as a plane wave in the nanowire simulation with periodic boundary conditions in transverse direction for both particles and fields. In the flat target case we focused the laser to a focal spot size of 12 µm (FWHM in diameter) with a Gaussian transverse profile, having an angle of incidence of 45°. In both simulations the material of the targets is non-preionized silicon which we assumed to be initially cold. To take into account ionization of the material both optical field and collisional ionization modules are included.

The spatial distribution of the bulk electron temperature along the nanowires at different moments of time we calculated with the PIC code is shown in Fig. 8.4(a). It reaches the maximum temperature of ≈ 600 eV within an approximately 1-µm-thick layer at the tip of the wires during the interaction with the laser pulse. After the laser pulse ($t = 300$ fs after its peak), the entire wire volume is heated almost homogeneously to approximately 50 eV.

The spatial distribution of the electron density in the wire volume computed by our PIC code is shown in Fig. 8.4(b). It reaches the maximum value $n_e \approx 6 \times 10^{23}$ cm^{-3}, corresponding to Si atoms ionized up to the Si^{12+} (He-like) charge state, within the hot $\approx$ 1-µm-thick upper layer of the wires on the timescale of the laser pulse duration. After the laser pulse ($t = 300$ fs after its peak), the main volume of the wires is ionized with the electron density $\approx 3 \times 10^{23}$ cm^{-3} and thermalizes to the electron temperature of about 30 eV. Considering the value of the critical density $n_{\rm cr} \approx 7 \times 10^{19}$ cm^{-3} at 3.9-µm laser wavelength, our simulations suggest that plasma as dense as about $\approx 10^4\, n_{\rm cr}$ is generated under the conditions of the experiment. Our simulations show also that the wires stay intact and high plasma density is maintained on the timescale of at least 2.9 ps. This timescale is significantly longer than a femtosecond timescale of wire explosion predicted for short-laser wavelength experiments [5, 18, 19]. Simulations suggest that at large values of a_0 pinching of the electron current driven by a relativistically intense laser pulse along the wire can effectively heat electrons and increase plasma density, which largely speeds up the hydrodynamic expansion of the plasma at $a_0 \geq 1$ (see chapter 4).

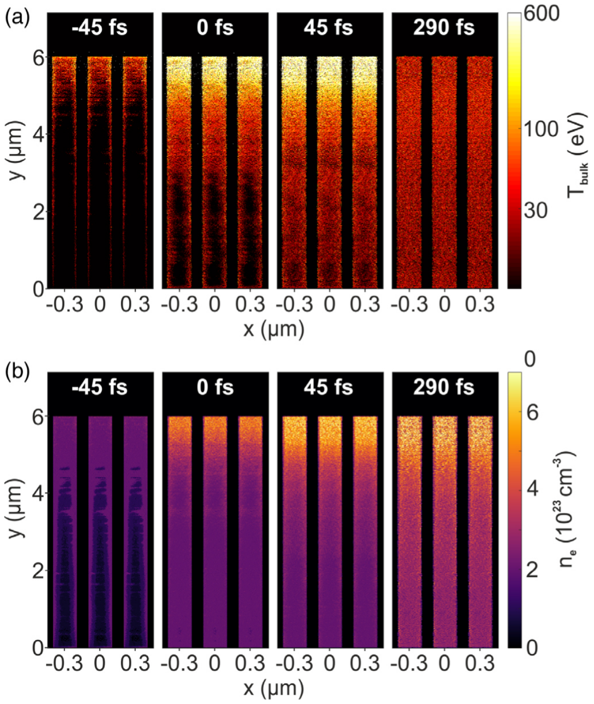

Figure 8.4: Spatial distribution of (a) the electron temperature and (b) electron density in Si nanowires retrieved from the PIC simulations. The zero moment of time corresponds to the moment of the peak intensity arrival at the tip of the wires. *(Source: [22], see summary 8.5 below for details.)*

The amplitude of the fields responsible for the pinch effect scales with the laser wavelength as λ^{-1}. Further, the number of forward-driven electrons is proportional to the critical density associated with the laser wavelength that scales as λ^{-2} (see Eq. 2.26). Simple estimates of our colleagues show that for long-wavelength laser sources, the laser-induced electron currents are too low to cause a significant pinching effect. Therefore, an unprecedentedly long lifetime of overdense plasma predicted by our simulations under the condition of the experiment is due to the long laser wavelength.

The $\approx 1\,\mu$m depth of the high-density and high-temperature plasma region is determined by the penetration depth of the laser pulses into the wire array, which, in turn, is limited by the absorption. Our simulations predict 76 % absorption efficiency of the laser energy which is concentrated mostly within the $\approx 1\,\mu$m layer (for the given 20-mJ laser pulse energy) due to an extremely high $n_e/n_{\rm cr}$ ratio.

As was discussed in chapter 5, high temperature and density of plasma enabled by nanowire morphology play a key role in reaching a high-charge state and efficient emission from He-like and H-like ions. Note that simulations based on the Popov-Perelomov-Terentiev ionization model [235] performed by our partners show that the optical field ionization for the experimental field parameters is capable of ionizing Si atoms up to a $\rm Si^{4+}$ charge state only, therefore higher charge states are the result of collisional plasma heating and generated via the electron impact ionization mechanism. The evolution of the charge states, populations of different excited ion states, and the corresponding emission spectrum are simulated by our collaborators using the kinetic FLYCHK code with the temporal history of the bulk and hot electron temperatures derived from our PIC simulations. The large volume of the dense plasma predicted by the PIC simulations results in large wavelength-dependent plasma opacity, causing strong reabsorption of the generated emission and, therefore, influencing the emission line ratio. To include the effect of opacity, our colleagues used the effective thickness of the emitting plasma layer as a fitting parameter to match the simulated spectra to the measured ones. The effective thickness of the emitting plasma layer providing the best match between the simulated and the measured x-ray spectra is found to be ≈ 0.5 µm.

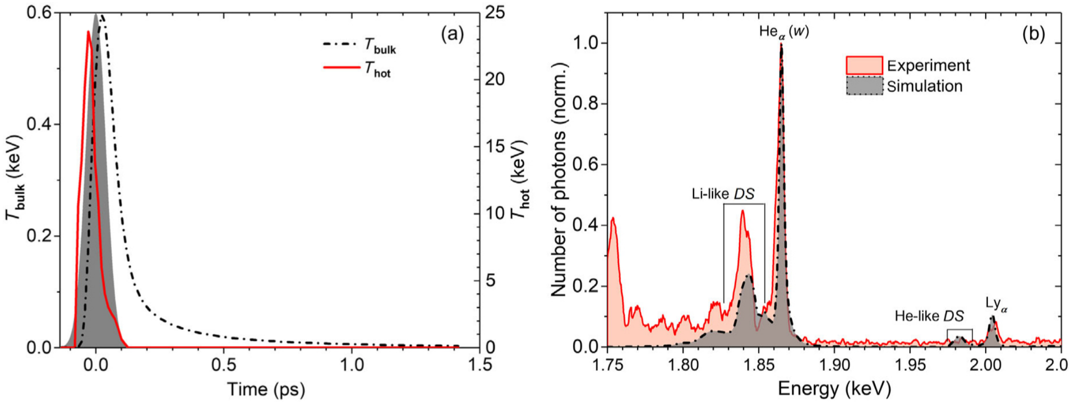

Figure 8.5: (a) The temporal evolution of the temperature of the "hot" (red line) and the bulk (black dash-dotted line) electron fractions averaged over the upper 0.5 µm length of the wire. The gray shaded curve is the temporal profile of the laser intensity. (b) The measured (red line) and the simulated (black dash-dotted line) spectra (time integrated). *(Source: [22], see summary 8.5 below for details.)*

The temporal evolution of the bulk and hot electron temperatures calculated by our collaborators by averaging our PIC results over the volume of the upper 0.5 µm layer of wires is shown in Fig. 8.5(a). The maximum average bulk temperature of ≈ 0.6 keV is reached by the end of the laser pulse and cools down with ≈ 100 fs time constant. The hot electron temperature reaches its maximum of about 25 keV within the laser pulse duration and vanishes as soon as the laser pulse is off. The calculated maximum is in very good agreement with the hot electron temperature estimated by our partners from their measured hard x-ray spectra (see Fig. 8.3). The emission spectrum simulated by our colleagues is shown in Fig. 8.5(b) and demonstrates an excellent agreement with the most energetic part of the experimental spectrum, consisting of He- and H-like Si emission lines and emitted at the maximum intensity region in the focal distribution. Note that the simulation result of our partners is quite sensitive to the changes of the input parameters and varying the electron temperature by more than 10 % cannot be simply compensated by a reasonable density adjustment. Therefore, it is concluded that the used set of plasma parameters indeed fits well to their experimental findings. It is worth mentioning also that the temporal evolution of the electron density during the laser pulse, calculated by our colleagues using the FLYCHK code, agrees well with the evolution of the electron density in our PIC simulations averaged over the 0.5-µm upper layer. After the laser pulse, the electron density predicted by their FLYCHK simulations drops by a factor of 2 within approximately 200 fs due to efficient recombination processes, which are not included in our PIC simulations.

In a next step, we want to understand the temporal structure of the emitted x-ray radiation. FLYCHK simulations allow getting insight into the temporal evolution of the charge states and the emitted spectrum [Fig. 8.6(a)], which are governed by the evolution of the bulk electron temperature and collisional and radiative rates. Formation of He-like and H-like Si ions occur due to the collisional ionization of Si^{11+} and Si^{12+}, respectively. Ionization of the L shell up to the charge state Si^{12+} takes place at the rising edge of the bulk electron temperature (about 25 fs after the peak of the laser pulse intensity) [Fig. 8.6(b)]. Meanwhile, ionization of the K shell requires electrons with a kinetic energy of more than 2 keV (ionization bottleneck). Since the rates of the collisional processes in plasma drop exponentially with an increasing ratio of the binding energy E_{bin} to the bulk electron temperature T_{bulk}, Si^{13+} ions are generated with a delay with respect to the appearance of Si^{12+} and approaching their highest density at roughly 75 fs [Fig. 8.6(c)]. After reaching their maxima, both ion densities decrease following the T_{bulk} behavior. The comparison of ion fractions obtained by our colleagues from time-dependent FLYCHK simulations with a steady-state distribution at $T_{\mathrm{bulk}} = 600\,\mathrm{eV}$ shows that the maximal value of the Si^{13+} fraction [8 % reached at ≈ 75 fs, Fig. 8.6(c)] is one order of magnitude lower than the value obtained in the steady temperature case, while the maximal value of the Si^{12+} fraction is twice higher [80 % reached at ≈ 25 fs, Fig. 8.6(b)]. Therefore, simulations suggest the transient character of the plasma under the experimental conditions.

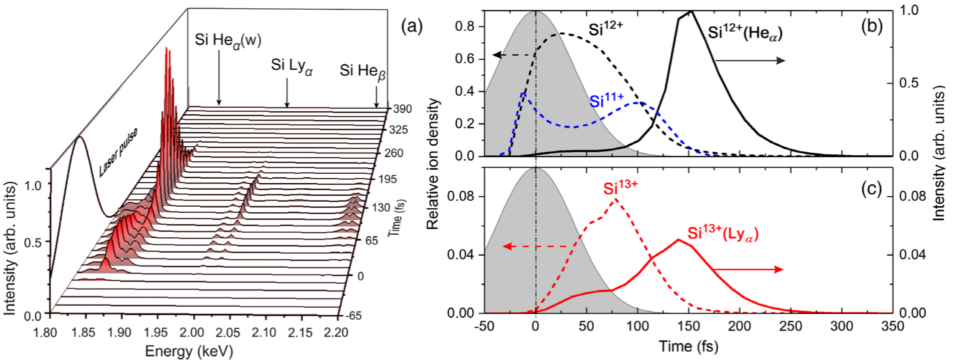

Figure 8.6: (a) The temporal evolution of the K-shell emission in the spectral region 1.8-2.2 keV. (b),(c) Time-dependent density of Si^{11+} (dashed blue line), Si^{12+} (dashed black line), and Si^{13+} (dashed red line) ions; intensity of He_α (solid black line) and Ly_α (solid red line) emission. The densities normalized to the density of neutral atoms. The shaded curve is the normalized laser pulse intensity. *(Source: [22], see summary 8.5 below for details.)*

The K-shell radiation (He_α and Ly_α) arises mainly from the collisional excitation of the K-shell electrons followed by the radiative decay back into the ground state. The timescale of the buildup of the Si^{12+} and Si^{13+} ion densities and the timescale of the corresponding electron impact excitations are similar. Therefore, the temporal evolution of the He_α and Ly_α line emission starts almost simultaneously to the corresponding ion density. Neglecting effects of opacity, the maximum of the emission is delayed by ≈ 25 fs for He_α and ≈ 50 fs for Ly_α with respect to the maximum of the corresponding ion density in accordance with the radiative decay times [226]. However, the He_α line resembles the second maximum in the emission related to the recombination channel of the population from H-like ions. The time-dependent opacity strongly modifies the temporal profile of the line emission resulting in ≈ 50 fs at FWHM pulse at the 1.865-keV He_α transition and ≈ 150 fs at FWHM pulse at the 2-keV Ly_α transition [Figs. 8.6(b) and 8.6(c)]. The expected shorter duration of the He_α emission is a consequence of higher opacity of the plasma at this emission wavelength. Overall, the ultrashort duration of the generated x-ray emission in relativistic interaction of ultrahigh contrast, ultrashort laser pulses with solids is intrinsically related to the transient character of high-density plasma. This transient nature of the plasma evolution has to be taken into account when estimating the timescale of radiation cooling processes and determining conditions for new regimes as we have described in chapter 6, where the plasma cooling caused by plasma self-radiation happens faster than hydrodynamic expansion. High electron density enables ultrafast collisional pumping. At the same time, high ionic density (in the corresponding charge state) leads to strong absorption of the emitted line radiation (opacity) and the reemission of the absorbed photons is strongly suppressed due to the collisional deexcitation by free electrons. Thus, a delay between the maximum of the laser pulse and maximum of the K-shell radiation is expected as it is demonstrated in Fig. 8.6. Therefore, it can be concluded that the high density and temperature of plasma, dynamically changing at subpicosecond timescale, in combination with (dynamically changing) effects of opacity are determining the femtosecond duration of the x-ray line emission in contrast to picosecond duration estimated from assumptions of optically thin plasma under steady-state conditions in chapter 6. In particular, the qualitative estimations depicted in Fig. 6.6 do not include reabsorption effects.

Finally, we have carried out simulations for spectra measured from a polished Si wafer to understand the differences in the emission for different morphologies of the samples. The results of the spatial and temporal evolution of the bulk electron temperature and density obtained in our PIC simulations are presented in Fig. 8.7. As follows from Fig. 8.7(b), the plasma density for flat targets can be as high as $3 \times 10^{23}\,\mathrm{cm}^{-3}$, which is comparable to the density calculated for nanowires [Fig. 8.4(b)]. However, the maximum bulk electron temperature is only 50 eV and reached just within an approximately 100-nm thin layer near the surface. Compared to nanowires, the substantially lower electron temperature is the consequence of a strong ($\approx 98\,\%$) reflection of the laser energy from the overcritical plasma. Simulations of the spectra by our partners using FLYCHK fail for such dense and low-temperature plasma.

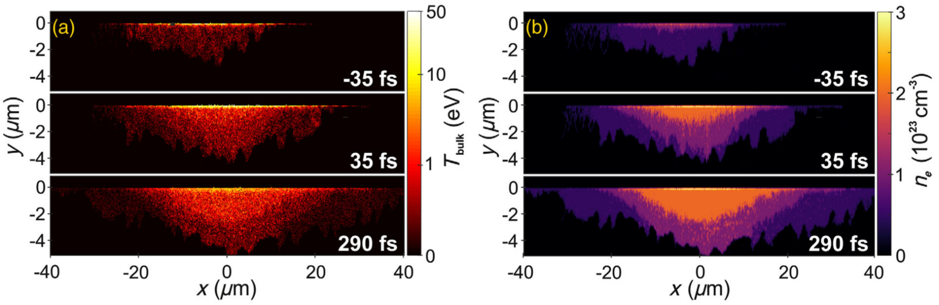

Figure 8.7: The results of PIC simulations for the spatial distribution of the (a) bulk electron temperature and (b) electron density at the flat Si target. The zero moment of time corresponds to the moment of the peak intensity arrival at the surface boundary. *(Source: [22], see summary 8.5 below for details.)*

The observed spectra can be understood by extending the concept of Brunel electron heating [36], into the relativistic regime [225]. With this mechanism, electrons are efficiently accelerated near the critical density and the subsequent collision creates holes in the K shell of neutral Si atoms followed by cold K_α emission. Using the same long-wavelength laser system as in the experiments of our collaborators, an enhanced conversion efficiency for K_α radiation from Cu foil has been demonstrated in [224]. Also, it is assumed that the weak emission in the range of 1.747-1.827 keV [Fig. 8.2(a)], observed by our colleagues for all the targets and originating from intermediate charge states of Si (up to Si^{10+}), is generated due to innershell collisional ionization by energetic electrons emerging in the Brunel heating process. The difference in the yield of this emission between the nanowires and the bulk target originates from the difference in the bulk electron temperature since mainly the bulk electrons are responsible for the evolution of the charge states in the plasma.

8.5 Summary

This chapter dealt with the relativistic interaction regime accessed by using a long-wavelength (mid-IR) laser pulse. We have described the results of our PIC simulations, that were used to model the experimental findings of our collaborators. The data drawn from our PIC simulations were used by our partners to generate synthetic emission spectra, which allow for a direct comparison with their experimental results. In the new interaction regime explored in this chapter, profiting from favorable λ^2 scaling of electron energies with the laser wavelength rather than linear scaling with intensity, the laser field ionization and creation of the preplasma on the rising edge of the laser pulse are strongly suppressed. As a consequence, the maximum of the laser pulse interacts with solid matter and ionization has predominantly a collisional character. Comparing the experimentally measured x-ray emission spectra of our colleagues with the results of numerical simulations confirms the importance of nanowire arrays as a solid target for overcoming the problem of the low critical plasma density at mid-IR wavelengths enabling very efficient absorption of the laser pulse energy ($\approx 80\,\%$). As a result, plasma with an electron density up to $6 \times 10^{23}\,\mathrm{cm}^{-3}$ is generated, which is a record high density if it is measured in critical density values and is more than 10^3 times the critical density. The high electron density of the created plasmas ensures high collision rates that govern ionization of the target material up to the H-like charge state (Si^{13+}) and 0.6 keV peak bulk electron temperature.

Using nanowire targets and mid-IR laser pulses enables to generate solid density plasmas with keV-level bulk temperatures using only 20-mJ energy per laser pulse, in contrast to Joule-energy UV sources used so far to generate plasmas with similar parameters [5], as we have seen in the previous chapters, particularly in chapter 5. Such relaxed requirements for laser energy pave the way to the experiments at high repetition rates, which is very promising for applications in laser-driven nuclear physics. For instance, the cross sections for the nuclear-excitation-by-electron-capture reactions in the hot plasma will be 3-4 orders of magnitude higher compared to the “cold” x-ray free-electron laser plasma case as reported in Refs. [236, 237]. Also, the simulations of the temporal evolution of the He_α and Ly_α emission suggest that ultrahigh-temporal contrast, relativistically intense femtosecond laser pulses enable ultrashort ($\leq 150\,\mathrm{fs}$) x-ray pulses (in contrast to the picosecond duration x-ray pulses described in chapter 6). Such pulses are very attractive for using them for time-resolved x-ray radiography of high-density plasmas [238].

The results presented in this chapter are reproduced from [22] © The Authors, which is licensed under CC BY 4.0. The figures were taken unchanged and the text was adopted literally with adaptations for fitting into the thesis. The author has conducted the PIC simulations, has computed the spatial and temporal temperature distribution from the PIC data and has provided our collaborators with the data necessary for their post-processing. Furthermore, the author has contributed to the writing of the published manuscript (the description of the simulations, their interpretation and proofreading with suggestions).

Chapter 9

Ion acceleration in nanowire targets

9.1 Introduction

The previous chapters were mainly concerned with producing plasmas in the UHED regime, understanding its fundamentals and exploring it with respect to applications. This chapter deals with another subject, namely the acceleration of ions. The picture of this active field was outlined in section 2.3.1 and has its own interesting applications, as described in section 2.3.4.

This chapter deals with ion acceleration by using again the targets that were considered in the previous chapters, the nanowire arrays. The work aims at better understanding the relation between the nanowire target parameters and the proton acceleration via enhanced TNSA. For this purpose, we performed three-dimensional PIC simulations, which were used by our collaborators at the University of Michigan and the Colorado State University to validate their two-dimensional PIC simulations. Our partners then used their computations to model a parametric experimental study that they carried out. In this chapter, we present these numerical and experimental results obtained by them.

We have seen in section 2.3.1 that one approach to get enhanced ion acceleration is the use of structured targets. They enable an increased absorption of laser energy (see section 2.2.1) and an improved formation of hot electrons, which benefits the TNSA mechanism. Besides different kinds of structures, there are no detailed studies on the nanowire arrays and their ability to produce enhanced proton acceleration. As we have seen in the introductory section 2.2.1 as well as in chapters 4 and 5, nanowire arrays are potent targets to produce plasmas in the UHED regime, which improves or enables some applications such as x-ray (chapter 6) and fusion neutron production (chapter 7). Other works have investigated the interaction with relativistic lasers [182] and the generation of intense THz radiation [239]. One recent publication [10] has studied microwires qualitatively with respect to enhanced proton acceleration. A full investigation of the influence of the nanowire parameters such as thickness, length and center-to-center distance, however, has not been done yet, which is the goal of the work presented in this chapter. It was found, that the key parameter for the proton acceleration is number of nanowires per focal spot.

In the following, the corresponding experimental setup and results (section 9.2) as well as the simulation results (section 9.3) of our colleagues will be described. The chapter is concluded with a summary (section 9.4).

9.2 Experimental setup and results

The experiment was conducted by our collaborators using the HERCULES [240] laser at the University of Michigan. The laser pulses of 3 J energy and 30 fs duration were focused to a focal spot of 1.7 µm, corresponding to an intensity of up to 1.5×10^{21} W cm^{-2}. A double plasma mirror (DPM) was used before the focusing, improving the amplified stimulated emission intensity contrast to 10^{-15} and the prepulses of the short pulse to 10^{-10} [241]. The contrast of the leading front of the main pulse at 350 fs before the peak was 6×10^{-9}. A Thomson parabola behind the target was used to detect the proton energies. Additional diagnostics, such as an x-ray pin diode and a photomultiplier to measure x-rays and gamma radiation, were used to assure that the target was irradiated for the case that no protons were measured (which was the case for some shots, as will be seen).

The targets of interest were gold nanowires, attached on a gold substrate as shown in Fig. 9.1. As enlisted in Tab. 9.1, our partners employed different target parameters such as lengths L, diameters D and average number of nanowires per focal spot N to investigate their influence on the proton acceleration. The targets were irradiated at normal incidence and with a repetition rate of one shot per minute.

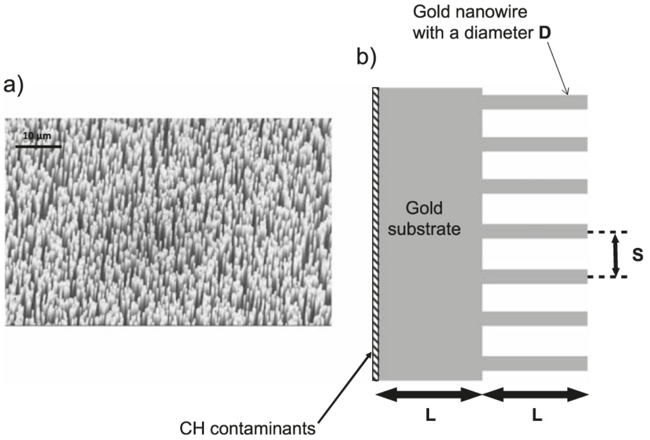

Figure 9.1: (a) SEM image of a target of sort C as specified in Tab. 9.1. The substrate is made of gold with a density of 19.30 g cm^{-3}, supporting gold nanowires with an average number of nanowires per µm^2 equals one. (b) Illustration of the target, consisting of nanowires of length L, diameter D and a center-to-center distance of S, covering a substrate of thickness L. On the rear side, the substrate has a thin CH contamination layer. *(Source: [23], see summary 9.4 below for details.)*

Target	D [nm]	L [µm]	ρ_{wires} [wires µm^{-2}]	N
A	55	7.4	59	130
B	400	7.1	1	2.2
C	400	15	1	2.2
D	600	18.2	0.5	1.1
E	800	13.7	0.2	0.44
F	1000	19.4	0.2	0.44

Table 9.1: Nanowire target parameters: Thickness D, length L, and the average number of nanowires per µm^2 ρ_A. *(Source: [23], see summary 9.4 below for details.)*

The thickness of the targets' substrates were greater than those usually used to accelerate protons via TNSA. Since there is an inverse relationship between target thickness and the proton energy [124], thinner targets are usually preferred. The goal of this work is however not to maximize the proton energy and to figure out the influence of the target parameters instead, where the bigger thickness does not pose a problem.

Using several nanowire samples with different properties as shown in Tab. 9.1 allowed our colleagues for an elaborate parametric study. As we will see, the average number of nanowires per focal spot, given by

$$N = A_{\text{laser}} \cdot \rho_{\text{wires}}, \tag{9.1}$$

was identified to be of particular importance, where $A_{\text{laser}} = 2.2\,\mu\text{m}^2$ is the area of the focal spot and ρ_{wires} the average number of nanowires per μm^2. The latter is determined by the density of the membrane pores used to grow the nanowires. The density of wires per μm^2 is related to the parameters defined in section 3.5 (see Eq. 3.24) by $\rho_{\text{wires}} = 1/d^2 = f/(\pi D^2)$, where d is the center-to-center distance and f the filling factor.

The set of target parameters as specified in Tab. 9.1 can be categorized into four different sectors, which are $0 < N < 1$ for targets E and F, $1 < N < 2$ for target D, $2 < N < 3$ for targets B and C, and $N \gg 3$ for target A. Since N is an averaged parameter, its value slightly fluctuates from shot to shot, depending on the irradiated area on the target. To reduce the influece of this variation, several shots were done to get fair statistics as included in Tab. 9.2.

To find out the enhancement caused by the nanowires, our partners conducted measurements where flat targets of different thicknesses were irradiated for comparison. The spectra of the two nanowire targets of sort E and D as well as two flat target spectra of thicknesses 10 and 25 µm are depicted in Fig. 9.2, where all spectra represent measurements yielding the best results. The arbitrary units "a.u" of the proton spectra intensity correspond to the CCD signal, that is proportional to the number of detected protons.

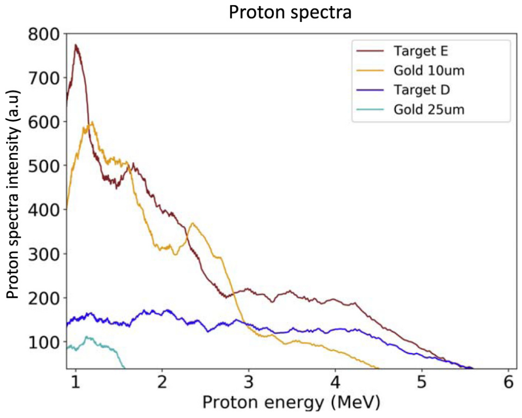

Figure 9.2: Experimentally measured proton spectra of the nanowire samples of sort E ($L = 13.7\,\mu\text{m}$ and $2L = 27.4\,\mu\text{m}$) and sort D ($L = 18.4\,\mu\text{m}$ and $2L = 36.8\,\mu\text{m}$) in comparison with flat targets of 10 and 25 µm thickness. *(Source: [23], see summary 9.4 below for details.)*

To compare the results from the nanowire and flat target cases, one needs to take into account the thickness of the target. In the case of the nanowires, they have a total thickness of $2L$, where only the last segment of length L is of solid density, and therefore directly comparable to the flat target. In the case of target E, the mere wires have a length of $L = 13.7$ µm, and along with the substrate present a total length of $2L = 27.4$ µm, which is comparable to the two flat targets shown in Fig. 9.2 of thickness 10 µm and 25 µm. The spectrum of nanowire target E (brown curve) exhibits higher maximum proton energies and higher number of protons compared to both flat target spectra. Furthermore, the thickness of 25 µm of one flat target (light blue curve) lies between $L = 18.4$ µm and $2L = 36.8$ µm of nanowire target D (dark blue curve). Both results can therefore be compared, yielding a substantial factor of 3.7 higher maximum proton energy in the nanowire target. This improvement that is facilitated by the nanowires, is however limited to targets D, E and F. As we will see shortly, this conclusion does not hold for targets A, B and C, as they do not demonstrate an improvement compared to the flat targets as seen in Fig. 9.2. This finding emphasizes the importance of the right choice of the nanowire parameters, as they do not provide an improvement otherwise.

	Intact nanowires			
	Averaged maximum p energy (±0.2 MeV)	Highest maximum p energy (±0.2 MeV)	Number of shots with no signal / total number of shots	Standard deviation of the data set [MeV]
Target A, $N = 130$	3.6 MeV	4.9 MeV	0/5	SD = 0.93
Target B, $N = 2.3$	0.74 MeV	3.7 MeV (the only shot with protons)	4/5	NA
Target C, $N = 2.3$	1 MeV	2.8 MeV	5/8	NA
Target D, $N = 1.1$	3.5 MeV	5.8 MeV	1/11	SD = 1.47
Target E, $0.44 \leq N \leq 1$	3.3 MeV	5.5 MeV	0/14	SD = 1.18
Target F, $0.45 \leq N \leq 1$	2 MeV	5.1 MeV	4/14	SD = 1.56
	Disrupted nanowires			
Target A, $N = 130$	4 MeV	4.5 MeV	0/4	SD = 0.93
Target B, $N = 2.3$	1.8 MeV	4 MeV	2/6	SD = 1.56
Target C, $N = 2.3$	0.6 MeV	1.8 MeV (the only shot with protons)	2/3	NA
Target D, $N = 1.1$	2.15 MeV	2.3 MeV	0/5	SD = 1.47
Target E, $0.44 \leq N \leq 1$	2.1 MeV	2.3 MeV	0/5	SD = 0.25
Target F, $0.45 \leq N \leq 1$	1.25 MeV	2.1 MeV	1/5	SD = 0.78

Table 9.2: The results of the proton spectra for each type of target, covering the two cases of intact and disrupted nanowires. *(Source: [23], see summary 9.4 below for details.)*

As was described in sections 2.1.4 and 2.2.1, prepulses can have a big impact on the laser-plasma interaction. This is also true for the proton acceleration [242, 243]. For a better understanding of how the nanowires properties affect the results, our collaborators conducted two different kinds of measurements, where the nanowires were either “intact” or “disrupted”. The features of the “intact” nanowires were preserved until the arrival of the main pulse, whereas the “disrupted” nanowires have already dissolved at that time due to the prepulse. This was experimentally realized by either using the DPM, defining the “intact” measurements, or without DPM, resulting in the data considered as the “disrupted” case. The results of targets defined in Tab. 9.1 are demonstrated in Tab. 9.2 and enlist the averaged maximum proton energies, as well as the highest maximum proton energies. Our partners calculated the average from at least 5 shots (of almost all targets) of same laser and target parameters. In target B with intact nanowires and target C with disrupted nanowires only one shot obtained protons. In these cases, the poor proton signal could not be registered in the sensitivity range of the detector in spite of three to five shots.

Two trends become evident in the data shown in Tab. 9.2. Firstly, targets D, E and F have higher averaged and maximum proton energies when in the intact state, compared to their disrupted condition, which will be revisited in the next section about the simulation results. Secondly, targets A, B and C exhibit comparable spectra in both states, intact and disrupted. Furthermore, target B and C reveal the highest relative number of shots with no signal.

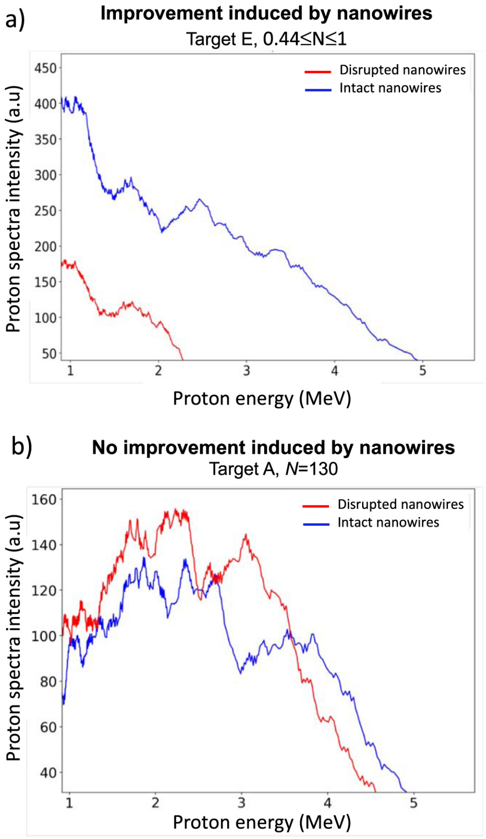

Figure 9.3: Experimentally measured proton spectra from (a) target E and (b) target A, with intact (blue) or disrupted (red) nanowires. *(Source: [23], see summary 9.4 below for details.)*

These tendencies are shown exemplarily for targets E and A in Fig. 9.3 with representative spectra. A substantial difference exists between intact and disrupted nanowires in case of target E [Fig. 9.3(a)], as the nanowires yield a higher number of protons as well as an increased maximum proton energy by a factor of 2.3. In contrast, target A did not facilitate an enhanced proton acceleration, as it exhibits similar spectra for intact and disrupted nanowires. One important difference between both types of targets is the parameter N, and in fact, the evaluation of the data in Tab. 9.2 shows an enhanced proton acceleration only for the targets with $N \approx 1$ or $N < 1$ (targets E, D and F).

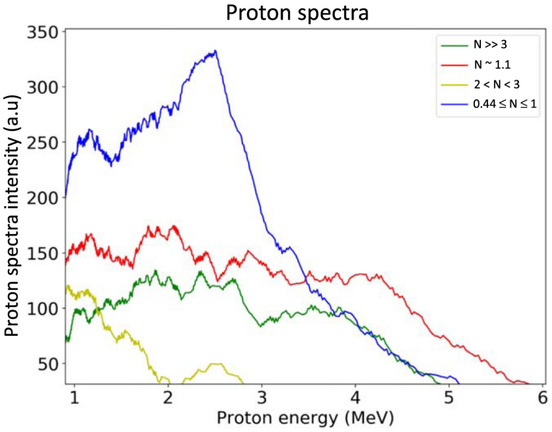

Figure 9.4: Best measured spectra for intact nanowires with different N parameters: target A (green curve), target C (yellow curve), target D (red curve) and target F (blue curve). *(Source: [23], see summary 9.4 below for details.)*

This finding is independent of different lengths and diameters of the nanowires. Figure 9.4 illustrates the best measured spectra for the targets A, C, D and F, all having different N parameters. It is evident that for increasing N the results become steadily worse, especially for $N > 1$. An additional observation underlines the importance of N. The benefit of taking a thinner target such as target A ($L = 7.4\,\mu\mathrm{m}$, $N = 130$), which one would expect to boost the TNSA mechanism, is outweighed by the effect of the N parameter in a thicker target such as target F ($L = 19.4\,\mu\mathrm{m}$, $N = 0.44$). In particular, target A (green curve) has a slightly lower maximum proton energy and a substantially lower number of protons, compared to target F (blue line). Thus, the data suggests N as the dominating parameter, which is even more important than the essential influence of the thickness in the TNSA scheme.

9.3 Simulation results

To examine the physics in the laser-nanowire interaction and gain insight of how it influences the proton acceleration, our collaborators conducted 2d3v PIC simulations using the code described in [244, 245]. They were validated by our three-dimensional PIC simulations, which are more accurate but also more computationally intensive. In the following, the results of the extensive two-dimensional results of our partners are described. The laser parameters were chosen to match the experimental values, and the pulse was modeled imposing a $\sin^2$ temporal and Gaussian transverse profile. The simulation box extent was $100 \times 72\,\mu\mathrm{m}$, containing cells of the size $20 \times 20\,\mathrm{nm}$, comprising 15 particles per cell. The laser propagates in the positive x direction, with a linear polarization pointing in z

direction (perpendicular to the 2D plane, s-polarization) and hitting the target at normal incidence. The initialization of the target is presented in Fig. 9.1. It consists of the flat substrate of $7 \times 65\,\mu\text{m}$ size, supporting the rectangular nanowires of thickness D, length $L = 7\,\mu\text{m}$ and N nanowires per focal spot. It is defined as $N = D_{\text{beam}}/S$, where D_{beam} is the beam width and S the center-to-center distance of the wires. Both the nanowires and the substrate consist of gold with initially a solid mass density of $\rho_{\text{Au}} = 19.3\,\text{g}\,\text{cm}^{-3}$ and correspondingly a particle density of $n_{\text{Au}} = 5.87 \times 10^{22}\,\text{cm}^{-3}$. Next, there is a 5 nm thin CH contamination layer of mass density $\rho_{\text{CH}} = 1\,\text{g}\,\text{cm}^{-3}$ and particle density $n_{\text{C}} = n_{\text{H}} = 4.6 \times 10^{22}\,\text{cm}^{-3}$ at the rear side of the flat part, which provides the protons to be accelerated. The three different particles species (Au, C and H) all have an initial ionization state of +1 and a kinetic energy of 1 eV, initializing a cold and dense plasma before the interaction with the laser pulse. The code used incorporates modules for field and collisional ionization to account for the ionization process.

Our colleagues chose the laser polarization to be s-polarized, in contrast to the convention of using p-polarization in two-dimensional simulations. This is motivated by recent results [246, 247], which observed an artificial electron heating that consequently leads to an overestimation of the TNSA energies in the p-polarization. On the other hand, the s-polarization was determined to have a better agreement with the more reliable and accurate three-dimensional simulations.

The first simulations addressed the two cases of “intact” and “disrupted” nanowires. In the “intact” case, the nanowires were left in their undisturbed condition, while in the “disrupted” case a low density plasma (1 % solid density) of singly charged gold was placed into the gaps between the wires. This is to design the plasma expansion that would be caused by a prepulse. The difference in the numerical spectra is shown in Fig. 9.5.

In the “intact” case, the interwire gaps are initially free, allowing for the penetration of the laser pulse into the structure. In the interaction with the nanowires, it will pull out electrons, which gradually fill the voids with low density plasma ($\approx n_{\text{cr}}$). However, this does not pose a problem for continued laser propagation, as long as the density stays below the relativistic critical density γn_{cr} (see subchapter 2.1.4 and Eq. 2.27). On the contrary, this thin plasma enhances the transfer of laser energy into hot electrons [Fig. 9.5(b)], giving rise to an improved ion acceleration. This is the case as shown in Fig. 9.6(a), where a simulated electron density distribution with a low density plasma in the gaps with $n < \gamma n_{\text{cr}}$ is depicted. When the nanowires are in the “disrupted” condition, the plasma that is located in the gaps from the beginning is rapidly ionized to above the relativistic critical, effectively shutting down further light penetration, leading to an inferior acceleration efficiency in comparison to the “intact” nanowires.

These observations are comparable to the results found by Khaghani *et al.* [10], despite them having used different laser and target parameters, especially a much lower intensity of $\sim 10^{18}\,\text{W}\,\text{cm}^{-2}$ and very high N parameter of ≈ 800. In both cases, however, the underdense plasma is observed to promote laser energy absorption, leading to a more efficient proton acceleration.

In the next step, our partners evaluate the influence of the N parameter. In the simulations of “intact” nanowires with $N \gg 1$ the interwire gaps are smaller, with the consequence that they are quickly filled with plasma after the onset of the interaction. This is illustrated in Fig. 9.6(b) for $N = 3$. Generally, in this case an overdense plasma is formed near the tips, which effectively forbids further coupling of the laser into the structure, resembling in principle (for the case for a too high N parameter, $N > 2$) the “disrupted” nanowires. This may be an explanation for the fact that the targets A, B and

C have comparable spectra from “intact” and “disrupted” nanowires (Tab. 9.2).

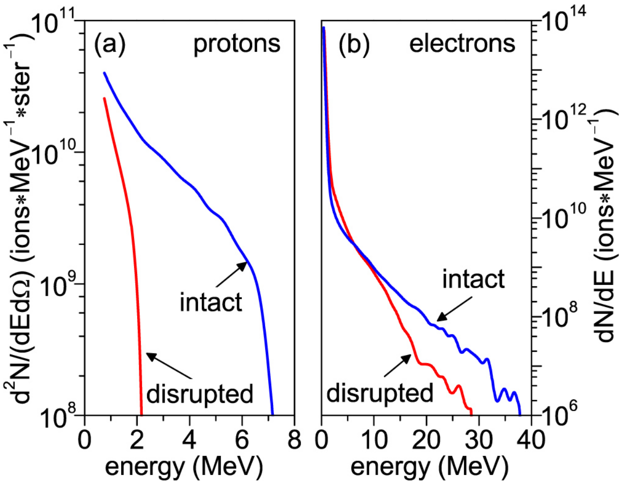

Figure 9.5: (a) Numerical proton spectra from a nanowire target in an “intact” and “disrupted” condition with $L = 7\,\mu\text{m}$, $D = 0.8\,\mu\text{m}$, $S = 2\,\mu\text{m}$ and $N = 0.75$. Only protons in forward direction within 10 degrees were taken into account. (b) Corresponding numerical spectra from the electrons. *(Source: [23], see summary 9.4 below for details.)*

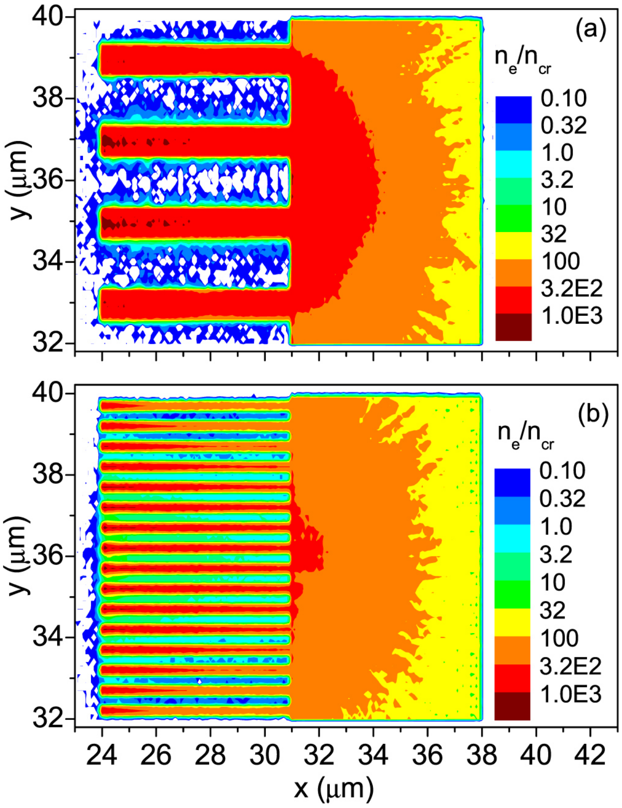

Figure 9.6: Numerical electron density profiles of a nanowire target with $L = 7\,\mu\text{m}$ at the end of the laser pulse for (a) $D = 0.8\,\mu\text{m}$, $S = 2\,\mu\text{m}$, $N = 0.75$; and (b) $D = 0.2\,\mu\text{m}$, $S = 0.5\,\mu\text{m}$, $N = 3$. The relativistically corrected critical density equals $\gamma n_{\text{cr}} = 26 n_{\text{cr}}$. *(Source: [23], see summary 9.4 below for details.)*

Further simulations were performed by our collaborators to investigate the “intact” nanowires as shown in Fig. 9.7 with varying diameters D, periods S and numbers of nanowires per focal spot N. It shows the proton spectra for $0.5 \leq N \leq 3$ (left) and the maximum proton energy over N (right). The proton acceleration efficiency first rises for increasing N, and then drops for $N = 3$. At very low $N \ll 1$, the distance between the wires is so large, that the laser pulse barely interacts with the wires (if at all), which is comparable to a flat target case. With increasing N this interaction increases, and it goes through an optimum at $N \approx 1 - 1.5$ where the spacing is small enough to have sufficient interaction to draw electrons into the gaps at a suitable density for enhanced laser absorption, but at the same time large enough to not interrupt the free laser propagation. At higher nanowires per focal spot $N \gg 1$, the maximum energy decreases as the “nanograss” is too dense and creates an overdense plasma [Fig. 9.6(b)], which overrides the beneficial absorption capability of the nanowires and shuts down the enhancement of proton acceleration.

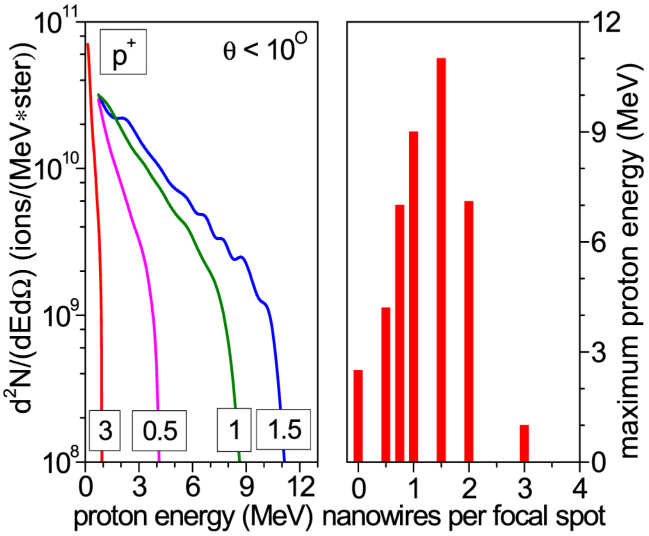

Figure 9.7: (Left) Simulated proton spectra in forward direction from intact nanowire targets at different N values and nanowire length and substrate thickness $L = 7\,\mu m$. The parameters are: red: $D = 0.2\,\mu m$, $S = 0.5\,\mu m$, $N = 3$; blue: $D = 0.4\,\mu m$, $S = 1\,\mu m$, $N = 1.5$; green: $D = 0.6\,\mu m$, $S = 1.5\,\mu m$, $N = 1$; magenta: $D = 1.2\,\mu m$, $S = 3\,\mu m$, $N = 0.5$. (Right) Maximum proton energy, plotted as a function of nanowires per focal spot N, where $N = 0$ corresponds to a flat target without nanowires. *(Source: [23], see summary 9.4 below for details.)*

In the interaction of the disrupted nanowires, the diameter D may be also of great importance besides the number of nanowires per focal spot N, since the laser pulse interacts with an already slightly disintegrated plasma structure instead of with the actual nanowires. This assumption would explain why target A with a much thinner diameter yields better results than targets B and C.

Reviewing the data obtained by our colleagues from experimental measurements and PIC simulations, one finds agreeing trends. It should be noted, however, that there is a displacement in the optimal N (1.1 in the experiments and 1.5 in PIC simulations), possibly owed to the lower dimensionality of the simulations.

Further simulation results obtained by our partners are illustrated in Fig. 9.8, having fixed periods $S = 1.5\,\mu\text{m}$ and thus fixed $N = 1$, but varying diameters D. In other words, the runs had varying filling factors, which in analogy to Eq. 3.24 can be defined in two dimensions as $f_{2\text{D}} = D/S$. It is found that the diameter has a negligible influence, except for a diameter of $D = 0.8\,\mu\text{m}$, where a decreased maximum proton energy is obtained. This is possibly due to the large filling factor leading to a high reflection at the nanowire tip, accounting for more than 50 % of the surface.

The numerical results presented in Figs. 9.7 and 9.8 basically show the same essential features as seen in the experiment, except for continuously higher maximum proton energies. The experimental measurement with optimal parameters (target D, $D = 0.6\,\mu\text{m}$, $S = 1.5\,\mu\text{m}$ and $N = 1$) for example yielded a maximum proton energy of $\approx 6\,\text{MeV}$, whereas the corresponding numerical result is 9 MeV. This difference can be traced back to the thinner substrate used in the simulations ($L = 7\,\mu\text{m}$) compared to the experiment ($L = 18 - 20\,\mu\text{m}$), which possibly leads to an overestimation of the proton energy. Generally, the substrate may play a role in the scenario of proton acceleration [248, 249], but a conclusion cannot be drawn due to the insufficiency of the present data.

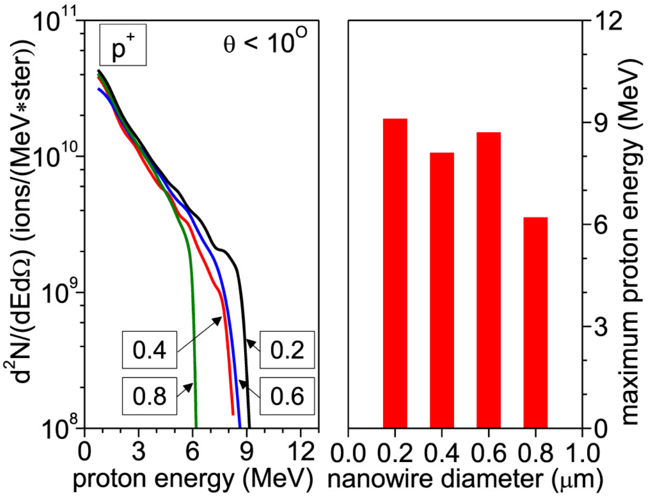

Figure 9.8: (Left) Simulated proton spectra in forward direction from intact nanowire targets at fixed period $S = 1.5\,\mu\text{m}$ and therefore fixed $N = D_{\text{beam}}/S = 1$. Nanowire length and substrate thickness were $L = 7\,\mu\text{m}$ and the targets had different diameters D. The parameters are: black: $D = 0.2\,\mu\text{m}$, red: $D = 0.4\,\mu\text{m}$, blue: $D = 0.6\,\mu\text{m}$; green: $D = 0.8\,\mu\text{m}$. (Right) Maximum proton energy, plotted as a function of nanowire diameter D. *(Source: [23], see summary 9.4 below for details.)*

Lastly, even though the effect of the length parameter L was not evaluated experimentally, it did not show to have a crucial influence in the obtained data, in contrast to the important N parameter. Nevertheless, the available data does not suffice to draw conclusions about the role of L.

9.4 Summary

This section dealt with proton acceleration in laser-irradiated nanowire-covered surfaces by means of both experimental and theoretical investigations performed by our collaborators. Their numerical model, consisting of two-dimensional PIC simulations, was applied after being validated by our more reliable three-dimensional PIC computations. A careful choice of the nanowire parameters has shown to improve both the maximum proton energies and the energy coupling compared to flat targets. The parametric study identified the number of nanowires per focal spot to be the key parameter, where an optimum is found to be between one and two. On the one hand, a too low number does not facilitate sufficient interaction between the wires and the laser, and on the other hand a too high number inhibits the laser light penetration into the structure and therefore prevents the enhanced absorption of laser energy. The relationship between maximum proton energy and the number of nanowires per focal spot is in qualitative agreement with the results of PIC simulations. Although this work gives an important insight into the still open question of how the nanowire parameters influence the laser-plasma interaction, an elaborate investigation has yet to be done. In particular, an analytic description of the laser light propagation at the transition between vacuum and nanowire target (including all parameters L, D, S etc.) may be promising for a better understanding of the interaction, and the ability for an efficient use in applications.

The results presented in this chapter are reproduced from [23]. The figures and tables were taken unchanged, and the text was rephrased and adapted for fitting into the thesis. The author has performed the three-dimensional PIC simulations and provided our collaborators with the data necessary for post-processing. Our three-dimensional PIC simulations were used by our colleagues for comparison and validation of their two-dimensional simulation results.

Chapter 10

Ion acceleration in microstructured targets

10.1 Introduction

In the last chapter, we have seen the use of nanowire arrays as a means to enhance hot electron production and hence proton acceleration thanks to the structuring of the target. The main acceleration method there is the TNSA (see subchapter 2.3.2). In subchapter 2.3.3 it was described that for thinner foils and/or higher laser intensities the RPA mechanism becomes significant. In this chapter, we see, to the best of our knowledge, the results for the first detailed study on the combination of an ultrathin ($\sim$ 110 nm) and tailored target, benefiting from both acceleration schemes mentioned above. Our colleagues at the Heinrich-Heine-University in Düsseldorf have conducted an experiment in which the targets are irradiated by a linearly polarized femtosecond laser pulse at an intensity of $1\times10^{20}\,\mathrm{W\,cm^{-2}}$. We have performed numerical PIC simulations at the conditions of the experiment to model the experimentally measured results. Enhanced proton acceleration compared to the classical TNSA scheme is obtained, and going towards higher intensities with a further simulation, the transition into the hybrid regime of TNSA and RPA is observed. Our PIC simulations predict a maximum proton energy of about 70 MeV by using 18 J of laser energy. From simulations for different laser intensities we evaluate an energy scaling $E_{\text{cut-off}} \propto I_0^{0.73}$, which represents an improvement with regard to the classical TNSA and lies in the expected range for the hybrid regime between $\propto I_0^{0.5}$ and $\propto I_0$ [118].

In a recent study on µm-thick microcone targets irradiated with 80 J of laser energy, 67.5 MeV protons were measured, which was a record energy at the time of its publication in 2011 [250]. The report reveals a mechanism in which additional electrons extracted from the target front side are supplied to the hot electron population on the rear side, which was called direct laser light pressure acceleration (DLLPA). This is a phenomenon, that was not included in the regular TNSA scheme and represents an improvement. In this chapter, we perform a detailed investigation of the amplification of the longitudinal accelerating electric field and the influence of the laser polarization. The DLLPA scheme in combination with ultrathin tailored targets shows to reliably enhance ion energies over a wide range of intensities. The results suggest that smaller laser systems can benefit from this method as it indicates an enabled access to ion energies as high as those produced by larger laser facilities while reducing the necessary laser input energies. This, for instance, is of particular importance for hadron therapy (see section 2.3.4) that requires small and cost-effective lasers with sufficiently high repetition rates for practicability.

This chapter is structured as follows. First, the experimental setup and results of our partners will be presented in part 10.2, followed by our numerical modeling by PIC simulations in section 10.3 and a concluding summary in subchapter 10.4.

10.2 Experimental setup and results

The experiment was carried out by our collaborators at the Heinrich-Heine-University in Düsseldorf at the ARCTURUS 200-TW laser system, which is based on a double CPA Ti:sapphire architecture with a pulse duration of 30 fs and a pulse energy of up to 7 J before compression. The initial laser contrast, which is better than 1:10^{-8} at 80 ps before the main pulse, is further enhanced by another three orders of magnitude using a single plasma mirror based on the design of Ref. [251]. The experimental arrangement is shown in Fig. 10.1. The 100 mm diameter beam was focused by an $f/2$ off-axis parabolic mirror (OAP) under normal incidence onto the target. A freestanding parylene-foil (C_8H_8) with a thickness of d = 110 nm imprinted with a pattern of spherical hollow half shells (hemispheres) of same thickness (Fig. 10.1 inset) was used. Those shells were measured to have a diameter of D = (8.8±1.2) µm, separated by a center-to-center distance of 35 µm from each other.

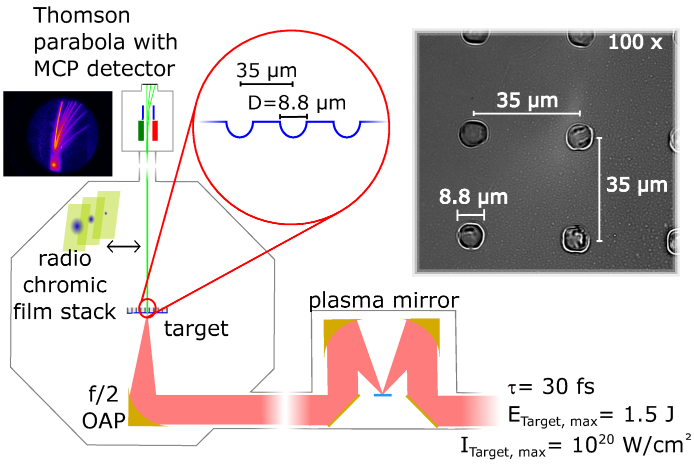

Figure 10.1: The experimental setup is shown. The contrast of the laser pulse is improved by a plasma mirror before it impinges onto the target under normal incidence. As diagnostic a Thomson parabola spectrometer equipped with an MCP readout system for energy measurements, or alternatively a stack of radiochromic films for reconstruction of the spatial beam profile, is used. (Inset picture) Microscope image of the 110 nm-thick free-standing target used for the experiment. The homogeneous pattern of the hemispheres is visible. *(Source: [84], see summary 10.4 below for details.)*

The laser beam was focused to a diameter of 7 µm (FWHM), corresponding to a focal spot size of 40 µm^2. The on-target energy of 1.3 J gives an intensity of $1{\times}10^{20}\,\mathrm{W\,cm^{-2}}$, equivalent to a normalized vector potential of a_0 = 6.8. The target was positioned and verified to be in focus before each shot. Note that the pointing stability of the laser system was measured to be (2.1±3.1) µm over 30 minutes. Aligning always onto the center of the hemisphere and taking the focus diameter as well as the pointing-stability into account it can be assumed that the structure was fully or at least partially irradiated on every shot.

Our collaborators measured the energy spectra by a Thomson parabola spectrometer in forward direction (Fig. 10.2), for which a cross-calibration with CR-39 nuclear track detector was done to provide the absolute proton flux [252]. A typical energy resolution of about 10 % is retrieved taking the pinhole size into account.

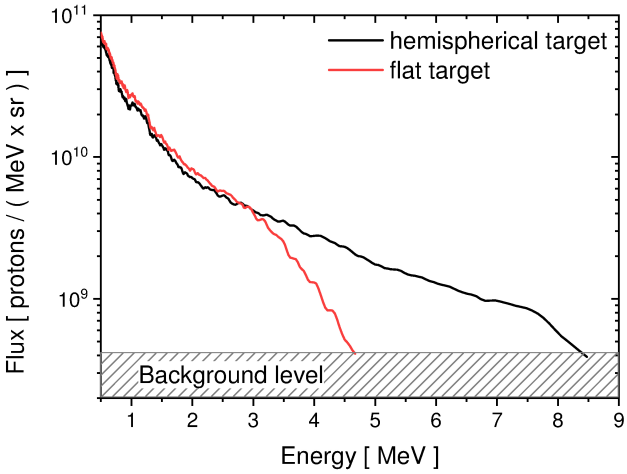

Figure 10.2: Proton energy spectra recorded by a Thomson parabola in laser forward direction for $a_0 = 6.8$. *(Source: [84], see summary 10.4 below for details.)*

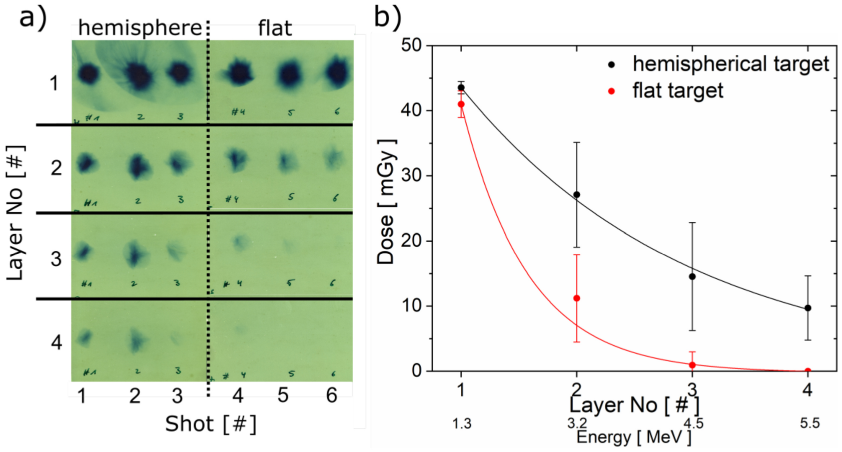

Figure 10.3: a) Raw image of a four-layer RCF stack for three shots each recorded on hemispherical- and flat targets. b) Evaluated dose, depending on the layer number/energy for these two cases. *(Source: [84], see summary 10.4 below for details.)*

For the flat foil a proton cut-off energy of 4.6 MeV was achieved, while with the same laser parameters impinging on the hemispherical structures an energy of 8.5 MeV was measured. This corresponds to an energy gain by a factor of 1.8 by the hemispherical target. Figure 10.3(a) shows the raw image of three consecutive laser shots on the hemispherical structures and three consecutive shots on the flat target positions in between, recorded by a radiochromic film (RCF). The evaluation of the absolute dose is given in Fig. 10.3(b), using a cross-calibration of the particular RCF batch done at a cyclotron. The measured dose reveals significantly more high energetic protons from the hemispherical target compared to the flat target. This finding is in agreement with the energy spectra obtained by the Thomson parabola in Fig. 10.2 for both targets.

10.3 Simulation results and discussion

To investigate the cause of the energy gain by the tailored targets, we carried out numerical three-dimensional PIC simulations at the conditions of the experiment. The laser pulse of $\lambda = 800\,\mathrm{nm}$ wavelength was modeled as a focused pulse with a focal spot of $7\,\mathrm{\mu m}$ diameter (FWHM) for the normalized laser amplitudes of $a_0 = 6.8, 21.6$ (corresponding to $I = 1 \times 10^{20}\,\mathrm{W\,cm^{-2}}$, $1 \times 10^{21}\,\mathrm{W\,cm^{-2}}$) and as a plane wave for $a_0 = 3.1$ (corresponding to $I = 2 \times 10^{19}\,\mathrm{W\,cm^{-2}}$). The temporal profile is a Gaussian function. For the size $x \times y \times z$ of the simulation box the measures $x = 12.1\,\mathrm{\mu m}$ and $y = z = 24\,\mathrm{\mu m}$ (plane wave) or $27.2\,\mathrm{\mu m}$ (focused pulse) and grid steps $\Delta x = 9.2\,\mathrm{nm}$ and $\Delta y = \Delta z = 72\,\mathrm{nm}$ were used. In case of the simulations with a shifted laser pulse (see below) we increased the lateral size $y = z$ to $36\,\mathrm{\mu m}$ to fit the pulse into the box. In the high intensity case $a_0 = 21.6$ the grid steps were $\Delta x = 7.4\,\mathrm{nm}$, $\Delta y = \Delta z = 79.6\,\mathrm{nm}$ and the longitudinal size x was increased to $20.1\,\mathrm{\mu m}$ to have enough space for acceleration. The simulation time was 150 laser cycles, corresponding to 400 fs, with a time step of $\Delta t = 0.016\,\mathrm{fs}$. The target with ion number density $\mathrm{n_C}$:$\mathrm{n_H}$=8:8, similar to the parylene target used in the experiment, was assumed to be not pre-ionized at a density of $\mathrm{n_{C_8H_8}} = 6.4 \times 10^{21}\,\mathrm{cm^{-3}}$. We placed a 110 nm thick layer, either a flat target or a hemisphere (with radius $R = 4.4\,\mathrm{\mu m}$) surrounded by a flat area, in the box and irradiated it by the laser pulse at normal incidence from the convex side of the shell.

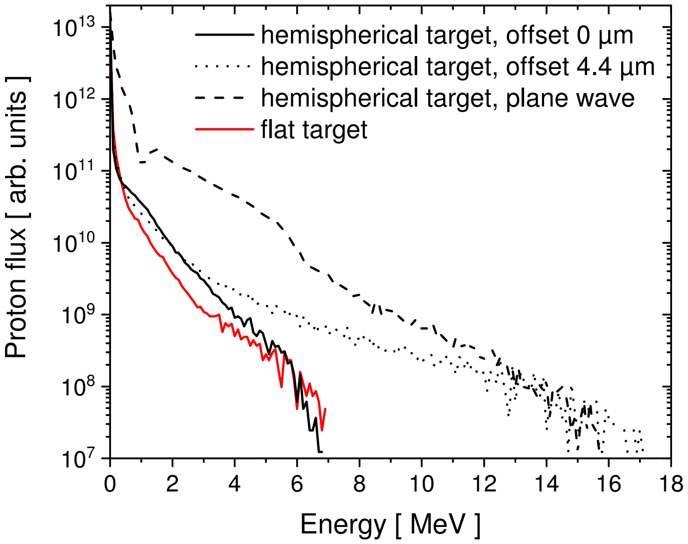

Figure 10.4: Integrated proton spectra for a flat (red line) and a hemispherical target (black line) at $a_0 = 6.8$, for different irradiation positions relative to the center of the hemispherical structure obtained from the simulation. All spectra show a TNSA-like particle distribution. The cut-off energy is enhanced by the structured target up to a factor of up to 2.1 compared to a flat foil. *(Source: [84], see summary 10.4 below for details.)*

To obtain the numerical time-integrated energy spectra of the protons (Figs. 10.4 and 10.9), we summed up all particles that move away from the back of the foil, whereby information on particles leaving the simulation box were also taken into account. Modeling the experimental conditions at an intensity of $1 \times 10^{20}\,\mathrm{W\,cm^{-2}}$ ($a_0 = 6.8$) yields an achieved cut-off energy with the flat target of about 7.0 MeV (Fig. 10.4). We conducted three simulations for the hemispherical target. The first, with the focused pulse hitting the center of the hemisphere, another one for which the focus is shifted by the hemisphere radius of 4.4 µm in polarization direction y, hitting the edge of the hemisphere, and a third one with a plane wave (Fig. 10.4). It turns out that the irradiation position plays an important role as the focal spot diameter (7 µm) is comparable to the hemisphere diameter (8.8 µm). While the on-axis pulse does not yield higher energies compared to the flat target, one finds proton energies of 15-17 MeV for the case of a shifted pulse and a plane wave, which denotes an energy enhancement factor larger than 2.1 for the hemispherical target compared to the flat foil. Note that the plane wave gives rise to a higher number of particles along the lower energy range, owed to the TNSA taking place across the whole target, in contrast to the irradiation of a finite area as in the case of a focussed pulse. From these special cases, it can be deduced that cut-off energies between 7 MeV and 15 MeV are expected in the experiment.

As experiment and numerical simulations point out, there is an increase in the maximum particle energy, visible as an elongation of the tail above the cut-off energy of the flat target. This is an indication that a part of the protons gain more energy in the case of a hemispherical target. It remains to be clarified what the cause is and where those protons originate from. For a further investigation we filtered out the trajectories and energies of protons with > 7.5 MeV (hemispherical target) and > 2 MeV (flat target) of all particles recorded during the full simulation in order to identify where exactly they stem from. For the sake of simplification, we chose the plane wave simulation for the hemispherical target in all following illustrations, as the physics of the results do not differ from the focussed pulse case. Figure 10.5 shows a projection of those trails, while the color encodes the particle energy.

For the flat target [Fig. 10.5(a)], the particles move normal to the surface and parallel to each other, with a homogeneous energy gain distributed over the laser focal spot. In the case of the hemispherical target [Fig. 10.5(b)] the particles that have a higher energy than in the flat target case (compare in Fig. 10.4) are depicted. They mainly stem from an about 5 µm wide flat foil area at the sides of the hemisphere along the laser polarization direction and move normal to the target. The reason behind this observation implies two modifications to the classical TNSA acceleration scheme and the evolution of the electron sheath field.

First, the void in the foil given by the implemented hemisphere alters the motion of the accelerated electrons at the rear side of the target. Due to the lack of positively charged ions in that gap the electrons are radially pulled in the outward direction and thereby dragged back by the ions of the surrounding flat foil. In this process, they form arc-like structures in the electric field E_x normal to the target around the $z = 0$ plane [Fig. 10.6(a)]. Note that the linear polarization of the pulse points in y direction. These structures are superimposed to the classical TNSA sheath field, which is the only component present in the perpendicular plane [Fig. 10.6(b)] and is generated by the electron space charge. The electric field strength is more pronounced in the $y - x$ plane at the edges [Figs. 10.6(a) and 10.6(c)]. The transverse cross section of the electric field at a distance of $0.5\,\lambda$ behind the foil [Fig. 10.6(c)] reveals the same pattern as the configuration of the trajectory origins in Fig. 10.5(b).

Secondly, there are additional electrons directly extracted out of the hemisphere by the laser electric field. Once they move freely in vacuum, they are pushed forward and through the foil by the $\vec{v}\times\vec{B}$ force, which becomes substantial for relativistic intensities, as their momenta scale like $\sim a_0^2$ compared to the transverse direction, which scale like $\sim a_0$ (see subchapter 2.1.3). This effect of the so-called direct laser light pressure acceleration was observed by *Gaillard et al.* before [250] for µm-thick targets, in the regime of classical TNSA.

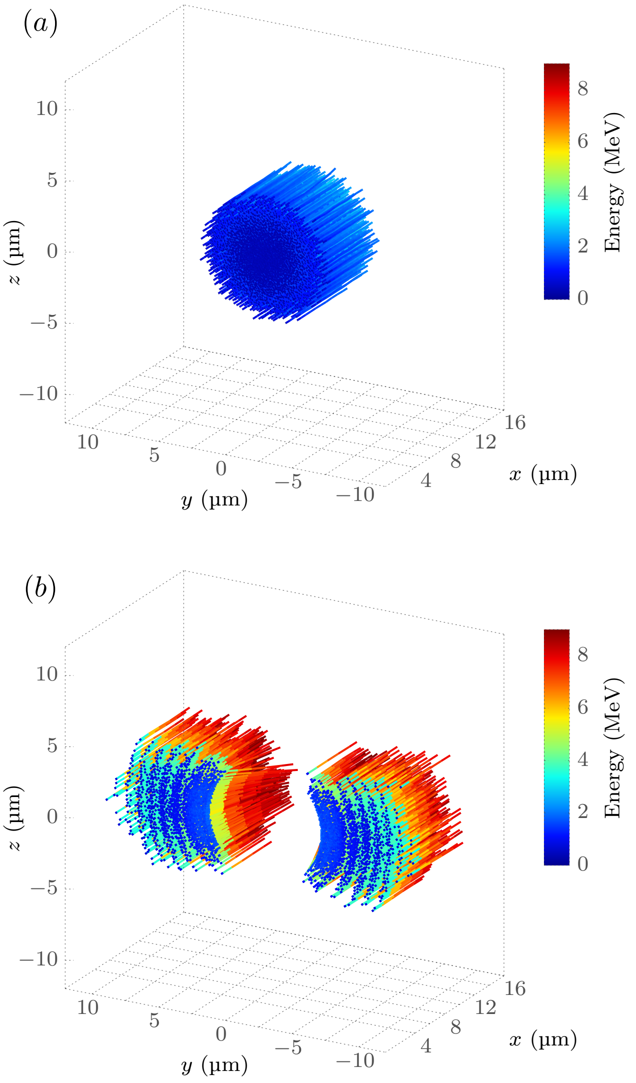

Figure 10.5: (a) Trajectories of the protons that reach energies of at least 2.0 MeV, using a focused laser pulse with an intensity of $a_0 = 6.8$ and a focal spot of 7 µm at FWHM irradiating a flat C_8H_8 foil of $d = 110$ nm thickness. (b) Trajectories of protons reaching at least 7.5 MeV, using a plane wave with $a_0 = 6.8$ irradiating a C_8H_8 foil of $d = 110$ nm thickness with a hemispherical hollow shell of 8.8 µm diameter. The laser pulse in (a) and (b) has a wavelength of $\lambda = 800$ nm, pulse duration of $t_L = 35$ fs and enters the simulation box at $x = 0$. *(Source: [84], see summary 10.4 below for details.)*

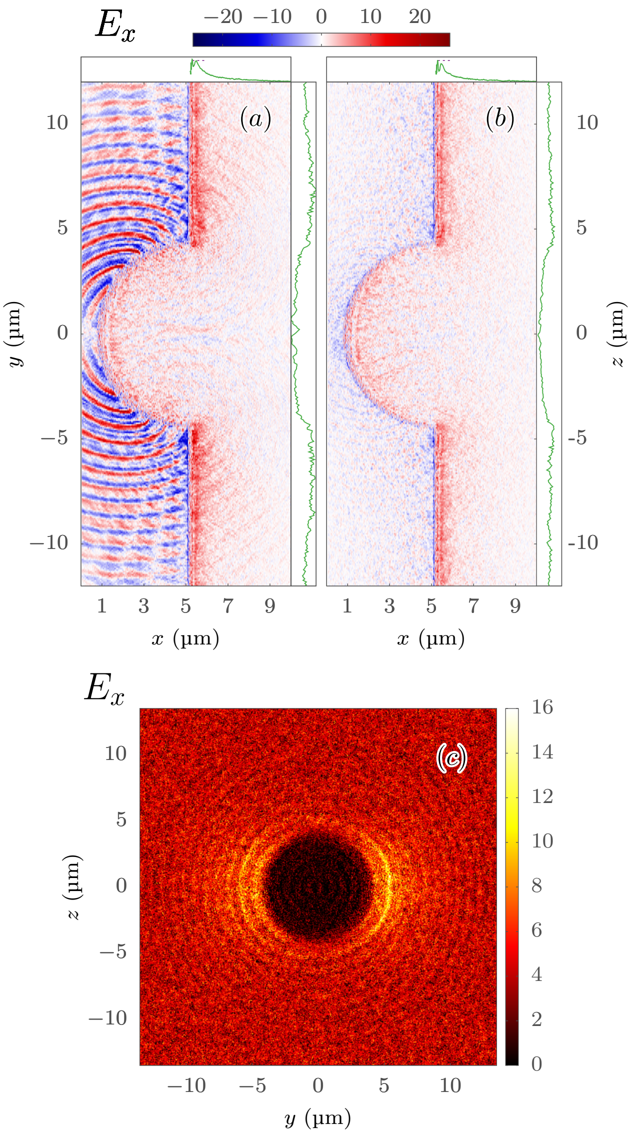

Figure 10.6: Cross sections of the electric field component E_x [TV/m] normal to the surface in (a) the plane of polarization $(y-x)$, (b) perpendicular to it $(z-x)$ and (c) in the transverse plane ($z-y$, at $x = 0.5\,\lambda = 0.4\,\mu\text{m}$ behind the foil) at $t = 7.6T_0 = 20.3\,\text{fs}$ after the peak of the laser pulse reached the tip of the target. The electric field responsible for the TNSA mechanism is that generated by the electron sheath at the rear of the foil at $x > 5.3\,\mu\text{m}$ (a) and (b), whereas the field structure in front of the target generated by plasma currents is of minor importance for the proton acceleration. The one-dimensional graphs (green) illustrate the average of the electric field E_x in the range $x \in [5.2, 10]\,\mu\text{m}$, computed along the y or z direction (graphs at top) or along the x direction (graphs at the side), where the corresponding graphs in (a) and (b) have the same scales. The rings of the sideways pattern in (c) have a thickness of $\approx \lambda$. The simulation parameters are the same like in Fig. 10.5(b). *(Source: [84], see summary 10.4 below for details.)*

Depending on the surface conductivity, the incoming pulse will be reflected, resulting in a modulated electromagnetic field responsible for the forward motion of the electrons in the locally longitudinal electric field [253]. Taking a closer look into the extraction process of those electrons, we see a strong dependence on the laser polarization direction. In the y-direction – which is the direction of the laser electric field – the electron current density component normal to the target j_x in the corresponding $y-x$ plane is significant [Fig. 10.7(a)], while nonexistent in the perpendicular $z-x$ plane [Fig. 10.7(b)]. This can be understood envisioning the projections of the hemisphere.

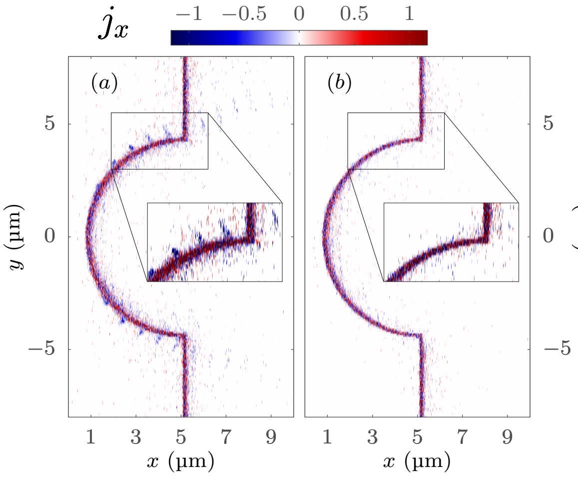

Figure 10.7: Lateral cross section of the current density component j_x [MA/µm^2] normal to the surface in (a) the plane of polarization $(y-x)$ and (b) perpendicular to it $(z-x)$ at $t = 7.6T_0 = 20.3\,\text{fs}$ after the peak of the laser pulse reached the tip of the target. The magnified inset (a) reveals electron bunches of distance $\approx \lambda$ drawn out of the target, which do not exist in (b). The simulation parameters are the same like in Fig. 10.5(b). *(Source: [84], see summary 10.4 below for details.)*

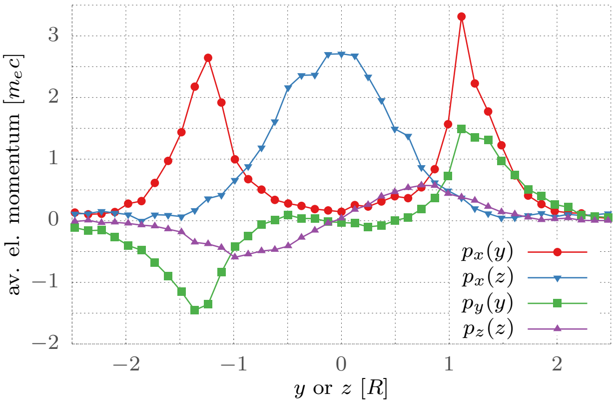

Figure 10.8: Averaged electron momenta over the transverse direction y or z in units of the hemisphere radius $R = D/2 = 4.4\,\text{µm}$. The time is $t = 6.6\,T_0 = 17.6\,\text{fs}$ after the laser pulse impinges on the target. In longitudinal direction (x), only electrons at least $0.5\,\lambda = 0.4\,\text{µm}$ behind the foil were taken into account to filter out the offset created by the electron sheath at the back of the foil [see Fig. 10.6(a) and 10.6(b)]. In the transverse direction (y or z) the momenta were averaged along the direction perpendicular to the regarded coordinate. The simulation parameters are the same like in Fig. 10.5(b). *(Source: [84], see summary 10.4 below for details.)*

It is much easier to extract electrons in the direction normal to the ultrathin target, which is the case along the y axis, compared to the parallel extraction which would be the case along the z axis. The blue bunches, separated by distances of $\approx \lambda$, indicate forward moving electron packs outside of the target. These occur periodically at the edges between the shell and the surrounding foil and move through the target to the rear side where they contribute to a higher electron density. Consequently, the electric field E_x has its maximum at these specific regions and exhibits concentric rings of thickness $\approx \lambda$ [Figs. 10.6(a) and 10.6(c)] due to the cyclical electron bunch generation and transportation by the laser pulse.

A further proof of the above presented theory is the analysis of the phase space of the electrons from the hemispherical target (Fig. 10.8). The electrons situated behind the target solely due to heating would have a symmetric outward directed momentum $p(r)$ as described by the point-symmetric purple curve $p_z(z)$, giving evidence that electrons have zero transverse momentum in the center and the strongest momentum at the edge ($r = R = D/2$, where R is the shell radius). The momentum in polarization direction $p_y(y)$ (green curve) is point-symmetric as well, however it is essentially zero for $|y| < R$. It has higher maxima, which lie slightly outside at $\approx 1.25\,R$. This can be attributed to the above-mentioned effect, that electrons are radially pulled out of the hemispherical part of the target at which the electric field vector $\vec{E}$ of the pulse has a component normal to the surface. The forward momentum $p_x(y)$ has its peaks at the same positions $\approx \pm 1.25R$ (red curve), whereas in the perpendicular view $p_x(z)$ the peak of same magnitude is at the center $z = 0$ (blue curve). This describes the currents that are strongest at the edges of the hemisphere in the $y - x$ plane and become weaker for $|z| > 0$ (Fig. 10.7), as the component of $\vec{E}$ normal to the surface becomes smaller.

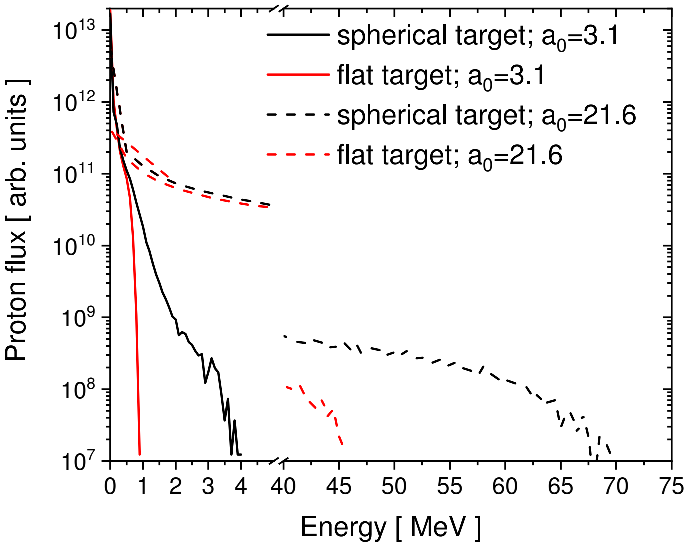

Figure 10.9: Computed proton spectra for intensities $2 \times 10^{19}\,\mathrm{W\,cm^{-2}}$ ($a_0 = 3.1$) and $1 \times 10^{21}\,\mathrm{W\,cm^{-2}}$ ($a_0 = 21.6$) as an extrapolation from the experimental parameters. *(Source: [84], see summary 10.4 below for details.)*

In order to further study the intensity dependence over a wider range, were carried out additional simulations for irradiation intensities of $2 \times 10^{19}\,\mathrm{W\,cm^{-2}}$ ($a_0 = 3.1$) and $1 \times 10^{21}\,\mathrm{W\,cm^{-2}}$ ($a_0 = 21.6$), as shown in Fig. 10.9. The obtained proton energies are 1 MeV (flat target) and 4 MeV (hemispherical target) in the low intensity case for a plane wave and 46 MeV (flat target) and 70 MeV (hemispherical target) in the high intensity case for a focused laser beam 4.4 µm off-center of the hemisphere. Both simulations imply an increased energy in the case of the hemispherical target by a factor of 3.5 at the lower intensity and 1.5 at the higher intensity. A closer look into the particle trajectories reveals that the DLLPA mechanism supports the acceleration process at both additionaly studied intensities and can therefore be attributed as the driving mechanism over at least two orders of magnitude in intensity. The results for the three different intensities can be used for a rough intensity scaling, as shown in Fig. 10.10. From the three data points it can be deduced that the proton cut-off energy scales with $E_{\text{cut-off}} \propto I_0^{0.73}$. The red point marks the experimentally obtained energy.

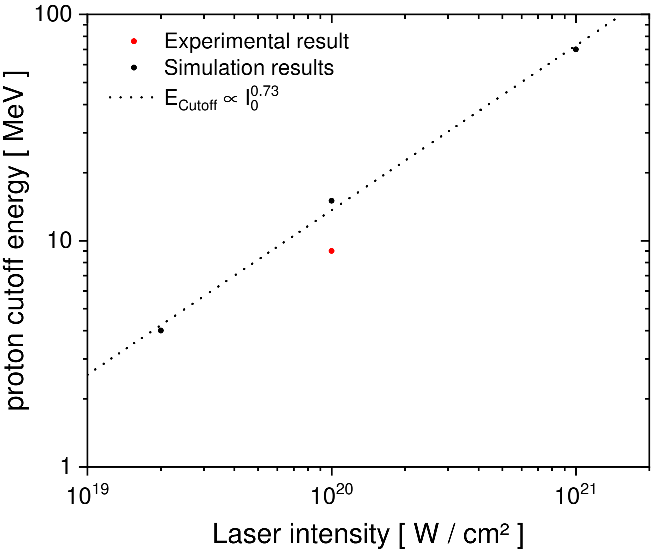

Figure 10.10: Scaling of the maximum proton energy as a function of the laser intensity: Simulation results and a fit yielding a $\propto I_0^{0.73}$ scaling. *(Source: [84], see summary 10.4 below for details.)*

Comparing this finding to the intensity scaling of TNSA with $E_{\text{cut-off;TNSA}} \propto I_0^{0.5}$ and the scaling of RPA with $E_{\text{cut-off;RPA}} \propto I_0$ [118], we find ourselves in a hybrid regime, which was observed by other groups before, e.g. *Higginson et al.* holding the current energy record of about 94 MeV protons [119]. While TNSA is still the driving mechanism, boosted by the additional electrons of the DLPPA process, an onset of a collective mechanism like the RPA regime is observed. However, RPA does not become the dominant mechanism, even for the highest intensities. This is due to the use of linear polarized light, which causes heating of the electrons and therefore favours the TNSA scheme (see subchapter 2.3.3). In fact, in the simulation at a foil thickness of 110 nm the target is found to explode due to the interaction with the laser, which is likely due to the violent removal of the electrons by the linearly polarized field. On the one hand, this limits the collective acceleration effects and on the other hand removes the electrons necessary for building up the sheath field for TNSA. Redoing the simulations for thicker targets reveals a suppression of a direct explosion but at the same time, a decrease in the maximum proton energy since the target becomes too thick for the collective acceleration and weakens the TNSA mechanism [120].

To classify the benefit of the tailored ultrathin targets we calculate the maximum proton energy per Joule of laser energy as done in [250]. Compared to their measurement achieving 0.82 MeV/J and the measurements of *Higginson et al.* with 0.42 MeV/J, we obtained a value of 6.5 MeV/J experimentally. For the simulations the comparable energy gain was 11.5 MeV/J for a_0=3.1, 13.5 MeV/J for a_0=6.2 and 5.4 MeV/J for a_0=21.6.

It remains the question of the optimal target geometry. The fundamental requirement for this process is that a part of the target structure needs to be parallel to the laser direction and perpendicular to the electric field vector, for example realizable by elongated structures like ellipsoids, cuboids or wires. At the same time, the electric field on those structures needs to be sufficiently high to be able to extract and accelerate the additional electrons. Therefore, structures on the order of the laser focal diameter or smaller are advisable. The targets used in this study have a center-to-center distance so high that the electrons extracted from the shell-structures do not significantly interfere with the neighboring hemispheres or prevent the laser pulse from propagating down to the bottom of the target. In the case of micro- [10] and nanowires [23] (see also previous chapter 9) it was shown that for higher density of the wires the surrounding gaps fill with plasma. Depending on the extent of the filling, either this can aid the absorption of laser light into hot electrons or it leads to reflection of the incoming laser pulse if a critical density layer has formed. It might therefore be beneficial for the TNSA part of acceleration to engineer the filling factor in a way to additionally profit from a filling within the vacancies of the target. While for the sake of studying the isolated effect of the tailored structure a large separation between the hemispheres was chosen, this distance can be minimized in further applications, allowing an easier experimental alignment of the target without the need of adjusting it onto a specific single structure.

10.4 Summary

In this chapter, the benefit in energy gain by using ultrathin hemispherical targets compared to flat targets was demonstrated. An energy increase by a factor of 1.8 was measured experimentally by our collaborators. By means of numerical PIC simulations, we could identify this increase as protons originating from an area of about 5 µm from the flat part of the target around the hemisphere. It turns out that additional electrons extracted out of the hemisphere, which are pushed through the target by the laser pulse enhance the accelerating sheath field at the rear side of the target. This leads to an increased maximum energy of the protons. While before, this effect of DLPPA was only observed at high-energy lasers for µm-thick targets, an energy gain with only 1.3 J of laser energy, which corresponds to a maximum proton energy to input laser energy ratio of 6.5 MeV/J was experimentally achieved in the present work. It was shown in simulations that by a simple target geometry DLPPA can be scaled over a wide intensity range achievable at many of today's already existing laser systems. This wide range scalability of the process holds promise for many applications since it can be universally applied, making it a potent candidate for hadron therapy, as a driver for fast ignition in inertial confinement fusion or for probing magnetic and electric fields with high spatiotemporal resolution.

The results presented in this chapter are submitted to [84]. The figures were taken unchanged and the text was adopted literally with adaptations for fitting into the thesis. After submission of the thesis, the publication was accepted and published in [24]. The author has conducted the PIC simulations, analyzed and interpreted the numerical data. Figures 10.5, 10.6, 10.7 and 10.8 were created by the author, and the data for Figs. 10.4, 10.9 and 10.10 was computed and provided by the author. Furthermore, the author has written the major part of the published manuscript to which co-authors have contributed.

Chapter 11

Summary and Outlook

The present thesis dealt with nanowire-covered targets in order to explore the advantages that can be exploited due to their highly light-absorptive nature. Specifically with regard to the generation of high energy densities they draw attention and open the path to fundamental studies. A summary of the results obtained in the course of this work is given in section 11.1, followed by concluding thoughts about their relevance in the context of the research field and an outlook in section 11.2. All experiments were conducted by our collaborative groups. The three-dimensional PIC simulations were all conducted by the author. In chapters 4 and 10 the evaluation and interpretation of the numerical data were carried out by the author.

11.1 Summary

After the theoretical framework relevant for the thesis was introduced in chapter 2, chapter 3 dealt with the PIC method as the technique used in the following chapters.

First, simulation results were shown in which the process of ionization and the ability to produce a self-generated Z-pinch were described (see chapter 4). It turns out that carbon nanowires are basically fully ionized in a few laser cycles when irradiated with relativistic laser pulses. Circular polarization was found to be slightly more effective than linear polarization. After the formation of a plasma due to the ionization, the laser extracts electrons out of the nanowires giving rise to a strong return current within the wires and subsequently to the generation of an azimuthal magnetic field. The associated radially inward directed $\vec{j} \times \vec{B}$ force effectively compresses the nanowires to a fraction of their initial radius. As a result, extreme particle densities exceeding 1000 critical densities and energy densities of some $\mathrm{TJ\,cm^{-3}}$ are created. The Z-pinch was shown to be a relativistic effect and proved to be stronger at higher irradiation intensities.

Next, the question of the heating depth in the nanowires was tackled by using two-component nanowires (chapter 5). A numerical model was used, consisting of our PIC simulations and subsequent computation of synthetic emission spectra of the characteristic radiation from the two different materials by our collaborators at the Colorado State University. Varying the length of the top section allowed to determine the heat penetration depth by monitoring the decreasing signal of the tracer material. The numerical model was first validated by experimental results of our partners, showing a penetration depth of several micrometers, and then extrapolated to higher laser intensities to predict energy densities on the $\mathrm{TJ\,cm^{-3}}$ scale.

Chapter 6 dealt with the question of conversion efficiency of laser light into x-ray pulses in the nanowire targets. The approach was to achieve a radiation cooling time shorter than the hydrodynamic cooling time to enter the radiation loss dominated regime. Our PIC simulations and hydrodynamic and atomic kinetic computations of our partners at the Colorado State University pointed out a much larger heated volume of high density material in the nanowires compared to flat targets, which is a key requirement for enhanced conversion into x-rays. The radiation cooling times were found to be shorter than the hydrodynamic cooling times in the nanowire arrays in contrast to the flat targets. The x-ray emission coming out of nickel and gold nanowires was experimentally measured by our colleagues at various diameters and different angles. A record conversion efficiency to x-rays of $> 1\,\mathrm{keV}$ energy of above $20\,\%$ in $4\pi\,\mathrm{sr}$ was registered by them in 80 nm gold nanowires.

Furthermore, nanowires containing deuterium were deployed to investigate the potential presence of neutrons produced in fusion reactions due to efficient heating (chapter 7). To this end, our collaborators at the Colorado State University mounted neutron detectors at certain distances to irradiated nanowires. Their evaluation of the recorded data showed the arrival of neutrons at the expected times for 2.45 MeV neutrons. Our partners found the integrated neutron signal from nanowires to be 500 times larger than in flat targets at the same irradiation conditions. Furthermore, 3.6×10^6 neutrons were detected by our colleagues using a laser pulse of 1.64 J energy in the best experimentally measured shot, corresponding to 2.2×10^6 neutrons per joule. We performed PIC simulations to model the experimental findings, which describe that the volumetrically heated nanowires explode and accelerate deuterium ions to 3 MeV, near the peak of the fusion cross sections. Our simulations for higher irradiation intensities predict a shift of the deuterons to higher energies, promising a greater neutron yield.

An alternative approach to enter the relativistic laser-plasma regime by using a mid-infrared laser with a larger wavelength of 3.9µm was presented in chapter 8. It allowed for using lower laser intensities, which reduces the formation of disruptive preplasmas. The results of our PIC simulations, which were in a good agreement with experimental measurements of our partners in Jena, obtained a high absorption of about 80 % of the laser light, leading to long-lasting plasmas of keV-temperature with highly charged ions.

The question about the influence of the nanowire structure parameters on enhanced ion acceleration was approached in chapter 9. We performed three-dimensional PIC simulations that were used by our colleagues at the University of Michigan and the Colorado State University to validate their two-dimensional PIC calculations. These were used to model the experimental findings of our partners in Michigan. The proton energies were measured by them experimentally for nanowires of different lengths, diameters, distances and their corresponding two-dimensional PIC simulations confirmed the obtained trends. It turned out that the number of nanowires per focal spot was the leading parameter that determined a more efficient interaction with the laser field for a value between one and two.

In chapter 10, it was demonstrated that also a different kind of target consisting of ultrathin foils with stamped hemispherical shells could advance ion acceleration in comparison with ordinary flat foils. Our numerical PIC simulations have reproduced the trend found in experimental measurements of our colleagues at the Heinrich-Heine-University in Düsseldorf. Experimentally, proton energies were found to be increased by a factor of 1.8 compared to flat foils. Our simulations revealed additionally drawn electrons that amplify the accelerating electric field to be responsible for increased proton energies. We performed a simulation at higher laser intensity, which estimated the achievable proton energies to be comparable to those produced in larger laser systems, by only using joule-class tabletop lasers.

11.2 Outlook

The cornerstone for the research topic in the present thesis was recently set by Purvis *et al.* [5] that demonstrated for the first time the accessibility of volumetric dense heating in nanowire structures. This raised the question of how this outcome could be leveraged and hence, the goal of this thesis was to research the strengths of nanowires in certain fundamental aspects and applications.

The common denominator of the presented results is to use structured targets to capitalize on two points. First, the structured targets open the path to a regime that was unaccessible before. For instance, the energy density in the core of the sun is exceeded by more than a factor of approximately 100 in the nanoscale Z-pinch. Then, the conversion efficiency to x-ray emission and the yield of fusion neutrons was improved in both cases by more than one order of magnitude compared to previous works. Second, the requirements for creation of desired effects is lowered. The use of midinfrared lasers allowed for generation of plasmas with keV-temperatures by applying laser pulses of only 20 mJ, as opposed to the joule-level pulses used in the preceding works. Next, the use of thin and shaped foils irradiated with only joule-level tabletop laser pulses showed to be capable of generating proton energies comparable to those created in large laser facilities.

The relevance of these results becomes apparent in the record values that could be accomplished and also in the acceptance of publication in high-impact journals due to its contribution to the field. Moreover, there is an increasing interest in this topic that expresses itself also during conferences and meetings. The theoretical prediction of the nanoscale pinch effect for instance attracted the interest of experimental groups that consider its verification and lead to one numerical publication based on it. There is a demand for collaborations and numerical simulations from several groups, which could not all be reacted to. This underlines the interest in this subject and the crucial importance of numerical simulations, without whom experimental findings can sometimes be a mysterious puzzle. The contribution of the author in the projects described above was to appropriately model given experimental conditions with PIC simulations, to analyze the data and interpret the results. This enabled an understanding of the physical processes in both experimental and theoretical studies.

Based on the results of this thesis, one possible future step is to find a signature of the nanoscale pinch that can be identified in experimental measurements to help its verification. In this regard, a close cooperation with experimental groups would be advisable. Furthermore, a better comparison with experimental results may require the computation on timescales longer than feasible in PIC simulations. This situation was encountered during the joint work with experimental groups. For this purpose, subsequent hydrodynamic simulations based on the output of PIC results may be worth a consideration. Additionally, an analytical model for the nanowire-laser interaction is yet to be established. It would provide a better understanding of the absorption mechanisms and could lead to new concepts for improvements and applications.

Finally, the current and foreseeable progress in 3D printing technology, in manufacturing of nanostructures, and in laser technology can be assumed to keep alive or even strengthen interest in laser-irradiated nanowire arrays. The greater precision of those targets as well as cleaner laser pulses will allow to approach the ideal conditions supposed in theoretical models, create further diagnostic options (by for example using sophisticated spatially resolved multi-component targets) and a better yield in applications. Upcoming large research facilities and improved measurement techniques with higher resolution will facilitate to prove theoretically predicted effects and investigate new phenomena in the relativistic regime. In summary, this young and fruitful research field has a lot of interesting physics to offer and is therefore expected to contribute new insights for at least a certain period of time in the near future.

References

[1] J. Nuckolls, L. Wood, A. Thiessen, and G. Zimmerman. *Laser Compression of Matter to Super-High Densities: Thermonuclear (CTR) Applications.* Nature 239(5368), 139–142 (1972).

[2] D. Strickland and G. Mourou. *Compression of amplified chirped optical pulses.* Optics Communications 56(3), 219 – 221 (1985).

[3] The ELI collaboration. *Whitebook.* Report, ELI - Extreme Light Infrastructure (2011).

[4] National Research Council. *Frontiers in High Energy Density Physics: The X-Games of Contemporary Science.* The National Academies Press, Washington, DC (2003).

[5] M. A. Purvis, V. N. Shlyaptsev, R. Hollinger, C. Bargsten, A. Pukhov, A. Prieto, Y. Wang, B. M. Luther, L. Yin, S. Wang, and J. J. Rocca. *Relativistic plasma nanophotonics for ultrahigh energy density physics.* Nature Photonics 7, 796–800 (2013).

[6] J. Jeevanandam, A. Barhoum, Y. S. Chan, A. Dufresne, and M. K. Danquah. *Review on nanoparticles and nanostructured materials: history, sources, toxicity and regulations.* Beilstein journal of nanotechnology 9, 1050–1074 (2018).

[7] B. O'Regan and M. Grätzel. *A low-cost, high-efficiency solar cell based on dye-sensitized colloidal TiO2 films.* Nature 353(6346), 737–740 (1991).

[8] C. Alexiou, W. Arnold, P. Hulin, R. Klein, A. Schmidt, C. Bergemannand, and F. G. Parak. *Therapeutic efficacy of ferrofluid bound anticancer agent.* Magnetohydrodynamics 37, 318–322 (2001).

[9] J.-P. Déry, E. F. Borra, and A. M. Ritcey. *Ethylene Glycol Based Ferrofluid for the Fabrication of Magnetically Deformable Liquid Mirrors.* Chemistry of Materials 20(20), 6420–6426 (2008).

[10] D. Khaghani, M. Lobet, B. Borm, L. Burr, F. Gartner, L. Gremillet, L. Movsesyan, O. Rosmej, M. E. Toimil-Molares, F. Wagner, and P. Neumayer. *Enhancing laser-driven proton acceleration by using micro-pillar arrays at high drive energy.* Scientific Reports 7(1), 11366 (2017).

[11] K. Nishikawa and M. Wakatani. *Plasma Physics: Basic Theory with Fusion Applications.* Springer Series on Atomic, Optical, and Plasma Physics. Springer Berlin Heidelberg (2013).

[12] P. Gibbon. *Short Pulse Laser Interactions with Matter.* Published by Imperical College Press and distributed by World Scientific Publishing Co. (2005).

[13] A. Pukhov. *Strong field interaction of laser radiation.* Reports on Progress in Physics 66(1), 47–101 (2002).

[14] R. P. Drake. *High-Energy-Density Physics: Fundamentals, Inertial Fusion, and Experimental Astrophysics.* Springer, Berlin, Heidelberg (2006).

[15] R. P. Drake. *Perspectives on high-energy-density physics.* Physics of Plasmas 16(5), 055501 (2009).

[16] R. C. Davidson, T. Katsouleas, J. Arons, M. Baring, C. Deeney, L. Di Mauro, T. Ditmire, R. Falcone, D. Hammer, W. Hill, B. Jacak, C. Joshi, F. Lamb, R. Lee, B. G. Logan, A. Melissinos, D. Meyerhofer, W. Mori, M. Murnane, B. Remington, R. Rosner, D. Schneider, I. Silvera, J. Stone, B. Wilde, and Z. W. *Frontiers for Discovery in High Energy Density Physics.* Technical report, United States (2004).

[17] V. Kaymak, A. Pukhov, V. N. Shlyaptsev, and J. J. Rocca. *Strong ionisation in carbon nanowires.* Quantum Electronics 46(4), 327–331 (2016).

[18] V. Kaymak, A. Pukhov, V. N. Shlyaptsev, and J. J. Rocca. *Nanoscale Ultradense Z-Pinch Formation from Laser-Irradiated Nanowire Arrays.* Phys. Rev. Lett. 117, 035004 (2016).

[19] C. Bargsten, R. Hollinger, M. G. Capeluto, V. Kaymak, A. Pukhov, S. Wang, A. Rockwood, Y. Wang, D. Keiss, R. Tommasini, R. London, J. Park, M. Busquet, M. Klapisch, V. N. Shlyaptsev, and J. J. Rocca. *Energy penetration into arrays of aligned nanowires irradiated with relativistic intensities: Scaling to terabar pressures.* Science Advances 3(1) (2017).

[20] R. Hollinger, C. Bargsten, V. N. Shlyaptsev, V. Kaymak, A. Pukhov, M. G. Capeluto, S. Wang, A. Rockwood, Y. Wang, A. Townsend, A. Prieto, P. Stockton, A. Curtis, and J. J. Rocca. *Efficient picosecond x-ray pulse generation from plasmas in the radiation dominated regime.* Optica 4(11), 1344–1349 (2017).

[21] A. Curtis, C. Calvi, J. Tinsley, R. Hollinger, V. Kaymak, A. Pukhov, S. Wang, A. Rockwood, Y. Wang, V. N. Shlyaptsev, and J. J. Rocca. *Micro-scale fusion in dense relativistic nanowire array plasmas.* Nature Communications 9(1), 1077 (2018).

[22] Z. Samsonova, S. Höfer, V. Kaymak, S. Ališauskas, V. Shumakova, A. Pugžlys, A. Baltuška, T. Siefke, S. Kroker, A. Pukhov, O. Rosmej, I. Uschmann, C. Spielmann, and D. Kartashov. *Relativistic Interaction of Long-Wavelength Ultrashort Laser Pulses with Nanowires.* Phys. Rev. X 9, 021029 (2019).

[23] M. Dozières, G. M. Petrov, P. Forestier-Colleoni, P. Campbell, K. Krushelnick, A. Maksimchuk, C. McGuffey, V. Kaymak, A. Pukhov, M. G. Capeluto, R. Hollinger, V. N. Shlyaptsev, J. J. Rocca, and F. N. Beg. *Optimization of laser-nanowire target interaction to increase the proton acceleration efficiency.* Plasma Physics and Controlled Fusion 61(6), 065016 (2019).

[24] V. Kaymak, E. Aktan, M. Cerchez, B. Elkin, M. Papenheim, R. Prasad, A. Pukhov, H.-C. Scheer, A.-M. Schroer, O. Willi, and B. Aurand. *Boosted acceleration of protons by tailored ultra-thin foil targets.* Scientific Reports 9(1), 18672 (2019).

[25] J. Bittencourt. *Fundamentals of Plasma Physics*, volume 3 (2004).

[26] A. Peratt. *Physics of the Plasma Universe.* Springer New York (2014).

[27] W. Kruer. *The physics of laser plasma interactions.* Frontiers in physics. Addison-Wesley (1988).

[28] F. Chen. *Introduction to plasma physics.* Plenum Press (1974).

[29] J. Meyer-ter Vehn, A. Pukhov, and Z.-M. Sheng. *Relativistic Laser Plasma Interaction*, pages 167–192. Springer US, Boston, MA (2001).

[30] S. Atzeni. *Introduction to Laser-Plasma Interaction and Its Applications*, pages 119–144. Springer US, Boston, MA (2001).

[31] L. Keldysh. *Ionization in the Field of a Strong Electromagnetic Wave.* Sov. Phys. JETP 20, 1307 (1965).

[32] M. V. Ammosov, N. B. Delone, and K. V. P. *Tunnel ionization of complex atoms and of atomic ions in an alternating electromagnetic field.* Sov. Phys. JETP 64, 1191 (1986).

[33] W. Lotz. *An empirical formula for the electron-impact ionization cross-section.* Zeitschrift für Physik 206(2), 205–211 (1967).

[34] V. Silin. *Nonlinear High-frequency Plasma Conductivity.* Sov. Phys. JETP 20, 1510 (1965).

[35] G. J. Pert. *Inverse bremsstrahlung in strong radiation fields at low temperatures.* Phys. Rev. E 51, 4778–4789 (1995).

[36] F. Brunel. *Not-so-resonant, resonant absorption.* Phys. Rev. Lett. 59, 52–55 (1987).

[37] W. L. Kruer and K. Estabrook. *J×B heating by very intense laser light.* The Physics of Fluids 28(1), 430–432 (1985).

[38] K. Miyamoto. *Plasma Physics and Controlled Nuclear Fusion.* Atomic, Optical, and Plasma Physics. Springer (2005).

[39] D. Giulietti and L. A. Gizzi. *X-ray emission from laser-produced plasmas.* La Rivista del Nuovo Cimento (1978-1999) 21(10), 1–93 (1998).

[40] D. Attwood, A. Sakdinawat, and L. Geniesse. *X-Rays and Extreme Ultraviolet Radiation: Principles and Applications.* Cambridge University Press (2017).

[41] R. Nora, W. Theobald, R. Betti, F. J. Marshall, D. T. Michel, W. Seka, B. Yaakobi, M. Lafon, C. Stoeckl, J. Delettrez, A. A. Solodov, A. Casner, C. Reverdin, X. Ribeyre, A. Vallet, J. Peebles, F. N. Beg, and M. S. Wei. *Gigabar Spherical Shock Generation on the OMEGA Laser.* Phys. Rev. Lett. 114, 045001 (2015).

[42] T. R. Dittrich, O. A. Hurricane, D. A. Callahan, E. L. Dewald, T. Döppner, D. E. Hinkel, L. F. Berzak Hopkins, S. Le Pape, T. Ma, J. L. Milovich, J. C. Moreno, P. K. Patel, H.-S. Park, B. A. Remington, J. D. Salmonson, and J. L. Kline. *Design of a High-Foot High-Adiabat ICF Capsule for the National Ignition Facility.* Phys. Rev. Lett. 112, 055002 (2014).

[43] P. M. Nilson, W. Theobald, J. F. Myatt, C. Stoeckl, M. Storm, J. D. Zuegel, R. Betti, D. D. Meyerhofer, and T. C. Sangster. *Bulk heating of solid-density plasmas during high-intensity-laser plasma interactions.* Phys. Rev. E 79, 016406 (2009).

[44] D. Hoarty, S. James, C. Brown, B. Williams, H. Chung, J. Harris, L. Upcraft, B. Crowley, C. Smith, and R. Lee. *Measurements of emission spectra from hot, dense germanium plasma in short pulse laser experiments.* High Energy Density Physics 6(1), 105 – 108 (2010).

[45] C. R. D. Brown, D. J. Hoarty, S. F. James, D. Swatton, S. J. Hughes, J. W. Morton, T. M. Guymer, M. P. Hill, D. A. Chapman, J. E. Andrew, A. J. Comley, R. Shepherd, J. Dunn, H. Chen, M. Schneider, G. Brown, P. Beiersdorfer, and J. Emig. *Measurements of Electron Transport in Foils Irradiated with a Picosecond Time Scale Laser Pulse.* Phys. Rev. Lett. 106, 185003 (2011).

[46] V. Dervieux, B. Loupias, S. Baton, L. Lecherbourg, K. Glize, C. Rousseaux, C. Reverdin, L. Gremillet, C. Blancard, V. Silvert, J.-C. Pain, C. Brown, P. Allan, M. Hill, D. Hoarty, and P. Renaudin. *Characterization of near-LTE, high-temperature and high-density aluminum plasmas produced by ultra-high intensity lasers.* High Energy Density Physics 16, 12 – 17 (2015).

[47] K. U. Akli, S. B. Hansen, A. J. Kemp, R. R. Freeman, F. N. Beg, D. C. Clark, S. D. Chen, D. Hey, S. P. Hatchett, K. Highbarger, E. Giraldez, J. S. Green, G. Gregori, K. L. Lancaster, T. Ma, A. J. MacKinnon, P. Norreys, N. Patel, J. Pasley, C. Shearer, R. B. Stephens, C. Stoeckl, M. Storm, W. Theobald, L. D. Van Woerkom, R. Weber, and M. H. Key. *Laser Heating of Solid Matter by Light-Pressure-Driven Shocks at Ultrarelativistic Intensities.* Phys. Rev. Lett. 100, 165002 (2008).

[48] O. N. Rosmej, Z. Samsonova, S. Höfer, D. Kartashov, C. Arda, D. Khaghani, A. Schoenlein, S. Zähter, A. Hoffmann, R. Loetzsch, A. Saevert, I. Uschmann, M. E. Povarnitsyn, N. E. Andreev, L. P. Pugachev, M. C. Kaluza, and C. Spielmann. *Generation of keV hot near-solid density plasma states at high contrast laser-matter interaction.* Physics of Plasmas 25(8), 083103 (2018).

[49] F. Y. Khattak, R. J. Clarke, E. J. Divall, M. Edwards, P. S. Foster, C. J. Hooker, A. J. Langley, P. Mistry, D. Neely, O. A. M. B. P. du Sert, J. Smith, C. Spindloe, G. Tallents, M. Tolley, and D. Riley. *Enhanced He-α emission from "smoked" Ti targets irradiated with 400 nm, 45 fs laser pulses.* Europhysics Letters (EPL) 72(2), 242–248 (2005).

[50] H. A. Sumeruk, S. Kneip, D. R. Symes, I. V. Churina, A. V. Belolipetski, T. D. Donnelly, and T. Ditmire. *Control of Strong-Laser-Field Coupling to Electrons in Solid Targets with Wavelength-Scale Spheres.* Phys. Rev. Lett. 98, 045001 (2007).

[51] M. M. Murnane, H. C. Kapteyn, S. P. Gordon, J. Bokor, E. N. Glytsis, and R. W. Falcone. *Efficient coupling of high intensity subpicosecond laser pulses into solids.* Applied Physics Letters 62(10), 1068–1070 (1993).

[52] S. P. Gordon, T. Donnelly, A. Sullivan, H. Hamster, and R. W. Falcone. *X rays from microstructured targets heated by femtosecond lasers.* Opt. Lett. 19(7), 484–486 (1994).

[53] G. Kulcsár, D. AlMawlawi, F. W. Budnik, P. R. Herman, M. Moskovits, L. Zhao, and R. S. Marjoribanks. *Intense Picosecond X-Ray Pulses from Laser Plasmas by Use of Nanostructured "Velvet" Targets.* Phys. Rev. Lett. 84, 5149–5152 (2000).

[54] P. P. Rajeev, P. Taneja, P. Ayyub, A. S. Sandhu, and G. R. Kumar. *Metal Nanoplasmas as Bright Sources of Hard X-Ray Pulses.* Phys. Rev. Lett. 90, 115002 (2003).

[55] S. Mondal, I. Chakraborty, S. Ahmad, D. Carvalho, P. Singh, A. D. Lad, V. Narayanan, P. Ayyub, G. R. Kumar, J. Zheng, and Z. Sheng. *Highly enhanced hard x-ray emission from oriented metal nanorod arrays excited by intense femtosecond laser pulses.* Phys. Rev. B 83, 035408 (2011).

[56] T. Nishikawa, S. Suzuki, Y. Watanabe, O. Zhou, and H. Nakano. *Efficient water-window X-ray pulse generation from femtosecond-laser-produced plasma by using a carbon nanotube target.* Applied Physics B 78(7), 885–890 (2004).

[57] S. H. Glenzer, D. A. Callahan, A. J. MacKinnon, J. L. Kline, G. Grim, E. T. Alger, R. L. Berger, L. A. Bernstein, R. Betti, D. L. Bleuel, T. R. Boehly, D. K. Bradley, S. C. Burkhart, R. Burr, J. A. Caggiano, C. Castro, D. T. Casey, C. Choate, D. S. Clark, P. Celliers, C. J. Cerjan, G. W. Collins, E. L. Dewald, P. DiNicola, J. M. DiNicola, L. Divol, S. Dixit, T. Döppner, R. Dylla-Spears, E. Dzenitis, M. Eckart, G. Erbert, D. Farley, J. Fair, D. Fittinghoff, M. Frank, L. J. A. Frenje, S. Friedrich, D. T. Casey, M. Gatu Johnson, C. Gibson, E. Giraldez, V. Glebov, S. Glenn, N. Guler, S. W. Haan, B. J. Haid, B. A. Hammel, A. V. Hamza, C. A. Haynam, G. M. Heestand, M. Hermann, H. W. Hermann, D. G. Hicks, D. E. Hinkel, J. P. Holder, D. M. Holunda, J. B. Horner, W. W. Hsing, H. Huang, N. Izumi, M. Jackson, O. S. Jones, D. H. Kalantar, R. Kauffman, J. D. Kilkenny, R. K. Kirkwood, J. Klingmann, T. Kohut, J. P. Knauer, J. A. Koch, B. Kozioziemki, G. A. Kyrala, A. L. Kritcher, J. Kroll, K. La Fortune, L. Lagin, O. L. Landen, D. W. Larson, D. LaTray, R. J. Leeper, S. Le Pape, J. D. Lindl, R. Lowe-Webb, T. Ma, J. McNaney, A. G. MacPhee, T. N. Malsbury, E. Mapoles, C. D. Marshall, N. B. Meezan, F. Merrill, P. Michel, J. D. Moody, A. S. Moore, M. Moran, K. A. Moreno, D. H. Munro, B. R. Nathan, A. Nikroo, R. E. Olson, C. D. Orth, A. E. Pak, P. K. Patel, T. Parham, R. Petrasso, J. E. Ralph, H. Rinderknecht, S. P. Regan, H. F. Robey, J. S. Ross, M. D. Rosen, R. Sacks, J. D. Salmonson, R. Saunders, J. Sater, C. Sangster, M. B. Schneider, F. H. Séguin, M. J. Shaw, B. K. Spears, P. T. Springer, W. Stoeffl, L. J. Suter, C. A. Thomas, R. Tommasini, R. P. J. Town, C. Walters, S. Weaver, S. V. Weber, P. J. Wegner, P. K. Whitman, K. Widmann, C. C. Widmayer, C. H. Wilde, D. C. Wilson, B. Van Wonterghem, B. J. MacGowan, L. J. Atherton, M. J. Edwards, and E. I. Moses. *Cryogenic thermonuclear fuel implosions on the National Ignition Facility.* Physics of Plasmas 19(5), 056318 (2012).

[58] H. F. Robey, P. A. Amendt, J. L. Milovich, H.-S. Park, A. V. Hamza, and M. J. Bono. *Hohlraum-Driven Mid-Z (*$\mathrm{SiO_2}$*) Double-Shell Implosions on the Omega Laser Facility and Their Scaling to NIF.* Phys. Rev. Lett. 103, 145003 (2009).

[59] A. F. Koenderink, A. Alù, and A. Polman. *Nanophotonics: Shrinking light-based technology.* Science 348(6234), 516–521 (2015).

[60] B. A. Remington, R. E. Rudd, and J. S. Wark. *From microjoules to megajoules and kilobars to gigabars: Probing matter at extreme states of deformation.* Physics of Plasmas 22(9), 090501 (2015).

[61] S. Fujioka, H. Takabe, N. Yamamoto, D. Salzmann, F. Wang, H. Nishimura, Y. Li, Q. Dong, S. Wang, Y. Zhang, Y.-J. Rhee, Y.-W. Lee, J.-M. Han, M. Tanabe, T. Fujiwara, Y. Nakabayashi, G. Zhao, J. Zhang, and K. Mima. *X-ray astronomy in the laboratory with a miniature compact object produced by laser-driven implosion.* Nature Physics 5, 821 EP (2009).

[62] B. A. Remington, D. Arnett, R. Paul, Drake, and H. Takabe. *Modeling Astrophysical Phenomena in the Laboratory with Intense Lasers.* Science 284(5419), 1488–1493 (1999).

[63] S. H. Glenzer, B. J. MacGowan, P. Michel, N. B. Meezan, L. J. Suter, S. N. Dixit, J. L. Kline, G. A. Kyrala, D. K. Bradley, D. A. Callahan, E. L. Dewald, L. Divol, E. Dzenitis, M. J. Edwards, A. V. Hamza, C. A. Haynam, D. E. Hinkel, D. H. Kalantar, J. D. Kilkenny, O. L. Landen, J. D. Lindl, S. LePape, J. D. Moody, A. Nikroo, T. Parham, M. B. Schneider, R. P. J. Town, P. Wegner, K. Widmann, P. Whitman, B. K. F. Young, B. Van Wonterghem, L. J. Atherton, and E. I. Moses. *Symmetric Inertial Confinement Fusion Implosions at Ultra-High Laser Energies.* Science 327(5970), 1228–1231 (2010).

[64] O. A. Hurricane, D. A. Callahan, D. T. Casey, P. M. Celliers, C. Cerjan, E. L. Dewald, T. R. Dittrich, T. Döppner, D. E. Hinkel, L. F. B. Hopkins, J. L. Kline, S. Le Pape, T. Ma, A. G. MacPhee, J. L. Milovich, A. Pak, H.-S. Park, P. K. Patel, B. A. Remington, J. D. Salmonson, P. T. Springer, and R. Tommasini. *Fuel gain exceeding unity in an inertially confined fusion implosion.* Nature 506, 343 EP (2014).

[65] T. R. Dittrich, B. A. Hammel, C. J. Keane, R. McEachern, R. E. Turner, S. W. Haan, and L. J. Suter. *Diagnosis of Pusher-Fuel Mix in Indirectly Driven Nova Implosions.* Phys. Rev. Lett. 73, 2324–2327 (1994).

[66] P. Y. Chang, G. Fiksel, M. Hohenberger, J. P. Knauer, R. Betti, F. J. Marshall, D. D. Meyerhofer, F. H. Séguin, and R. D. Petrasso. *Fusion Yield Enhancement in Magnetized Laser-Driven Implosions.* Phys. Rev. Lett. 107, 035006 (2011).

[67] G. Ren, J. Yan, J. Liu, K. Lan, Y. H. Chen, W. Y. Huo, Z. Fan, X. Zhang, J. Zheng, Z. Chen, W. Jiang, L. Chen, Q. Tang, Z. Yuan, F. Wang, S. Jiang, Y. Ding, W. Zhang, and X. T. He. *Neutron Generation by Laser-Driven Spherically Convergent Plasma Fusion.* Phys. Rev. Lett. 118, 165001 (2017).

[68] D. Klir, J. Krasa, J. Cikhardt, R. Dudzak, E. Krousky, M. Pfeifer, K. Rezac, O. Sila, J. Skala, J. Ullschmied, and A. Velyhan. *Efficient neutron production from subnanosecond laser pulse accelerating deuterons on target front side.* Physics of Plasmas 22(9), 093117 (2015).

[69] D. P. Higginson, J. M. McNaney, D. C. Swift, G. M. Petrov, J. Davis, J. A. Frenje, L. C. Jarrott, R. Kodama, K. L. Lancaster, A. J. Mackinnon, H. Nakamura, P. K. Patel, G. Tynan, and F. N. Beg. *Production of neutrons up to 18 MeV in high-intensity, short-pulse laser matter interactions.* Physics of Plasmas 18(10), 100703 (2011).

[70] M. H. Key, M. D. Cable, T. E. Cowan, K. G. Estabrook, B. A. Hammel, S. P. Hatchett, E. A. Henry, D. E. Hinkel, J. D. Kilkenny, J. A. Koch, W. L. Kruer, A. B. Langdon, B. F. Lasinski, R. W. Lee, B. J. MacGowan, A. MacKinnon, J. D. Moody, M. J. Moran, A. A. Offenberger, D. M. Pennington, M. D. Perry, T. J. Phillips, T. C. Sangster, M. S. Singh, M. A. Stoyer, M. Tabak, G. L. Tietbohl, M. Tsukamoto, K. Wharton, and S. C. Wilks. *Hot electron production and heating by hot electrons in fast ignitor research.* Physics of Plasmas 5(5), 1966–1972 (1998).

[71] Y. Kitagawa, Y. Mori, O. Komeda, K. Ishii, R. Hanayama, K. Fujita, S. Okihara, T. Sekine, N. Satoh, T. Kurita, M. Takagi, T. Watari, T. Kawashima, H. Kan, Y. Nishimura, A. Sunahara, Y. Sentoku, N. Nakamura, T. Kondo, M. Fujine, H. Azuma, T. Motohiro, T. Hioki, M. Kakeno, E. Miura, Y. Arikawa, T. Nagai, Y. Abe, S. Ozaki, and A. Noda. *Direct Heating of a Laser-Imploded Core by Ultraintense Laser-Driven Ions.* Phys. Rev. Lett. 114, 195002 (2015).

[72] W. Bang, G. Dyer, H. J. Quevedo, A. C. Bernstein, E. Gaul, J. Rougk, F. Aymond, M. E. Donovan, and T. Ditmire. *Optimum laser intensity for the production of energetic deuterium ions from laser-cluster interaction.* Physics of Plasmas 20(9), 093104 (2013).

[73] G. Pretzler, A. Saemann, A. Pukhov, D. Rudolph, T. Schätz, U. Schramm, P. Thirolf, D. Habs, K. Eidmann, G. D. Tsakiris, J. Meyer-ter Vehn, and K. J. Witte. *Neutron production by 200 mJ ultrashort laser pulses.* Phys. Rev. E 58, 1165–1168 (1998).

[74] M. Strobl, I. Manke, N. Kardjilov, A. Hilger, M. Dawson, and J. Banhart. *Advances in neutron radiography and tomography.* Journal of Physics D: Applied Physics 42(24), 243001 (2009).

[75] D. I. Svergun and M. H. Koch. *Advances in structure analysis using small-angle scattering in solution.* Current Opinion in Structural Biology 12(5), 654 – 660 (2002).

[76] E. Prince. *Neutron Scattering Instrumentation: A Tutorial Review.* Applied Spectroscopy Reviews 34(3), 159–172 (2004).

[77] J. Kline, S. Batha, L. Benedetti, D. Bennett, S. Bhandarkar, L. B. Hopkins, J. Biener, M. Biener, R. Bionta, E. Bond, D. Bradley, T. Braun, D. Callahan, J. Caggiano, C. Cerjan, B. Cagadas, D. Clark, C. Castro, E. Dewald, T. Döppner, L. Divol, R. Dylla-Spears, M. Eckart, D. Edgell, M. Farrell, J. Field, D. Fittinghoff, M. G. Johnson, G. Grim, S. Haan, B. Haines, A. Hamza, E. Hartouni, R. Hatarik, K. Henderson, H. Herrmann, D. Hinkel, D. Ho, M. Hohenberger, D. Hoover, H. Huang, M. Hoppe, O. Hurricane, N. Izumi, S. Johnson, O. Jones, S. Khan, B. Kozioziemski, C. Kong, J. Kroll, G. Kyrala, S. LePape, T. Ma, A. Mackinnon, A. MacPhee, S. MacLaren, L. Masse, J. McNaney, N. Meezan, J. Merrill, J. Milovich, J. Moody, A. Nikroo, A. Pak, P. Patel, L. Peterson, E. Piceno, L. Pickworth, J. Ralph, N. Rice, H. Robey, J. Ross, J. Rygg, M. Sacks, J. Salmonson, D. Sayre, J. Sater, M. Schneider, M. Schoff, S. Sepke, R. Seugling, V. Smalyuk, B. Spears, M. Stadermann, W. Stoeffl, D. Strozzi, R. Tipton, C. Thomas, P. Volegov, C. Walters, M. Wang, C. Wilde, E. Woerner, C. Yeamans, S. Yi, B. Yoxall, A. Zylstra, J. Kilkenny, O. Landen, W. Hsing, and M. E. and. *Progress of indirect drive inertial confinement fusion in the United States.* Nuclear Fusion 59(11), 112018 (2019).

[78] F. J. Marshall, P. W. McKenty, J. A. Delettrez, R. Epstein, J. P. Knauer, V. A. Smalyuk, J. A. Frenje, C. K. Li, R. D. Petrasso, F. H. Séguin, and R. C. Mancini. *Plasma-Density Determination from X-Ray Radiography of Laser-Driven Spherical Implosions.* Phys. Rev. Lett. 102, 185004 (2009).

[79] C. M. Huntington, C. M. Krauland, C. C. Kuranz, R. P. Drake, H.-S. Park, D. H. Kalantar, B. R. Maddox, B. A. Remington, and J. Kline. *Development of a short duration backlit pinhole for radiography on the National Ignition Facility.* Review of Scientific Instruments 81(10), 10E536 (2010).

[80] E. L. Dewald, M. Rosen, S. H. Glenzer, L. J. Suter, F. Girard, J. P. Jadaud, J. Schein, C. Constantin, F. Wagon, G. Huser, P. Neumayer, and O. L. Landen. *X-ray conversion efficiency of high-Z hohlraum wall materials for indirect drive ignition.* Physics of Plasmas 15(7), 072706 (2008).

[81] J. E. Bailey, T. Nagayama, G. P. Loisel, G. A. Rochau, C. Blancard, J. Colgan, P. Cosse, G. Faussurier, C. J. Fontes, F. Gilleron, I. Golovkin, S. B. Hansen, C. A. Iglesias, D. P. Kilcrease, J. J. MacFarlane, R. C. Mancini, S. N. Nahar, C. Orban, J.-C. Pain, A. K. Pradhan, M. Sherrill, and B. G. Wilson. *A higher-than-predicted measurement of iron opacity at solar interior temperatures.* Nature 517, 56 EP (2014).

[82] B. Yaakobi, T. R. Boehly, D. D. Meyerhofer, T. J. B. Collins, B. A. Remington, P. G. Allen, S. M. Pollaine, H. E. Lorenzana, and J. H. Eggert. *EXAFS Measurement of Iron bcc-to-hcp Phase Transformation in Nanosecond-Laser Shocks.* Phys. Rev. Lett. 95, 075501 (2005).

[83] A. Cavalleri, C. W. Siders, F. L. H. Brown, D. M. Leitner, C. Tóth, J. A. Squier, C. P. J. Barty, K. R. Wilson, K. Sokolowski-Tinten, M. Horn von Hoegen, D. von der Linde, and M. Kammler. *Anharmonic Lattice Dynamics in Germanium Measured with Ultrafast X-Ray Diffraction.* Phys. Rev. Lett. 85, 586–589 (2000).

[84] V. Kaymak, E. Aktan, M. Cerchez, B. Elkin, M. Papenheim, R. Prasad, A. Pukhov, H. C. Scheer, A. M. Schroer, O. Willi, and B. Aurand. *Boosted acceleration of protons by tailored ultra-thin foil targets.* Scientific Reports (submitted) (2019).

[85] E. L. Clark, K. Krushelnick, M. Zepf, F. N. Beg, M. Tatarakis, A. Machacek, M. I. Santala, I. I. Watts, P. A. Norreys, and A. E. Dangor. *Energetic heavy-Ion and proton generation from ultraintense laser-plasma interactions with solids.* Phys Rev Lett 85(8), 1654–7 (2000).

[86] R. A. Snavely, M. H. Key, S. P. Hatchett, T. E. Cowan, M. Roth, T. W. Phillips, M. A. Stoyer, E. A. Henry, T. C. Sangster, M. S. Singh, S. C. Wilks, A. MacKinnon, A. Offenberger, D. M. Pennington, K. Yasuike, A. B. Langdon, B. F. Lasinski, J. Johnson, M. D. Perry, and E. M. Campbell. *Intense high-energy proton beams from Petawatt-laser irradiation of solids.* Phys Rev Lett 85(14), 2945–8 (2000).

[87] T. E. Cowan, J. Fuchs, H. Ruhl, A. Kemp, P. Audebert, M. Roth, R. Stephens, I. Barton, A. Blazevic, E. Brambrink, J. Cobble, J. Fernandez, J. C. Gauthier, M. Geissel, M. Hegelich, J. Kaae, S. Karsch, G. P. Le Sage, S. Letzring, M. Manclossi, S. Meyroneinc, A. Newkirk, H. Pepin, and N. Renard-LeGalloudec. *Ultralow emittance, multi-MeV proton beams from a laser virtual-cathode plasma accelerator.* Phys Rev Lett 92(20), 204801 (2004).

[88] J. Fuchs, P. Antici, E. dHumières, E. Lefebvre, M. Borghesi, E. Brambrink, C. A. Cecchetti, M. Kaluza, V. Malka, M. Manclossi, S. Meyroneinc, P. Mora, J. Schreiber, T. Toncian, H. Pepin, and P. Audebert. *Laser-driven proton scaling laws and new paths towards energy increase.* Nature Physics 2(1), 48–54 (2005).

[89] S. C. Wilks, W. L. Kruer, M. Tabak, and A. B. Langdon. *Absorption of ultra-intense laser pulses.* Phys Rev Lett 69(9), 1383–1386 (1992).

[90] P. Mora. *Plasma expansion into a vacuum.* Phys Rev Lett 90(18), 185002 (2003).

[91] B. Qiao, X. F. Shen, H. He, Y. Xie, H. Zhang, C. T. Zhou, S. P. Zhu, and X. T. He. *Revisit on ion acceleration mechanisms in solid targets driven by intense laser pulses.* Plasma Physics and Controlled Fusion 61(1) (2019).

[92] H. Schwoerer, S. Pfotenhauer, O. Jackel, K. U. Amthor, B. Liesfeld, W. Ziegler, R. Sauerbrey, K. W. Ledingham, and T. Esirkepov. *Laser-plasma acceleration of quasi-monoenergetic protons from microstructured targets.* Nature 439(7075), 445–8 (2006).

[93] B. Ramakrishna, M. Murakami, M. Borghesi, L. Ehrentraut, P. V. Nickles, M. Schnürer, S. Steinke, J. Psikal, V. Tikhonchuk, and S. Ter-Avetisyan. *Laser-driven quasimonoenergetic proton burst from water spray target.* Physics of Plasmas 17(8) (2010).

[94] S. Ter-Avetisyan, M. Schnurer, P. V. Nickles, M. Kalashnikov, E. Risse, T. Sokollik, W. Sandner, A. Andreev, and V. Tikhonchuk. *Quasimonoenergetic deuteron bursts produced by ultraintense laser pulses.* Phys Rev Lett 96(14), 145006 (2006).

[95] T. Toncian, M. Borghesi, J. Fuchs, E. d'Humieres, P. Antici, P. Audebert, E. Brambrink, C. A. Cecchetti, A. Pipahl, L. Romagnani, and O. Willi. *Ultrafast laser-driven microlens to focus and energy-select mega-electron volt protons.* Science 312(5772), 410–3 (2006).

[96] B. M. Hegelich, B. J. Albright, J. Cobble, K. Flippo, S. Letzring, M. Paffett, H. Ruhl, J. Schreiber, R. K. Schulze, and J. C. Fernandez. *Laser acceleration of quasi-monoenergetic MeV ion beams.* Nature 439(7075), 441–4 (2006).

[97] S. M. Pfotenhauer, O. Jäckel, J. Polz, S. Steinke, H. P. Schlenvoigt, J. Heymann, A. P. L. Robinson, and M. C. Kaluza. *A cascaded laser acceleration scheme for the generation of spectrally controlled proton beams.* New Journal of Physics 12(10) (2010).

[98] B. Aurand, L. Senje, K. Svensson, M. Hansson, A. Higginson, A. Gonoskov, M. Marklund, A. Persson, O. Lundh, D. Neely, P. McKenna, and C.-G. Wahlström. *Manipulation of the spatial distribution of laser-accelerated proton beams by varying the laser intensity distribution.* Physics of Plasmas 23(2), 023113 (2016).

[99] Y. Sentoku, T. E. Cowan, A. Kemp, and H. Ruhl. *High energy proton acceleration in interaction of short laser pulse with dense plasma target.* Physics of Plasmas 10(5), 2009–2015 (2003).

[100] W. D. Newhauser and R. Zhang. *The physics of proton therapy.* Phys Med Biol 60(8), R155–209 (2015).

[101] T. Esirkepov, M. Yamagiwa, and T. Tajima. *Laser ion-acceleration scaling laws seen in multiparametric particle-in-cell simulations.* Phys Rev Lett 96(10), 105001 (2006).

[102] J. Fuchs, C. A. Cecchetti, M. Borghesi, T. Grismayer, E. d'Humieres, P. Antici, S. Atzeni, P. Mora, A. Pipahl, L. Romagnani, A. Schiavi, Y. Sentoku, T. Toncian, P. Audebert, and O. Willi. *Laser-foil acceleration of high-energy protons in small-scale plasma gradients.* Phys Rev Lett 99(1), 015002 (2007).

[103] A. A. Andreev, J. Limpouch, J. Psikal, K. Y. Platonov, and V. T. Tikhonchuk. *Laser ion acceleration in a mass limited targets.* The European Physical Journal Special Topics 175(1), 123–126 (2009).

[104] S. Buffechoux, J. Psikal, M. Nakatsutsumi, L. Romagnani, A. Andreev, K. Zeil, M. Amin, P. Antici, T. Burris-Mog, A. Compant-La-Fontaine, E. d'Humières, S. Fourmaux, S. Gaillard, F. Gobet, F. Hannachi, S. Kraft, A. Mancic, C. Plaisir, G. Sarri, M. Tarisien, T. Toncian, U. Schramm, M. Tampo, P. Audebert, O. Willi, T. E. Cowan, H. Pépin, V. Tikhonchuk, M. Borghesi, and J. Fuchs. *Hot Electrons Transverse Refluxing in Ultraintense Laser-Solid Interactions.* Phys. Rev. Lett. 105, 015005 (2010).

[105] O. Klimo, J. Psikal, J. Limpouch, J. Proska, F. Novotny, T. Ceccotti, V. Floquet, and S. Kawata. *Short pulse laser interaction with micro-structured targets: simulations of laser absorption and ion acceleration.* New Journal of Physics 13(5), 053028 (2011).

[106] A. Andreev, K. Platonov, J. Braenzel, A. Lübcke, S. Das, H. Messaoudi, R. Grunwald, C. Gray, E. McGlynn, and M. Schnürer. *Relativistic laser nano-plasmonics for effective fast particle production.* Plasma Physics and Controlled Fusion 58(1), 014038 (2015).

[107] D. Margarone, O. Klimo, I. J. Kim, J. Prokůpek, J. Limpouch, T. M. Jeong, T. Mocek, J. Pšikal, H. T. Kim, J. Proška, K. H. Nam, L. Štolcová, I. W. Choi, S. K. Lee, J. H. Sung, T. J. Yu, and G. Korn. *Laser-Driven Proton Acceleration Enhancement by Nanostructured Foils.* Phys. Rev. Lett. 109, 234801 (2012).

[108] A. Zigler, T. Palchan, N. Bruner, E. Schleifer, S. Eisenmann, M. Botton, Z. Henis, S. A. Pikuz, A. Y. Faenov, D. Gordon, and P. Sprangle. *5.5–7.5 MeV Proton Generation by a Moderate-Intensity Ultrashort-Pulse Laser Interaction with* H_2O *Nanowire Targets.* Phys. Rev. Lett. 106, 134801 (2011).

[109] I. Thiele, J. Ferri, E. Siminos, L. Gremillet, E. Smetanina, A. Dmitriev, G. Cantono, C. G. Wahlström, and T. Fülöp. *Enhancement of laser-driven ion acceleration in non-periodic nanostructured targets.* arXiv e-prints page arXiv:1905.11131 (2019).

[110] T. Esirkepov, M. Borghesi, S. V. Bulanov, G. Mourou, and T. Tajima. *Highly Efficient Relativistic-Ion Generation in the Laser-Piston Regime.* Phys. Rev. Lett. 92, 175003 (2004).

[111] A. P. L. Robinson, M. Zepf, S. Kar, R. G. Evans, and C. Bellei. *Radiation pressure acceleration of thin foils with circularly polarized laser pulses.* New Journal of Physics 10(1), 013021 (2008).

[112] A. Macchi, S. Veghini, and F. Pegoraro. *"Light Sail" Acceleration Reexamined.* Phys. Rev. Lett. 103, 085003 (2009).

[113] B. Qiao, S. Kar, M. Geissler, P. Gibbon, M. Zepf, and M. Borghesi. *Dominance of Radiation Pressure in Ion Acceleration with Linearly Polarized Pulses at Intensities of* $10^{21}\ W cm^{-2}$. Phys. Rev. Lett. 108, 115002 (2012).

[114] A. Henig, S. Steinke, M. Schnurer, T. Sokollik, R. Horlein, D. Kiefer, D. Jung, J. Schreiber, B. M. Hegelich, X. Q. Yan, J. Meyer-ter Vehn, T. Tajima, P. V. Nickles, W. Sandner, and D. Habs. *Radiation-pressure acceleration of ion beams driven by circularly polarized laser pulses.* Phys Rev Lett 103(24), 245003 (2009).

[115] X. Q. Yan, C. Lin, Z. M. Sheng, Z. Y. Guo, B. C. Liu, Y. R. Lu, J. X. Fang, and J. E. Chen. *Generating high-current monoenergetic proton beams by a circularly polarized laser pulse in the phase-stable acceleration regime.* Phys Rev Lett 100(13), 135003 (2008).

[116] B. Aurand, B. Elkin, L.-O. Heim, B. Lommel, B. Kindler, M. Tomut, C. Rödel, S. Kuschel, O. Jäckel, J. Barz, and T. Kuehl. *Preparation and characterization of nanometer-thin freestanding polymer foils for laser-ion acceleration.* Journal of Polymer Science Part B: Polymer Physics 51(18), 1355–1360 (2013).

[117] B. Aurand, S. Kuschel, O. Jäckel, C. Rödel, H. Zhao, S. Herzer, A. Paz, J. Bierbach, J. Polz, B. Elkin, A. Karmakar, P. Gibbon, M. Kaluza, and T. Kuehl. *Enhanced radiation pressure-assisted acceleration by temporally tuned counter-propagating pulses.* Nuclear Instruments and Methods in Physics Research Section A: Accelerators, Spectrometers, Detectors and Associated Equipment 740, 83 – 86 (2014).

[118] B. Qiao, X. F. Shen, H. He, Y. Xie, H. Zhang, C. T. Zhou, S. P. Zhu, and X. T. He. *Revisit on ion acceleration mechanisms in solid targets driven by intense laser pulses.* Plasma Physics and Controlled Fusion 61(1), 014039 (2018).

[119] A. Higginson, R. J. Gray, M. King, R. J. Dance, S. D. R. Williamson, N. M. H. Butler, R. Wilson, R. Capdessus, C. Armstrong, J. S. Green, S. J. Hawkes, P. Martin, W. Q. Wei, S. R. Mirfayzi, X. H. Yuan, S. Kar, M. Borghesi, R. J. Clarke, D. Neely, and P. McKenna. *Near-100 MeV protons via a laser-driven transparency-enhanced hybrid acceleration scheme.* Nature Communications 9(1), 724 (2018).

[120] M. Roth and M. Schollmeier. *Ion Acceleration—Target Normal Sheath Acceleration.* CERN Yellow Reports 1(0), 231 (2016).

[121] A. Macchi. *A Review of Laser-Plasma Ion Acceleration.* arXiv:1712.06443 (2017).

[122] E. L. Clark, K. Krushelnick, J. R. Davies, M. Zepf, M. Tatarakis, F. N. Beg, A. Machacek, P. A. Norreys, M. I. K. Santala, I. Watts, and A. E. Dangor. *Measurements of Energetic Proton Transport through Magnetized Plasma from Intense Laser Interactions with Solids.* Phys. Rev. Lett. 84, 670–673 (2000).

[123] S. C. Wilks, A. B. Langdon, T. E. Cowan, M. Roth, M. Singh, S. Hatchett, M. H. Key, D. Pennington, A. MacKinnon, and R. A. Snavely. *Energetic proton generation in ultra-intense laser–solid interactions.* Physics of Plasmas 8(2), 542–549 (2001).

[124] A. Macchi, M. Borghesi, and M. Passoni. *Ion acceleration by superintense laser-plasma interaction.* Rev. Mod. Phys. 85, 751–793 (2013).

[125] A. P. L. Robinson, P. Gibbon, M. Zepf, S. Kar, R. G. Evans, and C. Bellei. *Relativistically correct hole-boring and ion acceleration by circularly polarized laser pulses.* Plasma Physics and Controlled Fusion 51(2), 024004 (2009).

[126] A. Macchi, S. Veghini, T. V. Liseykina, and F. Pegoraro. *Radiation pressure acceleration of ultrathin foils.* New Journal of Physics 12(4), 045013 (2010).

[127] A. Macchi. *A Superintense Laser-Plasma Interaction Theory Primer* (2013).

[128] A. Macchi and C. Benedetti. *Ion acceleration by radiation pressure in thin and thick targets.* Nuclear Instruments and Methods in Physics Research Section A: Accelerators, Spectrometers, Detectors and Associated Equipment 620(1), 41 – 45 (2010).

[129] F. Pegoraro and S. V. Bulanov. *Photon Bubbles and Ion Acceleration in a Plasma Dominated by the Radiation Pressure of an Electromagnetic Pulse.* Phys. Rev. Lett. 99, 065002 (2007).

[130] C. Scullion, D. Doria, L. Romagnani, A. Sgattoni, K. Naughton, D. R. Symes, P. McKenna, A. Macchi, M. Zepf, S. Kar, and M. Borghesi. *Polarization Dependence of Bulk Ion Acceleration from Ultrathin Foils Irradiated by High-Intensity Ultrashort Laser Pulses.* Phys. Rev. Lett. 119, 054801 (2017).

[131] A. P. L. Robinson. *Production of high energy protons with hole-boring radiation pressure acceleration.* Physics of Plasmas 18(5), 056701 (2011).

[132] A. P. L. Robinson, R. M. G. M. Trines, N. P. Dover, and Z. Najmudin. *Hole-boring radiation pressure acceleration as a basis for producing high-energy proton bunches.* Plasma Physics and Controlled Fusion 54(11), 115001 (2012).

[133] G. Marx. *Interstellar Vehicle Propelled By Terrestrial Laser Beam.* Nature 211(5044), 22–23 (1966).

[134] R. L. Forward. *Roundtrip interstellar travel using laser-pushed lightsails.* Journal of Spacecraft and Rockets 21(2), 187–195 (1984).

[135] S. V. Bulanov and V. S. Khoroshkov. *Feasibility of using laser ion accelerators in proton therapy.* Plasma Physics Reports 28(5), 453–456 (2002).

[136] V. S. Khoroshkov and E. I. Minakova. *Proton beams in radiotherapy.* European Journal of Physics 19(6), 523–536 (1998).

[137] C. Windsor, M. Keilhacker, J. D. Lawson, G. J. Pert, D. C. Robinson, and O. Willi. *Inertial-confinement fusion with fast ignition.* Philosophical Transactions of the Royal Society of London. Series A: Mathematical, Physical and Engineering Sciences 357(1752), 555–574 (1999).

[138] M. Roth, T. E. Cowan, M. H. Key, S. P. Hatchett, C. Brown, W. Fountain, J. Johnson, D. M. Pennington, R. A. Snavely, S. C. Wilks, K. Yasuike, H. Ruhl, F. Pegoraro, S. V. Bulanov, E. M. Campbell, M. D. Perry, and H. Powell. *Fast ignition by intense laser-accelerated proton beams.* Phys Rev Lett 86(3), 436–9 (2001).

[139] M. Tabak, J. Hammer, M. E. Glinsky, W. L. Kruer, S. C. Wilks, J. Woodworth, E. M. Campbell, M. D. Perry, and R. J. Mason. *Ignition and high gain with ultrapowerful lasers**. Physics of Plasmas 1(5), 1626–1634 (1994).

[140] B. Y. Sharkov, D. H. Hoffmann, A. A. Golubev, and Y. Zhao. *High energy density physics with intense ion beams.* Matter and Radiation at Extremes 1(1), 28–47 (2016).

[141] M. Borghesi, A. Schiavi, D. H. Campbell, M. G. Haines, O. Willi, A. J. MacKinnon, L. A. Gizzi, M. Galimberti, R. J. Clarke, and H. Ruhl. *Proton imaging: a diagnostic for inertial confinement fusion/fast ignitor studies.* Plasma Physics and Controlled Fusion 43(12A), A267–A276 (2001).

[142] M. Borghesi, D. H. Campbell, A. Schiavi, M. G. Haines, O. Willi, A. J. MacKinnon, P. Patel, L. A. Gizzi, M. Galimberti, R. J. Clarke, F. Pegoraro, H. Ruhl, and S. Bulanov. *Electric field detection in laser-plasma interaction experiments via the proton imaging technique.* Physics of Plasmas 9(5), 2214–2220 (2002).

[143] T. Tuckmantel, A. Pukhov, J. Liljo, and M. Hochbruck. *Three-Dimensional Relativistic Particle-in-Cell Hybrid Code Based on an Exponential Integrator.* IEEE Transactions on Plasma Science 38(9), 2383–2389 (2010).

[144] O. Buneman. *Dissipation of Currents in Ionized Media.* Phys. Rev. 115, 503–517 (1959).

[145] J. Dawson. *One-Dimensional Plasma Model.* The Physics of Fluids 5(4), 445–459 (1962).

[146] C. Birdsall and A. Langdon. *Plasma physics via computer simulation.* The Adam Hilger series on plasma physics. McGraw-Hill (1985).

[147] R. Hockney and J. Eastwood. *Computer Simulation Using Particles.* Advanced book program: Addison-Wesley. McGraw-Hill (1981).

[148] J. M. Dawson. *Particle simulation of plasmas.* Rev. Mod. Phys. 55, 403–447 (1983).

[149] C. K. Birdsall and A. B. Langdon. *Plasma Physics via Computer Simulation* (1991).

[150] J. P. Verboncoeur. *Particle simulation of plasmas: review and advances.* Plasma Physics and Controlled Fusion 47(5A), A231–A260 (2005).

[151] S. Gedney. *Introduction to the Finite-Difference Time-Domain (FDTD) Method for Electromagnetics.* Synthesis Lectures on Computational Electromagnetics. Morgan & Claypool Publishers (2011).

[152] A. Pukhov. *Three-dimensional electromagnetic relativistic particle-in-cell code VLPL (Virtual Laser Plasma Lab).* Journal of Plasma Physics 61(03), 425–433 (1999).

[153] A. Pukhov. *Particle-In-Cell Codes for Plasma-based Particle Acceleration.* CERN Yellow Reports 1(0), 181 (2016).

[154] E. Gabriel, G. E. Fagg, G. Bosilca, T. Angskun, J. J. Dongarra, J. M. Squyres, V. Sahay, P. Kambadur, B. Barrett, A. Lumsdaine, R. H. Castain, D. J. Daniel, R. L. Graham, and T. S. Woodall. *Open MPI: Goals, Concept, and Design of a*

Next Generation MPI Implementation. In *Proceedings, 11th European PVM/MPI Users' Group Meeting*, pages 97–104, Budapest, Hungary, (2004).

[155] J. Anderson, P. J. Burns, D. Milroy, P. Ruprecht, T. Hauser, and H. J. Siegel. *Deploying RMACC Summit: An HPC Resource for the Rocky Mountain Region.* In *Proceedings of the Practice and Experience in Advanced Research Computing 2017 on Sustainability, Success and Impact*, PEARC17, pages 8:1–8:7, New York, NY, USA, ACM (2017).

[156] M. Folk, G. Heber, Q. Koziol, E. Pourmal, and D. Robinson. *An Overview of the HDF5 Technology Suite and Its Applications.* In *Proceedings of the EDBT/ICDT 2011 Workshop on Array Databases*, AD '11, pages 36–47, New York, NY, USA, ACM (2011).

[157] J. P. Boris. *Relativistic plasma simulation-optimization of a hybrid code.* Proc. 4th Conf. Num. Sim. Plasmas pages 3–67 (1970).

[158] H. Qin, S. Zhang, J. Xiao, J. Liu, Y. Sun, and W. M. Tang. *Why is Boris algorithm so good?* Physics of Plasmas 20(8), 084503 (2013).

[159] K. Yee. *Numerical solution of initial boundary value problems involving maxwell's equations in isotropic media.* IEEE Transactions on Antennas and Propagation 14(3), 302–307 (1966).

[160] A. Taflove and S. Hagness. *Computational Electrodynamics: The Finite-difference Time-domain Method.* Artech House antennas and propagation library. Artech House (2005).

[161] D. Rawtani, T. Sajan, A. Twinkle R, and Y. Agrawal. *Emerging strategies for synthesis and manipulation of nanowires: A review.* Reviews on Advanced Materials Science 40, 177–187 (2015).

[162] A. L. Prieto, M. S. Sander, M. S. Martín-González, R. Gronsky, T. Sands, and A. M. Stacy. *Electrodeposition of Ordered Bi2Te3 Nanowire Arrays.* Journal of the American Chemical Society 123(29), 7160–7161 (2001).

[163] L. Zaraska, G. D. Sulka, and M. Jaskuła. *Fabrication of free-standing copper foils covered with highly-ordered copper nanowire arrays.* Applied Surface Science 258(19), 7781 – 7786 (2012).

[164] W. H. Bennett. *Magnetically Self-Focussing Streams.* Phys. Rev. 45, 890–897 (1934).

[165] A. B. Severnyi. Soviet Astronomy 2, 310 (1958).

[166] A. Ciardi, T. Vinci, J. Fuchs, B. Albertazzi, C. Riconda, H. Pépin, and O. Portugall. *Astrophysics of Magnetically Collimated Jets Generated from Laser-Produced Plasmas.* Phys. Rev. Lett. 110, 025002 (2013).

[167] M. G. Haines. *A review of the dense Z-pinch.* Plasma Physics and Controlled Fusion 53(9), 093001 (2011).

[168] M. G. Haines, S. V. Lebedev, J. P. Chittenden, F. N. Beg, S. N. Bland, and A. E. Dangor. *The past, present, and future of Z pinches.* Physics of Plasmas 7(5), 1672–1680 (2000).

[169] M. Kruskal and M. Schwarzschild. *Some instabilities of a completely ionized plasma.* Proc. R. Soc. Lond. A 223, 348 (1954).

[170] R. J. Tayler. *Hydromagnetic Instabilities of an Ideally Conducting Fluid.* Proceedings of the Physical Society. Section B 70(1), 31–48 (1957).

[171] C. A. Coverdale, C. Deeney, M. R. Douglas, J. P. Apruzese, K. G. Whitney, J. W. Thornhill, and J. Davis. *Optimal Wire-Number Range for High X-Ray Power in Long-Implosion-Time Aluminum Z Pinches.* Phys. Rev. Lett. 88, 065001 (2002).

[172] C. L. Ruiz, G. W. Cooper, S. A. Slutz, J. E. Bailey, G. A. Chandler, T. J. Nash, T. A. Mehlhorn, R. J. Leeper, D. Fehl, A. J. Nelson, J. Franklin, and L. Ziegler. *Production of Thermonuclear Neutrons from Deuterium-Filled Capsule Implosions Driven by Z-Pinch Dynamic Hohlraums.* Phys. Rev. Lett. 93, 015001 (2004).

[173] C. A. Coverdale, C. Deeney, A. L. Velikovich, R. W. Clark, Y. K. Chong, J. Davis, J. Chittenden, C. L. Ruiz, G. W. Cooper, A. J. Nelson, J. Franklin, P. D. LePell, J. P. Apruzese, J. Levine, J. Banister, and N. Qi. *Neutron production and implosion characteristics of a deuterium gas-puff Z pinch.* Physics of Plasmas 14(2), 022706 (2007).

[174] B. A. Remington, R. P. Drake, and D. D. Ryutov. *Experimental astrophysics with high power lasers and Z pinches.* Rev. Mod. Phys. 78, 755–807 (2006).

[175] T. W. L. Sanford, G. O. Allshouse, B. M. Marder, T. J. Nash, R. C. Mock, R. B. Spielman, J. F. Seamen, J. S. McGurn, D. Jobe, T. L. Gilliland, M. Vargas, K. W. Struve, W. A. Stygar, M. R. Douglas, M. K. Matzen, J. H. Hammer, J. S. De Groot, J. L. Eddleman, D. L. Peterson, D. Mosher, K. G. Whitney, J. W. Thornhill, P. E. Pulsifer, J. P. Apruzese, and Y. Maron. *Improved Symmetry Greatly Increases X-Ray Power from Wire-Array Z-Pinches.* Phys. Rev. Lett. 77, 5063–5066 (1996).

[176] J. J. Rocca, O. D. Cortázar, B. Szapiro, K. Floyd, and F. G. Tomasel. *Fast-discharge excitation of hot capillary plasmas for soft-x-ray amplifiers.* Phys. Rev. E 47, 1299–1304 (1993).

[177] J. J. Rocca, V. Shlyaptsev, F. G. Tomasel, O. D. Cortázar, D. Hartshorn, and J. L. A. Chilla. *Demonstration of a Discharge Pumped Table-Top Soft-X-Ray Laser.* Phys. Rev. Lett. 73, 2192–2195 (1994).

[178] B. R. Benware, C. D. Macchietto, C. H. Moreno, and J. J. Rocca. *Demonstration of a High Average Power Tabletop Soft X-Ray Laser.* Phys. Rev. Lett. 81, 5804–5807 (1998).

[179] W. A. Stygar, H. C. Ives, D. L. Fehl, M. E. Cuneo, M. G. Mazarakis, J. E. Bailey, G. R. Bennett, D. E. Bliss, G. A. Chandler, R. J. Leeper, M. K. Matzen, D. H. McDaniel, J. S. McGurn, J. L. McKenney, L. P. Mix, D. J. Muron, J. L. Porter, J. J. Ramirez, L. E. Ruggles, J. F. Seamen, W. W. Simpson, C. S. Speas, R. B. Spielman, K. W. Struve, J. A. Torres, R. A. Vesey, T. C. Wagoner, T. L. Gilliland, M. L. Horry, D. O. Jobe, S. E. Lazier, J. A. Mills, T. D. Mulville, J. H. Pyle, T. M. Romero, J. J. Seamen, and R. M. Smelser. *X-ray emission from z pinches at* 10^7 *A: Current scaling, gap closure, and shot-to-shot fluctuations.* Phys. Rev. E 69, 046403 (2004).

[180] Niansheng Qi, S. F. Fulghum, R. R. Prasad, and M. Krishnan. *Space and time resolved electron density and current measurements in a dense plasma focus Z-pinch.* IEEE Transactions on Plasma Science 26(4), 1127–1137 (1998).

[181] G. Avaria, M. Grisham, J. Li, F. G. Tomasel, V. N. Shlyaptsev, M. Busquet, M. Woolston, and J. J. Rocca. *Extreme Degree of Ionization in Homogenous Micro-Capillary Plasma Columns Heated by Ultrafast Current Pulses.* Phys. Rev. Lett. 114, 095001 (2015).

[182] S. Jiang, L. L. Ji, H. Audesirk, K. M. George, J. Snyder, A. Krygier, P. Poole, C. Willis, R. Daskalova, E. Chowdhury, N. S. Lewis, D. W. Schumacher, A. Pukhov, R. R. Freeman, and K. U. Akli. *Microengineering Laser Plasma Interactions at Relativistic Intensities.* Phys. Rev. Lett. 116, 085002 (2016).

[183] F. N. Beg, E. L. Clark, M. S. Wei, A. E. Dangor, R. G. Evans, A. Gopal, K. L. Lancaster, K. W. D. Ledingham, P. McKenna, P. A. Norreys, M. Tatarakis, M. Zepf, and K. Krushelnick. *High-Intensity-Laser-Driven Z Pinches.* Phys. Rev. Lett. 92, 095001 (2004).

[184] M. J.-E. Manuel, N. Sinenian, F. H. Séguin, C. K. Li, J. A. Frenje, H. G. Rinderknecht, D. T. Casey, A. B. Zylstra, R. D. Petrasso, and F. N. Beg. *Mapping return currents in laser-generated Z-pinch plasmas using proton deflectometry.* Applied Physics Letters 100(20), 203505 (2012).

[185] R. F. Benjamin, G. H. McCall, and A. W. Ehler. *Measurement of Return Current in a Laser-Produced Plasma.* Phys. Rev. Lett. 42, 890–893 (1979).

[186] A. Hauer and R. J. Mason. *Return-Current Heating and Implosion of Cylindrical CO_2-Laser-Driven Targets.* Phys. Rev. Lett. 51, 459–462 (1983).

[187] Z. Lécz and A. Andreev. *Laser-induced extreme magnetic field in nanorod targets.* New Journal of Physics 20(3), 033010 (2018).

[188] A. P. Shevelko. *X-ray spectroscopy of laser-produced plasmas using a von Hamos spectrograph.* Proc. SPIE 3406, 91–108 (1998).

[189] J. Davis. *Tensile Testing, 2nd Edition.* ASM International (2004).

[190] V. N. Shlyaptsev, J. J. Rocca, and A. L. Osterheld. *Dynamics of a capillary discharge x-ray laser.* Proc. SPIE 2520, 365–372 (1995).

[191] M. Klapisch, M. Busquet, and A. Bar-Shalom. *A New And Improved Version Of HULLAC.* AIP Conference Proceedings 926(1), 206–215 (2007).

[192] L. M. Biberman, V. S. Vorob'ev, and I. T. Yakubov. *Kinetics of Nonequilibrium Low-Temperature Plasmas.* Springer (1987). 498 pp.

[193] T. Holstein. *Imprisonment of Resonance Radiation in Gases.* Phys. Rev. 72, 1212–1233 (1947).

[194] D. Ryu, I. Chattopadhyay, and E. Choi. *Equation of State in Numerical Relativistic Hydrodynamics.* The Astrophysical Journal Supplement Series 166(1), 410–420 (2006).

[195] D. S. Clark, C. R. Weber, J. L. Milovich, J. D. Salmonson, A. L. Kritcher, S. W. Haan, B. A. Hammel, D. E. Hinkel, O. A. Hurricane, O. S. Jones, M. M. Marinak, P. K. Patel, H. F. Robey, S. M. Sepke, and M. J. Edwards. *Three-dimensional simulations of low foot and high foot implosion experiments on the National Ignition Facility.* Physics of Plasmas 23(5), 056302 (2016).

[196] T. Ditmire, J. Zweiback, V. P. Yanovsky, T. E. Cowan, G. Hays, and K. B. Wharton. *Nuclear fusion from explosions of femtosecond laser-heated deuterium clusters.* Nature 398(6727), 489–492 (1999).

[197] S. Kahaly, S. K. Yadav, W. M. Wang, S. Sengupta, Z. M. Sheng, A. Das, P. K. Kaw, and G. R. Kumar. *Near-Complete Absorption of Intense, Ultrashort Laser Light by Sub-λ Gratings.* Phys. Rev. Lett. 101, 145001 (2008).

[198] T. Nishikawa, H. Nakano, K. Oguri, N. Uesugi, M. Nakao, K. Nishio, and H. Masuda. *Nanocylinder-array structure greatly increases the soft X-ray intensity generated from femtosecond-laser-produced plasma.* Applied Physics B 73(2), 185–188 (2001).

[199] A. Ovchinnikov, O. Kostenko, O. Chefonov, O. Rosmej, N. Andreev, M. Agranat, J. Duan, J. Liu, and V. Fortov. *Characteristic X-rays generation under the action of femtosecond laser pulses on nano-structured targets.* Laser and Particle Beams 29(2), 249–254 (2011).

[200] P. P. Rajeev, P. Ayyub, S. Bagchi, and G. R. Kumar. *Nanostructures, local fields, and enhanced absorption in intense light–matter interaction.* Opt. Lett. 29(22), 2662–2664 (2004).

[201] M. J. May, Y. P. Opachich, G. E. Kemp, J. D. Colvin, M. A. Barrios, K. W. Widmann, K. B. Fournier, M. Hohenberger, F. Albert, and S. P. Regan. *Demonstration of a long pulse X-ray source at the National Ignition Facility.* Physics of Plasmas 24(4), 042701 (2017).

[202] F. Pérez, J. J. Kay, J. R. Patterson, J. Kane, B. Villette, F. Girard, C. Reverdin, M. May, J. Emig, C. Sorce, J. Colvin, S. Gammon, J. Jaquez, J. H. Satcher, and K. B. Fournier. *Efficient laser-induced 6-8 keV x-ray production from iron oxide aerogel and foil-lined cavity targets.* Physics of Plasmas 19(8), 083101 (2012).

[203] E. L. Dewald, M. Rosen, S. H. Glenzer, L. J. Suter, F. Girard, J. P. Jadaud, J. Schein, C. Constantin, F. Wagon, G. Huser, P. Neumayer, and O. L. Landen. *X-ray conversion efficiency of high-Z hohlraum wall materials for indirect drive ignition.* Physics of Plasmas 15(7), 072706 (2008).

[204] D. Babonneau, M. Primout, F. Girard, J.-P. Jadaud, M. Naudy, B. Villette, S. Depierreux, C. Blancard, G. Faussurier, K. B. Fournier, L. Suter, R. Kauffman, S. Glenzer, M. C. Miller, J. Grün, and J. Davis. *Efficient multi-keV X-ray sources from laser-exploded metallic thin foils.* Physics of Plasmas 15(9), 092702 (2008).

[205] D. Babonneau, M. Primout, F. Girard, J.-P. Jadaud, M. Naudy, B. Villette, S. Depierreux, C. Blancard, G. Faussurier, K. B. Fournier, L. Suter, R. Kauffman, S. Glenzer, M. C. Miller, J. Grün, and J. Davis. *Efficient multi-keV X-ray sources from laser-exploded metallic thin foils.* Physics of Plasmas 15(9), 092702 (2008).

[206] A. L. Prieto, M. Martín-González, J. Keyani, R. Gronsky, T. Sands, and A. M. Stacy. *The Electrodeposition of High-Density, Ordered Arrays of Bi1-xSbx Nanowires.* Journal of the American Chemical Society 125(9), 2388–2389 (2003).

[207] D. H. Martz, D. Alessi, B. M. Luther, Y. Wang, D. Kemp, M. Berrill, and J. J. Rocca. *High-energy 13.9 nm table-top soft-x-ray laser at 2.5 Hz repetition rate excited by a slab-pumped Ti:sapphire laser.* Opt. Lett. 35(10), 1632–1634 (2010).

[208] A. V. Vinogradov and V. N. Shlyaptsev. *Characteristics of a laser plasma x-ray source (review).* Soviet Journal of Quantum Electronics 17(1), 1–14 (1987).

[209] W. B. Thompson. *Thermonuclear Reaction Rates.* Proceedings of the Physical Society. Section B 70(1), 1–5 (1957).

[210] *Evaluated Nuclear Data File.* Available at: `https://www-nds.iaea.org/exfor/endf.htm`, (2017).

[211] Ziegler, J. James. *SRIM & TRIM.* `http://www.srim.org`, (2017).

[212] M. Roth, D. Jung, K. Falk, N. Guler, O. Deppert, M. Devlin, A. Favalli, J. Fernandez, D. Gautier, M. Geissel, R. Haight, C. E. Hamilton, B. M. Hegelich, R. P. Johnson, F. Merrill, G. Schaumann, K. Schoenberg, M. Schollmeier, T. Shimada, T. Taddeucci, J. L. Tybo, F. Wagner, S. A. Wender, C. H. Wilde, and G. A. Wurden. *Bright Laser-Driven Neutron Source Based on the Relativistic Transparency of Solids.* Phys. Rev. Lett. 110, 044802 (2013).

[213] C. Zulick, F. Dollar, V. Chvykov, J. Davis, G. Kalinchenko, A. Maksimchuk, G. M. Petrov, A. Raymond, A. G. R. Thomas, L. Willingale, V. Yanovsky, and K. Krushelnick. *Energetic neutron beams generated from femtosecond laser plasma interactions.* Applied Physics Letters 102(12), 124101 (2013).

[214] G. Mourou, Z. Chang, A. Maksimchuk, J. Nees, S. V. Bulanov, V. Y. Bychenkov, T. Z. Esirkepov, N. M. Naumova, F. Pegoraro, and H. Ruhl. *On the design of experiments for the study of relativistic nonlinear optics in the limit of single-cycle pulse duration and single-wavelength spot size.* Plasma Physics Reports 28(1), 12–27 (2002).

[215] M. N. Polyanskiy, M. Babzien, and I. V. Pogorelsky. *100-terawatt CO2 laser: Design and current status.* AIP Conference Proceedings 1777(1), 110006 (2016).

[216] S. Tochitsky, F. Fiuza, and C. Joshi. *Prospects and directions of CO2 laser-driven accelerators.* AIP Conference Proceedings 1777(1), 020005 (2016).

[217] G. Andriukaitis, T. Balčiūnas, S. Ališauskas, A. Pugžlys, A. Baltuška, T. Popmintchev, M.-C. Chen, M. M. Murnane, and H. C. Kapteyn. *90 GW peak power few-cycle mid-infrared pulses from an optical parametric amplifier.* Opt. Lett. 36(15), 2755–2757 (2011).

[218] V. Shumakova, S. Ališauskas, P. Malevich, C. Gollner, A. Baltuška, D. Kartashov, A. M. Zheltikov, A. V. Mitrofanov, A. A. Voronin, D. A. Sidorov-Biryukov, and A. Pugžlys. *Filamentation of mid-IR pulses in ambient air in the vicinity of molecular resonances.* Opt. Lett. 43(9), 2185–2188 (2018).

[219] P. Gibbon and A. R. Bell. *Collisionless absorption in sharp-edged plasmas.* Phys. Rev. Lett. 68, 1535–1538 (1992).

[220] S. C. Wilks and W. L. Kruer. *Absorption of ultrashort, ultra-intense laser light by solids and overdense plasmas.* IEEE Journal of Quantum Electronics 33(11), 1954–1968 (1997).

[221] P. Mulser, S. M. Weng, and T. Liseykina. *Analysis of the Brunel model and resulting hot electron spectra.* Physics of Plasmas 19(4), 043301 (2012).

[222] T. Liseykina, P. Mulser, and M. Murakami. *Collisionless absorption, hot electron generation, and energy scaling in intense laser-target interaction.* Physics of Plasmas 22(3), 033302 (2015).

[223] J. Wu and C. Guo. *Wavelength Effects on Strong-Field Single Electron Ionization.* Adv. Stud. Theor. Phys. 2, 271 (2008).

[224] J. Weisshaupt, V. Juvé, M. Holtz, S. Ku, M. Woerner, T. Elsaesser, S. Alisauskas, A. Pugzlys, and A. Baltuska. *High-brightness table-top hard X-ray source driven by sub-100-femtosecond mid-infrared pulses.* Nature Photonics 8, 927 EP (2014).

[225] J. Weisshaupt, V. Juvé, M. Holtz, M. Woerner, and T. Elsaesser. *Theoretical analysis of hard x-ray generation by nonperturbative interaction of ultrashort light pulses with a metal.* Structural Dynamics 2(2), 024102 (2015).

[226] H.-K. Chung, M. Chen, W. Morgan, Y. Ralchenko, and R. Lee. *FLYCHK: Generalized population kinetics and spectral model for rapid spectroscopic analysis for all elements.* High Energy Density Physics 1(1), 3 – 12 (2005).

[227] G. Mourou. *The ultrahigh-peak-power laser: present and future.* Applied Physics B 65(2), 205–211 (1997).

[228] C. Hahn, G. Weber, R. Märtin, S. Höfer, T. Kämpfer, and T. Stöhlker. *CdTe Timepix detectors for single-photon spectroscopy and linear polarimetry of high-flux hard x-ray radiation.* Review of Scientific Instruments 87(4), 043106 (2016).

[229] A. C. Thompson and D. Vaughan. *X-Ray Data Booklet*, page 1–16. Ernest Orlando Lawrence Berkeley National Laboratory, Berkeley, CA, USA, 3 edition (2009).

[230] M. R. Khan and M. Karimi. *K_β/K_α ratios in energy-dispersive x-ray emission analysis.* X-Ray Spectrometry 9(1), 32–35 (1980).

[231] Z. Samsonova, S. Höfer, R. Hollinger, T. Kämpfer, I. Uschmann, R. Röder, L. Trefflich, O. Rosmej, E. Förster, C. Ronning, D. Kartashov, and C. Spielmann. *Hard X-ray Generation from ZnO Nanowire Targets in a Non-Relativistic Regime of Laser-Solid Interactions.* Applied Sciences 8(10) (2018).

[232] G. H. McCall. *Calculation of X-ray bremsstrahlung and characteristic line emission produced by a Maxwellian electron distribution.* Journal of Physics D: Applied Physics 15(5), 823–831 (1982).

[233] M. Roth and M. Schollmeier. *Ion Acceleration—Target Normal Sheath Acceleration.* CERN Yellow Reports 1(0), 231 (2016).

[234] M. Sherlock. *Universal scaling of the electron distribution function in one-dimensional simulations of relativistic laser-plasma interactions.* Physics of Plasmas 16(10), 103101 (2009).

[235] A. M. Perelomov, V. S. Popov, and M. V. Terent'ev. *Ionization of Atoms in an Alternating Electric Field.* Sov. Phys. JETP 23, 924 (1966).

[236] J. Gunst, Y. A. Litvinov, C. H. Keitel, and A. Pálffy. *Dominant Secondary Nuclear Photoexcitation with the X-Ray Free-Electron Laser.* Phys. Rev. Lett. 112, 082501 (2014).

[237] J. Gunst, Y. Wu, N. Kumar, C. H. Keitel, and A. Pálffy. *Direct and secondary nuclear excitation with x-ray free-electron lasers.* Physics of Plasmas 22(11), 112706 (2015).

[238] A. Morace, L. Fedeli, D. Batani, S. Baton, F. N. Beg, S. Hulin, L. C. Jarrott, A. Margarit, M. Nakai, M. Nakatsutsumi, P. Nicolai, N. Piovella, M. S. Wei, X. Vaisseau, L. Volpe, and J. J. Santos. *Development of x-ray radiography for high energy density physics.* Physics of Plasmas 21(10), 102712 (2014).

[239] S. Mondal, Q. Wei, W. J. Ding, H. A. Hafez, M. A. Fareed, A. Laramée, X. Ropagnol, G. Zhang, S. Sun, Z. M. Sheng, J. Zhang, and T. Ozaki. *Aligned copper nanorod arrays for highly efficient generation of intense ultra-broadband THz pulses.* Scientific Reports 7, 40058 EP (2017).

[240] V. Yanovsky, V. Chvykov, G. Kalinchenko, P. Rousseau, T. Planchon, T. Matsuoka, A. Maksimchuk, J. Nees, G. Cheriaux, G. Mourou, and K. Krushelnick. *Ultra-high intensity- 300-TW laser at 0.1 Hz repetition rate.* Opt. Express 16(3), 2109–2114 (2008).

[241] F. Dollar, C. Zulick, T. Matsuoka, C. McGuffey, S. S. Bulanov, V. Chvykov, J. Davis, G. Kalinchenko, G. M. Petrov, L. Willingale, V. Yanovsky, A. Maksimchuk, A. G. R. Thomas, and K. Krushelnick. *High contrast ion acceleration at intensities exceeding* $10^{21}\ Wcm^{-2}$. Physics of Plasmas 20(5), 056703 (2013).

[242] D. C. Carroll, D. Batani, R. G. Evans, Y. Glinec, C. Homann, R. Jafer, S. Kar, F. Lindau, O. Lundh, K. Markey, D. Neely, F. Nürnberg, A. Persson, M. N. Quinn, A. P. Robinson, M. Roth, C.-G. Wahlström, X. Yuan, M. Zepf, and P. McKenna. *Dynamic control and enhancement of laser-accelerated protons using multiple laser pulses.* Comptes Rendus Physique 10(2), 188 – 196 (2009).

[243] P. McKenna, D. Carroll, O. Lundh, F. Nürnberg, K. Markey, S. Bandyopadhyay, D. Batani, R. Evans, R. Jafer, S. Kar, and et al. *Effects of front surface plasma expansion on proton acceleration in ultraintense laser irradiation of foil targets.* Laser and Particle Beams 26(4), 591–596 (2008).

[244] G. M. Petrov and J. Davis. *A generalized implicit algorithm for multi-dimensional particle-in-cell simulations in Cartesian geometry.* Physics of Plasmas 18(7), 073102 (2011).

[245] G. M. Petrov and J. Davis. *Parallelization of an Implicit Algorithm for Multi-Dimensional Particle-in-Cell Simulations.* Communications in Computational Physics 16(3), 599–611 (2014).

[246] J.-L. Liu, M. Chen, J. Zheng, Z.-M. Sheng, and C.-S. Liu. *Three dimensional effects on proton acceleration by intense laser solid target interaction.* Physics of Plasmas 20(6), 063107 (2013).

[247] D. J. Stark, L. Yin, B. J. Albright, and F. Guo. *Effects of dimensionality on kinetic simulations of laser-ion acceleration in the transparency regime.* Physics of Plasmas 24(5), 053103 (2017).

[248] I. J. Kim, K. H. Pae, C. M. Kim, H. T. Kim, J. H. Sung, S. K. Lee, T. J. Yu, I. W. Choi, C.-L. Lee, K. H. Nam, P. V. Nickles, T. M. Jeong, and J. Lee. *Transition of Proton Energy Scaling Using an Ultrathin Target Irradiated by Linearly Polarized Femtosecond Laser Pulses.* Phys. Rev. Lett. 111, 165003 (2013).

[249] L. Torrisi, M. Cutroneo, and J. Ullschmied. *TNSA and ponderomotive plasma production in enriched carbon polyethylene foils.* Physics of Plasmas 24(4), 043112 (2017).

[250] S. A. Gaillard, T. Kluge, K. A. Flippo, M. Bussmann, B. Gall, T. Lockard, M. Geissel, D. T. Offermann, M. Schollmeier, Y. Sentoku, and T. E. Cowan. *Increased laser-accelerated proton energies via direct laser-light-pressure acceleration of electrons in microcone targets.* Physics of Plasmas 18(5), 056710 (2011).

[251] C. Roedel, M. Heyer, M. Behmke, M. Kuebel, O. Jaeckel, W. Ziegler, D. Ehrt, M. C. Kaluza, and G. G. Paulus. *High repetition rate plasma mirror for temporal contrast enhancement of terawatt femtosecond laser pulses by three orders of magnitude.* Applied Physics B 103(2), 295–302 (2010).

[252] B. G. Cartwright, E. K. Shirk, and P. B. Price. *A nuclear-track-recording polymer of unique sensitivity and resolution.* Nuclear Instruments & Methods in Physics A 153(2-3), 457–460 (1978).

[253] D. A. Serebryakov, E. N. Nerush, and I. Y. Kostyukov. *Near-surface electron acceleration during intense laser–solid interaction in the grazing incidence regime.* Physics of Plasmas 24(12), 123115 (2017).

Danksagung

Nach dem Abschluss des Studiums dachte ich mir, dass das noch nicht alles gewesen sein konnte und es ging mit der Promotion in die nächste Runde. Ich habe die Zeit ausgesprochen genossen, und zwar nicht nur das Fachliche, sondern auch das Leben als Promotionsstudent. Es ist ein eigener Lebensabschnitt, der nun nach fast sechs Jahren zu Ende geht und den ich sicherlich in guter Erinnerung behalten werde. Dieses große Projekt stemmt man natürlich nicht vollkommen alleine und losgelöst wie auf einer einsamen Insel. Es sind viele Menschen involviert, denen ich an dieser Stelle danken möchte.

Mein Dank gebührt an erster Stelle meinem Doktorvater Prof. Dr. Alexander Pukhov dafür, dass er meine Arbeit mit großem Vertrauen betreut hat. Ich schätze seine Erfahrung, von der ich profitieren durfte, sowie die Freiheiten, die er mir gewährt hat und die es mir erlaubt haben, mich zu entfalten. Auch für die Finanzierung meiner Forschungstätigkeit und der Teilnahme an Konferenzen möchte ich mich bedanken.

Herrn Prof. Dr. Dr. Carsten Müller und Herrn Prof. Dr. (i.R.) Karl-Heinz Spatschek möchte ich dafür danken, ein Mitglied ihres Institutes gewesen sein zu dürfen. Ein besonderer Dank geht dabei an Herrn Prof. Dr. Dr. Carsten Müller, der sich freundlicherweise bereit erklärt hat, mein Mentor und Korreferent zu sein. Auch für seine vielen Ratschläge und die unterhaltsamen Gespräche während der Zeiten des Mittagessens bin ich dankbar.

Another word of thanks goes to Prof. Dr. Jorge Rocca, Dr. Slava Slyaptshev and Dr. Reed Hollinger from the Colorado State University; Dr. Daniil Kartashov, Prof. Dr. Christian Spielmann and Dr. Zhanna Samsonova from the Friedrich-Schiller-Universtity and the Helmholtz Institute in Jena; Prof. Dr. Oswald Willi and Dr. Bastian Aurand (thanks also for proofreading) from our Heinrich-Heine-University in Düsseldorf; Prof. Dr. Farhat Beg and Dr. Maylis Dozieres from the University of California, San Diego and all further members of all groups for the fruitful cooperation that generated new insights and great publications.

Die großartige Unterstützung bei bürokratischen Angelegenheiten durch Frau Elvira Gröters, der ich weiterhin einen wundervollen Ruhestand wünsche, und nun Frau Ute Birkenkamp, hat eine große Last abgenommen. Und was wären wir ohne unseren Systemadministrator Evgenij Braun? Er ist der unterste Jenga-Klotz des Instituts. Wenn er länger als eine Woche Urlaub hatte, löste dies unterschwellige Ängste aus, da die Gefahr für technische Ausfälle der Computer und Cluster gefühlsmäßig immer um die Ecke wartete. Aber selbst dann hat er sich per Smartphone um die Technik gekümmert und auch schon einmal seinen Urlaub unterbrochen, um erste Hilfe bei Problemen zu leisten. Ich möchte ihm auch für die vielen interessanten Gespräche danken, die wir hatten.

Auf der Zeitskala von Promotionen gelte ich mit meiner sechsjährigen Zeitdauer mittlerweile als Fossil und konnte deshalb viele Kolleginnen und Kollegen kennenlernen (und überdauern). Die Zeit am Institut wäre ohne sie nicht halb so unterhaltsam gewesen, weshalb ich einen großen Dank an Christoph Baumann, Dr. Phuc Tanh-Luu, Dr. Tobias Tückmantel, Dr. John Farmer, Camilla Willim, Dr. Friedrich Schluck, Dr. Matthias

Dellweg, Dr. Martin Jansen, Dr. Götz Lehmann, Dr. Johannes Thomas, Lars Reichwein, Dr. Roberto Martorelli, Dr. Oliver Jansen, Dr. Mykyta Cherednychek, Dr. Longqing Yi, Dr. Zi-Yu Chen, Dr. Debin Zou, Dr. Liangliang Ji, Dr. Selym Viallalba-Chavez, Alina Golub und Fiona Grüll aussprechen möchte.

Auch möchte ich all meinen Freunden aus Oberhausen und allen Anderen meinen Dank ausdrücken, die mir auch in der Freizeit immer eine kurzweilige Zeit ermöglicht haben.

Am allermeisten möchte ich aber ganz herzlich meinen Eltern (Dr. h. c) Belgüzar und (Dr. h. c) Bayram sowie meinen Geschwistern (Dr. h. c) Neşe, (Dr. h. c) Neslihan & (Dr. h. c) Frank danken. Sie haben gespannt meinen Werdegang mitverfolgt und mich geduldig mit offenem Ohr, Tatkraft und Fürsorge unterstützt, wo sie nur konnten. Ohne sie wäre ich nicht da, wo ich jetzt bin und dafür steht ihnen eigentlich ein Teil des Verdienstes zu, vielleicht in Form eines Ehrendoktortitels.